UNIVERSITY OF SOUTHAMPTON

FACULTY OF ENGINEERING, SCIENCE & MATHEMATICS

OPTOELECTRONICS RESEARCH CENTRE

Engineering Electronic and Plasmonic Materials for Novel Photonic Devices

Laura Lagonigro

Thesis for the degree of Doctor of Philosophy

December 2010

UNIVERSITY OF SOUTHAMPTON

ABSTRACT

FACULTY OF ENGINEERING, SCIENCE & MATHEMATICS
OPTOELECTRONICS RESEARCH CENTRE

Doctor of Philosophy

ENGINEERING ELECTRONIC AND PLASMONIC MATERIALS FOR NOVEL PHOTONIC DEVICES

by Laura Lagonigro

In the last decade well known materials such as metals and silicon have emerged as new materials for photonic applications leading to the growth of two important fields: plasmonics and silicon photonics. This thesis is divided in two parts with part I focusing on plasmonics, and silicon photonics are the target of part II.

Novel substrates exploiting plasmonic effects are currently the subject of extensive research in areas such as biological sensing, medicine, optical microscopy and nano-photonics. Here a new class of silver impregnated polycarbonate substrates will be presented. The fabrication process using a supercritical impregnation technique will be described and the substrates morphologically characterised before being tested for Surface Enhanced Raman Spectroscopy and Metal Enhanced Fluorescence. These substrates exhibit an excellent plasmonic response and benefit from being flexible, robust, inexpensive and biocompatible. The demonstrated ability of post processing the nanocomposites provides an additional degree of design control for a wide range of applications.

In part II semiconductor modified microstructured optical fibres (MOFs) will be presented. The combination of semiconductor materials within microstructured optical fibres can lead to highly engineerable devices with wide control over both photonic and electronic properties for both linear and non-linear photonic applications. The presented fabrication process consists of a high pressure chemical vapour deposition method which allows for conformal inclusion of materials such as silicon and germanium within the extremely high aspect ratio pores of MOFs. The deposited material is structurally characterised using SEM, TEM and Raman spectroscopy demonstrating good quality amorphous and polycrystalline growth. The project then focuses on investigating the use of these fibres for silicon photonics applications. Loss measurements performed on a range of samples reveal transmission losses potentially compatible with a wide range of non-linear photonic devices.

Declaration of Authorship

I, Laura Lagonigro, declare that the thesis entitled:

ENGINEERING ELECTRONIC AND PLASMONIC MATERIALS FOR NOVEL PHOTONIC DEVICES

and the work presented in it are my own. I confirm that:

- this work was done wholly while in candidature for a research degree at this university;
- where any part of this thesis has previously been submitted for a degree or any other qualification at this University or any other institution, this has been clearly stated;
- where I have consulted the published work of others, this is always clearly attributed;
- where I have quoted from the work of others, the source is always given. With the exception of such quotations, this thesis is entirely my own work;
- I have acknowledged all main sources of help;
- where the thesis is based on work done by myself jointly with others, I have made clear exactly what was done by others and what I have contributed myself;
- parts of this work have been published as:

Journal papers:

1.L. Lagonigro, N. Healy, J. R. Sparks, N. F. Baril, P. J. A. Sazio, J. V. Badding, and A. C. Peacock *"Low loss silicon fibers for photonics applications"* **Applied Physics Letters, 96, 041105 (2010)**

2.L. Lagonigro, A. C. Peacock, S. Rohrmoser, T. Hasell, S. M. Howdle, P. J. A. Sazio, P. Lagoudakis "*Time and spectrally resolved enhanced fluorescence using silver nanoparticle impregnated polycarbonate substrates*", **Applied Physics Letters, 93, 261114 (2008)**

3.T. Hasell*, L. Lagonigro*, A. C. Peacock, S. Yoda, P. D. Brown, P. J. A. Sazio, S. M. Howdle "*Silver Nanoparticle Impregnated Polycarbonate Substrates for Surface Enhanced Raman Spectroscopy*", **Advanced Functional Materials, 18, 1265-1271 (2008)**

Conference papers:

1.L. Lagonigro, N. V. Healy, J. R. Sparks, N. F. Baril, P. J. A. Sazio, J. V. Badding, A. C. Peacock "Wavelength-dependent loss measurements in polysilicon modified optical fibres" **CLEO/Europe-IQEC 2009**, Munich (Germany) – 15/06/2009

2.L. Lagonigro, A. C. Peacock, S. Rohrmoser, T. Hasell, S. M. Howdle, P. J. A. Sazio, P. Lagoudakis "Silver nanoparticle impregnated polycarbonate substrates for plasmonic applications" **IEEE/LEOS Winter Topicals 2009,** Innsbruck (Austria) - 12-14/01/2009

3.L. Lagonigro, A. C. Peacock, P. J. A. Sazio, T. Hasell, P.D. Brown and S. M. Howdle "Surface-Enhanced Raman Spectroscopy using silver impregnated polycarbonate substrates" **CLEO/Europe-IQEC 2007**, Munich (Germany) – 18/06/2007

Laura Lagonigro

December 2010

Acknowledgements

At the end of this journey I have the opportunity to thank all the people that made this work possible, some of them contributing to practical work, others to my mental sanity, but most of all I thank those who managed to contribute in both ways.

First, of course, I wish to thank my research group: my supervisor Pier Sazio for his guidance, patience and trust in my judgement; my co-supervisor Anna Peacock for keeping a close eye on me, pushing me when I needed and most of all for working hard for me too; Noel Healy for making many hours in the lab not so heavy and for his precious contributions to the silicon fibre work and Adrian Amezcua-Correa for tracing a clear path before me.

I thank the whole ORC staff for the outstanding support, in particular James Wilkinson for his suggestions at the intermediate steps reports and Claudio Oton for his help with the prism coupling technique.

I thank John Badding and his group at Penn State University for providing the semiconductor modified fibres and for the enjoyable collaboration, as well as for hosting me during my WUN visit. A special thanks to Venkat Gopalan and his group for the stimulating chats. Acknowledgments also have to go to WUN (Worldwide Universities Network) for funding my visit to Penn State University, which contributed enormously to my understanding of the overall aspects of the project and strengthened the collaboration.

I want to thank Pavlos Lagoudakis at the Physics Department in Southampton University, for his dedication and the enlightening chats, and his group, in particular Stefan Rohrmoser, for being a great collaborator and a lovely friend. Also I have to thank Steve Howdle and his group at the University of Nottingham for providing the plasmonic substrates.

I deeply thank Trina and Angela for always being there (I mean it ... even at 11pm!), both for theoretical and technical scientific questions or for the chats and relieving tea/coffee breaks, they made the sun shine in the office!

I want to thank Simos and Andy for the laughter and their sarcasm as well as the love they showed me; Despina for giving me the perfect starting year of my life in Southampton, being a great friend, lovely flatmate and for the crowded party arranged together; and my friends Sophie, Joel, Marty, Francesco, Valerio, Giggino, Pamela, Katia, Ophelia and many more for their incredible support!

Last but not least I thank my family for providing me with the tools to face and solve problems. I made a fair use of them in the past and it looks like I am going to need them in the future.

“Fatti non foste a viver come bruti, ma per seguir virtute e canoscenza”

(You were not born to live like brutes, but to follow virtue and knowledge)

Dante Alighieri, Inferno, canto XXVI, 119-120.

Contents

List of Figures

List of Tables

List of Abbreviations

AgPC	Silver polycarbonate
a-Si	Amorphous silicon
a-Si:H	Hydrogenated amorphous silicon
ATP	4-Aminothiophenol
CVD	Chemical vapour deposition
EDFA	Erbium doped fibre amplifier
EDX	Energy density X-ray
FET	Field effect transistor
FWHM	Full width half maximum
HC	High concentration
HPCVD	High pressure chemical vapour deposition
LC	Low concentration
LPCVD	Low pressure chemical vapour deposition
LSP	Localised surface plasmons
MEF	Metal enhanced fluorescence
MOF	Microstructured optical fibre
PBGF	Photonic bandgap fibre
PC	Polycarbonate
PD	Photodiode
PECVD	Plasma enhanced chemical vapour deposition
poly-Si	Polycrystalline silicon
PSU	Penn State University
Rh6G	Rhodamin 6G
RIE	Reactive ion etching
$scCO_2$	Supercritical carbon dioxide
SCF	Supercritical fluid
SEM	Scanning electron microscopy
SERS	Surface enhanced Raman spectroscopy
SOI	Silicon on insulator

SP	Surface plasmon
SPM	Self phase modulations
TE	Transverse electric
TEM	Transmission electron microscopy
TM	Transverse magnetic
TPA	Two photon absorption

Chapter 1

Introduction

1.1 Manipulating and controlling light on a "small" scale

Figure 1.1 *Narcissus by Caravaggio. The painter was famous for his use of light.*

In 1960 the important new field of photonics started with the advent of the first laser, for which Townes, Basov and Prokhorov won the Nobel Prize in Physics in 1964. A few years later, in 1970, the first optical fibre for telecommunication was fabricated and a new technological era based on photonic devices started. Since then generating, controlling and detecting photons has meant engineering materials on a "small" scale. Specifically this can be achieved by combining knowledge of the materials optical properties, such as refractive indexes, with the ability to engineer structures on a micrometre down to nanometre scale. This process of material manipulation has led to the discovery of new photonic applications for materials traditionally used as conductors or semiconductors.

Noble metals such as silver and gold have been "reinvented" for photonic applications and are currently the subject of extensive research in light manipulation. In fact, light can be coupled with the electronic cloud in a metallic material so that the electrons start vibrating at an optical frequency (plasmon) and propagate along the metallic surface. Moreover, when the metal has dimensions comparable with the wavelength of light then the vibration is localised and the metallic nanoparticle acts as a nanoantenna, enhancing the local electromagnetic field by several orders of magnitude. This effect has laid the foundation for the establishment of plasmonics. Surface Plasmon resonances excited on metal nanoparticles are of great interest for applications including molecular sensing, medicine, optical microscopy and nano-photonics.

Semiconductor materials such as silicon have dominated electronics for decades, with a very well established, multi-billion dollars manufacturing infrastructure. In the last decade silicon has also been "rediscovered" as a material for photonics and silicon optical interconnectors are believed to be the best candidate for replacing modern copper interconnectors [*1*], which are now the limiting factor for the development of new on-chip devices, both in terms of dimension and performance. Ultracompact lightwave circuits to be implemented on chip require strong light confinement, which is guaranteed by a high refractive index of the waveguide material. Ideally optical signals need be at telecom wavelengths in order to ease interfacing with optical fibre technology, so transparency in the infrared is also essential. Silicon not only satisfies these requirements, but its high non-linear

refractive index allows also for non-linear optical processing and non-linearities engineering [*2*]. More importantly, its compatibility with pre-existing technology allows for the possibility of low-cost production enabled by monolithic integration, which is of great interest for large scale production.

The key to exploiting these well-established materials for new applications is the ability to engineer smaller and smaller structures to modify their optical properties. Fabricating new structures can use two main approaches: top-down and bottom-up techniques. The first approach consists of etching or growing a material and is normally used to realise complex planar structures, but it can require considerable effort to obtain features with scale below a hundred nanometres. Alternatively, the bottom-up approach employs a pre-formed template to host the desired material. By using a tailored fabricated template, this technique is less restricted in terms of available materials and possible geometries. Moreover, structured pre-existing devices can be used as canvases to integrate specific materials leading to hybrid devices and tailored properties.

For example, structures like photonic crystals have been developed and applied to optical fibres. Optical fibres have been modified with tiny holes running along their entire length to create microstructured optical fibres (MOFs). These fibres can exhibit novel optical properties such as broadband single mode guidance and high nonlinearities, but most of all their parameters can be engineered by modifying the cladding lattice structure. Prior to this, dopant materials such as erbium have been introduced in the silica glass leading to the first erbium doped fibre amplifier (EDFA), which enabled signals to be amplified optically, removing the need for electronic repeaters in long haul data transmission. The hollow pores of the MOFs, however, could represent a potential template for the deposition of functional materials, enabling other operations.

In general, photonics consists of engineering materials on a scale which is “small” enough to be comparable with the optical wavelength, i.e. down to a few nanometres. This thesis will show two examples of how to exploit hybrid properties and integrated technologies by embedding different kinds of materials (semiconductors

and metals) both in a planar configuration and in microstructured optical fibres for novel photonic devices.

1.2 Thesis Structure

This thesis consists of two parts: the first part presents a new class of plasmonic substrates, whilst the second describes semiconductor modified microstructured optical fibres.

Part I introduces plasmonic materials. The mechanism of light coupling with the electronic cloud trapped on metal surfaces will be described in Chapter 2 using a classical Drude model as the starting point. Furthermore, the dependence of the resonance wavelength on the size, shape, local dielectric environment and interparticle spacing will be discussed as it enables engineering of the metal nanoparticle substrates to target specific requirements. Surface enhanced Raman spectroscopy (SERS) and metal enhanced fluorescence (MEF) will also be described focusing on the elements that are relevant for the experimental results described in Chapter 4.

In Chapter 3 silver-polymer nanocomposites will be presented as a new class of plasmonic substrates. Firstly the fabrication process of the substrates will be described followed by the characterisation of these nanocomposites using transmission electron microscopy (TEM), energy dispersive X-ray (EDX), absorption and reflectivity measurements and prism coupling technique.

In Chapter 4 our substrates will be shown to give excellent responses both for surface-enhanced Raman spectroscopy and metal-enhanced photoluminescence applications. These substrates exhibit a number of key features such as temporal stability and mechanical flexibility. Moreover, the ability to post-process such substrates will be demonstrated adding a further degree of freedom in the design of future devices.

Chapter 5 concludes the first part with a summary and a discussion about potential future works.

Part II is focused on pioneering work in semiconductor modified optical fibres for potential applications in telecommunications. In Chapters 6 and 7 optical fibres and semiconductors will be introduced, respectively. Specifically in Chapter 6 the basic mechanism of guiding light within step index optical fibres will be described together with the relevant coupling parameters. Transmission losses and non-linear behaviour will be discussed starting from the non-linear Schrödinger equation. The chapter concludes with an overview on microstructured optical fibres.

In Chapter 7, semiconductor materials are described in terms of their electronic and crystal structure, with a focus on silicon and germanium. This section will then examine the emerging field of silicon photonics reviewing some of the recent work on crystalline and amorphous silicon devices reported in the literature.

MOFs and semiconductors will then be merged in Chapter 8 presenting semiconductor modified optical fibres. The fabrication technique based on a high pressure deposition method will be described and will show how the tiny pores (~5 μm diameter) of a microstructured optical fibre can act as a chemical chamber in which silicon and/or germanium semiconductors can be integrated. This will enable new photonic and electronic functionality in the fibres, paving a way to a new generation of all-fibre optoelectronics. The structural characterization of the deposited materials using scanning electron microscopy (SEM), TEM and Raman spectroscopy will be presented together with previously published field effect transistor (FET) measurements.

In Chapter 9 experimental results on transmission loss measurements will be presented for a range of amorphous and polycrystalline silicon deposited in capillaries with diameter of ~6 μm and ~1 μm. The obtained results are promising for applications in a wide range of photonics devices, from optical modulators to Raman amplification.

Chapter 10 will summarise the results presented in Part II and will discuss two potential directions for future works and applications.

Finally Chapter 11 will conclude this thesis, collating the work of both Part I and II.

PART I

Plasmonic materials

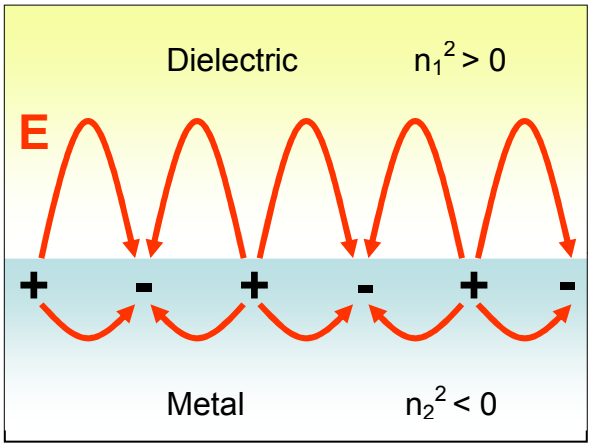

Figure I-1 *Plasmon oscillations at the dielectric metal interface.*

Plasmons are collective oscillations of the free electron density typically at optical frequencies. When a metal is irradiated, the electromagnetic fields of the incident light induce a displacement in the electronic cloud, which results in an optical absorption, and then a polarisation state. Under specific conditions, this state propagates in the form of a plasmon along the metal surface and the polarisation is induced in the surrounding medium.

Propagating surface plasmons (which exist on noble metal thin films on a dielectric) and localised surface plasmons (noble metal nanoparticles surrounded by a dielectric) have been extensively studied in the last three decades, being of great interest for applications including molecular sensing [*3*], optical microscopy [*4*], medicine [*5*] and nano-photonics [*6*]. In particular, the research work described in this part of the thesis is focused towards the development of a new class of plasmonic substrates for sensing applications.

Most plasmonic devices have been created using gold, resonant in the red, and silver, resonant in the UV-blue, but some have also been made using copper and aluminium. In particular, silver shows superior plasmonic properties to other noble metals [*7*], but it is often overlooked for plasmonic substrates due to its strong affinity to oxidation, and hence poor temporal stability. The embedding of nanoscopic metal structures into polymeric matrices, as demonstrated here, represents a convenient way to stabilise a controlled dispersion of protected nanoparticles. Supercritical carbon dioxide ($scCO_2$) has been used to produce silver nanoparticles in optically transparent polycarbonate (PC) matrices allowing for a fine scale dispersion of particles to be produced within a prefabricated polymer component. These substrates can offer significant benefits over more conventional plasmonic substrates as they are cheap, flexible, mechanically robust and temporally stable. Moreover the use polycarbonate as embedding material makes them potentially biocompatible [*8*], which is of interest for potential bio-sensing applications.

The substrates will be shown to yield excellent SERS responses for both 4-aminothiophenol and rhodamine 6G target molecules and have also been investigated for metal-enhanced photoluminescence of a blue emitting dye molecule (coumarin 102) using simultaneous time and spectrally resolved photoluminescence (Chapter 5). Post-processing the films via simple etching techniques provides an additional degree of design control and the potential to fabricate devices with unique excitation and detection geometries for a wide range of applications.

Chapter 2

Metal Nanoparticles

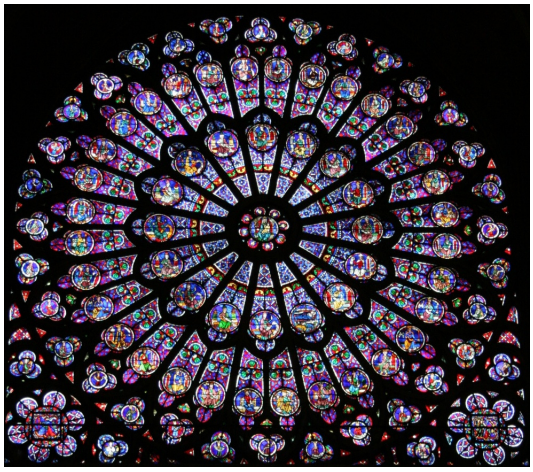

Figure 2.1 *Stained glass in Notre Dame, Paris. Metal nanoparticles embedded in the glass scatter light at different frequencies giving a range of colours [9].*

The optical properties of metal nanoparticles have been known for centuries by artists who have used them to create stained glass (Figure 2.1). These artists learnt to colour glass by adding metal salts and oxides, so that it would capture specific portions from the spectrum of white light allowing the human eye to perceive various colours.

In the last few decades scientists have investigated these optical properties in depth and now can explain the observed behaviour. In particular, the observed colour, a combination of absorption and scattering of light, depends on the size and shape of the metallic nanoparticles, the index of the surrounding material, and also on the concentration of the particles (particle interactions). A new branch of physics, plasmonics, was born. Using this knowledge the properties [of what?] can be controlled and tailored, finding application from optical filters [*10, 11*] to barcodes [*12*].

In this chapter propagating surface plasmons will be introduced in order to better understand localised surface plasmons (LSP) associated with metal nanoparticles, which will be studied in more detail in Section 2.2. For the study of localised surface plasmons, Mie theory describes the scattering of electromagnetic radiation by small particles starting from Maxwell's equations and is generally used to provide an analytical description of the field distribution around a spherical nanoparticle irradiated with light. However Mie theory's formalism can be quite extensive. Alternatively, the Drude model, which classically describes free electrons transport properties in a metal, is also used as classic approach to analytically describe the plasmonic peak position, width and medium dependence when an analytical expression of the field distribution around the nanoparticle is not necessary. This model is mathematically not "exact", but as it is free from heavy mathematical formalism it has the advantage of representing the physics in a more intuitive way.

Here, localised surface plasmons will be investigated using the Drude model to theoretically describe the optical properties of plasmonic nanoparticles embedded in a dielectric material. It will be shown how a metal nanoparticle can behave like an antenna resonating at a specific wavelength (plasmon resonance). The plasmon resonance will be shown to be tunable by changing parameters such as the size and shape of the metal nanoparticle. The interaction between adjacent particles also plays an important role, generating an even stronger enhancement of the electromagnetic field at the nanoparticles interspace (hot spots). Consequently optical processes in close proximity to the nanoparticles can be enhanced. Surface enhanced Raman spectroscopy and metal enhanced fluorescence will be investigated in Sections 2.3 and 2.4 respectively.

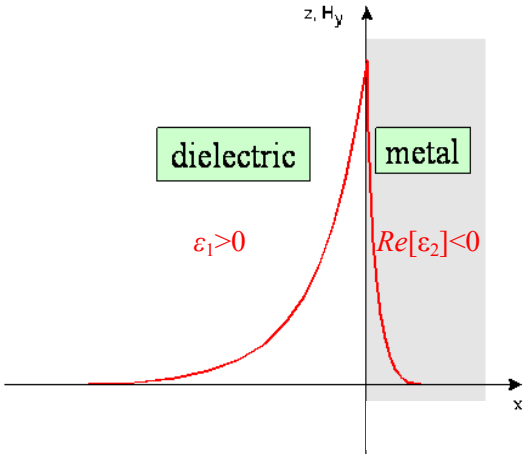

Figure 2.2 *Intensity of the electromagnetic field at the dielectric/metal interface. The mode is confined at the interface and decays exponentially moving away from the surface.*

2.1 Surface Plasmons

In a metal the electrons are quasi free particles dislocated in a type of cloud, known as a plasma. These electrons oscillate at a specific frequency, usually at UV-visible wavelengths, which is referred to as the plasma frequency.

When irradiated with light, the optical electromagnetic field couples into the plasma which starts to vibrate at optical frequencies, inducing a polarisation state. If the metal has a negative dielectric constant (gold, silver, copper etc.) and the surrounding medium has a positive dielectric constant (air, water, polymers etc.) this state propagates as a quasi-particle called a plasmon along the metal surface.

Mathematically these conditions arise from solving Maxwell's equations under the appropriate boundary conditions [*13*] to obtain the dispersion relations:

$$k_z = k_z' + ik_z'' = \frac{\omega}{c}\sqrt{\frac{\varepsilon_1\varepsilon_2}{\varepsilon_1+\varepsilon_2}}\ , \tag{2.1}$$

$$k_x = k_x' + ik_x'' = \frac{\omega}{c}\sqrt{\frac{\varepsilon_j^2}{\varepsilon_1 + \varepsilon_2}} \quad , \qquad j=1,2 \tag{2.2}$$

where ω is the electromagnetic field frequency in free space, ε_1 is the dielectric constant of the dielectric (real and positive) and ε_2 is the dielectric constant of the metal, generally complex, so that $\varepsilon_2 = \varepsilon_2' + i\varepsilon_2''$. For a bound mode, k_x must be imaginary so $\varepsilon_1 + \varepsilon_2$ must be negative, and k_z' must be real (hence $\varepsilon_2 < 0$), consequently the condition

$$\varepsilon_2' < -\varepsilon_1 \tag{2.3}$$

is required for a propagating plasmon to exist.

The plasmon is therefore confined to the surface of the metal and propagates along the metal-dielectric interface for a distance that depends on the material losses (ε_2''). If we consider $k_{SP} = k_x = k_{SP}' + ik_{SP}''$, the propagation length δ_{SP} is defined as the distance where the intensity ($I_{SP} \propto \exp(-2k_{SP}z)$)[*13*] is reduced by a factor 1/*e* and is inversely proportional to the imaginary part of the momentum k_{SP}'' according to the following:

$$\delta_{SP} = \frac{1}{2k_{SP}''} = \frac{c}{\omega}\left(\frac{\varepsilon_2' + \varepsilon_1}{\varepsilon_2'\varepsilon_1}\right)^{\frac{3}{2}} \frac{(\varepsilon_2')^2}{\varepsilon_2''} \quad . \tag{2.4}$$

δ_{SP} for silver is in the order of ten to hundreds of microns in the visible and goes up to a millimetre in the infrared [*14*].

Perpendicular to the surface the field decays exponentially both in the dielectric (δ_1) and in the metal (δ_2), with a characteristic constant expressed by;

$$\delta_i = \frac{c}{\omega}\sqrt{\frac{|\varepsilon_2'| + \varepsilon_1}{\varepsilon_i^{\,2}}} \qquad i=1,2 \tag{2.5}$$

which is generally of the order of 20-30 nm in the metal (skin depth) and of the order of a few hundred nanometres in the dielectric [*3*].

The possibility of trapping light in sub-wavelength structures exploiting propagating surface plasmons has already been investigated [*14*]. The propagation length is in fact more than enough to be used in miniaturised components and devices [*15, 16*] so information can be carried optically through plasmons. Waveguides [*17-20*] and other structures [*21, 22*] supporting propagating SPs have also been investigated, for example an interesting application is the possibility of adiabatically focusing plasmon energy using tapered metal waveguides [*23*] for enhancement of nonlinear effects [*24*] amongst other applications [*25*].

2.2 Localised Surface Plasmons

In the case of a metal nanoparticle (dimension ~5-100 nm) the plasmon is confined to the particle and will radiate an electromagnetic field characteristic of the dipolar plasmon resonance. This radiation is characterised by a spatial energy distribution where energy density is higher in some areas surrounding the particle so that any molecule in those areas experiences an enhanced local electromagnetic field.

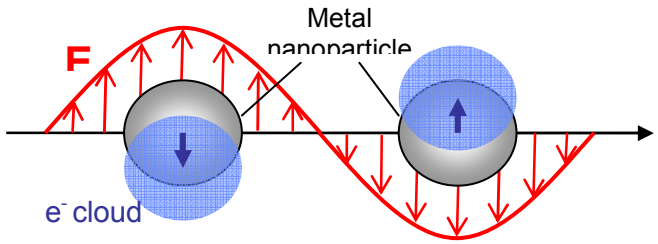

Figure 2.3 *Schematic of localised surface plasmons. LSPs consist of a periodic oscillation of the electronic cloud on the surface of the particle induced by the incident radiation [26].*

Electromagnetic theory explains why plasmons occur only in nanostructures in the range of 5-100 nm. In bigger structures the excitation beam can pump non-radiative higher order multipole plasmons, decreasing the efficiency of the dipolar plasmon pumping. For smaller (<5 nm) nanoparticles the effective conductivity of the metal

nanoparticles decreases as a result of electronic scattering processes at the particles surface and the pseudo-bulk description implicit in the definition of surface plasmons, no longer applies [*7*].

In the case of a metal nanoparticle, the dimension is smaller than the wavelength of light so that the polarisation is localised into the whole particle which starts to behave as an antenna. Consequently the electromagnetic field in the vicinity of the particle is greatly enhanced so that any material close to the metal nanoparticles can experience an enhancement of the energy density induced by the metal surface.

As previously discussed, this process is formally described through the absorption and scattering by a sphere, known as Mie theory [*27*]. This theory provides an exact solution and consequently computational tools to predict the distribution of energy in the case of a perfect sphere. For a qualitative analysis, however, an electrostatic approximation provides a good model for our problem [I'm not sure that you've explained what the problem is] and at the same time, provides a more intuitive approach to the physics behind it. In this approximation a metal particle in an electric field is described as a dipole, where the negative charges are displaced from the positive charges.

The electrostatic model will provide an estimation of the LSP frequency and will show how a localised surface plasmon depends on the material of choice (both metal and surrounding medium), but also the diameter and shape of the particle.

2.2.1 The electrostatic model

Metal nanoparticles have diameters typically in the range 1 nm to 50 nm, while the light used to excite the localised surface plasmons is in the region 350 nm to 800 nm. It is therefore justified to consider a quasi-static approximation for the electromagnetic field.

In an electrostatic approximation a metal nanoparticle having a diameter of 2R, irradiated by light with a wavelength $\lambda > R$ can be considered as a homogeneous,

isotropic sphere, dielectric constant ε_s, immersed in a medium (ε_m) and irradiated with a uniform electric field $\vec{E}_m = E_0\hat{z}$ (Figure 2.4).

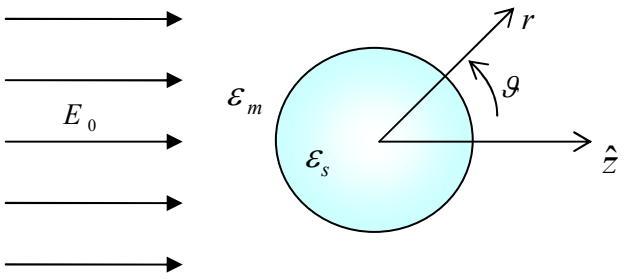

Figure 2.4 *Schematic of metal nanoparticle in uniform electromagnetic field.*

The presence of the metal sphere will distort the electric field so that [*27*]:

$$\vec{E}_s = -\nabla\Phi_s \qquad \text{for r < R} \qquad (2.6)$$

$$\vec{E}_m = -\nabla\Phi_m \qquad \text{for r > R} \qquad (2.7)$$

where $\vec{E}_s$ and $\vec{E}_m$ are the electric fields and $\Phi_s = \Phi_s(r,\vartheta)$ and $\Phi_m = \Phi_m(r,\vartheta)$ are the scalar potentials, respectively, in the sphere and in the medium. For the cylindrical symmetry of the problem the scalar potentials are independent from the azimuthal angle.

For continuity they must satisfy:

$$\Phi_s = \Phi_m \qquad \text{and} \qquad \varepsilon_s \frac{\partial\Phi_s}{\partial r} = \varepsilon_m \frac{\partial\Phi_m}{\partial r} \qquad \text{for r=R} \qquad (2.8)$$

whilst at large distances from the sphere the field will be unperturbed, so:

$$\lim_{r\to\infty}\Phi_m = -E_0 r\cos\vartheta = -E_0 z \ . \qquad (2.9)$$

It is possible to verify that the following functions are solutions to Eq.(2.6) and Eq.(2.7) and satisfy the boundary conditions of Eq.(2.8) and Eq.(2.9)

$$\Phi_s = -\frac{3\varepsilon_m}{\varepsilon_s + 2\varepsilon_m} E_0 r \cos\vartheta \ , \tag{2.10}$$

$$\Phi_m = -E_0 r \cos\vartheta + E_0 \frac{\varepsilon_s - \varepsilon_m}{\varepsilon_s + 2\varepsilon_m} R^3 \frac{\cos\vartheta}{r^2} \ . \tag{2.11}$$

Now it can be seen that the scalar potential Φ_m in Eq.(2.11) results from the superposition of the applied field (first term) and a second term due to the presence of the nanoparticle. The latter can be rewritten in terms of the potential of an ideal dipole

$$\Phi_{dipole} = \frac{\vec{p} \cdot \vec{r}}{4\pi\varepsilon_0\varepsilon_m r^3} = \frac{p\cos\vartheta}{4\pi\varepsilon_0\varepsilon_m r^2} \ , \tag{2.12}$$

where $\vec{p} = qd \cdot \hat{z}$ is the dipole moment of two charges q and $-q$ separated by distance d. By comparing Eq.(2.11) and Eq.(2.12) we see that the nanoparticle contributes to the field in the surrounding medium as a dipole [*27*]:

$$\vec{p} = \alpha\varepsilon_m \vec{E}_0 = 4\pi\varepsilon_0 R^3 \frac{\varepsilon_s - \varepsilon_m}{\varepsilon_s + 2\varepsilon_m} \varepsilon_m \vec{E}_0 \ , \tag{2.13}$$

where $\alpha = 4\pi\varepsilon_0 R^3 \frac{\varepsilon_s - \varepsilon_m}{\varepsilon_s + 2\varepsilon_m}$ is the polarisability.

The resonant condition will be satisfied when $\left|\varepsilon_s + 2\varepsilon_m\right|$ takes the minimum value, so considering that $\varepsilon_s = \varepsilon_s(\omega) = \varepsilon_s'(\omega) + i\varepsilon_s''(\omega)$ the resonant condition is satisfied for:

$$\varepsilon_s'(\omega) + 2\varepsilon_m = 0 \ . \tag{2.14}$$

Here the frequency dependence of the medium dielectric constant has been neglected as it varies slowly compared with the metal dielectric constant. Only metals such as silver, gold or copper, having negative values of $\varepsilon_s'(\omega)$ in the visible spectrum can satisfy the resonant condition at convenient wavelengths. Also, from the resonant condition, it follows that the metal losses (ε_s'') contribute to the intensity of the polarisation vector and therefore to the intensity of the resonant peak.

One of the main effects of the resonantly enhanced polarisation is the enhancement of the absorption and scattering of the metal nanoparticle. In fact it is possible to obtain the absorption and scattering cross-section σ_{abs} and σ_{sca} from the expression of the polarisability α as below [*27*]:

$$\sigma_{abs} = k \cdot \mathrm{Im}\{\alpha\} = 4\pi\varepsilon_0 k R^3 \,\mathrm{Im}\left\{\frac{\varepsilon_s - \varepsilon_m}{\varepsilon_s + 2\varepsilon_m}\right\}, \tag{2.15}$$

$$\sigma_{sca} = \frac{k^4}{6\pi} \cdot |\alpha|^2 = \frac{8\pi}{3} \varepsilon_0 k^4 R^6 \left|\frac{\varepsilon_s - \varepsilon_m}{\varepsilon_s + 2\varepsilon_m}\right|^2, \tag{2.16}$$

where it is clear that both are enhanced at the LSP resonant condition. The extinction cross section $\sigma_{ext}(\omega) = \sigma_{abs}(\omega) + \sigma_{sca}(\omega)$ can be calculated and written as [*28*]:

$$\sigma_{ext}(\omega) = 9\frac{\omega}{c}\varepsilon_0 \varepsilon_m^{3/2} V \frac{\varepsilon_s''(\omega)}{[\varepsilon_s'(\omega) + 2\varepsilon_m(\omega)]^2 + \varepsilon_s''(\omega)^2}, \tag{2.17}$$

where V is the nanoparticle volume. The extinction coefficient therefore also has a resonance peak when $\varepsilon_s' = -2\varepsilon_m$. The sharpness of the resonance is determined by the imaginary part of the dielectric function, ε_s''. The lower ε_s'' value of silver, compared with other metals [*29*], makes it in theory the best candidate for plasmonic applications.

2.2.2 LSP resonance: medium dependence

According to the Drude model, which describes the "free electrons" behaviour in metals, the dielectric function ε for free electrons can be expressed as:

$$\varepsilon = 1 - \frac{\omega_p^2}{\omega^2 + i\gamma\omega}, \tag{2.18}$$

where ω_p is the plasma frequency and γ is the electronic scattering rate of the material, which is the inverse of the electronic mean free path; this parameter will be

discussed more in detail in Section 2.2.3. The plasma frequency is also a defining characteristic of the metal being written as:

$$\omega_p = \sqrt{\frac{n_e e^2}{m\varepsilon_0}} \quad , \tag{2.19}$$

where n_e is the density of free electrons in the metal, and m and e, respectively, are the effective mass and charge of the electron.

In the approximation of negligible losses ($\gamma \ll \omega$) [*30*], the Eq.(2.18) can be separated in real and imaginary part as:

$$\varepsilon' \cong 1 - \frac{\omega_p^2}{\omega^2} \quad , \tag{2.20}$$

$$\varepsilon'' \cong \frac{\omega_p^2 \gamma}{\omega^3} \quad . \tag{2.21}$$

Comparing the Eq.(2.20) with the resonant condition in Eq.(2.14) it is possible to obtain an estimation of the surface plasmon resonance frequency as a function of the plasma frequency:

$$\omega_{SP} \cong \frac{\omega_p}{\sqrt{1+2\varepsilon_m}} \quad . \tag{2.22}$$

This relation shows how the surface plasmon resonance is related to the choice of the metal and the surrounding medium. In the case where air is the surrounding medium then $\varepsilon_m = 1$ and $\omega_{SP}(air) \cong \omega_p / \sqrt{3}$.

2.2.2.1 Bound electrons correction

The Drude model takes into account only the free electrons as they move in a fixed system of positive ions, but in reality the bound electrons also contribute to the optical properties of the free electrons. Eq.(2.20) can be rewritten to include the bound electron contribution ε_b to the dielectric constant as:

$$\varepsilon' \cong \varepsilon_b + 1 - \frac{\omega_p^2}{\omega^2} \quad . \tag{2.23}$$

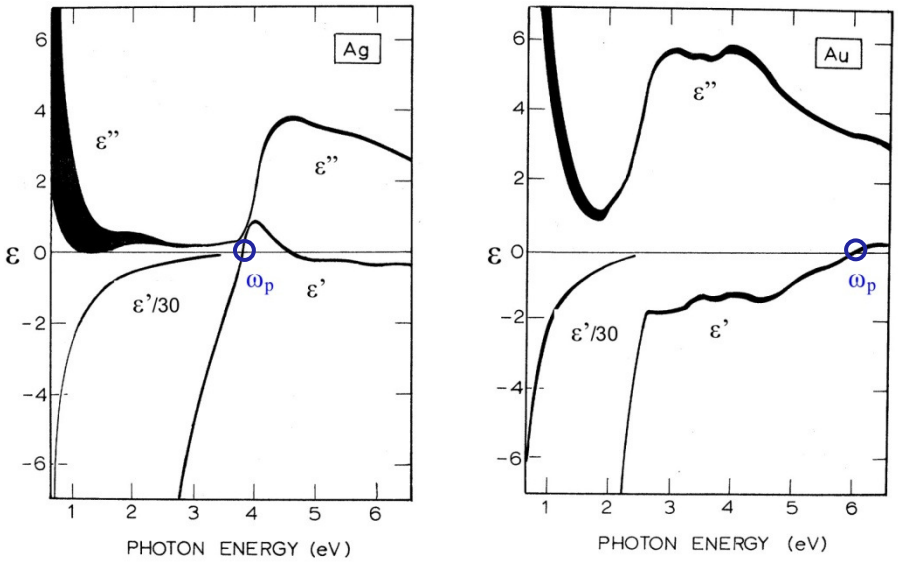

Figure 2.5 *Dielectric constants (experimental measurements) as a function of energy for silver (left) and gold (right). The line width of the curves is representative of the instrumental error [29].*

The bound electron contribution is positive and a function of the frequency. It can be determined by the difference between experimental measurements of the dielectric constant and theoretical data. In silver, for example, the bound electron contribution is responsible for the peak in the experimental function ε' around 4 eV (see Figure 2.5) and shifts the experimental plasma frequency (defined as the frequency ω for which $\varepsilon'=0$) and therefore the surface plasmon resonance to a lower energy.

2.2.3 LSP resonance: size dependence

Experimentally a shift in the LSP resonant frequency has been observed when there is a change in the diameter of the spherical nanoparticle [*31, 32*]. Mathematically this is not directly evident in the electrostatic model, where a dependence on R is only exhibited in the polarisation peak intensity, as shown in Eq.(2.13). The size

dependence of the resonance is generally introduced by considering a size dependent dielectric constant $\varepsilon_s=\varepsilon_s(\omega,R)$ [*32*]. In the Mie theory [*27*], this shift is accounted for in terms of a higher order of approximation of the resonant condition, so that the Eq.(2.14) has to be modified as follows:

$$\varepsilon_s'(\omega,R) = -\left[2+\frac{12}{5}x(\omega,R)\right]\varepsilon_m \ , \tag{2.24}$$

where $x=kR$ is the size dependent parameter and k is the wavevector ($k=c/\omega=2\pi/\lambda$). So, the electrostatic approximation, where $R\ll\lambda$ and then $x \to 0$, is a particular case. Eq.(2.24) also indicates that if ε' is an increasing function with the frequency then an increase in size will shift the plasmonic peak towards longer wavelengths.

Another experimentally observed size dependent parameter is the width of the plasmonic peak, which is given by the electronic scattering rate γ [*32*]. This parameter is generally connected with bulk scattering processes and determines the electron lifetime, but as soon as the size of a nanoparticle shrinks down to a length comparable with the electron mean free path (order of tens of nanometres), the interaction of the electrons with the surface becomes important.

The contribution to the scattering rate is essentially determined by the volume to surface ratio, therefore the 1/R dependence of the modified parameter γ is given by:

$$\gamma = \gamma_0 + \frac{Av_F}{R} \tag{2.25}$$

where γ_0 is the bulk damping constant, v_F is the electrons velocity at Fermi energy and A is a constant which depends on the theory [*31, 33*].

2.2.3.1 Higher orders SP modes

By increasing the size of a spherical nanoparticle, modes of a higher order than dipole (quadrupole, etc) are possible [*26*] which can generate plasmonic peaks at shifted frequencies compared with the fundamental. It is possible to demonstrate that a general solution to Maxwell's equations (Eq.(2.6) and (2.7)) has angular solutions which are just spherical harmonics and a radial solution which depends on r^l and

$r^{-(l+1)}$, where l is the angular momentum (l=0,1,2,...). The dipole case corresponds to l=1, the quadrupole term to l=2 and so on.

The polarisability β of a quadrupole becomes:

$$\beta \propto R^5 \frac{\varepsilon_s - \varepsilon_m}{\varepsilon_s + 3/2\,\varepsilon_m} \tag{2.26}$$

so the quadrupole case has a blue-shifted resonance compared with the corresponding dipole. Extending to the general case the resonant condition will be:

$$\varepsilon_s' + \frac{(l+1)}{l}\varepsilon_m = 0 \tag{2.27}$$

where, as before, ε_s' is the real part of the metal dielectric constant and ε_m is the dielectric constant of the surrounding medium.

2.2.4 Other shapes and nanoparticle interactions

The growing interest in plasmonic properties soon moved researchers' efforts beyond synthesis of simple spheres. Rods [*34, 35*] and triangular nanoparticles [*36*], but also cubes [*35*] and even stars [*37*] have been realised using colloidal or lithographic techniques. If we drop the hypothesis of a perfect sphere and introduce other shapes the solutions to Maxwell's equations become more complicated.

Typically plasmonic peaks shift to longer wavelengths with increasing aspect ratio of the nanoparticle and this shift is significantly stronger than the shift that can be obtained by size-tuning a spherical nanoparticle. For example in the case of silver, a nanosphere has a plasmon resonance in the blue around 410 nm, while triangles and nanorods have their resonance in the red.

The plasmon resonance is also expected to change when two particles are close enough to let the localised modes interact [*6, 38*] and a further degree of control in tailoring plasmonic resonance is added by controlling the interparticle distance. In particular when the distance d is small enough ($d \ll \lambda$) a near-field interaction occurs.

In this case the relative direction of the excitation field with the position of the nanoparticles is also important and can induce an LSP resonance shift to either higher or lower frequencies [*39*]. Intuitively, if the electromagnetic field is polarised longitudinally (along the particles axis), the plasma restoring force is reduced by the

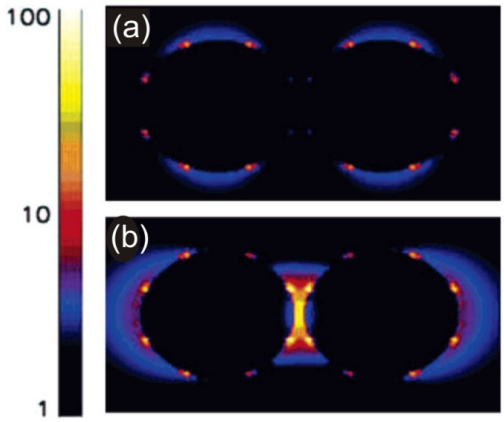

Figure 2.6 *Electromagnetic near-field enhancement at excitation laser wavelength (633 nm) for a 30 nm diameter nanoparticle dimer with (a) longitudinal incident field and (b) transversal incident field. The colour scale represents the electromagnetic field enhancement factor [38]*

coupling with the neighbour, so the resonance shifts to a lower frequency. On the other hand, if the electromagnetic field is transverse to the particles axis, the plasma restoring force is increased by the coupling with the neighbour, so the resonance shifts to a higher frequency.

Another interesting consequence of the near-field interaction, in the case of longitudinal excitation, is the strong localisation of the field in the interstitial space between the particles (hot-spot) [*38*]. Indeed the suppression of the scattering into the far-field by the neighbouring particle leads to an even stronger localisation of energy compared to that of a single particle. This can be responsible for very strong signals in optical enhancement effects such as surface enhanced Raman scattering and metal enhanced fluorescence, as shown in the next sections.

2.3 Surface Enhanced Raman Scattering

Up to this point we have described how localised surface plasmons are generated in metal nanoparticles irradiated by an electromagnetic field and that under certain conditions this results in an enhancement of the local field. When a probe molecule is placed in the vicinity of a metal nanoparticle irradiated under the above conditions, it experiences the local electromagnetic field, resulting in an enhanced response by its optical properties. One of the main applications of this effect is in Raman spectroscopy, so that it is studied and reported as the surface SERS effect.

2.3.1 Raman Scattering

Raman Scattering is an effect involving two photons and one phonon, where a photon is scattered inelastically by an atom with two possible results: a lower energy photon and a phonon are emitted (Stokes line) or a phonon is absorbed and a higher energy photon is emitted (anti-Stokes line). The phonon involved has energy typical of the material, because it corresponds to one of the vibrational states of the molecule.

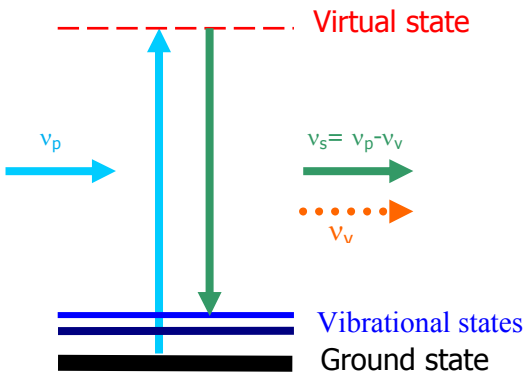

Figure 2.7 *Schematic of a Raman scattering process. Here a photon ν_p is inelastically scattered to a lower energy photon ν_s, generating a phonon ν_v.*

Raman scattering can be described by a classical electrodynamics model. For spontaneous scattering, the thermal vibration of the lattice produces a sinusoidal modulation of the polarisability $\alpha = \alpha_0 + \alpha_v \sin \omega_v t$, where ω_v is the vibrational frequency of the lattice. The incident field $E_p = E_0 \sin \omega_p t$ (where ω_p is the pump frequency) induce an electrical polarisation *P*:

$$P = \alpha \cdot E_p = \alpha_0 E_0 \sin \omega_p t + \alpha_v E_0 \left(\sin \omega_v t \cdot \sin \omega_p t\right) =$$

$$= \alpha_0 E_0 \sin \omega_p t + \frac{1}{2} \alpha_v E_0 \left[\cos\left(\omega_p - \omega_v\right) \cdot t - \cos\left(\omega_p + \omega_v\right) \cdot t\right], \qquad (2.28)$$

resulting in a component elastically scattered at the frequency ω_p and two generated waves at the difference frequency (Stokes waves) and at the sum frequency (anti-Stokes waves). According to the Bose statistics the Stokes power is $\frac{1+N}{N}$ times the anti-Stokes power, where

$$N = \frac{1}{\exp\left(\hbar \omega_v / kT\right) - 1}, \qquad (2.29)$$

is the Bose occupancy factor of the vibrational state and depends on the temperature *T*, whilst $\hbar$ and *k* are respectively Dirac and Boltzmann constants. It is clear that $N<1$, so the Stokes wave is stronger than the anti-Stokes.

Detecting the energy shift of the scattered photon provides a molecular fingerprint of the material, thus making it possible to get information about the nature of the material itself.

2.3.2 SERS spectroscopy

Surface enhanced Raman spectroscopy is a valuable tool for chemical structure analysis as a Raman signal is strongly enhanced by the surface plasmons in two different ways. The first is purely electromagnetic and its main features can be described through the electromagnetic theory shown in the previous sections and is

typically associated with enhancement factors of up to 10^8 in a single molecule [*40*]. A secondary effect, however, can arise when a chemical bond is formed between the molecule and the metal nanoparticle, causing an increase of the effective Raman cross section due to the hybridisation of the molecule and metal electron orbitals; this is often referred to as chemical enhancement [*41-43*] and is believed to contribute with an enhancement factor of up to 10^2.

Both effects can be described by the following: consider a probe molecule, vibrating at a characteristic frequency ν_v and irradiated at a certain frequency ν_p; the power $\wp_S$ of the inelastically scattered light at the Stokes band can be written as [*28*]:

$$\wp_S(\nu_S) = \sigma_{RS} I(\nu_p) \ , \tag{2.30}$$

where $\nu_S = \nu_p - \nu_v$ is the frequency of the Stokes band, σ_{RS} is the scattering cross section and $I(\nu_p)$ is the intensity of the incident light (pump). If the probe molecule is in proximity to a metallic nanoparticle the power of the scattered light can be modified as mentioned before in two ways: firstly the increase of the local electromagnetic field via surface plasmon excitation, and secondly the increase of the scattering cross section due to the chemical bond. The former effect is purely electromagnetic and increases both the incident light and the scattered light, so if we call

$$g(\nu) = |E_L(\nu)| / |E_0| \tag{2.31}$$

the enhancement factor of the local field, where $E_L(\nu)$ is the local field and E_0 is the incident field, the power of the scattered light can be rewritten as:

$$\wp_S{}^*(\nu_S) = \sigma_{SERS} g^2(\nu_S) \cdot I_p{}^* = \sigma_{SERS} g^2(\nu_S) \cdot g^2(\nu_p) I(\nu_p) \ . \tag{2.32}$$

where $\sigma_{SERS} = a\sigma_{RS}$, where a is a constant that takes into account the increase in scattering cross section due to the chemical enhancement, and $I_p{}^*$ is the locally enhanced pump intensity.

Since the Raman shift $\nu_p - \nu_S$ is much smaller than the plasmon linewidth, then

$$g(\nu_p) \approx g(\nu_S) = g \ , \tag{2.33}$$

which can be substituted in Eq.(2.32) obtaining the following expression for the scattered power:

$$\wp_S{}^*(\nu_S) = \sigma_{SERS} g^4 I(\nu_p) = G\sigma_{RS} I(\nu_p) = G\wp_S(\nu_S) \ , \tag{2.34}$$

with $G=ag^4$ being the total Raman response enhancement factor, a product of the chemical enhancement contribution a and of the electromagnetic contribution g^4. In particular from the Eq.(2.34) the electromagnetic contribution to SERS is found to be proportional to the fourth power of the local electromagnetic field enhancement [*44, 45*].

In the case of nanoparticle aggregates the expected Raman response has been calculated to depend only on the third power of the local field enhancement [*40, 46*]. In this context the theoretical value for G was estimated for both electromagnetic and chemical enhancement of spherical single particles with a result not greater than $\sim 10^{11}$. Experimental results however, have demonstrated enhancement up to 10^{14}, as in the case of single molecule detection [*47, 48*] showing that greater enhancement is possible but other effects have to be considered [*49, 50*].

2.4 Metal Enhanced Fluorescence

Photoluminescence (PL) plays a central role in many aspects of biological and medical research with applications including DNA sequencing [*51*], cell imaging [*52*] and sensing [*53*]. Similar to SERS, surface plasmons can also increase the PL response of molecules in close proximity to the metal [*54, 55*] by enhancing photon-matter interaction via a modification of the excitation cross section [55] and of the radiative decay rate k_r.

A simple estimation of the enhancement factor G as shown in the case of SERS, is not immediately found for MEF. Firstly, the main quantitative difference is to be found in the wavelength shift at which emission occurs. Whilst Raman shift is in the order of a few nanometers (vibrational energies), PL is normally shifted from the

pump wavelength of 10-100 nanometers (electronic energies), so Eq.(2.33) no longer applies and the emitted light is more likely to fall out of the plasmonic resonance. In this case $G_{PL} \propto g^2$, where g is the local field enhancement factor defined in Eq. (2.31), would be a better approximation [*56, 57*] and partially justify why in MEF experiments the observed enhancement factor are much lower than what reported for SERS. Furthermore, PL measurements involve also absorption and quantum efficiency, which can also be modified by surface plasmons coupling and hence make difficult to practically separate each effect.

Metal-enhanced fluorescence has been generally associated with a reduction in photons' lifetime τ [*58, 59*], where

$$\tau = \frac{1}{k_r + k_{nr}} , \tag{2.35}$$

and both the radiative and non-radiative rates are enhanced under plasmon coupling. In fact the enhancement of non-radiative channels (k_{nr}) results in some cases in photoluminescence quenching [*60, 61*]. Purcell Factor in MEF

The Purcell effect is a concept "borrowed" from cavity quantum electro-dynamics [*62, 63*], which studies the quantum interaction between matter (atoms) and an electromagnetic field (photons), specifically inside microresonators. In 1946 Purcell discovered that spontaneous emission of a fluorophore could be modified by placing it in a matching resonant cavity [*64, 65*]. In particular, the radiative rate k is enhanced or suppressed by a factor (Purcell factor) that depends on the cavity design, on the location of the emitter in the electromagnetic field and its relative orientation [*66*]. As such, it has been widely investigated for atoms in two-dimensional [*67*], three-dimensional [*66*] and photonic crystal structures [*68*].

Similarly the Purcell factor can be used to identify the enhancement (or quenching) of photoluminescence due to plasmon coupling in terms of a modified spontaneous emission rates via the relation:

$$F_P = \frac{k^*}{k} , \tag{2.36}$$

where k^* and k indicates, respectively, the plasmon modified and unmodified emission rates. The Purcell factor can also be expressed in terms of the photon lifetime $\tau=1/k$ as

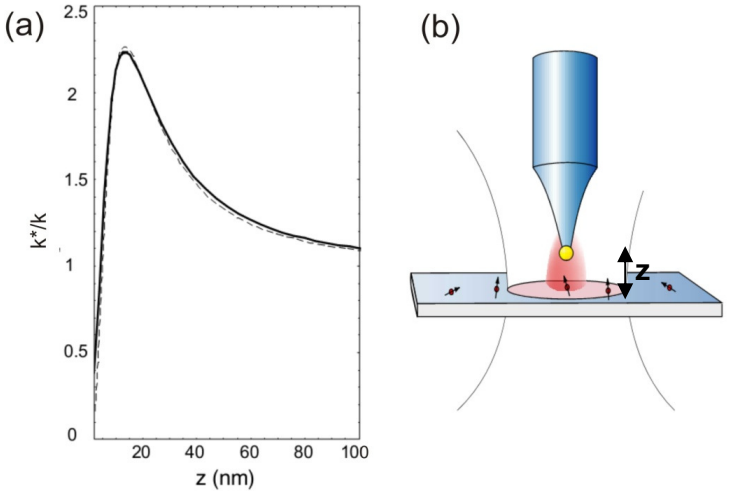

Figure 2.8 *(a) Fluorescence enhancement calculated as a function of the distance between a 60 nm diameter gold particle and the fluorophore. (b) Schematic of the experiment: the metal nanoparticle is attached to the end of a pointed tip to control the distance z from the fluorescent molecule [69].*

$$F_P = \frac{\tau}{\tau^*} \ . \tag{2.37}$$

In plasmonics the Purcell factor has been found to depend on the distance between the metal nanoparticle and the emitting molecule. Figure 2.8 shows an example of fluorescence enhancement calculated as a function of the distance. From this it can be seen that the luminescence quenching ($0 < F_P < 1$) occurs for distances up to 5 nm where the non-radiative channels from the molecule to the metal are dominant. As the distance increases the enhancement shows a maximum around z = 15 nm and then reduces towards a non-interactive distance ($F_P = 1$). The numbers given here depend on the system being investigated, and thus are only indicative. Quenching has been reported in literature to be observed for distances up to 16 nm [*61*], whilst the maximum of the enhancement has also been observed for a distance of ~10 nm [*69, 70*].

Previous work has shown that in terms of excitation wavelength, the maximum enhancement occurs for wavelengths slightly red-shifted compared with the plasmonic resonance [*69*]. Okamoto and co-workers reported the study of the Purcell factor as a function of the emission wavelength [*59, 71*] in the case of quantum dots and quantum wells.

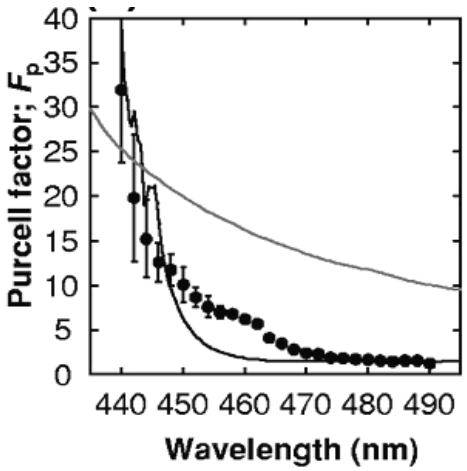

Figure 2.9 *Purcell enhancement factors plotted against wavelength of silver coated InGaN-GaN quantum wells. Fp was obtained by the ratio of PL lifetimes (dots), by the ratios of PL intensities (solid black line) and compared with theoretical values (grey line) [72].*

Results reported for enhanced PL in quantum wells are shown in Figure 2.9. The wavelength dependence of the Purcell factor qualitatively resembles the results obtained for the substrates investigated in this thesis, which will be discussed in Section 4.2.4.

Although the Purcell enhancement factor is typically found in the order of ~10 [*57, 73-75*], MEF has led to the demonstration of optical probes with enhanced brightness such that we expect it to play an important role in the next generation of photonic devices, from biosensors [*58*] to LEDs [*76*].

Chapter 3

Silver Impregnated Polycarbonate Substrates

Figure 3.1 *Image of a silver impregnated polycarbonate strip*

In the previous chapter it has been shown that surface plasmons induce enhanced electromagnetic fields in the vicinity of the metal surface when excited near the plasmon frequency. For the fabrication of a plasmonic substrate four main elements

need to be considered: the enhancement factor, the cost, the substrate lifetime and the signal reproducibility.

Silver nanoparticles are known to have superior plasmonic properties [*29*], so it certainly the best candidate for achieving the highest enhancement factor, but, as previously mentioned, has been overlooked for plasmonic substrates because they are predisposed to oxidation (in the order of days [*77*]) leading to problems with long term storage. Plasmonic substrates, in fact, generally have the active metal surface exposed to air so that, in the case of silver, they suffer from poor temporal stability, resulting from oxidation. Attempts have been made in coating silver nanoparticles to prevent oxidation, but this further step may clash with the need of a simple fabrication process. For this reason commercially available plasmonic substrates, such as Klarite by Renishaw Diagnostic, employ gold, which is evaporated or dispersed on silicon substrates. Whilst Klarite claims SERS enhancement factors in the order of 10^4-10^6, these substrates may to some degree sacrifice the quality of the plasmonic response which for gold is inferior compared with silver, for its chemical stability. Therefore, the solution to the issue of how to use silver in an efficient cost-effective way is still open.

Using conventional semiconductor processing technologies, plasmonic templates have been produced via electron beam lithography [*48, 78*], focused ion beam patterning [*79*], thermal evaporation [*80*], chemical colloid reactions [*81*] and chemical surface modification [*54*]. Recently, developments in the surface science and nano-processing techniques have permitted the fabrication of substrates that can provide high SERS signals reproducibility over the active region. Such processing techniques however, are sometimes costly and time consuming and often result in substrates which are fragile. So ideally a one step, or single reactor process, would simplify and cut the cost of production.

Furthermore, the choice of the hosting substrate material is ideally inexpensive robust and, for specific applications, biocompatible. Silicon is generally used as base material for commercially available plasmonic substrates because it is inexpensive, but in order to offer a high SERS signal reproducibility (eg. Klarite), the silicon substrates need to be microstructured via selective etching process prior to gold

evaporation. Overall the process can be quite expensive and the substrates fragile (so they need to be mounted on glass slides). Plastics in general can be very inexpensive and robust. Polycarbonate in particular is an excellent candidate in that it can be less expensive than silicon, polycarbonate costing ~$3000/tonnes (source ICIS).

If SERS and MEF are to be used readily in routine procedures, then ideally the substrates need to employ silver for its superior plasmonic properties and at the same time be inexpensive, robust and stable so that they can be stored for long lengths of time between measurements, which also should be reproducible.

The silver impregnated polycarbonate substrates presented in this thesis will address a number of issues discussed above. Prof. S. Howdle and co-workers at the University of Nottingham have successfully developed a supercritical technique for embedding metal nanoparticles into polymer hosts, such as Teflon® AF and poly(methyl-methacrylate) [*82*]. In collaboration with Howdle's group, this technique has been tailored to fabricate a new class of plasmonic substrate, where silver nanoparticles are embedded into polycarbonate strips for potential sensing applications.

These metal-polymer composites allow for the construction of optical-plasmonic devices that can exploit the mechanical robustness and flexibility of the polymer host, which also has the advantage of being potentially biocompatible [*8*]. Embedding silver nanoparticles in a polycarbonate provides protection of the metal from the surrounding environment, thus yielding a high degree of the substrate's temporal stability, which will be demonstrated to be at least in the order of months in Chapter 4.

In these substrates, only the metal nanoparticles impregnated within a few nanometres from the surface are expected to become in contact with the deposited analyte and hence to contribute to the plasmonic response. An important role is also played by the solvent used to deposit the analyte, in that some solvents may permeate into the substrates allowing for an increased particle-analyte interaction. The role of the solvent will also be investigated in Chapter 4.

In this chapter the concept of a supercritical fluid is introduced. Supercritical fluids are crucial both for the fabrication of the plasmonic substrates presented here and of the semiconductor modified MOFs studied in PART II. After describing their fabrication process, the characterisation of silver impregnated polycarbonate substrates will be presented using TEM to observe the embedded nanoparticles and EDX analysis to confirm the presence of metallic silver. Absorption and reflectivity spectra will reveal the plasmonic peaks and a prism coupling technique will be used to measure the refractive index of the impregnated film. The obtained results reveal the formation of silver nanoparticles, about 5-10 nm in size, uniformly distributed within a few microns of the surface and with an average refractive index that is higher compared with the unmodified polycarbonate. Samples fabricated with different synthesis parameters will also be investigated to better understand how these parameters affect the impregnation.

The plasmonic substrates used in this work were fabricated and partly characterised (TEM and EDX measurements) by Dr. Howdle's group at the University of Nottingham.

3.1 Supercritical fluid processing

A fluid is defined as supercritical (i.e. it is in the supercritical state) when the difference between coexisting liquid and vapour phases disappears. The supercritical phase of a fluid occurs when both its temperature and pressure are higher than certain values, which are characteristic of the fluid. For example in the case of CO_2 the critical temperature is T_c = 31.1 °C and the critical pressure P_c = 73.8 bar. A supercritical fluid (SCF) displays unusual and intriguing properties that can lead to new chemistries [*83, 84*].

Supercritical fluids exhibit the solvent properties of liquids associated with their high densities, combined with the advantage of the transportation properties of a gas, as they have no surface tension. Moreover, in the supercritical regime (see Figure 3.2), a state of liquid-like density can transform into one of vapour-like density by tuning the temperature or the pressure without the appearance of an interface [*85*].

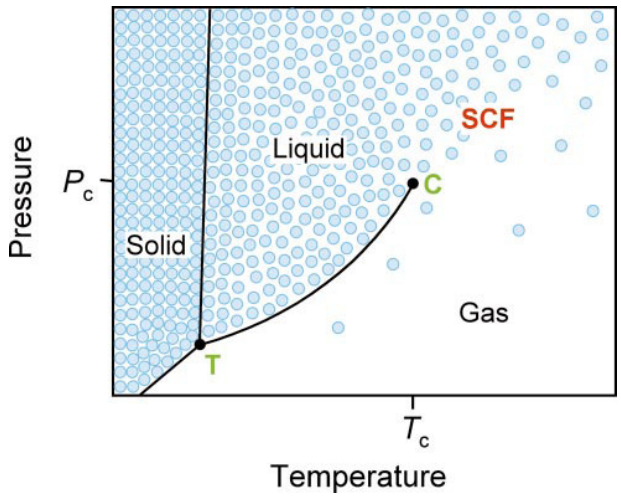

Figure 3.2 *Pressure temperature phase diagram for a pure substance. It shows the SCF state. The blue circles represent the variation in density. The triple point (T) and the critical point (c) are displayed [86].*

These characteristics of supercritical fluids make them ideal solvents for the infiltration of substances within microscale structures. In fact, since the solubility of solids depends on the density of the fluid, the tuning of the solubility in supercritical fluids can be exploited to control the composition and morphology of the materials which are to be deposited. At the same time, the absence of surface tension allows for a much faster diffusion in supercritical fluids than in liquid solvents.

Supercritical processing will be used again in Part II of this thesis, where a supercritical fluid acts as a solvent for the semiconductor precursors for the deposition of semiconductor materials inside the tiny pores of a microstructured optical fibre. In this chapter, supercritical processing has been exploited for the impregnation of a metal precursor inside a polymer strip to fabricate silver impregnated polycarbonate substrates, as described in the next section.

3.2 Fabrication

Deposition of metal nanoparticles on polymeric materials has been reported [*73*], however, most plastics do not possess an interfacial chemical structure suitable for

immobilizing metal particles, hence surface modification of either material is required. Supercritical carbon dioxide processing offers a simple route to produce the metal nanoparticles *in situ* within prefabricated polymeric materials [*87, 88*]. This method is preferable to incorporating pre-formed nanoparticles into a polymer as it does not require surface modification of the nanoparticles and avoids the possibility of aggregation of the particles during processing. Importantly, the polymeric materials can be impregnated with nanoparticles after they have been processed in their final form.

The single reactor process described here it has been developed at the University of Nottingham and it has been reported to be reproducible in terms of particle size [*82*] and deposition depth (see Figure 3.5). Moreover, it is highly flexible as it can be potentially adjusted for the impregnation of other metals in different polymers. As the plasmon resonance wavelength depends on the particle size, local dielectric environment and interparticle spacing (see Section 2.2), these substrates can be engineered to target specific requirements, simply by tuning the deposition conditions and/or by using different polymers.

Although, as described below, currently three samples of 1×2 cm size can be fabricated in three days, this process is highly scalable by scaling up the autoclave to allow for impregnation of large polymeric sheets (which could be easily cut in smaller pieces in a second stage, according to requirements) and the impregnation time can be optimised, reducing enormously the fabrication cost of a single substrate. A clear advantage is also to be found in the single reactor process, which means that only one chamber will be involved in the development of the apparatus and costs related to the space are also reduced compared with a multi-stage process.

For the purpose of this thesis polycarbonate strips were used and placed inside a custom built high pressure, clamp sealed autoclave of 60 ml volume which contains a directly coupled magnetically driven agitator [*83*]. The reactor was modified to enable the polycarbonate strips to be attached vertically to the sides of the agitator bar to provide a symmetric and dynamic environment during the reaction. Polycarbonate was obtained from Nigel Smith Alloys Ltd as 0.5 mm thick sheets and processed in house with typical final sample sizes of ~22×10 mm.

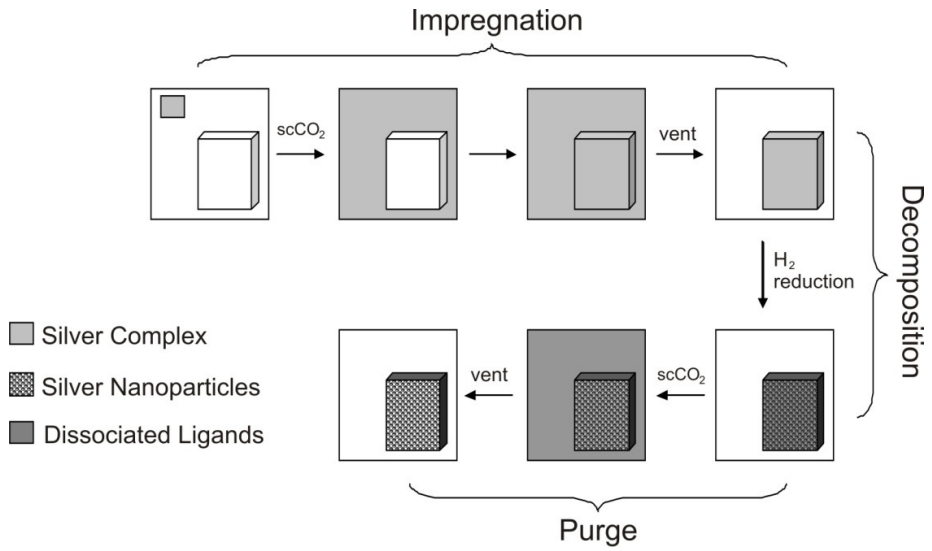

Figure 3.3 *Schematic of the three-step fabrication process of silver impregnated polycarbonate substrates.*

The fabrication process consists of three steps: impregnation, decomposition and purge. During impregnation, the polymer host (~500 mg) and the precursor complex (200 mg) were placed in the autoclave which was then filled with ~5.5 MPa of CO_2. The autoclave was then heated to 40 °C and topped up to either 9.0 MPa or 10.3 MPa. The $scCO_2$ was maintained under these conditions for a duration (normally 24 hours) in order to dissolve the precursor complex (1,5-cyclooctadiene)(1,1,1,5,5,5-hexafluoroacetylacetonate)silver(I) – Ag(hfac)COD and infuse it into the polymer. The $scCO_2$ was then vented evenly over 5 minutes, leaving the silver precursor dispersed within the polymer.

During decomposition, the precursor can then be reduced to form elemental silver nanoparticles by tuning the pressure and temperature of the chamber, which was monitored directly via an in situ thermocouple at all times. The autoclave was pressurised to 7.0 MPa of hydrogen and heated to 80 °C to let the gas permeate the substrate and start reducing the precursor. These conditions were maintained for 3 hours then $scCO_2$ was used again to remove all the residuals of the reaction, before venting the autoclave to atmospheric pressure over 5 minutes. All values of temperature and pressure used in the process did not appear to distort or chemically alter the polycarbonate strips, which retained the original shape and material composition.

3.3 Composite characterisation

A typical example of silver impregnated polycarbonate substrates resulting from the fabrication described above was shown in Figure 3.1. Substrates appear transparent, homogeneous and brown in colour, which is caused by the plasmonic peak of silver occurring around 400 nm. A range of substrates have been fabricated under a $scCO_2$ pressure of 9 and 10.3 MPa, a temperature of 40 ° C and with differing amounts of precursors.

TEM and EDX have been performed at the University of Nottingham to investigate formation and composition of nanoparticles as well as the efficiency of the purging stage, so no by-product chemicals would remain in the polycarbonate. This is important for future applications as the presence of residual chemicals in the polycarbonate could affect the quality of the substrate in terms of potential reaction with the analyte. Here I report results obtained for the two samples fabricated with 200 mg precursor (pressure of 9 and 10.3 MPa), because they will be demonstrated to give best results for SERS measurements, as shown in Section 4.1, and some information derived from TEM imaging, such as particle size and distribution, will be used in Section 4.1 to estimate SERS enhancement factor.

Absorption and reflectivity measurements have been performed to investigate the plasmonic peak intensity, position and width as well as the possible presence of strong nanoparticles interaction, which results in a secondary peak at longer wavelengths as discussed in Section 2.2.4. In particular, 5 different amounts of mass precursor have been used to fabricate many substrates in order to investigate how this synthesis parameter translates into plasmonic peak properties. In practice, absorption measurements were possible on lightly impregnated samples (fabricated with up to 175 mg precursor), whereas reflectivity measurements were performed on the samples fabricated with a larger amount of precursor, as they were not transparent enough to perform significant absorption measurements.

Finally, prism coupling techniques were performed in a second stage of the investigation process and measurements were limited to the only the two substrates which exhibited strong SERS enhancements. Indeed, after the good SERS results that

will be shown in Chapter 4, a potential sensor employing a waveguide configuration to increase device sensitivity has been envisioned. This prism coupling step is part of the analysis which targets this application. Such a device, in fact, would require a higher refractive index of the waveguide compared with the substrate, which is expected due to the high refractive index of silver. The increase in the refractive index is directly related to the amount of impregnated silver nanoparticles; hence these measurements also provide information about the nanoparticle densities in the two substrates, which can be directly compared with the TEM images.

3.3.1 Transmission Electron Microscopy

TEM is an imaging technique that uses a beam of electrons instead of light. Image resolution is proportional to the De-Broglie length of the particle used as the probe and the De-Broglie length of an electron when accelerated at 100eV is in the order of 10^{-12}m. The electron beam is focused on a thin slice of the specimen under investigation (where the thickness must be comparable with the electron mean free path which is only a few tens of nanometres) and emerges (transmitted beam) carrying information about the structure of the sample itself. Once magnified, the transmitted electron beam is projected onto a screen reproducing the image of the specimen with a sub-nanometre resolution.

TEM imaging was performed on cross sections of a range of substrates to allow the size and distribution of the nanoparticles to be observed. For the measurements, the samples were sectioned [I think that divided would be a better world] with a diamond knife to a thickness of ~100 nm, using a Reichet Ultra-microtome and supported on 300 mesh copper grids. Conventional bright field images were acquired using a JEOL JEM-2000 FXII TEM operating at 200 kV under low dose conditions to minimize sample degradation under the imaging electron beam.

TEM imaging of a sample A, produced with an impregnation time of 24 hours at a pressure of 10.3 MPa (Figure 3.4) reveals a nanoparticle band located along the outermost edge of the cross section of uniform thickness (~6.5 μm) and composition along the length of the sample.

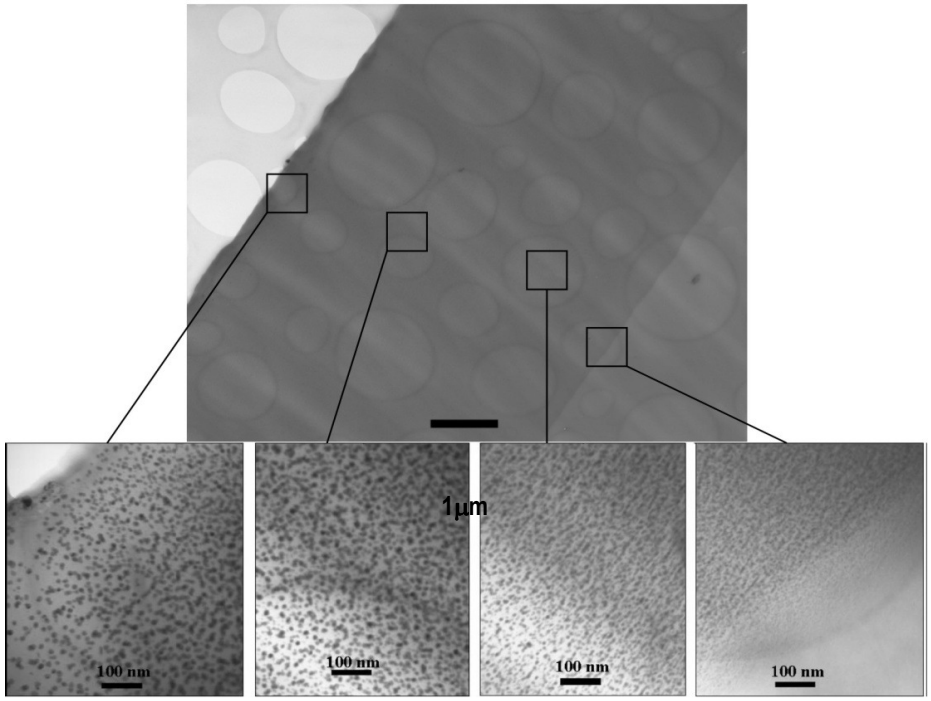

Figure 3.4 *TEM micrograph of a cross-section of the silver nanocomposites. The nanoparticles band is uniformly 6.5 μm thick and the size of the nanoparticles decrease with the depth from ~10 nm at the surface.*

The close up images show roughly spherical nanoparticles, with an estimated size of ~10 nm near the surface of the film, decreasing in size with the depth, but of relatively uniform size and distribution on a local scale. At the limit of furthest infusion a very definite boundary is evident, after which the nanoparticles cease abruptly. This depth limited incorporation of nanoparticles suggests a time dependent infusion of the organometallic precursor into the polymer during the impregnation step.

TEM imaging was performed on samples fabricated with different impregnation times varying from 1 hour up to 24 hours, whilst maintaining a constant pressure of 10.3 MPa. The results of the measurements are plotted in Figure 3.5 from which it is clear that the impregnation depth is time dependent and highly reproducible, especially for short impregnation depth. The rate of diffusion of the organometallic complex into the polycarbonate is relatively slow, allowing a degree of control to be obtained in terms of the thickness of the nanoparticle band produced.

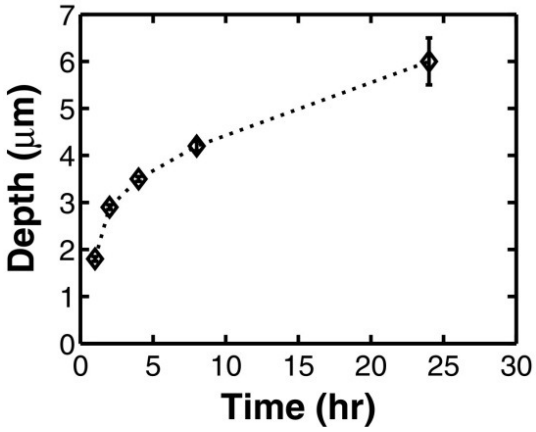

Figure 3.5 *Graph of the nanoparticle infusion depths found for different impregnation times and constant pressure (10.3 MPa). Each individual measurement was performed for three different samples, with the errorbars indicating the reproducibility of each impregnation depth.*

The TEM images can also provide information on the effect of the impregnation pressure. By comparing TEM micrographs of the cross-sections of sample A (10.3 MPa, Figure 3.4) with the ones of sample B produced at a lower pressure (9.0 MPa, Figure 3.6) it can be seen that in both cases there is a locally uniform distribution of embedded nanoparticles. However, it is also apparent that whilst substrate A has a defined film thickness of ~6.5 μm, the particles in substrate B penetrate much deeper, with no definite boundary of furthest infusion being observed.

At lower pressures it is well known that $scCO_2$ is less dense and has a lower solvating power for the silver complex [this doesn't sound right]. The relative percentage of silver complex that infuses into the polymer during the impregnation step depends on the ratio of the solubility in the $scCO_2$ compared to the solubility in the polymer. The partitioning of the silver complex into the polycarbonate at a lower pressure (sample B) is therefore likely to be favoured, leading to deeper impregnation of nanoparticles compared to the high pressure impregnation. Furthermore, at a lower pressure and $scCO_2$ density, the system may be less homogeneous which could also contribute to the loss of the definite nanoparticle limit.

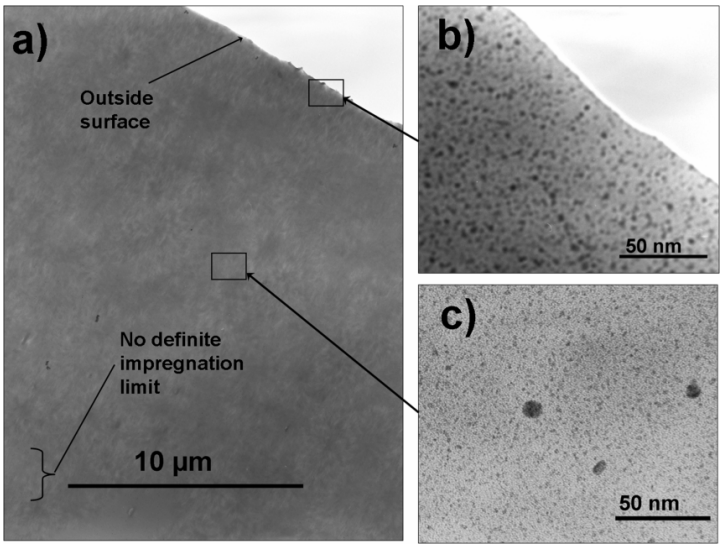

Figure 3.6 *TEM micrographs of sample B produced at 9.0 MPa impregnation pressure. (a) A cross-section near the top surface region of the polycarbonate. (b) and (c) show nanoparticles respectively at the surface and deeper into the polymer.*

3.3.1.1 Selected Area Electron diffraction pattern

In a typical TEM, a selected area aperture can be enabled in order to restrict the path of the electron beam to a specific area for investigation. Electrons travel across the ordered arrangement of atoms in the specimen and are diffracted by its crystal structure. The shape of the diffraction pattern depends on the crystalline nature of the material. Typically a pattern of dots will be observed if a single crystal material is investigated.

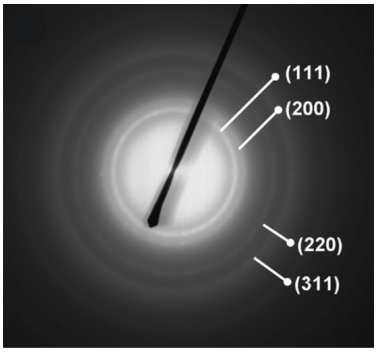

Figure 3.7 *Selected area electron diffraction pattern: the spacing between the bands identifies the nanoparticles as metallic silver.*

The position of the dots on the observed pattern provides information about the specimen crystal structure and how crystals are oriented relatively to the incident beam direction. In the case of polycrystalline and solid amorphous materials the irregular orientation of the crystalline regions (or of the atoms) translates in a symmetrical distribution of the diffracted electrons around the beam direction, so the observed pattern will consist of a series of concentric rings. The radial distance of the ring contains information about the preferred atomic arrangement in the material.

Selected area electron diffraction patterns were taken from the regions of both samples observed with TEM imaging and containing the nanoparticles. An example is shown in Figure 3.7: the observed bands, which are indicated by their correspondent Miller indexes (see Section 7.1.1), show them to be metallic silver [*89*].

3.3.2 Energy Dispersive X-ray

In this spectroscopic technique a high energy electron beam or an X-ray beam is used to eject an electron from an inner shell of the atoms in the investigated specimen. The vacancy left is occupied by another electron from a higher energy shell, which relaxes emitting X-rays with an energy characteristic of the atomic species. The energy of the emitted X-ray is measured through an energy dispersive spectrometer allowing identification of the atomic composition of the specimen, whilst the intensity of the peaks (measured in counts per second, cps) provides information on the number of atoms of each atomic species. No information is provided about the molecular bindings of the atom or about the existence of compounds.

Energy dispersive x-ray analysis was performed in order to demonstrate the presence of silver in the impregnated area, which was not present beyond the observed impregnation boundary, and the absence of other precursor residuals, demonstrating the success of the reaction. Combining these results with the TEM images of nanoparticles we must conclude that the observed nanoparticles were made of silver. EDX spectra taken within the nanoparticle band show a clear peak associated with silver (Figure 3.8), whilst spectra taken beyond the band further into the sample do

not show any presence of silver. The peak observed for silicon is likely to be caused by silicon containing oils removed from the sealing O-ring of the autoclave and impregnated into the polycarbonate by the action of the $scCO_2$.

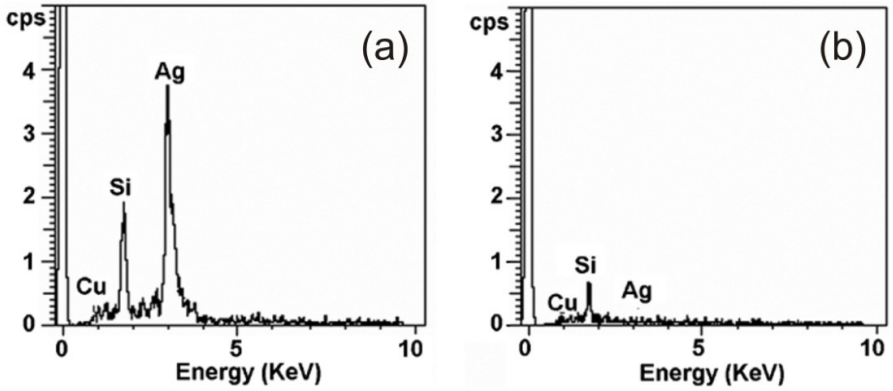

Figure 3.8 *EDX spectra taken (a) inside the nanoparticle region and (b) further into the polymer.*

3.3.3 Absorption and reflectivity

Spectroscopic characterisation of a range of substrates was performed through absorption and reflectivity measurements using a Jasco V570 UV/Vis/NIR spectrometer in both transmission and reflection configuration. The effect of using increasing precursor mass in the impregnation technique was investigated by performing absorption measurements on samples prepared using different amount of precursor, from 75 mg to 175 mg.

Figure 3.9 shows data collected using 75, 100, 150 and 175 mg of precursor. Firstly, it can be seen they all show a peak around 410 nm typical of the plasmonic absorption of the silver, but somewhat broader. It appears that increasing precursor mass does not result in increasing particle size, which would correspond to a peak shift, but results in stronger peak intensity associated with an increase in the number of nanoparticles.

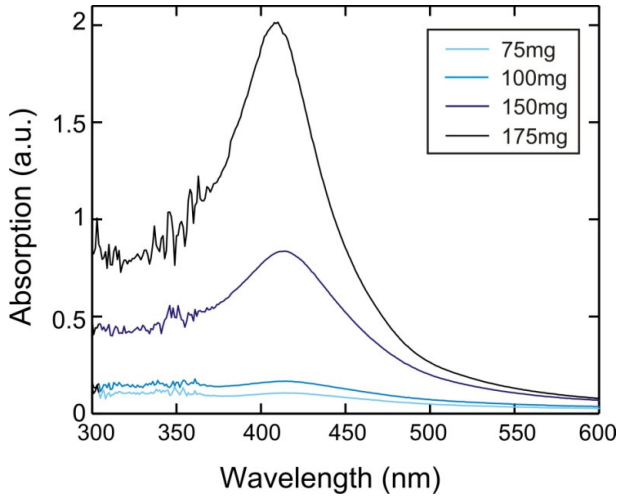

Figure 3.9 *Absorption measurements on silver polycarbonate samples prepared with different precursor mass (75, 100, 150, 175 mg) reveal an increase in nanoparticles density.*

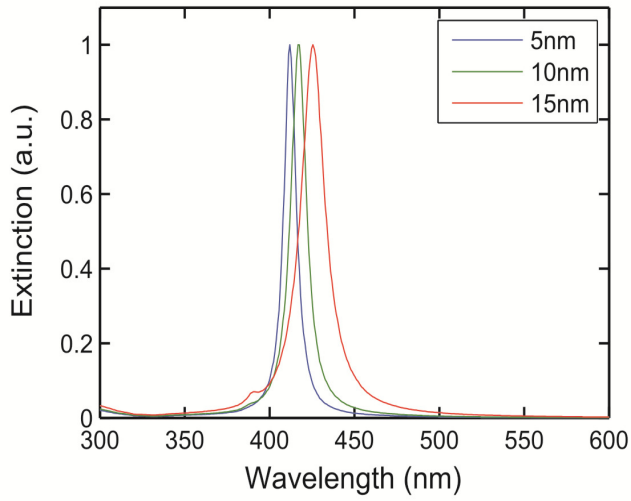

Figure 3.10 *Simulated extinction coefficient based on Mie Theory of 3 individual spherical Ag nanoparticle sizes embedded in a dielectric media with a refractive index of 1.585.*

The broad absorption peak is likely to be due to the overlap of the different sized particles across the examined section of the sample. In order to evaluate their size distribution, modelling of the Ag nanoparticle extinction based on Mie scattering theory [*27*] has been performed* for three individual particles with sizes in the range

* Code for extinction coefficient was provided by Dr Anna Peacock.

5-15 nm (as estimated from TEM images) with a surrounding refractive index medium of 1.585 (polycarbonate refractive index). The theory used for the modelling can be found in Appendix A and the results are shown in Figure 3.10. From this model it is clear that the expected plasmonic resonance for a single particle (or an ideal system of identical particles) is generally sharper. Interestingly the model also shows how the plasmonic peak shifts towards longer wavelengths and its width increases with the size of the nanoparticle, as discussed in Section 2.2.3. But the width of the experimental peak cannot only be justified by a presence of large particles since its position corresponds in the model to smaller particles. Thus for its position and width, the peak in Figure 3.9 is most likely to arise from a distribution of smaller sized particles.

Impregnation dependence on pressure was also investigated on the two samples fabricated at 10.3 MPa (substrate A) and 9.0 MPa (substrate B), where in both cases the impregnation time was 24 hours and the precursor mass was 200 mg. These measurements were performed using a spectrophotometer as for the previous absorption measurements, but in reflection configuration (see Figure 3.11(b)), as the absorption around 400 nm for both samples was greater than the upper limit of the measurable range of the spectrophotometer. The reflectivity spectra of the two samples are plotted in Figure 3.12

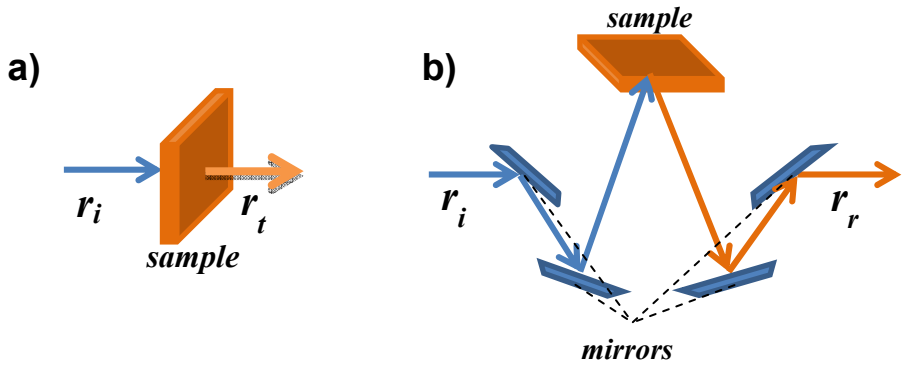

Figure 3.11 Schematic for (a) absorption and (b) reflectivity measurements. In the latter a system of mirrors collects the reflected light to be analysed by the spectrophotometer.

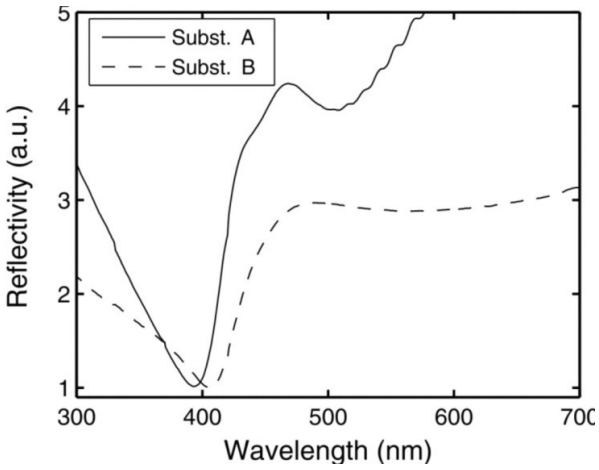

Figure 3.12 *Reflectivity spectra of two polycarbonate substrates, fabricated at 10.3 MPa (solid line) and 9.0 MPa (dashed line).*

The positions of the main absorption dips are close to the predicted extinction peak of ~ 410 nm for a distribution of particles with diameters < 10 nm, but slightly blue shifted. This can be attributed to a stronger contribution from the metal particles at the surface, which are partially exposed to air and hence will have their resonance peaks blue shifted, in the reflection configuration compared with the transmission configuration of the absorption spectra.

The slight difference in the relative position of the two dips might be due to a small increase in the observed particle sizes in substrate B. The appearance of a second dip at ~500 nm in substrate A is likely to arise due to interaction between neighbouring particles, as seen in Section 2.2.4. In fact, as observed in the absorption measurements, the increased number of nanoparticles associated with the increased precursor mass, inevitably leads to an increase in nanoparticles density. Hence it is likely that some nanoparticles will be at distances in the order of few nanometres and thus interact with each other. A weak interaction (long distance) would correspond to a weak peak at longer wavelengths, as it is visible in sample B, compared with a stronger interaction (shorter distance) which would correspond to a stronger peak at shorter wavelengths, as for Sample A. This difference suggests an increased silver density in substrate A compared to substrate B, as will be confirmed in the following section.

3.3.4 Prism coupling

The refractive index of the silver nanoparticles impregnated area and the nanoparticle density in substrates A and B were also investigated through refractive index measurements using a prism coupling technique [*90*]. In this technique a laser light is irradiated onto a thin film (n_{film}) through a high refractive index prism (n_{GGG}), as shown in Figure 3.12. By varying the incident angle, the angle θ can be varied so that for large values of θ the light is all reflected back (total internal reflection) and measured by the detector. The detector continuously measures the reflected light whilst the angle θ is gradually reduced. Once θ reaches the critical angle, light starts to be coupled into the film and a drop in the measured intensity of the reflected laser light is observed. This condition occurs for $n_{GGG} \sin\theta = n_{film}$, allowing for the determination of n_{film}. In addition, where a clear film-substrate interface is present, a further reduction of the angle θ leads to a periodical oscillation of the reflected intensity due to the interference with the light reflected off the lower film-substrate interface. The periodicity of these oscillations is related to the thickness of the film, hence can provide an estimate of this film parameter.

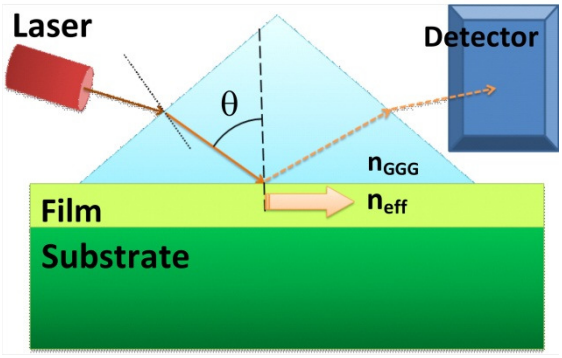

Figure 3.13 *Schematic of prism coupling technique set-up. Laser light is coupled into a film through a prism. Coupled light is indirectly measured through changes in reflected light*

For these measurements a 633 nm He-Ne source is launched onto the surface of our substrate through a GGG prism ($n_{GGG} = 1.965$). The collected transverse electric (TE)

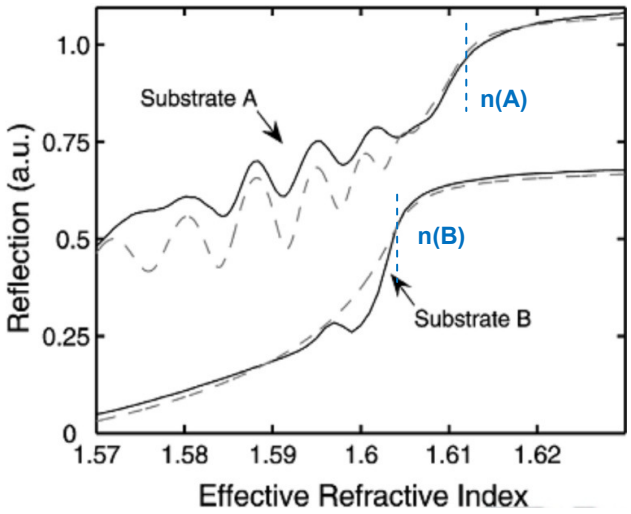

Figure 3.14 *Prism coupling measurements for substrates A and B, fabricated at 10.3 MPa and 9.0 MPa respectively (solid lines). Dashed lines represent multilayer reflection calculation fitting. Blue dashed lines indicate refractive indices for substrates A and B obtained from fitting.*

and transverse magnetic (TM) polarised spectra can be plotted as functions of the effective refractive index $n_{eff,} = n_{GGG} \sin\theta$, so that the refractive index of the composite film corresponds to the value of n_{eff} at which the reflection intensity starts to drop off.

TE spectra for both substrates A and B are plotted in Figure 3.14 (solid lines). The steep drop in the measured signals determines the refractive index of the corresponding film and shows that substrate A has a higher refractive index compared with B. The impregnated area shows a higher refractive index compared with pure polycarbonate due the contribution of silver, which has a refractive index ~4 at 633 nm. Consequently, an increased density of silver nanoparticles corresponds to a higher average refractive index of the film. Thus results obtained for substrate A and B confirm the higher particle density in the former compared with the latter as already observed via TEM analysis in Section 3.3.1.

The oscillations in substrate A are due to interference effects at the film interface and thus provide information about the film thickness. Their absence in substrate B is due

to the lack of well-defined silver film thickness, as already observed in the TEM images, and we attribute the single absorption dip to scattering losses.

To obtain the most accurate values for the film parameters the curves were fitted using a multilayer reflection calculation† based on the transfer matrix method [*91*] for both the TE and TM polarisation spectra (represented by the dashed line in Figure 3.14 in the case of TE). We obtained the refractive indices of n(A) = 1.611 ± 0.003 and n(B) = 1.602 ± 0.005 and a film thickness of ~7 μm for substrate A..

The demonstrated high refractive index of the silver nanoparticle film suggests the possibility of using these substrates in a waveguide configuration. In fact an extended propagation length can increase the signal-analyte interaction and thus could improve the performance of the films as sensing devices. In the next chapter some of the characterised substrates will be used as plasmonic devices and will be demonstrated to exhibit an excellent response both for SERS and MEF applications. The ability to post-process the substrates using oxygen reactive ion etching will also be demonstrated, thus offering an additional level of design.

† Multilayer reflection code was provided by Dr.Oton.

Chapter 4

Plasmonic Devices

In the previous chapters localised surface plasmons have been introduced as a mean of inducing a strong enhancement of the local electromagnetic field. This field enhancement can lead to the enhancement of optical processes occurring in a nearby molecule. Silver impregnated polycarbonate (AgPC) substrates were fabricated using a supercritical technique. As mention in the previous chapter, an ideal plasmonic substrate must show a high enhancement factor, be inexpensive, temporally stable and show signal reproducibility. The use of inexpensive materials and a simple single chamber process has the potential of offering a facile fabrication process.

In this chapter these substrates are tested for surface-enhanced Raman spectroscopy and metal enhanced fluorescence, showing them to be excellent candidates for plasmonic applications. SERS measurements have demonstrated an estimated enhancement factor in the order of $\sim 10^5$ in off-resonance conditions which is expected to increase in optimum conditions. This result is already comparable with enhancement factors claimed for gold-based commercially available substrates (Klarite®). Measurements have been performed in different points of the same samples and in samples fabricated with the same parameters, in order to investigate reproducibility of the signal and quantitation capability. Results show that signals can vary up to 90% with, in some cases, no SERS response (see Section 4.1.1) and

the best reproducibility obtained in post-processed samples (see Section 4.1.4). These results make these substrates not suitable at this stage for quantitative tests, i.e. to detect the specific amount of target molecule present in a certain sample.

Although reproducibility properties are not satisfying, these substrates can offer significant benefits over more conventional plasmonic substrates as they retain desirable properties of polycarbonate, such as flexibility, robustness and potentially biocompatibility [*8*], they are proven to be temporally stable, protecting the silver from oxidation (see Section 4.1.5) and, once the fabrication process is optimised, are potentially inexpensive. Other properties, such as strong plasmonic response and excellent mechanical properties, make these substrates suitable for applications in non-quantitative tests, where a large number of inexpensive tests need to be performed, and single-use applications. For example, they could be adopted in routine detection of illegal substances at the airports, when hundreds of tests could be performed daily and potentially dangerous substances could be involved (so substrates would have to be disposed of after each test).

The role of solvent on the enhancement has also been investigated by using an ethanol solution of 4-ATP and a water solution of Rhodamine 6G. Polycarbonate in fact is only moderately resistant to ethanol, so the analyte from this solution is expected to permeate into the substrates, gaining access to a higher number of silver nanoparticles. In contrast, the water-solution does not permeate, so in this case the enhancement should arise only from the nanoparticles which are impregnated within few nanometres from the surface.

The ability to post process the metal-polycarbonate substrates will be demonstrated using reactive ion etching (RIE). This not only allows access to particles situated deeper into the substrates, but also provides an additional degree of design control so that it could be possible to fabricate devices with unique excitation and detection geometries for a wide range of applications.

In section 4.2, metal-enhanced photoluminescence of a blue emitting dye molecule (Coumarin 102) is investigated. Although fluorescence is largely used in biotechnology as mentioned in Section 2.4, to the best of my knowledge there is no commercially available plasmonic substrate that specifically targets this application,

possibly because of the lower enhancement factor associated with MEF. Plasmonic substrates reported in the literature show fluorescence enhancement factors to be in the order of ~10 (see Section 2.4), reporting a factor 7 for a silver nanoparticles (surface) deposited polycarbonate substrates [*73*]. In this context, the discussed potential advantages in terms of fabrication, cost and biocompatibility of these silver impregnated polycarbonate substrates makes them good candidates for bio-sensing applications, such as high sensitivity substrates for fluorescent markers detection.

By considering simultaneous time and spectrally resolved photoluminescence, fluorescence enhancement resulting from plasmon coupling has been observed with an increase of the emission by a factor of ~8.5, with an associated reduction in the photon lifetime. The fast and slow components of the observed emission decay have been associated with the presence of both monomers and aggregates in the coumarin films and their different response to the plasmon coupling is discussed.

The set-up for MEF experiments was made available by Prof. Lagoudakis in the Department of Physics and Astronomy at the University of Southampton.

4.1 SERS response

The vibrational nature of Raman scattering provides a fingerprint by which to identify a molecule. So the ability of a substrate to increase the Raman signal by factors up to 10^{11} (ultra-high sensitivity) is of enormous interest for applications in sensing [*92*] and biology [*93, 94*], particularly for the detection of trace elements.

To investigate silver-impregnated polycarbonate substrates for SERS applications a range of substrates have been tested with different target molecules using a Raman spectroscopy set-up. A Raman spectrometer employs a system of mirrors and lenses to focus an external laser source onto the specimen to be analysed. The scattered light is then collected, filtered in order to remove the Rayleigh component (laser reflection) and detected using a CCD camera. The intensity of the detected signal depends on the laser power density at the sample surface and on the integration time, so the obtained data are normalised based on the experimental conditions.

Figure 4.1 *Picture of a Renishaw Raman Spectrometer set-up.*

All measurements were conducted using a conventional Renishaw Raman spectrometer in reflection detection geometry, with a 633 nm HeNe excitation source launched via a 50× microscope objective to produce a spot size of ~2 μm in diameter with 3 mW of optical power at the surface. In this set up, the 50× microscope objective was chosen for its high numerical aperture, which implies a more efficient collection of the signal, higher energy density and higher spatial resolution in probing the sample surface.

The optimal experimental condition for the SERS characterisation would have required a ~400 nm laser source, resonant with the main plasmonic peak as shown in Figure 3.12. Although not ideal, the 633 nm laser source was the only one available at the time of the experiments. The SERS response measured in this off-resonance condition is expected due to the second plasmonic peak associated with nanoparticles interaction, with a further contribution due to chemical enhancement, which should be in the order of 10^2 [40-42]. Hence these substrates are expected to show a stronger response in the case of resonant pump. An optimised enhancement factor can be estimated to be up to 10^8 based on SERS results reported for other plasmonic substrates characterised in both resonant and off-resonant conditions [*95*].

Samples were prepared using two different target molecules: 4-aminothiophenol (from ethanol solution) and Rhodamine G (from water solution). The choice of target molecules was based on their ability to be efficiently adsorbed on silver [*96, 97*] and their distinctive Raman features, as will be discussed in the respective sections. Also

the role of solvent in the SERS response is investigated, as polycarbonate is only moderately resistant to ethanol, such that the solution is expected to slightly permeate the substrates and thus access more of the silver nanoparticles resulting in a stronger SERS signal. For this reason, the water solution of Rhodamine 6G is expected to show a weaker SERS response, in that it should only arise from the silver nanoparticles close to the surface.

4.1.1 SERS of 4-Aminothiophenol

Metal-polycarbonate substrates have been tested for SERS activity choosing firstly 4–aminothiophenol (4–ATP) as a target molecule because of its very distinct Raman features. This molecule forms an ordered self-assembled monolayer on coinage-metal surfaces and its SERS spectrum on silver is well known [*98*].

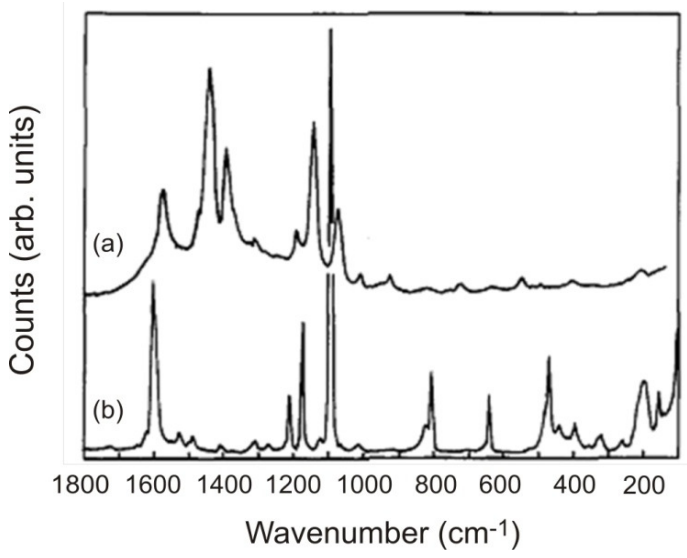

Figure 4.2 *SERS spectrum of (a) an ATP molecule adsorbed on silver (8nm thick film evaporated on a CaF_2 plate) compared with (b) a Raman spectrum of the same molecule in solid state [98].*

SERS spectra are generally expected to differ slightly from the usual Raman spectra of the same molecule due to chemical bonds that may arise. This can occur in the chemical enhancement effect, introduced in Section 2.3.2. In particular, this molecule presents a dramatically altered SERS spectrum (characteristic peaks at 1573, 1440, 1391, 1142 and 1070 cm^{-1}) compared with its Raman spectrum (characteristic peaks at 1595, 1206, 1173 and 1089 cm^{-1}) [*98*], as shown in Figure 4.2.

This difference has been attributed to a selective enhancement of some electronic levels which can be vibronically coupled with the silver, hence the different peak positions compared with the normal Raman spectrum. Peaks which exist under 1000 cm^{-1} are associated with molecules' interactions in bulk samples.

A range of substrates fabricated with different deposition parameters were tested for SERS. As preliminary investigations, nine measurements were taken in randomly selected points of the investigated substrates. Results suggested that substrates fabricated with 75 and 100 mg precursor mass show no or very weak SERS response (see Figure 4.3), whilst substrates fabricated with 150 and 175 mg precursor mass gave better results in terms of maximum SERS signal intensity (see Figure 4.4, respectively green and blue line).

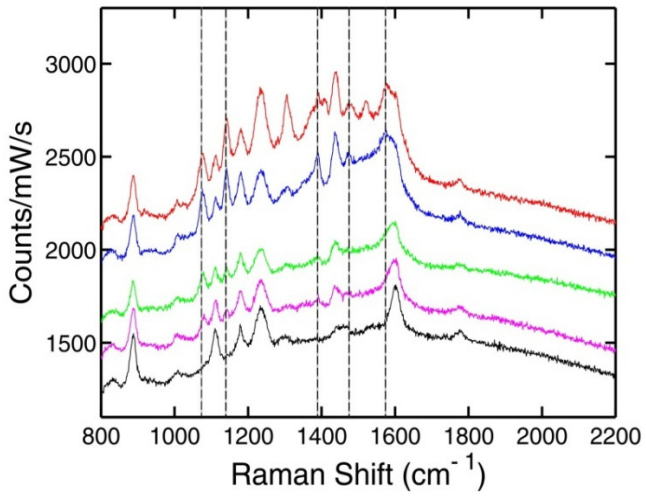

Figure 4.3 *SERS measurements of 4-ATP molecule, taken in different points of substrate fabricated with 100 mg precursor (coloured lines) plotted together with control samples of 4-ATP on pure polycarbonate (black line). The vertical dashed lines indicate the expected position of 4-ATP SERS peaks. Data are offset for clarity.*

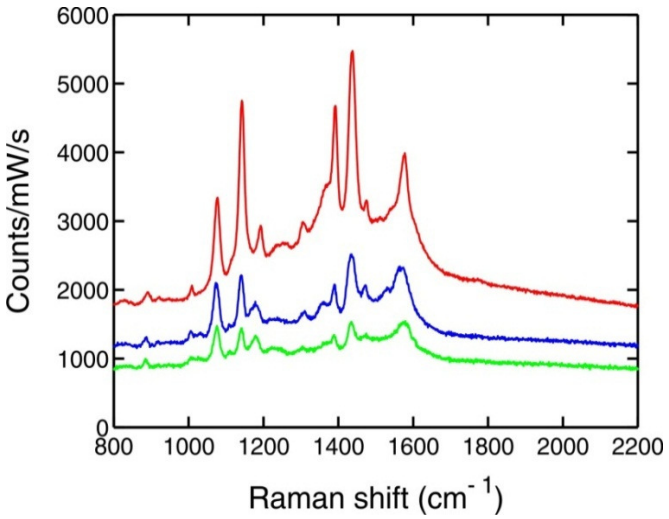

Figure 4.4 *SERS measurements of 4-ATP molecule, taken on three different substrates fabricated with 150 mg (green line), 175 mg (blue line) and 200 mg (red line) silver precursor mass.*

Finally substrates fabricated with 200 mg precursor mass gave satisfying results, reported and discussed below. During the time available, no other substrates were fabricated using a larger amount of precursor. Here results obtained from two representative samples fabricated with 200 mg precursor mass, which exhibited a good response, are reported. These substrates, A and B, were characterized in Section 3.3.

Substrate A was treated by drop casting a weak solution (0.5 mM) of 4–ATP in ethanol and allowing the solvent to evaporate. Control spectra were taken between 200 and 3200 cm^{-1} on a polycarbonate strip without silver nanoparticles (the same polycarbonate used for the fabrication of the silver modified substrates), on a 4-ATP treated polycarbonate strip (treated in the same manner as for substrate A) and on pure 4-ATP powder. All the spectra are shown in Figure 4.5. A strong SERS response is clear for the 4-ATP molecule when deposited on substrate A (black line). As expected the peaks appear in a different position compared with the peaks of a normal Raman response of the ATP powder (blue line), but instead they show strong SERS features of the main vibrational modes of the target molecule as assigned in the reported literature (see Figure 4.2). Furthermore monolayer detection of 4–ATP on the silver nanoparticles is confirmed via the absence of the bulk vibrational peaks below 1000 cm^{-1} in the spectrum, as previously discussed.

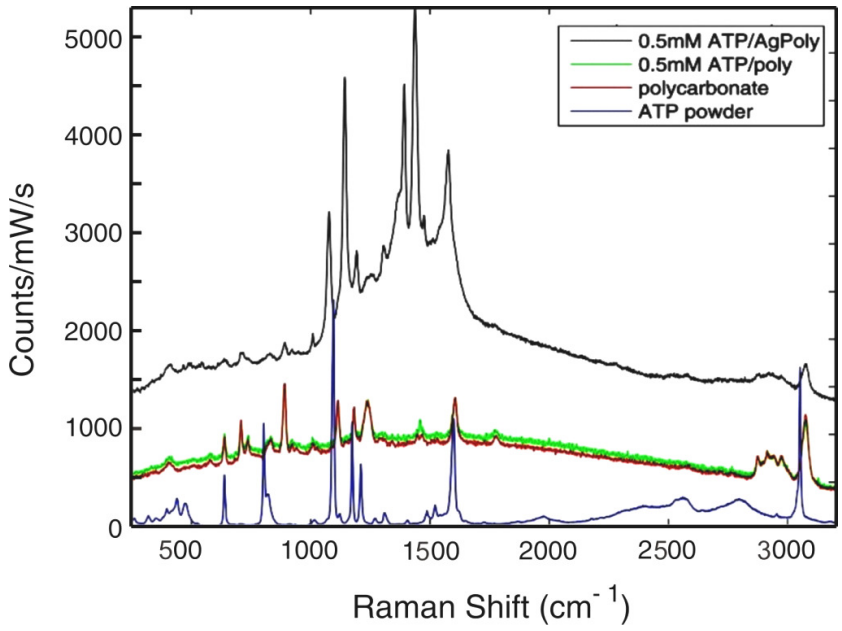

Figure 4.5 *SERS measurements of 4-ATP molecule deposited on substrate A (black line) plotted together with control samples of 4-ATP on polycarbonate (green line), polycarbonate (red line) and solid 4-ATP (blue line).*

The high intensity of the SERS response is clear by comparing the signal with the Raman response of the control samples, but quantifying the actual enhancement is difficult as no Raman response is visible from the molecule when deposited on pure polycarbonate (green line). The latter, in fact, only resembles the spectrum of the host polycarbonate, shown as a red line in Figure 4.5.

Calculation of the enhancement factor is further complicated since the SERS active metal nanoparticles are partially embedded in the substrate. An enhancement factor can still be estimated, however, through the following relation [*99, 100*]:

$$F = \frac{I_{SERS}}{I_{Bulk}} \cdot \frac{N_{Bulk}}{N_{Surf}} \quad , \tag{4.1}$$

where I_{SERS} and I_{Bulk} are, respectively, the peak intensities at 1078 cm^{-1} in the SERS spectrum and at 1091 cm^{-1} in the bulk Raman spectrum, which are assigned to the same stretch mode [*98*]. N_{Bulk} and N_{Surf} are the number of molecules excited in the bulk and on the substrate surface, respectively. Once the background is removed, the

peak intensities can be estimated as having the following values: I_{SERS} (1078) ~ 2.4×10^3 counts/mW/s and I_{Bulk} (1091) ~ 1.4×10^3 counts/mW/s.

The number of molecules excited on the substrate surface N_{Surf} can be estimated as the following:

$$N_{Surf} = A \cdot S_c(\%) \cdot C \ , \tag{4.2}$$

where A is the area excited by the laser (microscope spot size ≈ 2 μm), C is the concentration of molecules on the surface and $S_c(\%)$ is the silver nanoparticle surface coverage factor which takes into account the percentage of molecules that effectively interact with silver and, thus, undergo an enhancement.

From the TEM micrograph of substrate A an upper bound on the exposed silver is approximately 30% of the surface area. This has been estimated by graphical analysis of TEM images, as shown in Figure 4.6, by considering a few areas of size σ=100×100 nm and counting the number of nanoparticles in each area. An average N=37.6 number of nanoparticles, with an estimated 2R=10 nm diameter, gives a coverage according to the following:

$$S_c = N \cdot \pi \cdot R^2 / \sigma = 0.295 \ , \tag{4.3}$$

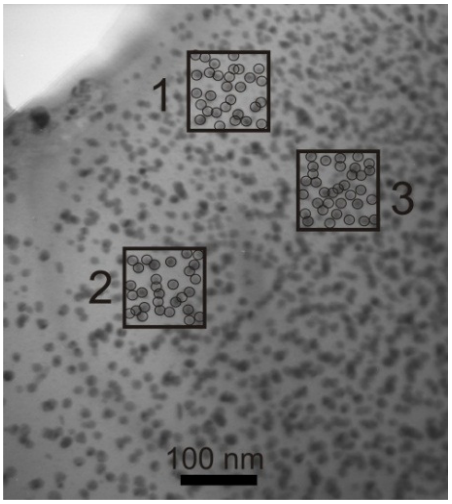

Figure 4.6 *Near-surface nanoparticles coverage study from TEM images. Area 1, 2 and 3 are all 100×100 nm and contain a number N_1=35, N_2=38 and N_3=40 of nanoparticles, with an estimated 10 nm diameter.*

Although the silver nanoparticles are randomly distributed, the laser spot size can be considered to be much larger than the range of variation of the local nanoparticle density; hence this percentage can be reasonably considered to be a good representative of the average nanoparticles coverage. Assuming a monolayer coverage and a packing density C of 8×10^{14} molecules/cm^2 [*101*], this results in a total estimated value of $N_{Surf} = 1.2\times10^6$.

The number of molecules excited in the bulk N_{Bulk} can be estimated by considering the volume V excited by the laser and the molecule density in the bulk, as:

$$N_{Bulk} = V \cdot \left(\frac{\rho}{m}\right) \cdot N_A \tag{4.4}$$

where V is calculated from experimental the conditions to be ~ 20 μm^3, ρ is the density (~ 1 g/cm^3), m is the molecular weight of 4-ATP (125.19 g/mol) and N_A is the Avogadro's number (6×10^{23} molecules/mol), obtaining an estimated value for $N_{Bulk}=1\times10^{11}$. Substituting all the estimated values in Eq.(4.1), the resulting enhancement factor is estimated to be in the order of 10^5, which is comparable to the enhancements reported elsewhere in the literature [*102-104*]. Considering that the experiment is performed at an excitation wavelength that is far from the main plasmonic resonance, this is an excellent enhancement as it is mostly due to the secondary plasmonic peak associated with nanoparticles interaction. As discussed in the previous section, this enhancement is expected to increase by factor in the order of 10^2 when performed in resonant condition.

The 4-ATP SERS spectrum shown in Figure 4.5 is representative of a typical SERS measurements obtained on substrate A, but in order to investigate the reproducibility of the SERS response, measurements were repeated over nine randomly selected points on the substrate, typically a few millimetres apart. Moreover, substrates A2 and A3 were fabricated with the same parameters as for substrate A and tested in the same manner. Obtained results are summarised in Table 4-1, which shows 4-ATP SERS signal strength of the 1078 nm peak, for ease of comparison, with the bottom rows indicating average values over all points and over the non-zero measurements only. Due to the small number of points, a statistical analysis is not significant.

I_{SERS} @ 1078cm^{-1}	A	A2	A3
	1.4×10^3	1.2×10^3	0
	0.9×10^3	0.4×10^3	1.3×10^3
	1.1×10^3	0	0.1×10^3
	0	0	0
	1.5×10^3	0.9×10^3	0
	0	1.4×10^3	1.4×10^3
	0.5×10^3	1.0×10^3	1.6×10^3
	1.4×10^3	0	0
	0	0.6×10^3	0
Average	7.5×10^2	6.1×10^2	4.9×10^2
Average over non-zero data	1.13×10^3	0.91×10^3	1.10×10^3

Table 4-1 *4-ATP SERS intensities (counts/mW/s) of the 1078 cm^{-1} peak measured on different points of substrates A, A2 and A3. The bottom rows indicate average values over all points and over the non-zero measurements.*

Assuming a uniform coverage of the analyte, the lack of SERS response in some points of the substrates implies the absence of interaction nanoparticles-analyte, which could be attributed to the absence of metal nanoparticles near the surface in that area. This has not been observed with TEM imaging but cannot be excluded. A possible absence of nanoparticles can be related either to the impregnation stage of the process, in case an insufficient amount of precursor is trapped on the surface, or to the purging stage, if some nanoparticles close to the surface escape together with the reaction by-products.

Alternatively, the absence of SERS response could be attributed to nanoparticles being more spaced out in that particular area, hence not interacting. In fact, the SERS response observed in off-resonance condition has been attributed to the secondary plasmonic peak at longer wavelengths, arising from nanoparticles interaction. If locally nanoparticles are not closely spaced, the nanoparticles interaction, hence the SERS response, can no longer be significative (I pretty sure that significant is the right word).

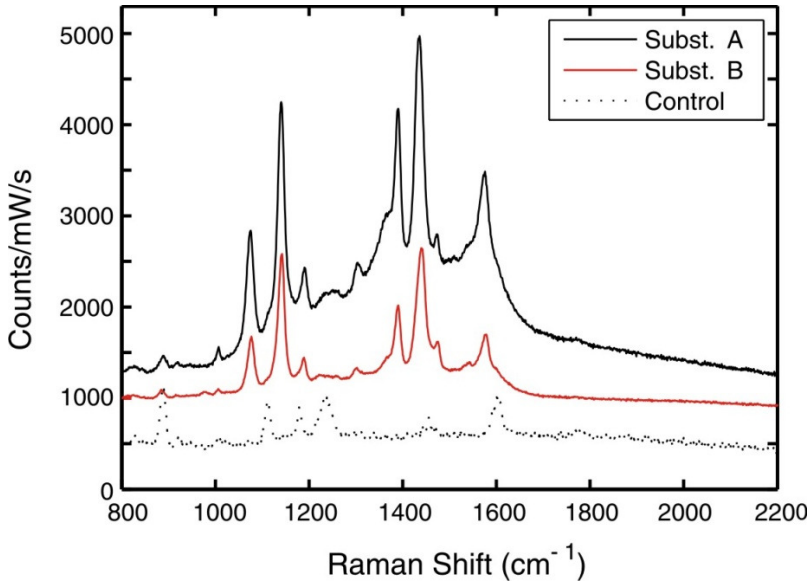

Figure 4.7 *SERS measurements on 4-ATP molecule deposited on substrate A (black line) and on substrate B (red line). Raman spectrum of a control sample of pure polycarbonate (dotted line).*

Where signal is present, some variation in signals strength (up to 90% in A2) has been found across the substrates. Comparing the average signals over non-zero data, substrates A, A2 and A3 show similar SERS response, indicating a good reproducibility for the same fabrication parameters.

In order to compare plasmonic properties of two different substrates, substrate B has been treated with the same concentration of 4-ATP and in the same manner as substrate A. Resulting measurements between 800 and 2200 cm^{-1} are plotted in Figure 4.7, together with the previous results obtained using substrate A and a control sample of silver free polycarbonate.

Comparing the SERS signals in Figure 4.7 at 1078 cm^{-1} at from the two metal composites, substrate A shows an enhancement 2.5× greater than substrate B. This is consistent with the higher nanoparticle density in substrate A and can also be related in part to the presence of the second plasmon resonance at 510 nm, which is closer to the laser excitation wavelength. The 633 nm laser emission is in fact off-resonance compared with the main plasmonic peak of the metal composite, which is around 410 nm, as shown in Section 3.3.3. Nonetheless, the SERS response is strong and is

expected to improve greatly as the excitation wavelength shifts towards the blue. A suitable laser source for measurements under resonant conditions was not available when the tests were performed.

Also in the case of substrate B, reproducibility of the SERS response have been investigated by repeating SERS measurements for nine different points, as shown in Table 4-2 together with the previous results for substrate A for comparison.

I_{SERS} @ 1078 cm^{-1}	A	B
	1.4×10^3	6.3×10^2
	0.9×10^3	6.1×10^2
	1.1×10^3	0
	0	3.2×10^2
	1.5×10^3	0
	0	0
	0.5×10^3	5.0×10^2
	1.4×10^3	5.1×10^2
	0	4.2×10^2
Average	7.5×10^2	3.3×10^2
Average over non-zero data	1.13×10^3	5.00×10^2

Table 4-2 *4-ATP SERS intensities (counts/mW/s) at 1078 cm^{-1} measured on different points of substrates A and B. The bottom rows indicate average values over all points and over the non-zero measurements.*

Also, in this case, assuming a uniform coverage of the analyte, a lack of SERS response in some points of the substrates is observed. Furthermore, substrate B shows an average SERS response which is about 44% of the other substrate, consistently with the behaviour previously discussed.

4.1.2 SERS of Rhodamine G in water

As previously discussed, if these samples are to find potential use in routine SERS analysis the substrates must be suitable for investigating a wide range of molecules. Their resistance to different solvents is therefore of great importance, as it determines the variety of molecules that can be analysed. The potential biocompatibility of the plasmonic substrates has inherent advantages for the detection of biological agents such as pathogens in their native aqueous environment [*105, 106*], thus water was chosen as the solvent to test the next target molecule. Water is also representative of solvents that do not permeate the polycarbonate, so only the nanoparticles exposed to air, or impregnated within a few nanometres of the surface, are expected to contribute directly to the enhancement.

A 2 mM solution of Rhodamine 6G (Rh6G) in distilled water was drop casted on substrate A and the resultant SERS activity investigated. The SERS spectrum, obtained in the same manner as before, is shown in Figure 4.8, plotted together with the Raman spectrum of polycarbonate as a control sample.

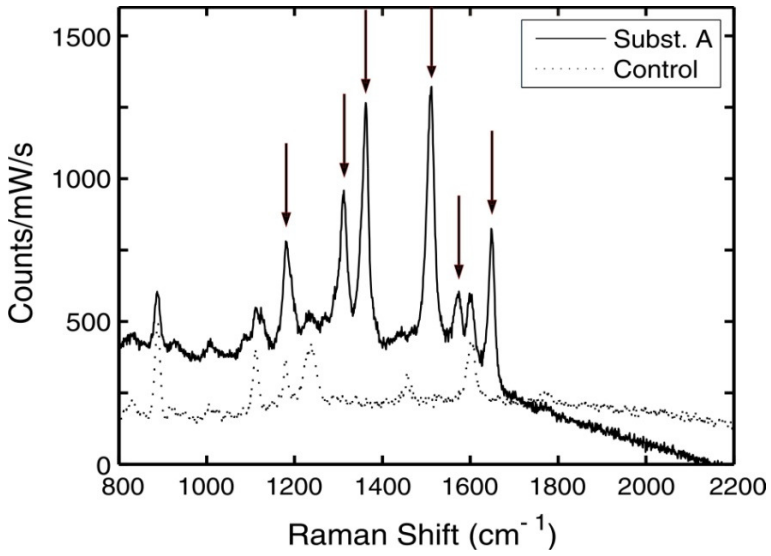

Figure 4.8 *SERS measurements on Rhodamine 6G deposited on substrate A (black line), plotted together with the Raman spectrum of a control sample of pure polycarbonate (dotted line).*

In this figure six vibrational bands of Rh6G can be identified at 1184, 1312, 1364, 1512, 1559 and 1651 cm^{-1} [*107, 108*], clearly distinguished from the remaining peaks being the underlying polycarbonate modes.

The SERS signal obtained using this dye is much weaker that the signal obtained with the 4-ATP. This difference can be attributed both to weaker bonding of the Rh6G molecules to the Ag metal, which may decrease the chemical enhancement contribution, and to the more passive nature of the water solvent so that only the exposed particles contribute to the response. Secondary effects may also arise from the larger size of the Rh6G molecules so that the effective molecule-nanoparticle distance is greater and also due to their tendency to attach to surfaces in a random orientation [*108*].

4.1.3 Post Processing

The ability to post-process the metal-polymer substrates is of significant interest as a means to introduce an additional level of structural design to the substrates. Controlled etching of the substrates not only allows access to deeper areas of the deposition, where the particle distribution may differ, but also allows, for example, the fabrication of optical waveguides. Incorporating waveguiding geometries into the devices is advantageous for a number of applications, for example in the case of SERS applications, as the extended propagation lengths average over many plasmon-analyte interactions thus offering increased sensitivity and reproducibility of the measured response.

Here the ability to post-process the substrates has been demonstrated by realising a simple step-like shape using oxygen plasma etching and a coverslip as a mask. The etching technique typically employed for the processing of pure polycarbonate substrates employs oxigen RIE [*109*]. However, using oxygen plasma etching could potentially result in the silver being oxidised so that substrate loses its plasmonic properties and thus alternative ways have also been explored. Argon plasma is also employed in polymer etching [*110*], hence two recipes have been tested: the first one employing argon only (20 sccm) and the second one oxygen and argon in equal part

(5 sccm each). Results show that not only does the mixture of oxygen and argon result in a faster etch rate of ~100 μm/min, versus the ~500 μm/hr obtained with argon only, but that the plasmonic properties are not affected by oxygen plasma. Indeed once tested, the substrate etched via argon-oxygen plasma shows that SERS response does not diminish, but in fact increases.

4.1.3.1 Reactive Ion Etching

In both cases, a coverslip, used as a simple mask, was placed over half of the substrate before loading it in an Oxford Instruments Plasma Technology RIE80plus Reactive ion etcher. The chamber was then evacuated to 5×10^{-6} torr before 5 sccm of oxygen and 5 sccm of argon were flowed into the chamber under a controlled pressure of 50 mtorr and applying a RF power of 25 W [*109*]. After 20 mins of etching the sample was removed and it was noted that the exposed part of the substrate was now darker and cloudier than the untreated side.

Transparency of the etched side was visibly improved on wiping with ethanol to remove some of the roughness in the surface layer. The resulting substrate was then analyzed using a stylus profiler (KLA Tencor P16) which revealed an etched step of ~2 μm, shown in Figure 4.10, and with a surface roughness of the etched region of less than 50 nm.

Figure 4.9 *Picture of an Oxford Instruments Plasma Technology RIE80plus Reactive ion etcher.*

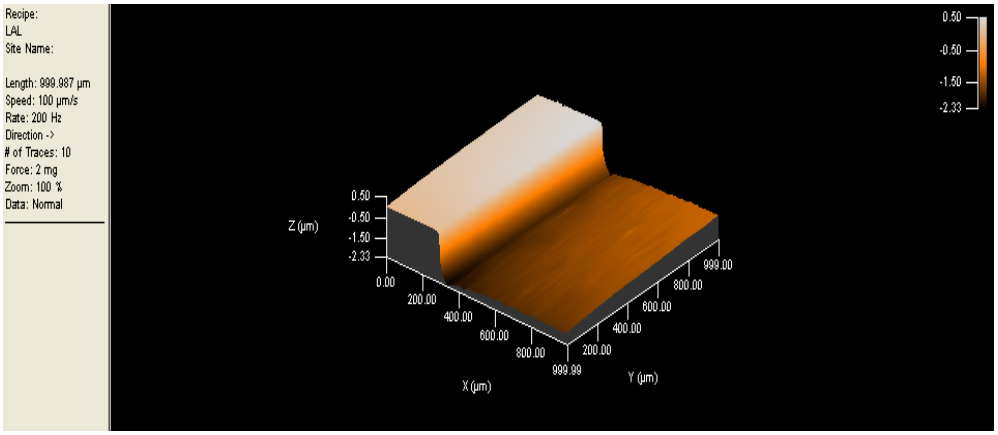

Figure 4.10 *3-D profile image of the silver-polycarbonate substrate*

Argon plasma etching was also performed in a similar configuration, so the chamber was evacuated to 5×10^{-6} torr before 20 sccm of argon were flowed into the chamber under a controlled pressure of 50 mtorr and applying a RF power of 25 W. The substrate was exposed to plasma for 30 min up to 2 hours, resulting in a good, but slower etch rate (~500 µm/hr).

4.1.4 SERS of post processed substrates

As mentioned previously, the oxygen RIE technique is commonly used for polycarbonate etching, but using oxygen could have led to oxidation of the silver nanoparticles and hence to the loss of plasmonic properties. An oxygen etched substrate was thus tested for its SERS response and compared with previous results on unprocessed substrates. The initial substrate was fabricated with similar parameters to substrate A and showed a correspondingly similar SERS response, as seen in Figure 4.5.

To test the SERS activity of the post-processed substrates a 2 µm step was etched down into the substrate as described in the previous section. The earlier Raman measurements using 4–ATP as the target molecule were repeated and the results obtained on both etched and unetched regions are plotted together in Figure 4.11.

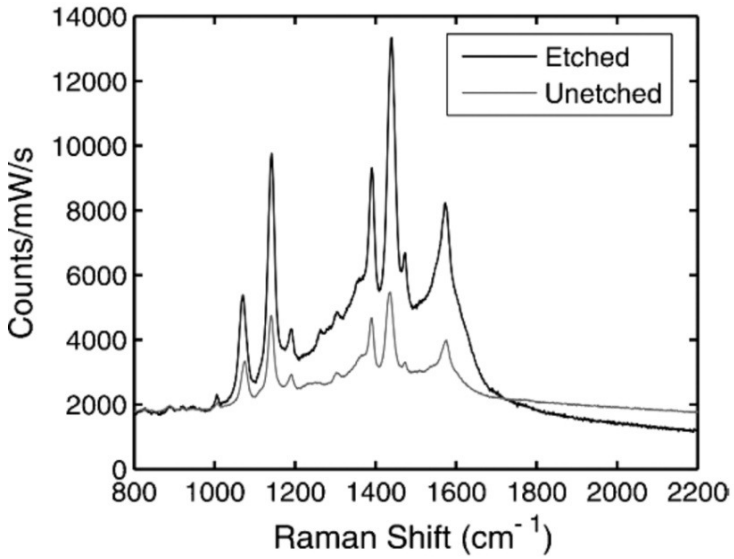

Figure 4.11 *SERS measurements on 4-ATP molecule deposited both on etched and unetched region of a silver polycarbonate substrate.*

I_{SERS} @ 1078 cm^{-1}	A	A+etching
	1.4×10^3	3.1×10^3
	0.9×10^3	3.6×10^3
	1.1×10^3	2.5×10^3
	0	3.1×10^3
	1.5×10^3	2.7×10^3
	0	3.2×10^3
	0.5×10^3	3.8×10^3
	1.4×10^3	2.9×10^3
	0	3.3×10^3
Average	7.5×10^2	2.7×10^3
Average over non-zero data	1.13×10^3	2.7×10^3

Table 4-3 *4-ATP SERS intensities (counts/mW/s) at 1078 cm^{-1} measured on different points of substrates A, before and after etch processing. The bottom rows indicate average values over all points and over the non-zero measurements.*

The etched region of the substrate shows a SERS response which is more than twice as stronge than the signal obtained in the unetched region. This additional enhancement can be partially attributed to an increase in the density of the nanoparticles going deeper into the film (as also observed from the TEM micrographs shown in Section 3.3.1). It is also likely to be due, in part, to a nanometre scale roughening of the etched surface so that more of the metal nanoparticles are exposed and the effective surface is increased. More importantly, by repeating the measurements across the etched region an improvement in the reproducibility of the SERS measurements has been observed, both by the consistent presence of signal across the substrate and by a reduction in the signal variation, indicating a more uniform distribution of silver nanoparticles deeper into the substrate (see Table 4-3).

4.1.5 Substrates lifetime

The temporal stability of the substrates is another important requirement if they are to find wide use in routine SERS analysis. The fact that the metal nanoparticles are embedded in the polycarbonate means that the substrates have an extremely long shelf life. A SERS response has been successfully measured from substrates (stored such that they are exposed to air) which are over a year old. What is more surprising, is the temporal stability of the substrates after use. Indeed, tested samples still yield comparable SERS measurements up to one month after treatment with a 4–ATP solution. Such long lifetimes are likely to be a result of the small percentage of silver that is exposed to the atmosphere and thus we expect that in this instance the bulk of the response is coming from Raman probe molecules which have penetrated down to attach to the more deeply embedded particles. This ability to check measurements over time scales of weeks is a significant advantage.

4.2 MEF response

Metal Enhanced Fluorescence has been introduced in Section 2.4 as fluorophore emission enhanced via surface plasmons. Fluorescence is largely used in biological

and medical research [*111*], for example biomolecules such as antibodies, amino acids and peptides can be related to specific disease conditions and are often tagged using fluorescent labelling to facilitate their detection. Enhancing the fluorescent response via plasmon coupling can increase the detection limit, potentially allowing for early stage diagnosis. Thus the availability of a biocompatible plasmonic substrate is highly desirable.

Considering the good plasmonic behaviour observed in the SERS experiments, a sample prepared with the same parameters as substrate A (precursor mass of 200 mg, pressure of 10.3 MPa, impregnation temperature 40 °C, impregnation time 24 hrs) was used to test the metal-polymer composites for MEF. Coumarin 102 was chosen as the target molecule because it exhibits an extinction spectrum around 400 nm, which overlaps the plasmonic absorption peak of silver nanoparticles.

In Figure 4.12 the normalized absorption (blue line) and emission (red line) spectra of Coumarin 102 deposited on a polycarbonate strip (no silver) are plotted for comparison with the extinction spectrum of a silver impregnated polycarbonate substrate (black line), already shown in Section 3.3.3.

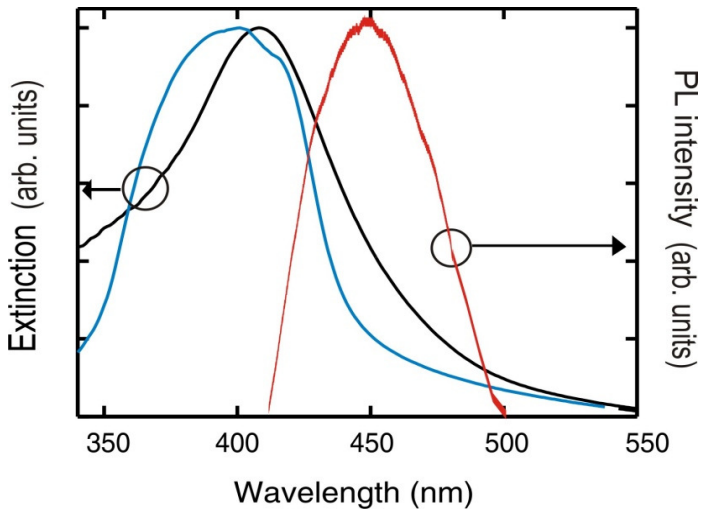

Figure 4.12 *Normalised extinction measurements for a Coumarin 102 film (blue line) and for silver modified polycarbonate substrate (black line). Normalised emission intensity of a Coumarin 102 film (red line).*

The strong spectral overlap between the plasmonic peak and the absorption spectrum of the fluorophore indicates resonance between the localised surface plasmon scattering and the electronic excited states of the dye molecule and this is expected to result in an efficient coupling [*112*] with transfer of oscillator strength.

Samples to be tested for MEF measurements were prepared using a weak 0.5 mM solution of Coumarin 102 (2,3,5,6-1H,4H-tetrahydro-8--methylquinolazin-[9,9a,1-gh], purchased from Radiant Dyes Laser & Accessories GmbH) in ethanol, which was spin-coated at 3000 rpm for 1 min on the silver-modified polycarbonate substrate and on the undoped polycarbonate substrates. The deposition conditions were monitored in order to reproduce the same solution film thickness for both samples, with an estimated value of a few nanometres.

This condition is important for photoluminescence measurements as emission intensity is not an intrinsic quantity, but depends on the amount of dye. When using a dye to test a plasmonic substrate, the sole observation of increased emission intensity could therefore be due to a thicker layer. Similarly, independent photoluminescence decay measurements can exhibit a reduction in photon lifetime, but this is not sufficient to guarantee an increase in emission. In fact the measured emission rate $k=k_r+k_{nr}$ has a radiative and a non-radiative component and both radiative and non-radiative processes may be enhanced. This means that in addition to the deposition precautions described above, it has been necessary to perform simultaneous time and spectrally resolved photoluminescence measurements as the concurrent observation of a reduction in photon lifetime and an enhanced photon emission can confirm MEF [*72*], as discussed in Section 2.4.

4.2.1 Time and spectrally resolved photoluminescence set-up

Simultaneous time and spectrally resolved photoluminescence measurements can provide a direct connection between the enhanced photon emission (via integrated photoluminescence) and the increased photon emission rate $k=1/\tau$, where τ is the photon lifetime. A schematic of the experimental set-up is shown in Figure 4.13.

The samples were excited with a frequency-doubled mode-locked Ti:sapphire laser (400 nm excitation wavelength, ~120 fs pulse width, 80 MHz repetition rate with an average power of 1.5 mW and a spot size of 30 μm), resonant with the plasmonic peak of the AgPC substrate. The emitted fluorescence from the dye molecules was collected in reflection, coupled into a multimode fibre and analysed by a synchroscan streak camera (Hamamatsu C5680) with a time resolution of 25 ps coupled to the exit of a 25 cm long monochromator with a 300 gr/mm grating.

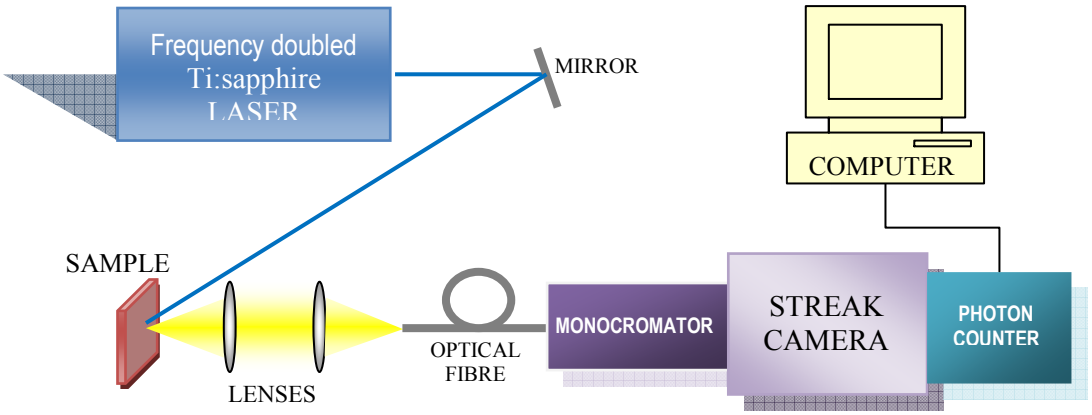

Figure 4.13 *Schematic of simultaneous time and spectrally resolved photoluminescence set-up.*

The streak camera operating principle is shown in Figure 4.14. Briefly, light pulses with different space-time coordinates and different intensities are projected through a slit and focused on the photocathode. The photocathode records the spatial displacement (horizontal coordinate) and transforms pulses into a number of electrons which is proportional to the signal intensity. The time sequence is converted into a vertical coordinate by a pair of high-speed sweep electrodes, where electrons arriving at different times are deflected at different angles onto the micro-channel plate (MCP). Here the electrons are multiplied several thousands of times and converted back to light onto a phosphor screen.

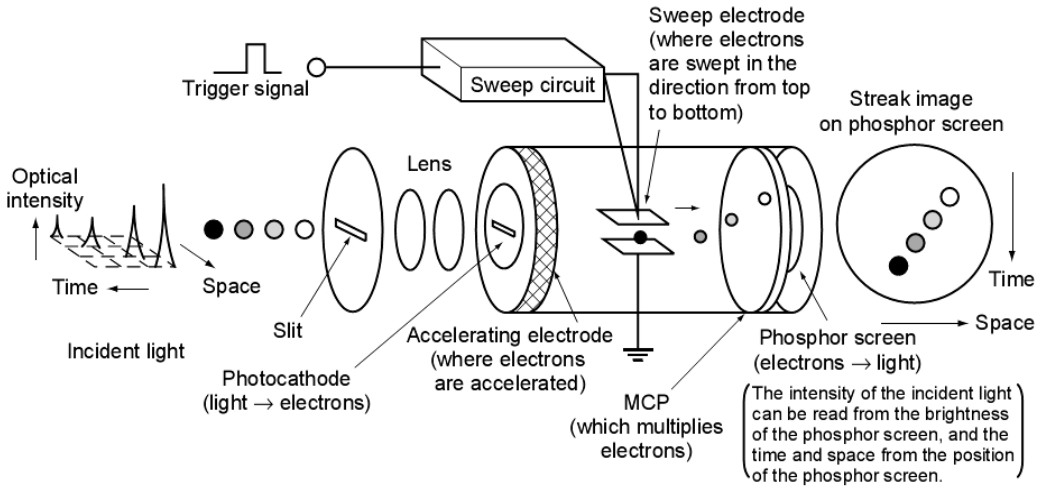

Figure 4.14 *Schematic of streak camera operating principle. From Hamamatsu, Universal Streak Camera C5680 manual.*

The streak camera is placed in between a monochromator and a photon counting integration system. The monochromator before the streak camera allows for the light emitted from the sample to be separated into different wavelengths so that the spectrum enters the streak camera along the horizontal coordinate. After the camera a photon counting integration system allows for photons arriving with the same time-space coordinates to be counted together and represented as photon emission intensity at that specific wavelength and with that specific lifetime. The different intensities will be represented with different colours.

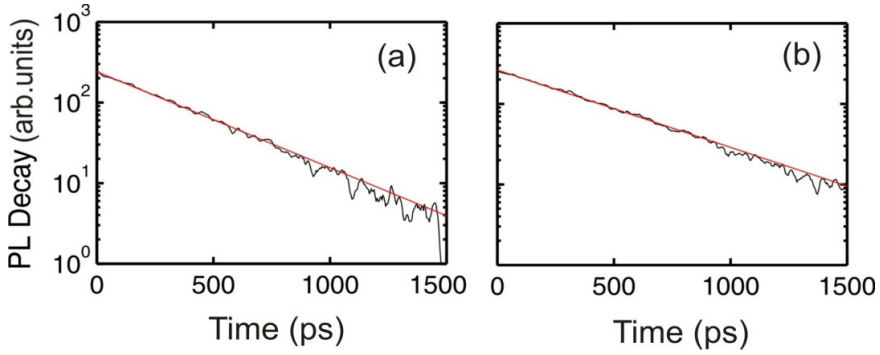

Figure 4.15 *Measured photon emission decays (black line) with single exponential fit (red line) for (a) high and (b) low concentration solution of Coumarin 102 in ethanol*

4.2.2 Photon lifetime measurements of Coumarin 102

Preliminary photon lifetime measurements were performed on both low (LC) and high (HC) concentration solutions of Coumarin 102 in order to estimate the luminescence decay rates of the isolated and interactive dye molecules. Specifically, a saturated solution (~0.04 M) of Coumarin 102 in ethanol and a 1000× diluted solution in ethanol were considered as high and low concentration solutions respectively. Measurements were taken using the streak camera set up and integrated along the wavelength coordinate between 440 and 460 nm. Resulting measurements are plotted in Figure 4.15 together with the fitting analysis, performed using the Matlab software fitting tool.

In both cases the photon lifetime decay curves could be fitted with a single exponential decay, with photon lifetimes equal to τ_{HC} = 364 ± 3 ps and τ_{LC} = 452 ± 3 ps respectively (error provided by the nonlinear least squares method), so the high concentration solution shows a faster decay compared with the low concentration solution. This difference is expected as in saturated solutions the intermolecular interactions introduce a further deactivation channel. In addition, an even shorter lifetime is expected once the dye molecules are deposited on the substrates due to the aggregation, which is known to speed up the deactivation process through the formation of exciton bands. This effect has been observed in thin film depositions [*113*] even down to monolayer coverage.

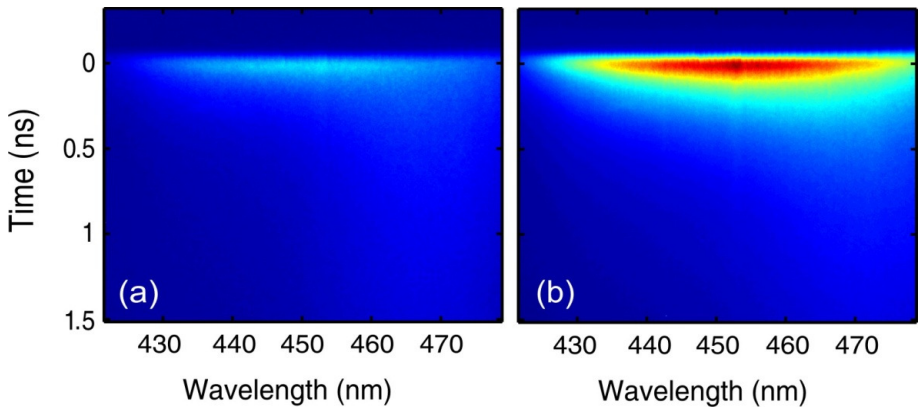

Figure 4.16 *Time and spectrally resolved photoluminescence for Coumarin spin-coated on (a) PC and (b) AgPC substrates.*

4.2.3 MEF of Coumarin 102

Time and spectrally resolved photoluminescence measurements were then performed on two samples of Coumarin 102 spin-coated (as described above, from weak 0.5 mM solution in ethanol) both on silver modified polycarbonate substrate and on silver free polycarbonate strip, to test MEF response. The resulting profiles are shown in Figure 4.16. From these images it is clear that an enhanced emission is observed from Coumarin 102 when deposited on silver impregnated polycarbonate substrates, compared with an unmodified substrate.

The PL decay at different wavelengths can be extracted from slices through these profiles and a qualitative comparison is shown in Figure 4.17. The PL decays of Coumarin 102 on a pure polycarbonate substrate (solid lines) are taken from Figure 4.16 (a) for decays at 435, 450 and 465 nm and plotted together with the respective PL decays of Coumarin 102 on silver-polycarbonate substrate (dotted lines), taken from Figure 4.16 (b). A clear reduction in photon lifetime is observed at each wavelength when Coumarin is deposited on the silver modified substrate. Furthermore, with the PL decay profiles plotted on a logarithmic scale, it is clear that the Coumarin films on both substrates are no longer governed by a single exponential behaviour, but are now, in fact, characterized by a bi-exponential behaviour. The possible reasons for this bi-exponential behaviour will be discussed after the quantitative analysis of the average fast and slow component.

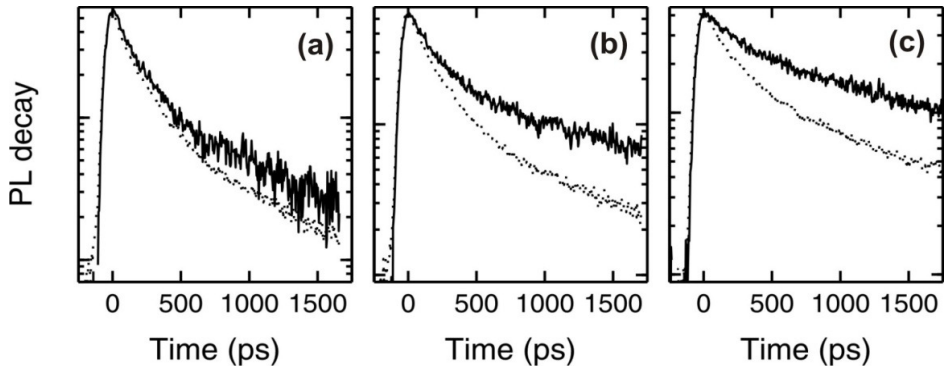

Figure 4.17 *From Figure 4.16 (a)&(b), PL decays of Coumarin 102 on polycarbonate strip (solid line) and on silver polycarbonate (dotted line) substrates at (a) 435 nm, (b) 450 nm and (c) 465 nm.*

For quantitative analysis, the time integrated PL spectra (Figure 4.18) was calculated by adding up the emission for the whole wavelength range over the time coordinate.

Comparing the PL spectra in Figure 4.18 the emission intensity for Coumarin deposited on the silver-polycarbonate substrate (dotted line) is about 8.5 times higher than the emission on the control sample (solid line). This enhancement factor is in the same order of those reported elsewhere in the literature [*114*].

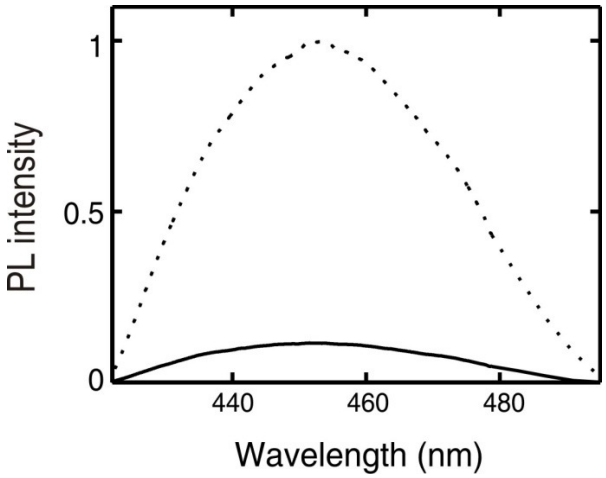

Figure 4.18 *Integrated PL spectra of Coumarin 102 on pure polycarbonate strip (solid line) and on silver polycarbonate (dotted line) substrates.*

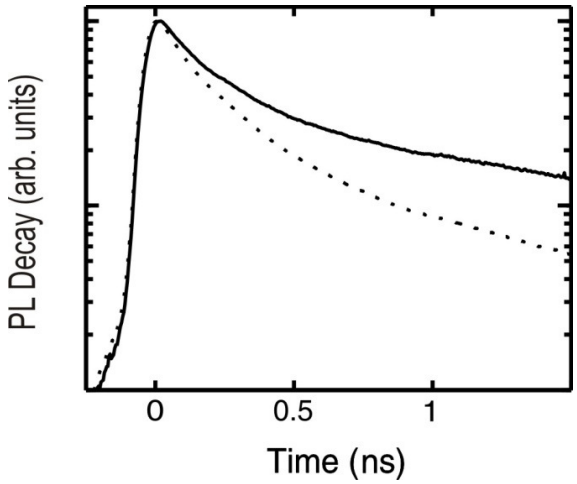

Figure 4.19 *Average PL decays for Coumarin on polycarbonate strip (solid line) and on silver polycarbonate (dotted line) substrates.*

The averaged PL decay curves, shown in Figure 4.19, were calculated for the wavelength range 438-468 nm where the emission was greatest. From the decay curves it is clear that the observed enhanced fluorescence is accompanied by a reduction in the photon lifetime. The bi-exponential behaviour was investigated by fitting these curves with double exponentials to obtain both the fast (τ_1) and slow (τ_2) components. PL decays (black lines) for Coumarin spin-coated on (a) PC and (b) AgPC substrates are plotted in Figure 4.20 together with the double exponential fit obtained using the Matlab software fitting tool (nonlinear least squares method).

The following photon lifetime values of $\tau_1 = 172 \pm 2$ ps and $\tau_2 = 1627 \pm 37$ ps were obtained for Coumarin 102 deposited on the pure polycarbonate substrate (a) and the modified lifetimes of $\tau_1^* = 154 \pm 3$ ps and $\tau_2^* = 889 \pm 26$ ps were obtained for Coumarin 102 on the silver-polycarbonate substrate (b).

This bi-exponential behaviour can be attributed to the coexistence of aggregates, as the fast species, and monomers, as slow species, in the films [*113, 115*]. In fact, in accordance with the preliminary photon lifetime measurements on the HC and LC Coumarin 102 solutions (Section 4.2.2), interactive molecules and aggregates are expected to exhibit a fast decay rate (small value of τ, comparable with τ_1) whilst monomers would exhibit a slower decay rate (τ in the same order of τ_2).

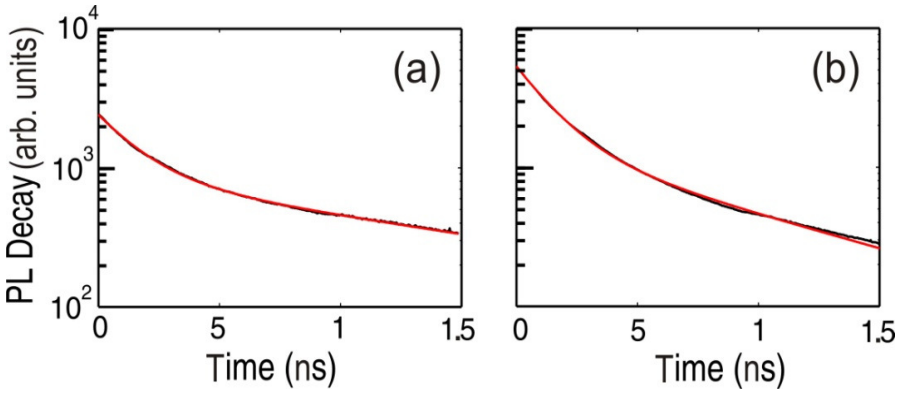

Figure 4.20 *Average PL decays for Coumarin (black line) on pure polycarbonate (a) and on silver polycarbonate (b) substrates together with double exponential fit (red line)*

Comparing the values of τ_i (i=1,2) with the corresponding values of τ_i*, it is clear that, although in both cases there is an observed reduction in lifetime, the lifetime of the monomers is more strongly affected by the presence of the silver nanoparticles.

The Purcell enhancement factor F [*116*], introduced in Section 2.4, has been calculated for the two species obtaining the values $F_1 = \tau_1/\tau_1^* = 1.12 \pm 0.03$ for the fast species associated with aggregates and $F_2 = \tau_2/\tau_2^* = 1.83 \pm 0.10$ for the slow species associated with the monomers. The difference in the enhancement factors can be attributed to a delocalization of the excitonic dipole in the aggregates, so that the overlap with the plasmon enhanced field is reduced for the aggregates compared with the monomers [*117*].

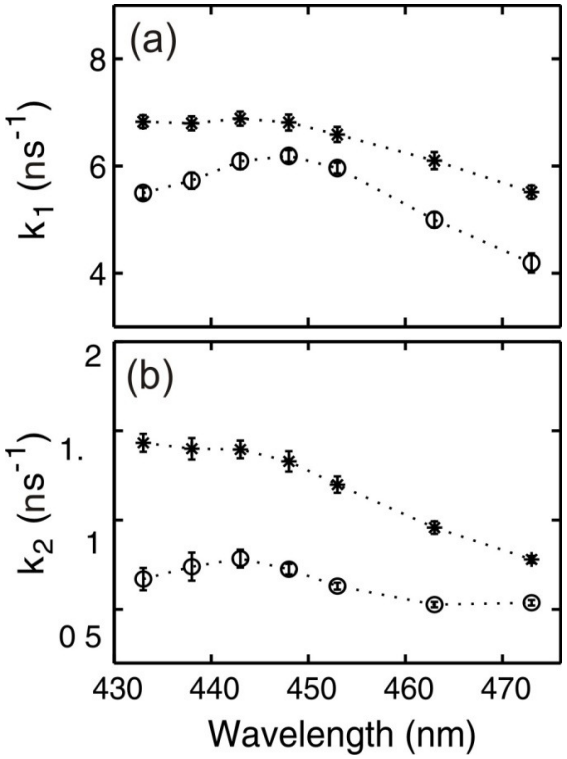

Figure 4.21 *(a) Fast and (b) slow components of the photon emission rate for Coumarin on polycarbonate (circle) and on silver polycarbonate (star) substrates as functions of wavelength.*

Comparing the enhancement factors measured by the time integrated emission (~8.5×) with the Purcell factors which take into account the reduction in photon lifetime (<1.83×), a discrepancy is observed. This difference suggests that the metal enhanced fluorescence is not only due to a modification of the radiative channels, but that additional factors, such as an increase of the absorption cross section [*75, 118, 119*], also need to be considered. In fact, localised surface plasmons have been demonstrated to enhance a range of optical mechanisms, such as absorption, but a quantitative evaluation of the contribution from a single mechanism has been limited by experimental factors.

4.2.4 Wavelength dependence of the Purcell factor

Using the time and spectrally resolved PL profiles in Figure 4.16, the emission rates and the Purcell enhancement factors have been investigated as functions of wavelength. The emission rates have been calculated from the PL decays for selected wavelengths over the emission peak (433, 438, 443, 448, 453, 463 and 473 nm). Each point has been obtained by averaging the PL decay over a ±5 nm range in order to reduce the errors. The resulting values for both the fast (k_1) and slow (k_2) components of the photon emission rate have been plotted for the two substrates in Figure 4.21 (a-b).

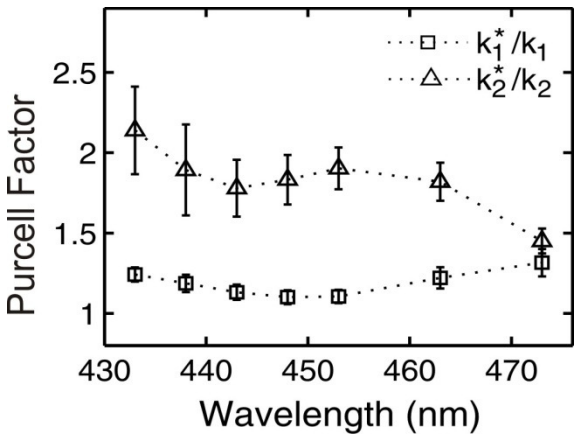

Figure 4.22 *Purcell factor F for the fast (square) and slow (triangle) components as a function of wavelength.*

At each wavelength the photon emission rate of Coumarin 102 clearly increases when deposited on silver modified substrates, but by different factors. In order to quantify these differences with the wavelength, the corresponding Purcell factors $F(\lambda) = k^*(\lambda)/k(\lambda)$ have been calculated and then plotted in Figure 4.22.

From this figure, it is clear that the fast and slow components show a different response to the surface plasmon excitation as a function of wavelength. In particular, the rate enhancement $F_2(\lambda)$ of the slow component, associated with the dye monomers, exhibits an oscillatory behaviour which is similar to the results previously reported by Okamoto et al. [*72*] (see Figure 2.9). The fast component $F1(\lambda)$ appears to only exhibit a minimum around the emission peak at 450 nm, though this could also be due to an oscillatory behaviour which occurs over a larger wavelength scale. Further investigation of this behaviour over a wider wavelength range was not possible due to the weakening of the emission spectrum of the dye molecule (see Figure 4.12).

In summary, silver impregnated polycarbonate substrates have been demonstrated to be excellent candidates for MEF applications, showing a PL enhancement factor in the order of 10. Photoluminescence is an important mechanism for analysis of biological samples and these substrates may be particularly suitable for this application due to the biocompatibility of the polycarbonate.

Chapter 5

Summary and future directions for Part I

In Part I of this thesis the fabrication and characterisation of silver impregnated polycarbonate substrates have been presented. After introducing plasmonic theory and some of the experimental findings in literature, the fabrication method of these metal-polymer composites based on a supercritical fluid impregnation technique was described.

These silver impregnated polycarbonate substrates were designed in collaboration with Nottingham University and tested as plasmonic substrates for sensing, potentially targeting bio-sensing applications. For this reason, the objectives were identified in obtaining a satisfying plasmonic response (SERS enhancement factor of at least 10^5 and MEF in the order of 10), reproducibility of the signal, temporal stability of the plasmonic properties whilst maintaining a low fabrication cost.

It is difficult to quantify costs involved in the fabrication, but there are several clear advantages in the presented fabrication method which can lead to inexpensive substrates. Firstly, the fabrication method is based on a single reactor process, so

costs of the space occupied by the necessary facilities are reduced; furthermore, the process is still to be optimised in terms of time necessary at each step and it is highly scalable to allow for impregnation of large polymeric sheets, reducing cost impact on the single substrate.

Characterisation of the fabricated substrates has been performed by varying impregnation parameters such as the amount of the precursors, the pressure and the impregnation time. TEM imaging of two substrates A and B fabricated at different pressure values revealed the formation of nanoparticles uniformly distributed within the first few microns from the surface. A clear inner boundary of the impregnated area was observed on substrate A and in general the impregnation depth was shown to depend on the impregnation time. The composition techniques (selected area electron diffraction and energy dispersive X-ray spectroscopy) confirmed the nanoparticles were made of metallic silver. Spectroscopic analysis (absorption and reflection spectra) showed a broad plasmon resonance peak due to a distribution of the nanoparticle size. Finally, the prism coupling technique was used to measure the impregnated film refractive index and identify a relative impregnation density.

Thanks to the feedback provided to the fabrication team, the plasmonic response target was achieved in that measurements of the SERS response of two different target molecules deposited by a drop cast method from ethanol and water solutions have revealed enhancement factors up to an estimated value of 10^5, in off-resonant conditions, comparable with commercially available plasmonic substrates such as Klarite®. The best result was achieved in a substrate fabricated with 200 mg mass precursor, at an impregnation pressure of 10.3 MPa, tested with an ethanol solution of 4-ATP. This result is even more remarkable as it was obtained in off-resonant conditions, so the enhancement factor is expected to increase of a further 10^2 in resonant conditions [*95*]. MEF response target for the same substrate has also been achieved, obtaining a PL enhancement factor of ~8.5 accompanied by a reduction in photon lifetime. In this context, Purcell Factor wavelength dependence has also been discussed. Considering the results, these plasmonic substrates are expected to show good performances for other enhanced optical phenomena, such as enhanced absorption or enhanced energy transfer [*120*], which could be the object of future work. As part of future work, resonant SERS measurements (at 400 nm excitation

wavelength) need to be performed to verify the higher enhancement factor achievable with these substrates. Moreover, biocompatibility of these substrates also needs to be demonstrated in order to target bio-sensing applications.

Temporal stability of these silver impregnated polycarbonate substrates has also been demonstrated by repeating SERS measurements after more than one month and obtaining comparable results. Moreover, signal was still present in substrates which were tested after more than one year.

Reproducibility of the SERS response was also tested, but, in this case, results were unsatisfactory, observing in standard (not post-processed) samples a signal variation of 90% where present and in some points no response at all. Results improved significantly in substrates which were post-processed by RIE etching, achieving SERS signal variation lower than 50% across the substrate. This improvement in reproducibility of the signal has been attributed to a more uniform distribution of the metal nanoparticles deeper into the substrates. The demonstrated ability to post-process the substrates using oxygen reactive ion etching has also introduced an additional level of structural design to the substrates. Controlled etching of the substrates can be employed as part of the fabrication in order to obtain a better reproducibility of the signal and, for future work, it will allow for fabricating structures such as optical waveguides. These geometries may be advantageous in the case of SERS applications as the enhanced propagation length averages over many plasmon-analyte interactions, thus offering increased sensitivity and reproducibility of the measured response.

The nanocomposites showed SERS and MEF responses comparable with the results of other substrates reported in the literature and they can offer some benefits over other conventional plasmonic substrates, in that they are temporally stable, potentially biocompatible and could be made relatively cheaply. These substrates are excellent candidates for applications in routine medical analysis, biological sensors and nanophotonics.

PART II

Semiconductor modified Microstructured Optical Fibres

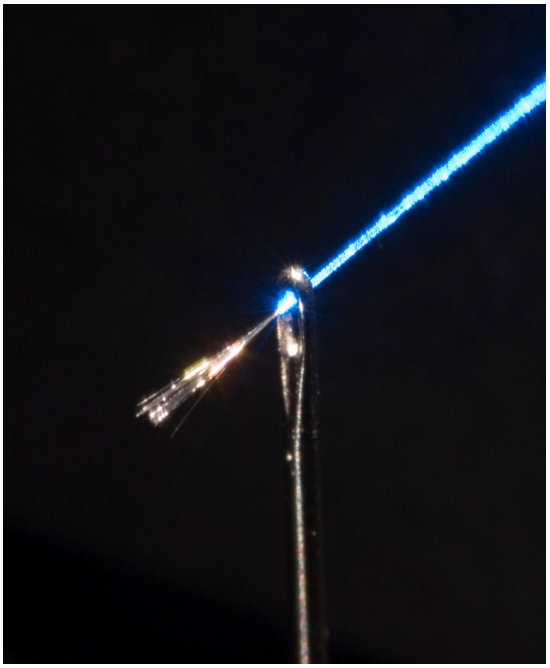

Figure II-1 *Bundle of germanium wires etched out from microstructured optical fibres. The glass fibre is glowing from blue laser light launched into the cladding [121].*

In 2009 the Nobel Prize in Physics was awarded to Charles K. Kao *"for groundbreaking achievements concerning the transmission of light in fibres for optical communication"*. In 1965 the available silica glass fibres transmitted light signals over only 20 meters and found their first applications in medicine for internal medical examinations. Kao suggested that the short transmission length was due to impurities in the silica glass and calculated that a pure silica glass fibre could transmit light signals over 100 kilometres [*122*]. In the 1970s the first high purity silica-glass fibre was fabricated [*123*]. At the same time a GaAs semiconductor laser, operating continuously at room temperature, was demonstrated. The availability of a compact optical source and low loss optical fibres lead to the development of the first telecommunication system.

Since then, optical fibres and semiconductor technologies have been developed simultaneously, with the achievements in one field boosting improvements in the other. Both constitute the backbone of modern communication technologies and have found applications in everyday life from medicine to the internet. Nowadays, more than one billion kilometres of optical fibre and as many semiconductor devices generate, transport, manipulate and detect light signals allowing for simultaneous phone calls and internet communications worldwide.

Nonetheless the process of converting photons to electrons and vice versa is not very efficient, as it requires coupling devices with an enormous loss of power, alignment restrictions, overall limitation in the bandwidth and the devices are cumbersome. For example, in the 80s the problem of the signal attenuation required placing solid-state repeaters every 60-70 km, limiting fibre communications to continental land (or you could put continental landmass), as electronic repeaters require easy access for maintenance. A more elegant solution to this problem was provided in 1985 with the invention of the erbium-doped fibre amplifier. EDFAs became commercially available in the early 90s and replaced the electronic devices creating a new all-fibre system and opening up to long haul (transoceanic) communications.

Solid state devices are still required to generate, process and detect light, but implementing semiconductor technology inside optical fibres could allow signals to be manipulated without having to leave the fibre. Deposition of semiconductors such

as silicon inside optical fibres can potentially lead to a new generation of integrated all-fibre devices, which could potentially have a huge impact on telecommunications in terms of increased speed and transmission efficiency.

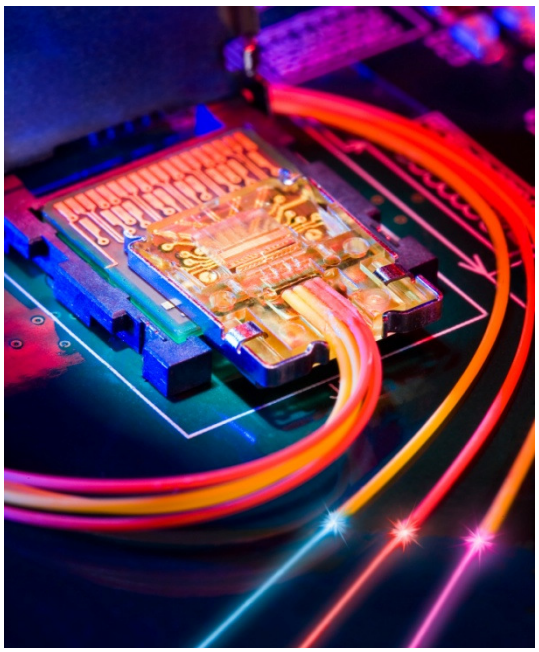

Figure II-2 *Light peak, by Intel. The world's largest semiconductor chip maker is launching in 2010 a new optical cable component to connect electronic devices with each other, starting at 10 Gb/s.*

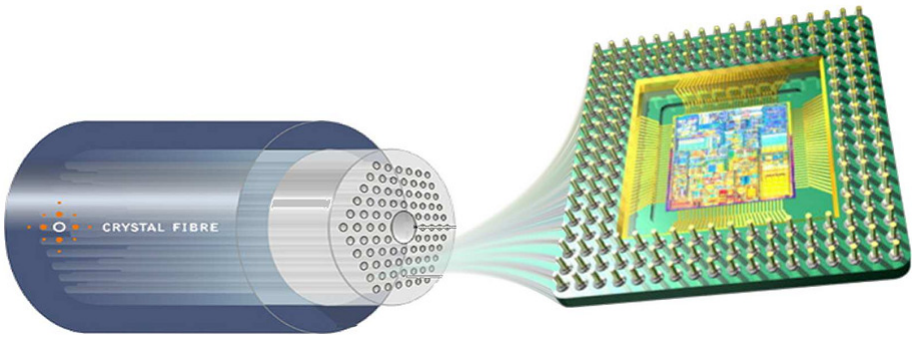

Figure II-3 *Picture of potential application of semiconductor modified microstructured optical fibre: semiconductor integration could be implemented inside optical fibres*

In PART II of this thesis our work in the deposition of semiconductor material inside optical fibres will be shown. After discussing optical fibres and their operation principle, semiconductor materials will be introduced with a particular focus on the electronic and optical properties of silicon (single crystalline, polycrystalline and amorphous) and germanium, which are the semiconductors used for this project.

The deposition process of semiconductor material inside optical fibres combines high pressure microfluidic with chemical vapour deposition (CVD) to deposit amorphous materials and requires further annealing to crystallise the semiconductor. The structural investigation of materials obtained with different deposition parameters has been necessary in order to tailor specific requirements. Part of the semiconductor wires have been etched out of the fibre and then characterised using imaging (SEM and TEM), whilst Raman spectroscopy has been performed on samples before (focusing through the silica glass) and after the etching.

Owing to the widespread interest in silicon photonics, as will be discussed in section 7.3, investigations have been focused on silicon modified capillaries. Transmission loss measurements have been performed on a range of amorphous and polycrystalline silicon samples, using a cut-back technique. The obtained results show loss values which are favourably comparable to values reported in literature. Both amorphous and polysilicon modified fibres can potentially find application in a range of photonic and signal processing devices.

Chapter 6

Optical Fibres

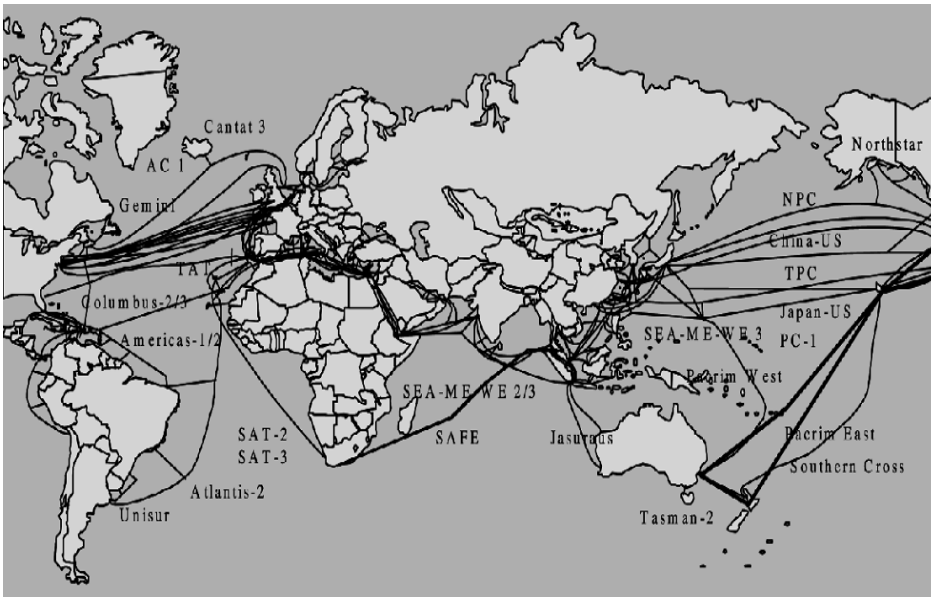

Figure 6.1 *International undersea network of fibre-optic communication system around year 2000 [124].*

Standard optical fibres transmit optical signals relying on the mechanism of total internal reflection, where the electromagnetic wave carrying the information can be trapped in a high refractive index core, and thus propagate along the fibre. Although

this fundamental mechanism has been known since 1854 [*125*], prototypes of glass fibres have only been dated from the beginning of 1920 [*126*]. In the 1950s a suitable low index, flexible material for the cladding was developed and optical fibres started being used to transfer images (in a mechanism similar to certain insect eyes), finding applications in medicine [*127, 128*]. It is not until the 1970s when fabrication technology was developed sufficiently to achieve a high purity silica glass and transmission losses were reduced to 20 dB/km [*123*] that fibres were ready for telecommunications. Optical fibres are now synonymous with telecommunication systems, although they still find applications in several other fields such as sensors and medicine.

The foundation of the optical fibre operation is the physical mechanism of total internal reflection, where the light that carries information propagates within a higher refractive index core surrounded by a lower index cladding. Optical fibre technology does not stop there, since the fabrication of the first optical fibre in 1970, research efforts have been focused on improving guiding properties and, in particular, reducing propagation losses. As soon as transmission losses were reduced enough to enable signal transmission over several kilometres, new challenges appeared such as the control of dispersion and non-linear effects.

Although the first attempts to introduce air gaps in the cladding are dated in the early 70s [*129*], it was not until more than 20 years later that this idea was developed and refined to bring practical advantages. In 1995, Birks and co-workers [*130*] proposed to implement microstructures into the cladding in order to introduce a further level of design and control of the fibre guiding properties. Air holes running along the fibre were adopted, setting off the establishment of the microstructured optical fibre.

In this chapter an overview on optical fibres will be presented. Starting with simple step index fibres, the guiding mechanism of total internal reflection will be presented. Coupling parameters such as numerical aperture and Fresnel reflections will be discussed together with transmission loss mechanisms, focusing on the specific case of silicon as the core material. Finally, microstructured optical fibres will be introduced as single material fibres presenting an arrangement of holes

running along the fibre length. These fibres can be used as 2D templates for material deposition.

6.1 Step-index fibres

Step index fibres are so called because of the abrupt change in refractive index between core and cladding (Figure 6.2). Specifically the core has a higher refractive index compared with the cladding and the principle of operation is total internal reflection.

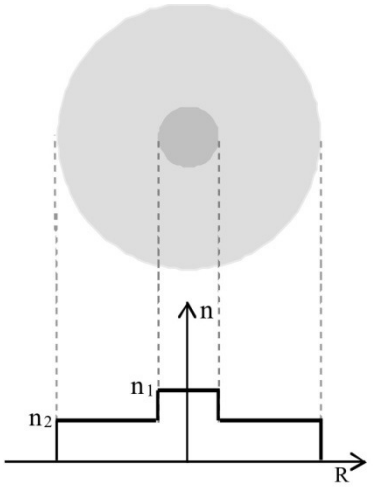

Figure 6.2 *Schematic of step-index fibre cross section with refractive index profile.*

6.1.1 Total internal reflection

When light travelling in a high refractive index material (n_1) meets an interface with a lower refractive index (n_2) then, in general, the ray is partially reflected back and partially refracted into the second medium, far from the normal to the interface (see Figure 6.3) according to Snell's law:

$$n_1 \sin\theta_i = n_2 \sin\theta_r \tag{6.1}$$

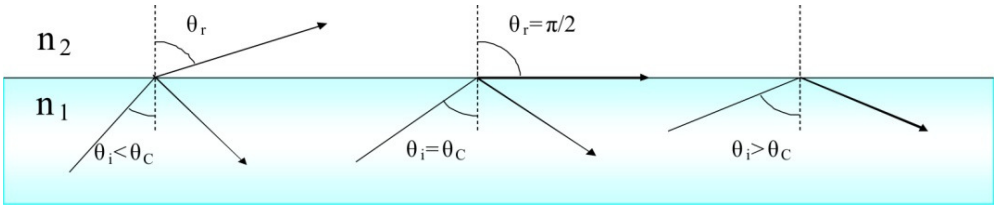

Figure 6.3 *Schematic of total internal reflection mechanism.*

where θ_i and θ_r are the incident and the refraction angle respectively. When θ_i is bigger than the critical angle θ_C, with θ_C such as:

$$\sin\theta_C = \frac{n_2}{n_1} \tag{6.2}$$

light is entirely reflected back in the same medium and this phenomenon is known as total internal reflection.

In an optical fibre, the cylindrical symmetry of the core-cladding interface guarantees that light which is totally reflected at the first interface will continue to be reflected, thus staying trapped and travelling along the fibre.

Before it can be guided, light must first be coupled efficiently inside the fibre itself. Coming from air, through lenses or from another fibre, two parameters must be considered: firstly the numerical aperture (NA), which is a geometrical factor that indicates the light-gathering capabilities of the fibre, and the Fresnel reflection which determines the coupling losses due to reflection at the input interface owing to differences in the refractive index.

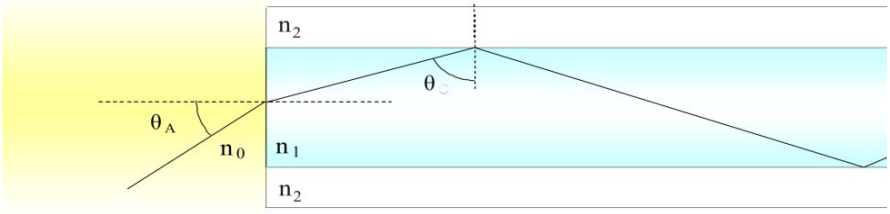

Figure 6.4 *Schematic of input coupling. Numerical aperture is obtained from the value of θ_A which correspond to $\theta=\theta_C$.*

6.1.2 Numerical aperture

As a general assumption, the medium at the input will have a refractive index (n_0) different from the cladding (n_2). Assuming that the input surface is perfectly perpendicular to the propagation direction, the numerical aperture is given by the maximum incident angle θ_A for a ray in order to generate total internal reflection ($\theta=\theta_C$) as for the following [*122*]:

$$NA = n_0 \sin\theta_A = n_1 \cos\theta_C \tag{6.3}$$

which, using Eq.(6.2) and trigonometric relations can be rewritten as:

$$NA = \left(n_1^2 - n_2^2\right)^{1/2} \tag{6.4}$$

showing that the numerical aperture only depends on the fibre material parameters.

In an approximation of a small refractive index difference ($n_1 \cong n_2$), Eq.(6.4) can be rewritten as:

$$NA = n_1\sqrt{2\Delta} \tag{6.5}$$

where Δ is the relative core-cladding index difference:

$$\Delta = \frac{n_1 - n_2}{n_1} \ . \tag{6.6}$$

The numerical aperture provides the acceptance angle of the optical fibre, therefore when launching light into the core, it is important to match the NA of the coupling lens to that of the fibre to obtain an efficient coupling.

6.1.3 Fresnel reflection

Fresnel equations provide the reflection and transmission coefficients for an electromagnetic wave which is incident on an interface. The reflection coefficients

$r_{//}$ and $r_{\perp}$ for the components polarised parallel and perpendicular respectively to the incident field can be expressed by the following:

$$r_{\perp} = \frac{n_0 \cos\theta_i - n_1 \cos\theta_t}{n_0 \cos\theta_i + n_1 \cos\theta_t} \qquad \text{and} \qquad r_{//} = \frac{n_0 \cos\theta_t - n_1 \cos\theta_i}{n_0 \cos\theta_t + n_1 \cos\theta_i} \tag{6.7}$$

where θ_i is the incident angle and θ_t is the transmitted angle, which is connected to θ_i and to the refractive index of the two mediums (n_0 and n_1) by the Snell's Law Eq.(6.1). The fraction of power that is reflected back is given by their respective squared values:

$$R_{\perp} = (r_{\perp})^2 \qquad \text{and} \qquad R_{//} = (r_{//})^2 \ . \tag{6.8}$$

In the case of unpolarised light the reflected power (%) is:

$$R = \frac{R_{\perp} + R_{//}}{2} \ . \tag{6.9}$$

For example, when coupling light into an optical fibre, Fresnel reflection takes into account the amount of light that is reflected back at the air/fibre interface because of the difference in the refractive index. This term becomes significant for free space coupling into a high refractive index core. If we consider the particular case of normal incidence ($\theta_i = \theta_t = 0$), then Eq.(6.7) can be rewritten as:

$$r_{\perp} = r_{//} = \frac{n_1 - n_0}{n_1 + n_0} \tag{6.10}$$

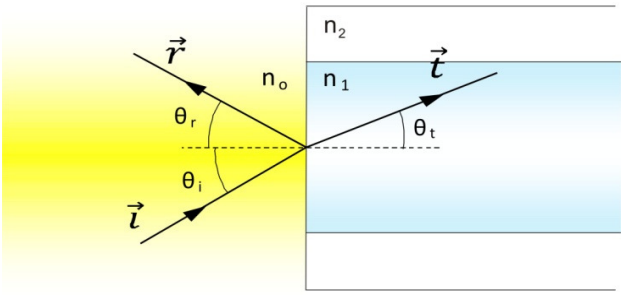

Figure 6.5 *Schematic of Fresnel reflection. $\vec{i}$, $\vec{r}$ and $\vec{t}$ are the incident, reflected and transmitted field, respectively.*

It can be shown that at the air/silicon interface, in the case of a silicon core with a refractive index of ~3.4, the Fresnel reflection R is about 30% of the incident power. This factor can be reduced by treating the input surface with anti-reflection coating, which can cut reflection losses to virtually zero [*131*].

6.2 Wave optics

Geometrical optics can help visualise light travelling in optical fibres and in some cases, as shown in Sections 6.1.2 and 6.1.3, it provides a simple tool to describe fibre optics phenomena. In general, however, another approach must be taken for the description of the guided signal. A rigorous approach starts from Maxwell's equations describing the propagation of the field components and provides a discrete and limited set of transverse modes, however the mathematical formalism is cumbersome.

Most of the material effects on the guided field can be described using a simpler approach, which only considers the amplitude of the guided field and is useful for designing lightwave systems. The amplitude A of the guided field varies along the propagating direction z according to the non-linear Schrödinger equation [*122*]:

$$\frac{\partial A(z,t)}{\partial z} = -\frac{i\beta_2}{2}\frac{\partial^2 A(z,t)}{\partial t^2} - \frac{\alpha}{2}A(z,t) + i\gamma\left|A(z,t)\right|^2 A(z,t) \qquad (6.11)$$

where β_2 is the dispersion parameter, α is the attenuation constant and γ is the non-linear parameter. The three terms on the right hand side of Eq. (6.11) account for the dispersion, losses and non-linearities in the fibre, respectively, and will be discussed in the following sections.

6.2.1 Dispersion

In a homogeneous medium, dispersion arises from different frequencies experiencing a slightly different refractive index, as $n = n(\omega)$ (chromatic dispersion). In waveguides, an additional dispersion contribution arises from the tail of the field

distribution extending into the cladding (low refractive index) by an amount that is different for each wavelength (waveguide dispersion). In both cases, each wavelength is caused to travel at a different speed and the pulse to spread in time. Interestingly, dispersion can be exploited [this word doesn't feel right, utilised might be better] in order to shape a pulse by adding dopants to the material or by engineering waveguide structures.

The dispersion length L_D provide the length scale over which dispersion becomes important and can be calculated as [*132*]:

$$L_D = \frac{T_0^2}{|\beta_2|} \tag{6.12}$$

where T_0 is the pulse width, measured where the pulse intensity is $1/e^2$ times its peak value. This value is proportional to the full width half maximum (FWHM), which is commonly provided, by a factor that depends on the pulse shape. For example, in the case of a gaussian pulse $T_{FWHM} = 1.665\ T_0$, whilst in the case of a hyperbolic secant pulse $T_{FWHM} = 1.763\ T_0$.

In a 5.6 μm diameter silicon wire, at 1540 nm, β_2 can be estimated to be ~1 ps^2/m [*133*]. Assuming a hyperbolic secant pulse with T_{FWHM} = 5 ps, the calculated dispersion length is $L_D \sim 8$ m. Due to the short length of the semiconductor modified samples presented in this thesis (~1 cm), dispersion contribution is negligible and will not be investigated further.

6.2.2 Fibre Losses

While coupling parameters such as numerical aperture and Fresnel reflections need to be accounted for in order to optimise the power coupled into the fibre, transmission losses are responsible for the amount of power loss during propagation in the fibre and hence for the signal attenuation. Losses are not only important in terms of transmission, but are especially important to determine whether or not non-linear processes can be observed, as they depend on the power density (see Section 6.2.3).

6.2.2.1 Attenuation

Considering only the loss term in Eq.(6.11) yields:

$$\frac{\partial A(z)}{\partial z} = -\frac{\alpha}{2} A(z) \tag{6.13}$$

which is readily solved, providing the expression of the field amplitude as a function of the distance *z*:

$$A(z) = A_0 \exp\left(-\frac{\alpha}{2} z\right) \tag{6.14}$$

where $A_0 = A(0)$. The expression for the power as a function of the propagation distance can be obtained by the square of Eq.(6.14) as

$$P(z) = P_0 \exp(-\alpha z) \tag{6.15}$$

where $P_0=P(0)$ represents the input (coupled) power.

The attenuation constant α can be expressed in dB/m using the following:

$$\alpha[dB/m] = -\frac{10}{L} \log_{10}\left(\frac{P(L)}{P_0}\right) \tag{6.16}$$

where L is the propagation distance in metres. This expression will be used in Section 9.2, where the technique used for loss measurements will be described.

6.2.2.2 Scattering losses

Together with absorption losses which depend on the material, scattering losses also contribute towards the overall signal attenuation. Different types of scattering can occur depending on the dimension of crystalline defects or irregularities compared with the wavelength of the propagating light [*122*].

When defects are smaller than the optical wavelength or the density in the material changes slightly due to the fabrication process, these irregularities can be seen by the propagating field as local fluctuations in the refractive index. In this case, Rayleigh

scattering occurs and the scattering cross section depends on the optical wavelength as λ^{-4}, so that the losses can be expressed as:

$$\alpha_{Rayleigh} = \frac{C}{\lambda^4} \tag{6.17}$$

where C is a constant dependent on the material.

Rayleigh scattering is the most common type of scattering loss, but Mie scattering should also be considered. This process has been explained in detail in Part I, in the context of light scattering from small metallic particles. Similarly, it can also be a source of propagation losses when defects and irregularities have dimensions comparable with the optical wavelength. For example, core-radius variation along the length of the fibre can result in Mie scattering losses [*134*].

6.2.3 Non-linear optics

The last term in Eq.(6.11) accounts for the non-linear response of the material, as suggested by the term's dependence on the third power of the field amplitude. Non-linear behaviour occurs when high power densities are present in a material. In this case the refractive index of the medium can be written as [*132*]:

$$n' = n_1 + n_2\left(\frac{P}{A_{eff}}\right) \tag{6.18}$$

where n_1 and n_2 are different from what was previously defined. In this context n_1 is the linear refractive index, n_2 is the non-linear refractive index (also referred to as the Kerr coefficient), P is the optical power and A_{eff} the effective mode area [*122*] (their ratio indicating the power density). For standard silica fibres, the value of n_2 is about 2.6×10^{-20} m^2/W, while for crystalline silicon it has been measured to be in the order of 10^{-18} m^2/W [*135*], showing that non-linearities in silicon are a hundred times larger than in silica.

The non-linear coefficient γ in Eq.(6.11) is related to the non-linear refractive index as follows:

$$\gamma = \frac{2\pi \cdot n_2}{A_{eff}\,\lambda} \tag{6.19}$$

This important parameter defines the fibre effective non-linearities by unit length ($[\gamma] = M^{-1}W^{-1}$) and suggests that nonlinearities can be controlled by engineering the effective mode area A_{eff} in order for them to be suppressed or enhanced. An optical fibre can be engineered to tightly confine the mode in a small core in order to enhance wanted non-linear effects or distribute the mode in a wide core to minimise unwanted non-linear effects. The highest degree of flexibility into optical fibre design has been obtained by employing microstructured optical fibres.

Some examples of non-linear effects include:

- Raman scattering, as discussed in Section 2.3.1 in a different context;
- Self-phase modulation (SPM) [*136*], which is caused by the intensity dependence of the non-linear refractive index term in Eq.(6.18). The propagating pulse induces a change in the refractive index which varies with the time. This results into a phase shift and, consequently, to spectral broadening of the pulse;
- Soliton generation [*137, 138*], where the non-linear response of the medium is used to balance the dispersion;
- Supercontinuum generation [*139*], where high power short pulses are broadened by different non-linear effects resulting in broadband frequency generation;

and many others [*132, 140, 141*].

6.2.4 Wave optics in silicon

In silicon waveguides, the non-linear Schrödinger equation (6.11) can be modified to take into account additional non-linear absorption that arises at high power regime. Two photon absorption (TPA) is a non-linear effect where the simultaneous absorption of two photons of frequency ω brings an electron to an excited state of

energy correspondent to 2ω. In semiconductors such as silicon, this non-linear effect causes the formation of electron-hole pairs and, hence, generates free carriers which can remain in the semiconductor material for a relatively extended period before recombining. This effect is detrimental for high power optical applications, as TPA-induced free carriers cause absorption and thus they represent an additional source of optical losses. Consequently, the Eq.(6.11) can be modified as follows:

$$\frac{\partial A(z,t)}{\partial z} = -\frac{i\beta_2}{2}\frac{\partial^2 A(z,t)}{\partial t^2} - \frac{\alpha + \sigma_f}{2}A(z,t) + i\gamma'\left|A(z,t)\right|^2 A(z,t) \ , \tag{6.20}$$

where $\gamma' = \gamma + i\frac{\beta_{TPA}}{2A_{eff}}$ is the modified non-linear parameter, with β_{TPA} being the TPA parameter, and σ_f represents the losses corresponding to the TPA-induced free carriers. TPA parameter has been reported in silicon to be β_{TPA}=5×10^{-12} m/W [*142*] at 1550 nm, whilst σ_f is proportional to the free carrier density N_f, with [*143*]

$$\frac{\partial N_f}{\partial t} = \frac{\beta_{TPA}}{2h\nu}\frac{\left|A(z,t)\right|^4}{A_{eff}^2} - \frac{N_f}{\tau_f} \tag{6.21}$$

where τ_f is the free carrier lifetime [*144*]. In silicon, this value has been reported to be in the order of few hundreds of picoseconds [*145*].

These equations must be considered for a quantitative analysis of non-linear experiments in silicon modified optical fibre. In particular for high power, non-linear applications, measurements of linear losses are not sufficient and non-linear losses need to be taken into account. Ultimately, overall low losses are the necessary condition for powers to stay high in the waveguide in order to observe non-linear effects. Although experiments reported in this thesis are conducted in linear regime, these considerations are preliminary to the intended non-linear applications of the silicon modified fibre. Moreover, the challenge related to optical losses caused by TPA induced free carrier is here formally introduced and it will be picked up again in Section 7.3, where some solutions reported in literature, aimed to overcome this problem, will be discussed.

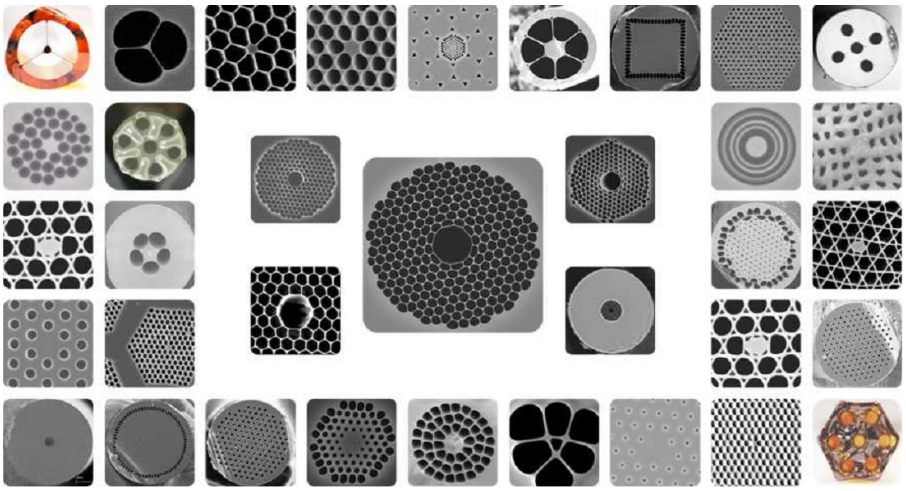

Figure 6.6 *Cross sectional micrograph of some of the microstructured optical fibres produced at the ORC.*

6.3 Microstructured Optical Fibres

Microstructured optical fibres are characterised by an arrangement of small holes that run along the fibre length so that the guiding mechanism can be different to the conventional step-index method. Specifically there are two main types of MOFs: holey fibres and photonic bandgap fibres (PBGFs).

In the first type, confinement is achieved using a modified total internal reflection, in that holes are placed around a solid core, not necessarily in a periodic way, and forming a structure whose size is comparable with the wavelength of the transmitted light. Light will therefore experience an average lower refractive index surrounding the core due to the presence of air in the holes analogous to a step index fibre.

Whereas photonic bandgap fibres (PBGFs) exploit the principle of photonic bandgap guiding (hence their name), which is completely different from total internal reflection. In this case, air holes are arranged periodically in the transverse dimension in order to reproduce a two-dimensional photonic crystal running along the fibre length so that some wavelength ranges are forbidden from entering the structured cladding (photonic bandgap) and it is consequently confined in the (defect) core. Since these fibres guide with a different mechanism they have the interesting feature of being able to guide light in a low refractive index (or hollow) core.

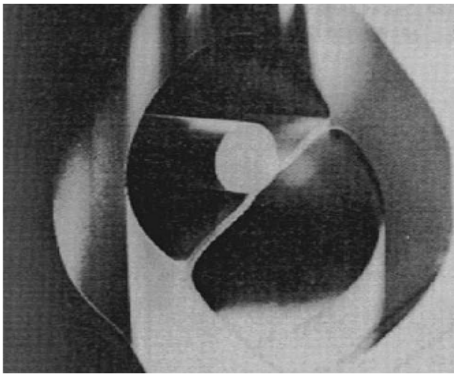

Figure 6.7 *First demonstration of an MOF by Kaiser and co-workers[129].*

Historically, the first steps towards MOFs were made in the early 1970s when Kaiser and co-workers fabricated a fibre consisting of a small rod suspended inside a bigger capillary by a thin glass strut (see Figure 6.7) in an attempt to reduce the transmission losses of silica glass fibres [*146, 147*], which were still suffering from high material losses.

Only a few years later Yariv and co-workers theoretically proposed a fibre where light would be confined in a lower index core by Bragg reflection [*148*], fabricated using alternating high and low index cladding materials. However, with the development of new techniques to improve the purity of silica used for optical fibres [*149*], transmission losses were enormously reduced so investigations into more complex structures were put on hold for several years.

In 1996 Russell and co-workers proposed implementing a photonic crystal structure inside an optical fibre [*150*]. They succeeded in producing an all-silica fibre with an hexagonally shaped pattern of air holes with a "lattice defect" introduced into the centre of the pattern in which the light could be guided (Figure 6.8).

Since this development a renewed interest in engineering optical fibres for a variety of applications has led to the fabrication of different kinds of structures able to carry more power [*151*], to have multiple cores [*152*], to show higher or lower non-linearities [*153*], or to exhibit higher birefringence [*154*] and/or to have widely engineerable dispersion profiles [*155*] etc.

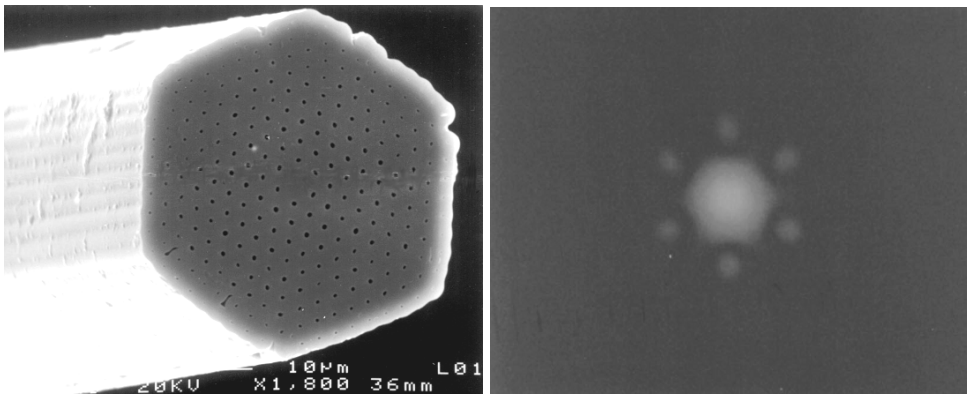

Figure 6.8 *SEM micrograph of the microstructured fibre proposed by Russell and co-workers in 1996. On the right, photographed far-field pattern at 632.8nm [150].*

MOFs have allowed progress in fields such as telecommunications, non-linear optics, supercontinuum generation, medical sciences and sensing. In particular, for sensing applications the holes can be used as channels to host gases or liquids to be analysed [*156*]. Furthermore, the inclusion of materials inside the running holes can also be used to tailor the spectral position and the extent of the bandgap [*157*]. The introduction of structured holes has not only brought in additional freedom in fibre design and in tailoring specific properties, but they can also be used as templates to host new materials and potentially integrate devices for the future generation of hybrid photonic device.

Chapter 7

Semiconductor materials

Since the first transistor was fabricated in 1946, semiconductor materials have been fundamental to modern technology. From radio to solar panels, semiconductor devices can be found in a large number of everyday gadgets and have transformed our lifestyles over the past 50 years.

In this chapter the fundamental properties of semiconductor materials will be introduced, showing how their electronic structure enables them to transform light signals into electrical signal and vice versa. The elemental semiconductors silicon and germanium will be presented as these materials have both been deposited inside the MOF templates (see Chapter 8). In particular, an insight into the exciting field of silicon photonics will be presented and the optical properties of the different crystalline states (single crystal, polycrystalline and amorphous silicon) will be discussed.

7.1 Semiconductors

Semiconductors are a class of material that present an energy gap E_g between valence band and conduction band that is of the order of a few electronvolts. This separation

is such that at ambient temperature, thermal energy can make electrons "jump" up to the conduction band (Figure 7.1).

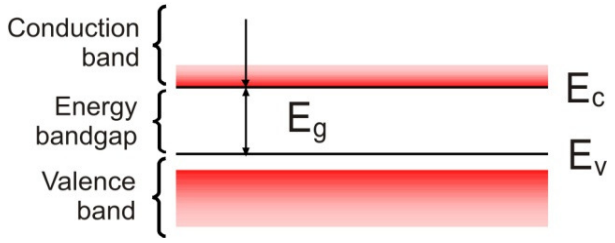

Figure 7.1 *Simplified energy band diagram of a semiconductor.*

The band gap value can be determined by optical absorption. In a direct bandgap material, a photon of energy $h\nu > E_g$ is absorbed by an electron that is excited to the conduction band leaving a hole in the valence band. This transition occurs "vertically", that is with the same value of the wavevector $\vec{k}$ (Figure 7.2).

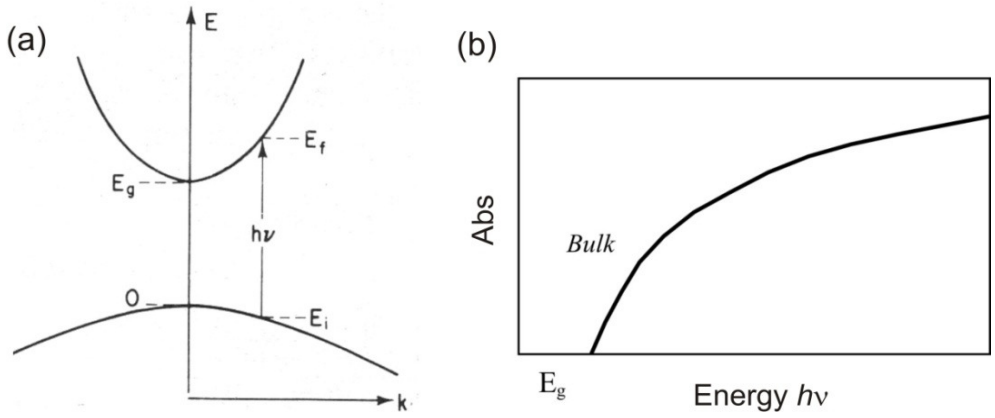

Figure 7.2 *Example of (a) band structure of a direct bandgap semiconductor and (b) corresponding absorption spectrum.*

The electron-hole pair is called an exciton. Optically the exciton can relax (recombination) and re-emit a photon with energy equal to the bandgap (photoluminescence). Alternatively, if an external field is applied the two charges will travel in different directions generating current (as happens in a detector). An exciton can also be generated by injecting an excess of carriers, which will recombine at the bandgap (i.e., an electrically pumped light source).

In an indirect bandgap semiconductor the band edges of the conduction and the valence band are separated in $\vec{k}$ space (see Figure 7.3), so the absorption of a photon of energy $h\nu > E_g$ will occur only if a phonon of wave-vector $\vec{k} \approx \vec{k}_g$ is involved, as required by the conservation of momentum laws. This restriction makes indirect bandgap materials much less efficient at emitting light compared to direct bandgap semiconductors.

Depending on their chemical composition, semiconductors can be intrinsic or extrinsic. An intrinsic semiconductor is basically a pure semiconductor, where the bonds are formed by sharing an electron between two adjacent atoms in the crystalline structure, so that electrons and holes are present in equal numbers. Extrinsic semiconductors are doped semiconductors, where impurities of different materials are used to create an excess number of electrons or holes, which contributes towards the total number of carriers.

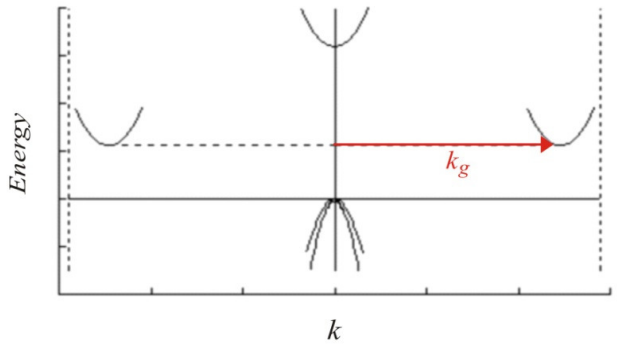

Figure 7.3 *Example of band structure of an indirect bandgap semiconductor.*

7.1.1 Crystal structures

On an atomic scale, semiconductor materials may present different atomic arrangements. Semiconductors are called amorphous when the position of the atoms is disordered and there is no long range order, crystalline when the atoms are arranged in a long range order and polycrystalline when there is a long range order, but ordered areas are oriented in different directions (see Figure 7.4).

In a crystalline structure a unit cell can be identified as the smallest structure that reproduces the arrangement of the atoms in the crystal when translated in three dimensions (lattice). This cell can de described by a set of vectors, $\vec{a}_1, \vec{a}_2, \vec{a}_3$, which identify the direct lattice (in the real space).

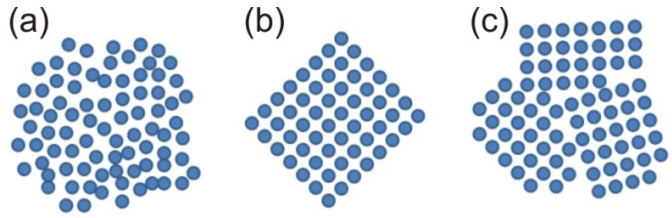

Figure 7.4 *Schematic of crystalline structures: (a) amorphous, (b) crystalline and (c) polycrystalline*

The periodicity of the lattice can also be expressed through a plane wave $\exp(i\vec{k} \cdot \vec{r})$ as a set of wave-vectors $\vec{K}$ such as for every value of $\vec{r}$:

$$\exp\left[i\vec{K} \cdot \vec{r}\right] = \exp\left[i\vec{K} \cdot \left(\vec{R} + \vec{r}\right)\right] \tag{7.1}$$

where $\vec{R}$ are generic points in the lattice, thus:

$$\exp\left(i\vec{K} \cdot \vec{R}\right) = 1 \tag{7.2}$$

The set of wave vectors $\vec{K}$ is a called reciprocal lattice and is usually indicated as $\vec{b}_1, \vec{b}_2, \vec{b}_3$.

Planes and directions in a lattice can be described by three numbers, l, m, n, called the Miller indices. These indices are used as coordinates to identify directions in the direct lattice and planes in the base of the reciprocal lattice. In particular [l m n] (i.e. square brackets) indicates a direction in the direct lattice base ($d = l\vec{a}_1 + m\vec{a}_2 + n\vec{a}_3$), whilst ($l$ m n) (i.e. round brackets) identifies a plane in the reciprocal lattice ($p = l\vec{b}_1 + m\vec{b}_2 + n\vec{b}_3$). In the particular case of a cubic unit cell the direct lattice is reduced to the Cartesian coordinates and the direction [l m n] is normal to the correspondent plane (l m n).

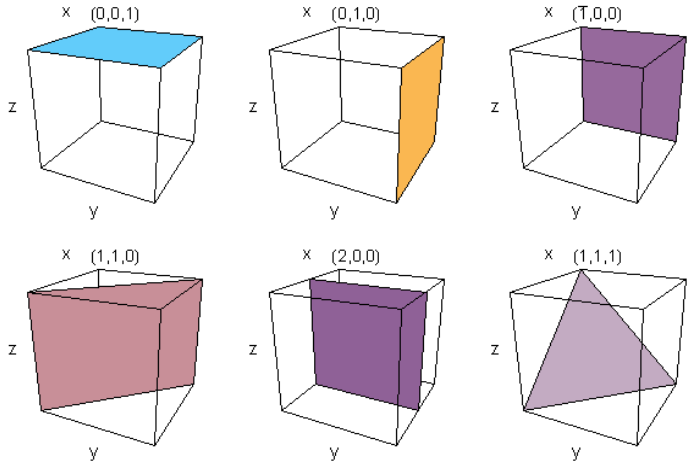

Figure 7.5 *Example Miller indices showing the plane of atoms they represent in a crystal lattice.*

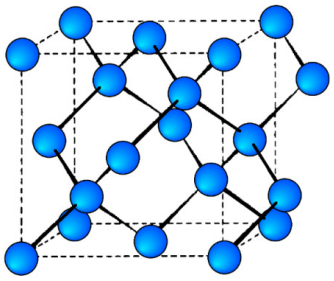

Figure 7.6 *Face centred cubic (fcc) silicon crystal structure.*

7.2 Group IV semiconductors

7.2.1 Silicon

Silicon is an intrinsic semiconductor and has an indirect bandgap of ~1.12 eV (1107 nm) at room temperature [*158*]. Its crystalline structure is a face centred cubic (fcc, see Figure 7.6) where each atom shares 4 electrons with the 4 nearest neighbour atoms and form the crystal (covalent) bond. For each atom then a total of 8 electrons (4 on its own and 4 from the nearest neighbour atoms) occupy the valence band. The bandgap of ~1.12 eV means that silicon absorbs all light in the visible spectrum (opaque) while it is transparent in the infrared.

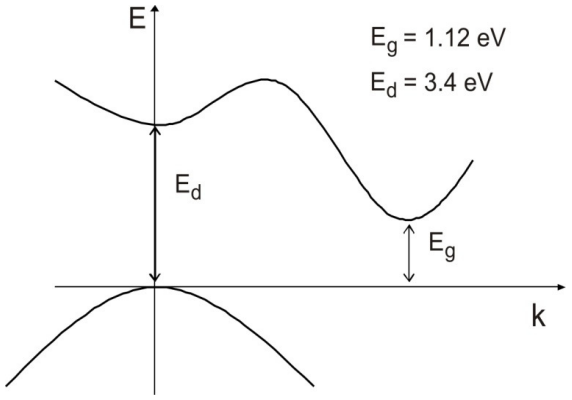

Figure 7.7 *Silicon energy indirect (E_g) and direct (E_d) bandgap.*

In crystalline silicon all the atoms are theoretically perfectly arranged, so that electrons that "jump" to the conduction band can travel efficiently along the crystal when an external field is applied. Conductivity in silicon is intrinsically limited by collisions of carriers with lattice vibrations (phonons) [*159*] and with ionised impurities [*160*].

Silicon electronic properties have been extensively studied and it is the most widely used semiconductor material in modern electronic devices. After dominating electronics, silicon is now attracting the attention of the engineering community as an

optical material, due to its well established processing technology and its desirable photonic properties, such as wide mid-infrared transparency (up to ~ 7 μm) [*161*] and high non-linearity ($n_2 \sim 10^{-18}$ m^2/W) [*162*]. This value of n_2 is two orders of magnitude higher than the non-linear coefficient of silica.

Some relevant properties of crystalline silicon are shown in Table 7-1. In particular, the melting point value is important for the annealing process and will be relevant for Section 8.1.1. Crystalline bulk silicon, used for integrated circuits, is generally produced by growing a seed of single crystal silicon in a melting of silica into a single crystal cylinder (boules), achieving a purity better than 99.99999%.

c-Silicon properties	
Intrinsic carrier concentration	$1x10^{10}$ cm^{-3}
Mobility electrons	≈ 1400 $cm^2/(V\ s)$
Mobility holes	≈ 450 $cm^2/(V\ s)$
Intrinsic resistivity	$3.3x10^5$ Ωcm
Refractive index (@1500 nm)	3.45
Melting point	1683 K

Table 7-1 *Some of crystalline silicon properties.*

7.2.2 Germanium

Germanium is chemically similar to silicon, being both part of group IV, with 4 valence electrons and with the same crystalline structure (fcc). Hence most of its electronic properties are very similar. Some of the properties of germanium are reported in Table 7-2. Germanium (indirect) bandgap occurs at 0.66 eV (1.878 μm), which is well into the infrared region. This means that this material absorbs at telecom wavelengths and for this reason has found applications in detectors and sensing [*163, 164*].

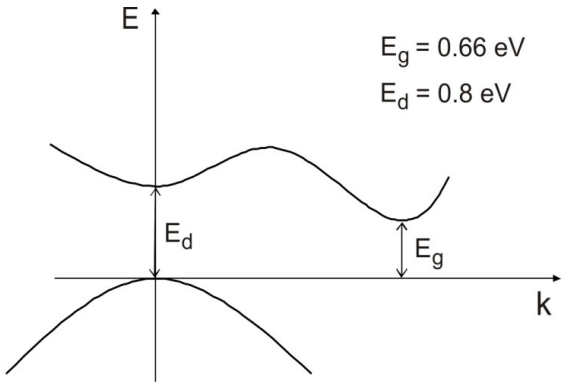

Figure 7.8 *Germanium energy indirect (E_g) and direct (E_d) bandgap.*

Germanium properties	
Intrinsic carrier concentration	$2x10^{13}$ cm^{-3}
Mobility electrons	≈ 3900 $cm^2/(V\ s)$
Mobility holes	≈ 1900 $cm^2/(V\ s)$
Intrinsic resistivity	47 Ωcm
Refractive index (@1500 nm)	~4
Melting point	937 °C

Table 7-2 *Some of crystalline germanium properties.*

On the other hand its transmission window is broader than silicon, stretching up to ~14 μm. Furthermore, germanium presents larger non-linearities compared with silicon [*161*]. These optical properties suggest that germanium can be used for a range of optical applications in the mid-IR.

7.3 Silicon photonics

As shown in Table 7-1, silicon refractive index value is quite high compared for example with silica (SiO_2) which is the main material used for optical fibre with a refractive index of about 1.45. This property, combined with silicon transparency at

telecom wavelengths, suggests silicon as a potential material also for optical applications such as waveguiding. A higher refractive index material allows for a stronger confinement of the electromagnetic field, thus it is very desirable for certain guiding properties and, particularly, for non-linear applications (the non-linear coefficient in Eq.(6.19) is larger because of a smaller A_{eff}).

In particular silicon has attracted great attention as it can provide a solution to the issue of modern optical interconnectors. In fact modern copper interconnections have reached their limit in bandwidth (around 10 GHz) due to frequency-dependent losses and dimensional scaling [*1*], resulting in the overall slow-down of devices. Silicon waveguides would solve the "interconnection bottleneck" issue since they could be easily integrated on-chip using pre-existing technology [*165*].

Optical losses in single crystal silicon waveguides have been reported in the order of 0.2-3 dB/cm [*166-169*] at telecom wavelengths, typically with the lowest value for relatively large core sizes (~5 μm) and increasing as the core size decrease. This can be explained in terms of overlap of the guiding mode with the core-cladding interface. The largest contribution to the losses is due to scattering at the surface due to roughness from the fabrication process [*168-170*]. This is particularly important in silicon-silica waveguides as scattering from the interface roughness increases for increasing index contrast [*171*], as it will be discussed later. Consequently, a lot of effort has been directed towards smoothing the waveguide sidewalls [*167, 172*] in order to reduce overall transmission losses.

Despite its many advantageous optical properties, silicon has also presented many challenges in photonics. Its indirect bandgap makes it an inefficient photon emitter, thus impeding laser operation. Nevertheless, the feasibility of a silicon laser has been proven by demonstrating hybrid silicon micro-ring and micro-disk lasers [*173*] and the first silicon Raman laser [*174, 175*], the latter exploiting the high non-linear coefficient of silicon. Due to its Raman gain coefficient, which is ~10^3 times the Raman gain in silica, as well as the highly confined mode, which is made possible in silicon due to its high refractive index, a Raman device can be realised on a much smaller scale compared with the hundreds of metres necessary in case of silica fibres.

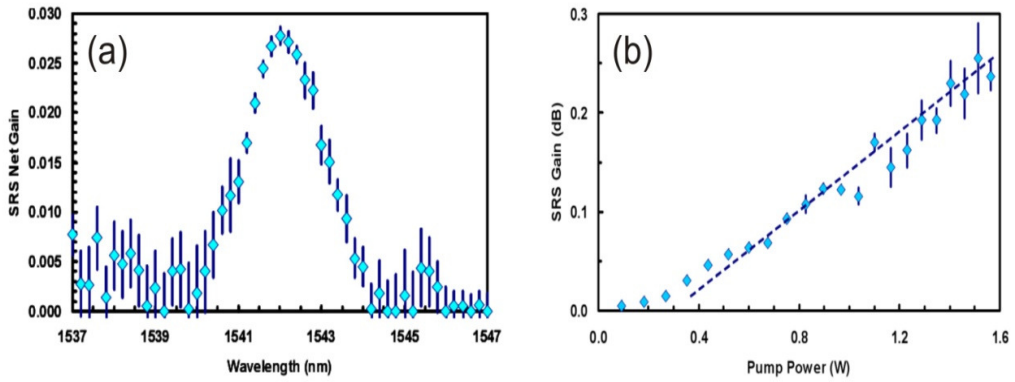

Figure 7.9 *Stimulated Raman Scattering gain in a silicon rib waveguide as function of (a) wavelength and (b) pump power [176].*

In 2004 the first silicon Raman laser was realised by Jalali and co-workers [*177*]. The main challenge in achieving an efficient Raman device has been identified in overcoming the detrimental effects of the two photon absorption process which occurs at high powers, as discussed in section 6.2.4.

Firstly, TPA can cause pump depletion, but this effect was found negligible by direct measurements [*176*]. Instead, TPA-induced free carriers can strongly increase absorption losses [*178-181*]. Two main solutions to overcome this problem have been adopted: the first by using a pulsed pump [*177*] with a long repetition rate compared with 10-200 ns free carrier lifetime and the second by realising a reverse biased p-i-n junction to sweep out free carriers, thus decreasing the free carrier lifetime. The former was used by Jalali and co-workers to demonstrate the first silicon Raman laser, whereas a year later, the latter allowed the demonstration of the first CW Raman laser by Paniccia and co-workers at Intel [*182*].

Numerous non-linear silicon photonic devices have been proposed in telecommunication networks [*165, 175, 183, 184*], including amplifiers, lasers, modulators, signal regeneration and wavelength converters [*185*]. Self-phase modulation in a 2 cm silicon wire waveguide has been recently demonstrated to broaden a 3 ps pulse (coupled peak power ~85 W) by a factor of ~2.5, which was then separated into three outputs at different wavelength by ring filters [*186*], as

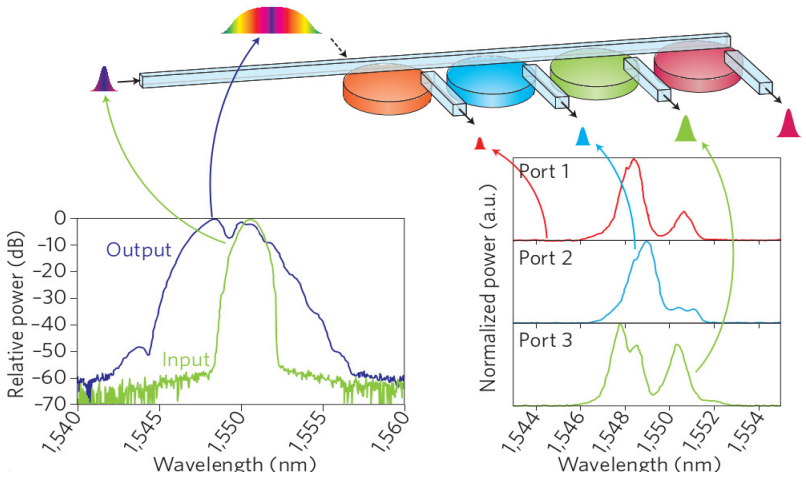

Figure 7.10 *Schematic and spectral characteristic of pulse broadening generated on silicon waveguide using SPM and then separated into outputs at different wavelengths [186].*

shown in Figure 7.10. Other potential applications have been proposed such as in sensing [*187, 188*], where lab-on-chips devices could be used to host the reaction and to perform the analysis.

Although telecom wavelengths have been the primary reason for the development of silicon photonics, alternative directions are moving towards longer wavelengths. Mid and far infrared regions are interesting for a range of areas from imaging and sensing (from 3 µm up to 100 µm or THz) to missile detection (around 20 µm) and other military applications [*189*].

Mid-IR silicon Raman lasers have already been considered due to the strong reduction of TPA effect (and consequent free carrier absorption) when photon energy is lower than half the bandgap energy (λ>2.2 µm). Jalali and co-workers have found virtually no non-linear absorption in a silicon waveguide using a Q-switched 2.9 µm Er-YAG laser with a pulse width of 75 ns and operating power of 25 mJ (see Figure 7.11) [*190*] and demonstrated a mid-IR silicon Raman amplifier reporting 12 dB gain [*191*] (see Chapter 10).

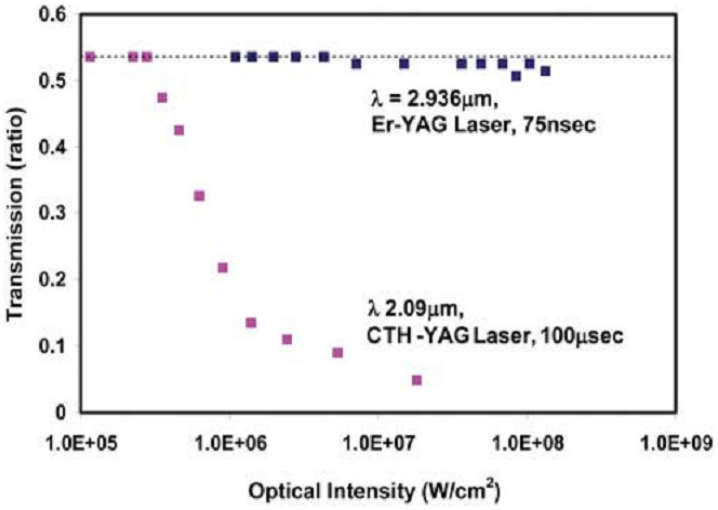

Figure 7.11 *Optical transmission in silicon as a function of optical intensity in cases of 2.09 and 2.936 μm pump sources. The enhanced non-linear losses at 2.09 μm due to TPA and free carrier absorption, and the absence of these losses at 2.936 μm can be seen [190]*

Despite the progress reported to date, with losses of a few dB/cm in silicon on insulator rib waveguides [*192*], silica absorption in the infrared (beyond 4 μm) [*193*] makes SOI materials unsuitable for the development of this technology, thus free standing [*194*] silicon waveguides have been considered (see Figure 7.12) together with other Si-Ge heterostructures [*192*].

If silicon is going to be the optimal choice to guide infrared light on chip using the same silicon layer as transistors, germanium will be the material of choice for detection of near-infrared light. In fact it is already used as a material for infrared photodetectors due to its high absorption coefficient at optical communication wavelengths. It is also compatible with standard CMOS processing allowing for an easy and inexpensive integration on chip.

Germanium waveguiding photodetectors (including polycrystalline germanium [*195*]) have already been demonstrated both on insulator [*196*] and on silicon [*197, 198*]. Here the detection occurs in a layer of germanium via evanescent coupling of the field guided in the silicon waveguide. The photodetector responsivity [is that a word, I'm not sure] in the waveguide geometry is expected to improve compared

with normal incident detection as the absorption efficiency depends on the waveguide length and not on

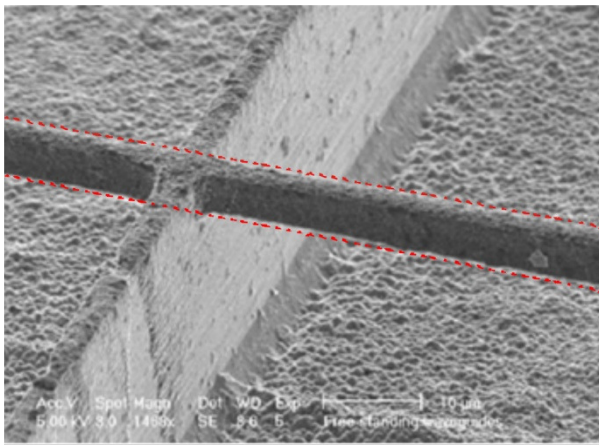

Figure 7.12 *Free standing silicon waveguide (red line) with a supporting pillar for far infrared silicon photonics applications. [194]*

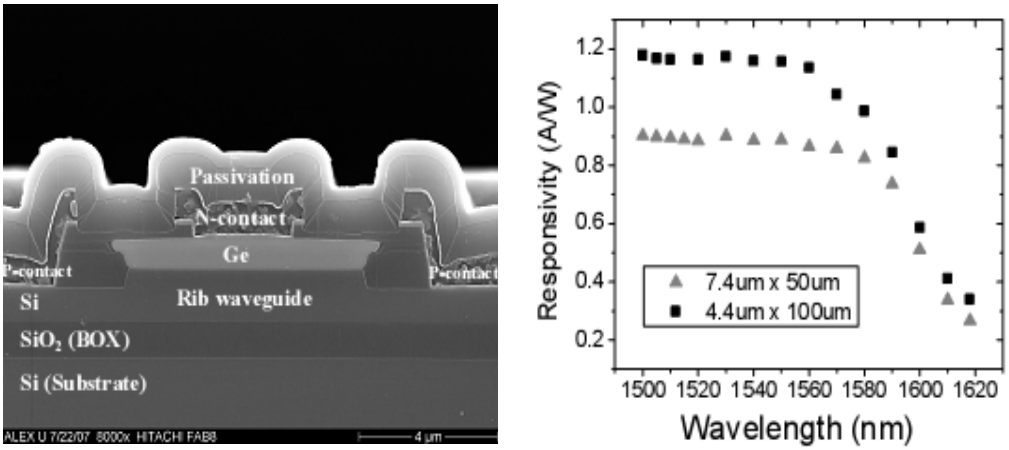

Figure 7.13 *(a) Cross section SEM picture of a n-i-p germanium waveguide photodetector. (b) Responsivity versus wavelength for a detector 7.4×50 µm, and a detector 4.4×100 µm, respectively, at -2V [197].*

the material thickness, thus avoiding the trade-off between bandwidth and sensitivity occurring in normal incidence detectors [*199*].

Germanium-silicon waveguides require design solutions that take into account the lattice mismatch of 4% between the semiconductors which usually involves the use of a thin middle layer of silica [*200*] or a buffering technique [*201*]. The higher refractive index of germanium (~4) [*202*] compared with silicon, also needs to be considered so that a sufficient percentage of the evanescent field penetrates into the germanium layer whilst keeping the device compact.

7.3.1 Amorphous silicon

Amorphous silicon is much easier to produce than single crystalline silicon as it can be deposited in thin films directly on a variety of substrates, including plastics, because of the low process temperatures. Optically it has a higher refractive index of ~3.7 (@1550 nm) [*203, 204*] and a higher bandgap of ~1.7 eV (~730 nm) [*205*] compared to crystalline silicon, but as a pure material it also shows higher optical losses.

In amorphous materials, optical losses arise mostly from absorption. Specifically in amorphous silicon, the atoms are not organised in a lattice and so it happens that for some atoms one of the four outermost electrons cannot find an available neighbouring atom to form a bond, thus leaving dangling bonds. These defects correspond to intermediate electronic states in the bandgap: here excitons recombine releasing phonons (heat) which leads to optical losses [*206*]. In order to reduce optical losses, dangling bonds are generally passivated by doping amorphous silicon with hydrogen. Hydrogen binds to the dangling bonds thus removing most of the trapping and recombination centres and improving both the optical and electronic properties.

Hydrogenated amorphous silicon is usually deposited by plasma enhanced chemical vapour deposition (PECVD) using silane (SiH_4), a silicon precursor, but deposition via jet-printing lithographic methods has also been reported to “write” TFT devices [*207*]. PECVD technique is preferred for large area deposition, being a cost-efficient production technique and for this reason it has been widely used for photovoltaic

devices [*206*]. In general, hydrogenated materials are largely preferred to pure amorphous silicon for photonic applications.

Hydrogenated amorphous silicon waveguides have been reported showing propagation losses of 0.5-1 dB/cm for multimode waveguides (height ~4 μm) [*208-210*] and 2-5 dB/cm for single mode waveguides (width ~1 μm) at telecom wavelength [*203, 208, 211*]. Figure 7.14 shows an example of silicon single mode rib waveguide, where propagation losses are calculated by measuring the intensity of the scattered light, which depends on the intensity of the guided light. The scattering losses are assumed to be constant along the waveguide, hence the angular coefficient of the signal provides an indirect estimation of the guiding losses, measured to be ~2 dB/cm at 1500 nm and ~5 dB/cm at 1300 nm.

Optical nonlinearities in hydrogenated silicon waveguides have been reported to be stronger than crystalline silicon waveguides, with a waveguide nonlinear coefficient $\gamma = 2003\ (\mathrm{Wm})^{-1}$ and a nonlinear refractive index $n_2 = 4.2\times10^{-17}\ \mathrm{m}^2/\mathrm{W}$ [*145*], which is higher that the values reported for single crystal silicon ($n_2 \sim 10^{-18}\ \mathrm{m}^2/\mathrm{W}$).

On the down side, amorphous silicon has limited electronic properties which narrow the range of applications in electro-optic devices.

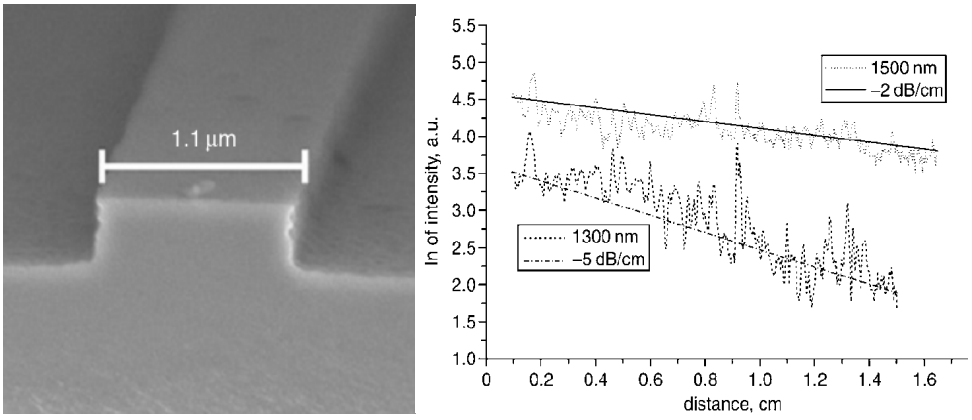

Figure 7.14 *SEM picture of single mode rib waveguide (left) and scattered light measurements at 1300 and 1500 nm [208].*

7.3.2 Polysilicon

Polycrystalline silicon (or polysilicon) provides a cheaper and easier solution in terms of deposition process compared with mono-crystalline silicon whilst retaining some of the crystalline properties with some compromise on performance.

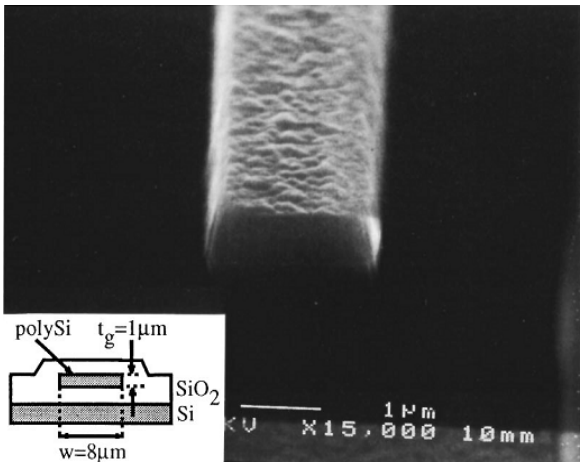

Figure 7.15 *SEM image of a polysilicon waveguide strip [212].*

Polysilicon optical properties also depend on its structural composition such as the grain size. Consequently, a variation in the refractive index and in the non-linear (Kerr) coefficient n_2 is expected. Values of non-linear coefficient have been reported in the order of $\sim 10^{18}$ m^2/W, similarly to single crystal silicon.

This material is already part of the very large scale integrated silicon technology being used for contacts in complementary metal-oxide semiconductors (CMOS) and has largely surpassed single-crystalline silicon in optoelectronic applications such as solar panels, where the large area of the device renders expensive crystalline silicon unsuitable for mass production. Polysilicon is usually produced via low pressure chemical vapour deposition (LPCVD) via pyrolysis of silane (SiH_4) in relatively low temperature furnaces (580-650 °C). Alternatively, a melt of low grade silicon can be cast in a mold and left to cool down. This method is preferred for photovoltaic

applications as using a square mold allows for the obtained rods to be sliced in square cells that can be packed in solar cells without any waste of space [*213*].

The challenge for polysilicon as a photonic material resides in its higher optical losses compared with single-crystal silicon due to additional scattering at the grain boundaries. Minimising optical losses is therefore a crucial factor for its application in optical devices. For example, in optical waveguides most of the research has focused on minimising scattering losses which can arise both from material and device design.

Kimerling and co-workers have reported a reduction in loss from 77 dB/cm [*212*] (waveguide shown in Figure 7.15) to 9 dB/cm [*214*] in a polysilicon waveguide with a silica cladding by improving the crystallinity [*214, 215*]. Here larger grain-size resulted in fewer interactions of light with the grain boundaries, and also resulted in a smoothening of the core cladding interface where roughness can also cause light scattering. This result is encouraging when compared with results from similar measurements on single-crystal silicon demonstrating losses of ~1 dB/cm [*212*].

The difference between both bulk and surface scattering needs to be taken into account. With crystalline and amorphous silicon waveguides, reducing the core of the waveguide from ~5 µm to 1 µm has been shown to increase optical losses because of the increased overlap in the guiding mode with the core-cladding interface thus increasing scattering (see Figure 7.16). Core size can also play an important role in the waveguide design as a balance

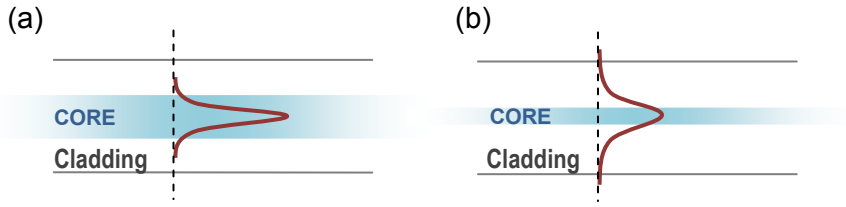

Figure 7.16 Schematic of the intensity profile of a guided mode in (a) large core waveguide and (b) small core waveguide.

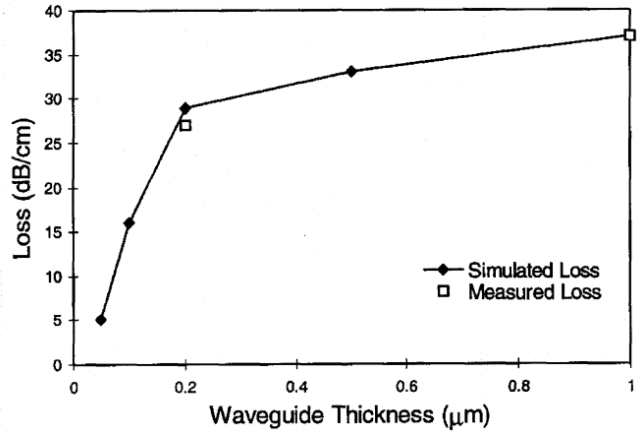

Figure 7.17 *Simulated and measured loss as a function of polysilicon waveguide core thickness [214].*

Further reduction of core sizes under 1 μm have also been studied in polysilicon waveguides [*214*] (Figure 7.17), demonstrating that optical losses could be reduced [*170, 214*] despite the expected increased overlap with the surface. This can be explained by the fact that when the core size is further reduced down to a few hundred nanometres, the mode expands to travel mainly in the cladding which is low-loss compared with the bulk silicon.

Polysilicon has also been reported as a preferred material compared with single crystalline silicon and amorphous silicon for applications in electro-optic devices [*216, 217*]. Compared with single crystalline silicon, polycrystalline silicon can be easily deposited in multiple layers by PECVD, enabling an easy vertical integration of components [*217*]. This is advantageous for separating optics and microelectronics on a chip, whilst still achieving devices which are compact and hence have low power consumption. On the other hand, compared with amorphous silicon, the higher carrier mobility of polysilicon enables integration of electrically active photonic devices. Furthermore, in terms of steady state conditions, a faster carrier recombination lifetime is induced at the grain boundaries thus a steady state carrier concentration is reached faster compared with the correspondent single crystal silicon device [*218*].

Chapter 8

Semiconductor modified MOFs

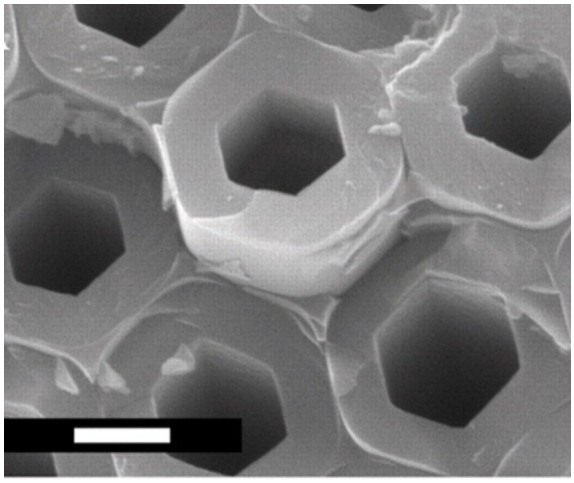

Figure 8.1 *Hexagonal silicon tubes in a honeycomb microstructured optical fibre template [219]. Scale bar 1μm.*

In the previous chapters both microstructured optical fibres and semiconductor materials have been introduced. The inclusion of semiconductor materials within MOFs can potentially lead to highly engineerable devices with wide control over both the photonic and electronic properties. The long term objective of this pioneering research is to create a completely new technology based on the inclusion

of optoelectronics devices inside optical fibres, so signals will no longer need to leave the optical cable to be processed, with clear practical advantages, as happened in the past with the introductions of the EDFAs. Furthermore, using these semiconductor materials, waveguide properties such as dispersion and non-linearities, can be tailored to specific requirements. In the short term, fabrication of compact all optical non-linear devices, which exploit the high non-linear coefficient of some semiconductor materials, is already within reach.

Silicon and germanium have excellent electro-optic responses and are probably the most well-known semiconductor materials in terms of their properties and deposition technologies. Furthermore, their unique optical properties have already led to their use in photonics applications, which has largely been driven by their compatibility with pre-existing electronic technologies. As a result silicon and germanium are ideal candidates for material inclusion inside MOFs to create a new versatile platform technology for optoelectronic and photonic all fibre devices.

This approach of depositing semiconductors inside optical fibre has been taken with the main intention of developing a new technology which sits at the interface between optical fibre and silicon chip technology, whist keeping an eye on the current progress of planar silicon photonics. The objective of this work is moving some of the on-chip photonic devices inside the optical fibre, with a clear advantage in terms of waveguide engineering and seamless coupling to existing optical fibre infrastructures.

As explained in the previous chapter, silicon for example has a Raman coefficient which is three orders of magnitude larger than silica, so that a silicon-based non-linear device would be a thousand time shorter than the silica-based counterpart. For comparison, other materials such as chalcogenide glasses have been used to fabricate compact non-linear devices [*220*]. Chalcogenide glasses have a non-linear refractive index n_2 up to three orders of magnitude higher than silica, so that for example 20 dB of Raman gain in a 1.1-m-long As–Se fibre has been demonstrated [*221*]. But although their non-linear optical properties may achieve better results than silicon, such materials suffer from issues such as photodarkening. Thus, the first target in order to realise optical silicon-based nonlinear devices is to reduce transmission

losses under a few dB/cm [*186*] and the core diameter to less than 1 μm, thus maintaining sufficiently high energy density along the waveguide, in order to obtain non-linear effects such as SPM or Raman amplification.

In this chapter pioneering work on semiconductor deposition inside microstructured optical fibres will be presented. A novel high pressure chemical vapour deposition technique has been developed in collaboration with Penn State University (PSU-USA) and will be described in Section 8.1. This technique uses high pressure to transport semiconductor precursors inside the high aspect ratio pores of an MOF, which is possible due to the high mechanical strength of optical fibres. An external furnace controls the temperature that allows for the precursors to react and deposit amorphous material until complete filling, whilst the smoothness of the internal walls of the fibre templates leads to a very high quality semiconductor-silica interface. A further annealing step is used to nucleate crystalline grains of semiconductor, which grow and merge into uniform crystalline tubes that can fill the pores. Although the successful deposition of semiconductors has been demonstrated for several MOFs templates, most of the work has been performed on the simplest microstructured optical fibre: a capillary. Silicon core step index fibres fabricated as described in this chapter will be used for photonic applications in Chapter 9.

In Section 8.2 morphological characterisation of the deposited semiconductor will be presented. A large amount of the structural characterisation (imaging, Raman and electrical characterisation) has been done in the past by other members of the group and reported back to the fabrication team in PSU for a first estimation of good parameters for the deposition of high quality material. This process involved analysis and feedback of over a hundred samples. My work started during the last part of this structural characterisation stage, when results were satisfactory in terms of quality of the material and the fabrication team was moving towards achieving long lengths of completely filled capillary, aiming at standard linear characterisation. Here an overview on the results obtained in this final stage of the morphological and structural characterisation is reported.

Firstly, the etching process used to expose the semiconductor wires will be described and then the results from imaging and structural characterisation will be presented.

The polysilicon grain size was investigated via SEM imaging analysis of Secco-etched samples [*222*] and via TEM. Moreover, using Raman spectroscopy the nature of material (crystalline or amorphous) is determined by the width of the Raman peak. SEM, TEM and part of the Raman analysis presented here have also been performed in collaboration with Penn State University and make up a series of preliminary measurements carried out for the optimisation of the deposition parameters. Here only the results that I have been involved with, and that are relevant for the silicon photonic application, are presented in Chapter 9.

Finally electrical characterisation of annealed samples of both silicon and germanium modified fibres has been performed realising field effect transistor (FET) devices. Although the FET results and analysis reported here have been conducted by other members of the group as part of the deposition parameter optimisation phase, I have also performed FET measurements with results consistent with the previous ones. FET measurements provide information about deposition uniformity along the fibre length and other key parameters such as resistivity, carrier type, mobility and concentration. Germanium modified samples show a better electronic behaviour (Section 8.3.2) and this is attributed to its lower melting point compared with silicon, which allows for achieving better material quality in the annealing step.

8.1 Si/Ge high-pressure deposition technique

Semiconductors are usually deposited for planar devices by chemical vapour deposition, in that a substrate is exposed to one or more volatile precursors which react on the surface to produce the desired material [*223*]. However standard CVD is not applicable to the narrow and long pores of MOFs as it is usually performed at low (1-10 Pa) to atmospheric (~10^5 Pa) pressures, making transport of the precursors impractical inside the tiny pores of MOFs. However, there is no restriction for CVD to be extended to high pressure.

Supercritical fluids have been introduced in Section 3.1 as they combine the solubility properties of liquids with the transport properties of gases because of the lack of surface tension. Furthermore, their physicochemical properties such as

viscosity and density are tunable by changing their pressure and temperature. In fact, supercritical fluid deposition has been successfully used to deposit silicon [*224*] and germanium [*225*] nanowires within mesoporous silica templates.

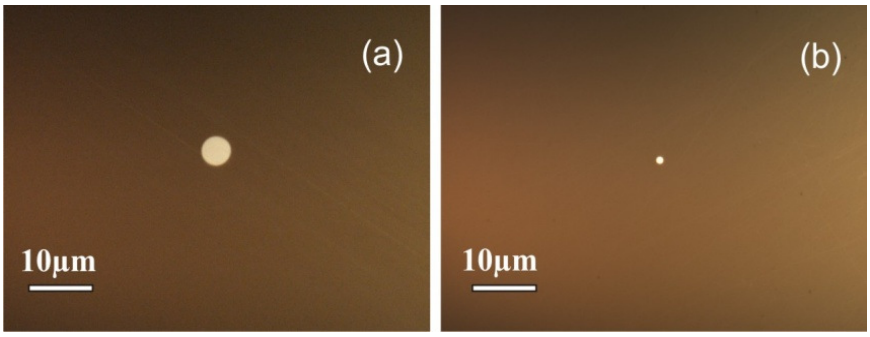

Figure 8.2 *Microscope images of fully filled silicon modified fibres polished cross sections in the case of (a) 5.6 µm core capillary, (b) 1.3 µm core capillary fabricated by PSU/ORC.*

The high tensile strength (well in excess of that of steel) of silica fibres and the small internal dimensions of the structured holes allow for MOFs to be used as high pressure reactors which can be pressurised to more than 10^8 Pa. Since the critical point of most fluids is typically less than 10^4 psi (~69 MPa) at 1000º C, which is well below the maximum pressure and temperature sustainable by MOFs, it is possible to take advantage of the unusual properties of high pressure fluids to deposit materials within the capillary voids.

The combination of the exceptional mechanical properties of the fibres, the transport and solubility properties of supercritical fluids, and the flexibility of CVD has led to the development of a new deposition technique for the impregnation of functional materials inside MOFs that will be described in the following section. It is worth observing that this technique has been successfully applied by our group to the deposition of other materials, including metals [*219, 226, 227*], which are not the object of this thesis.

8.1.1 High Pressure Chemical Vapour Deposition

For a typical high pressure chemical vapour deposition (HPCVD) process, a stainless steel reservoir is filled with a mixture of 5% semiconductor precursor and 95% inert carrier gas (argon or helium). Specifically SiH_4 (silane) has been used in the case of silicon deposition and GeH_4 (germane) in the case of germanium deposition. These precursors have the advantage of producing light by-products from the reaction (H_2), which can escape the silicon capillary. Moreover, in the case of deposition of amorphous silicon, it is possible to adjust the deposition parameters in order to leave some of the hydrogen in the deposited material thus obtaining hydrogenated amorphous silicon, as will be described later.

The mixture is contained in the reservoir at a pressure of 40 MPa so the high pressure fluid can flow through holes ranging from 50 nm to 50 μm. A fibre of about 75 cm length is then attached to the reservoir and placed in an inert chamber in order to evacuate air from the fibre holder: this step is very important as once the reservoir is opened silane would immediately react with the oxygen in the air and produce silica (SiO_2) blocking off the flow at the entrance to the fibre, if not causing it to explode!

The fibre is left in acetone for 20 minutes in order to strip off the polymer coating that would otherwise burn when in the furnace. It is then placed in a ~30 cm long furnace keeping the reservoir as close as possible to the entrance of the furnace in order to ensure the highest values of the pressure (which decreases along the fibre) i.e. in the heated area and, most importantly, the reproducibility of the distance between the reservoir and the centre of the furnace. The furnace is then heated up to 400 or 500 °C with a ramp ~2 °C/min and then kept constant until the end of the deposition process (3-4 days). The flow is checked by placing the output end of the fibre in mineral spirit and observing the formation of the bubbles.

The chosen set temperature is different in the case of silicon and germanium. In the case of germanium, temperature is set at 500 °C. Germanium has a crystalline point of ~375 °C so it starts as an amorphous material, but as soon as the temperature (ramped at ~2° C/min) hits 375 °C, crystalline grains nucleate and grow so the final sample is polycrystalline. Silicon, however, has a crystalline point of ~700 °C so

during deposition (temperature set at either 400 or 500 °C) it never reaches its crystalline point, so it is deposited entirely as amorphous. In the case of silicon, a set temperature of 500°C is chosen to deposit pure amorphous silicon, whilst 400 °C is favourable to maintain a higher level of hydrogen in the material, as a lower temperature means less hydrogen diffuses out. This allows for deposition of hydrogenated amorphous silicon, as will be confirmed by Raman measurements in Section 8.2.2.3.

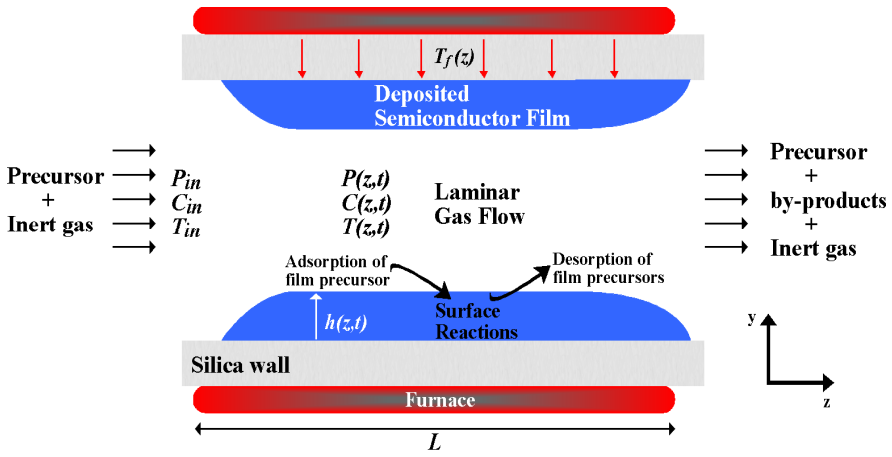

Figure 8.3 *Schematic of the high pressure CVD process for semiconductor deposition in a capillary.*

A further annealing step is performed on amorphous silicon samples deposited at 500°C in order to obtain polycrystalline silicon. Samples deposited at higher temperatures were chosen as they are expected not to contain hydrogen, which may diffuse out during the annealing leaving behind unwanted defects. The annealing consists of an increase of temperature up to ~725 °C holding for 30 minutes and then a further raise to 1325 °C for 20 minutes. Samples are then left to cool to room temperature inside the furnace before being removed.

High pressure CVD permits the deposition of uniform annular material which conforms to the internal walls of the MOFs (see Figure 8.1), thus maintaining a highly smooth semiconductor-silica interface [*219*]. This property is highly desirable for waveguide applications as scattering losses at the interface are expected to be

negligible. Complete filling has also been achieved over lengths of a few centimetres (typically ~1 cm but complete filling over almost 7 cm has been obtained).

The set-up used was completely custom made at Penn State University, with the advantage of being able to change almost all the parameters, such as the precursor concentration, the pressure and the deposition temperature. Figure 8.3 shows a schematic of the deposition process and the parameters involved. The optimisation of the instrumentation and of the process itself is ongoing. Thus, although low losses observed in the samples indicate good deposition parameters, there is scope for further optimisation.

Owing to the complexity of the process, an experimental trial and error approach has been chosen to determine the optimum parameter values, as also traditionally takes place for standard CVD. The condition of laminar gas flow is not easy to meet in practice, since especially when the hole diameter is reduced to under 50 nm irregularities in the deposition thickness may occur that potentially result in the hole being plugged.

Complete filling of the capillary could, in fact, be attributed to these irregularities occurring towards the final part of the deposition channel which ultimately cause the channel to seal (no bubbling is observed in the mineral spirit) so the channel fills backwards from this point. In the instance when these irregularities instead occur at the beginning of the channel, the capillary will not be completely filled and a hollow cylindrical shaped sample is obtained.

8.2 Morphological Characterisation

Semiconductor modified fibres obtained, as described above, are firstly examined from the side under a microscope to quickly identify areas with uniform deposition (see Figure 8.4), which are the good candidates to proceed to further analysis. This is possible due to the high refractive index of the semiconductors and thus their high reflectivity, which makes them appear as bright wires inside transparent silica. Consequently darker areas in the semiconductor wire are indicative of non-uniform deposition. The areas of uniform deposition which are normally a few centimetres

long are cut out of the main fibre for further cross sectional imaging and structural examination.

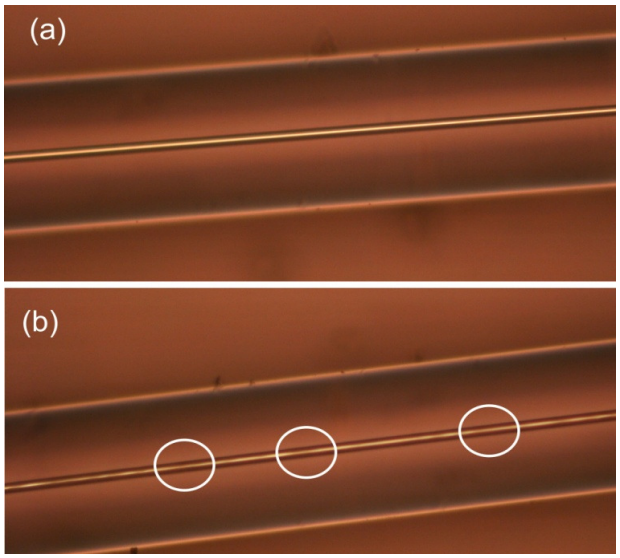

Figure 8.4 *Microscope images of germanium modified capillaries: (a) the bright uniform golden wire is indicative of homogeneous deposition (b) the wire presents darker areas (some highlighted with white circles), indicating non-uniform deposition.*

8.2.1 Silica etching process

In some cases exposure of part of the deposited semiconductor wire was required both for investigating their semiconductor-silica interface using imaging (Section 8.2.2) and in order to realise electrical contacts for FET measurements (Section 8.3.2). For these purposes a selective etching process has been used in order remove the silica template and expose the required part of semiconductor.

Silica has been selectively etched using a ~20% buffered solution of hydrofluoric acid (HF) in water. It was found that a weaker buffer (<15%) would not etch or be too slow, whilst a stronger buffer (>30%) would etch irregularly, attacking and permeating the semiconductor/silica interface as shown in Figure 8.5.

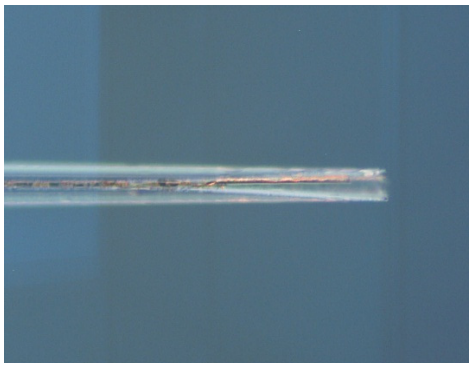

Figure 8.5 *Microscope image of 5 μm diameter silicon wire etched out of a silicon modified capillary using a 30% buffered solution of HF in water.*

For the etching process a Teflon® bar was used as a fibre holder, owing to its resistance to HF: samples were placed vertically along the purpose built v-grooves, protruding by ~1 mm on the underside of the bar. The bar was then placed on a Teflon® container of ~2 ml capacity where the HF buffered solution was held. A schematic of the set up used is shown in Figure 8.6. During the process the HF would etch the silica both transversally, reducing the external diameter of the glass capillary, and vertically from the base, leaving the semiconductor wire exposed at a rate of ≈ 0.1 μm/min.

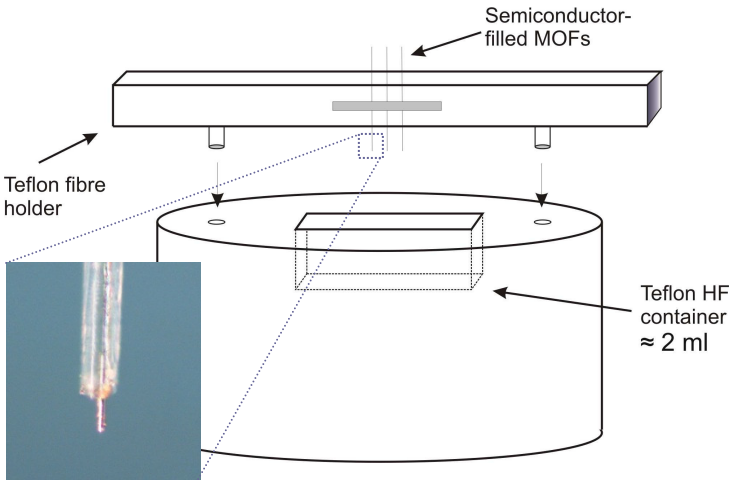

Figure 8.6 *Schematic of the etching set-up. Inset shows a close up microscope image of the etched end of a sample after the process, where a semiconductor wire is visibly exposed.*

A further etching process has been performed on polycrystalline silicon modified capillaries to investigate their grain size. This process is known as Secco etching [*222*] and its formulation consists of one part of HF with 2 parts of a 0.15 M solution of $K_2Cr_2O_7$ (potassium dichromate) in water. In this technique potassium dichromate penetrates and oxidises the silicon grain boundaries, reducing them to silica, whilst the HF etches them away. The process only lasts 20 seconds and the samples have then been investigated using SEM as shown in the next section.

8.2.2 Imaging and structural characterisation

The first step in the characterisation of the selected samples requires imaging and structural investigation of the deposited semiconductor, in order to assess the good quality of the material. In fact, in polysilicon, a high percentage of crystalline area is desirable for optical transmission of light, over defects and grain boundaries, which can be instead a source of scattering losses (see Section 6.2.2.2).

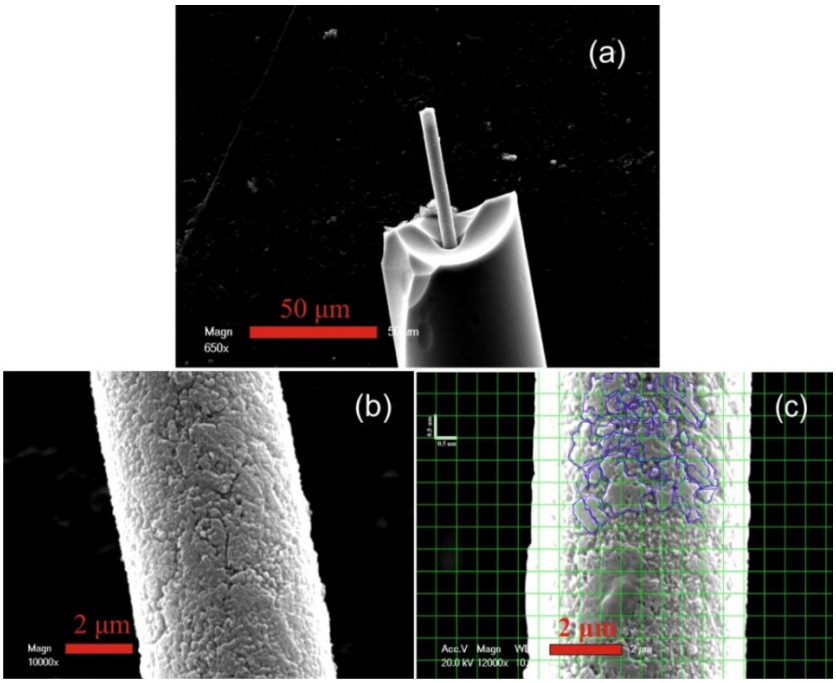

Figure 8.7 *(a) SEM micrograph of a polysilicon wire etched out of the silica capillary and treated with Secco etching to highlight grain boundaries. Scale bar 50 µm. (b) Close up of the polysilicon wire surface. Scale bar 2 µm.(c) The grain boundaries are highlighted by blue lines. Scale bar 2 µm.*

This analysis has been performed using SEM imaging of Secco etched polysilicon modified capillary, TEM imaging of polysilicon samples and Raman spectroscopy of a range of both silicon and germanium modified capillaries.

8.2.2.1 Scanning Electron Microscopy

In scanning electron microscopy a collimated beam of electrons is accelerated by high voltages (100 V to 100 kV) and focused through a series of electrostatic and magnetic lenses onto the sample under study. The number of back scattered and secondary electrons that emerge from the sample depend on the local composition and topography of the sample. Once detected, they are plotted as a function of the beam position, generating a 2D image of the object under investigation.

Figure 8.7 shows an SEM micrograph of a completely filled 5 μm core polysilicon modified capillary that has been treated with buffered HF etching and Secco etching as described in Section 8.2.1. In (a) a ~50 μm long silicon wire is protruding from the silica cladding, whilst in (b) a close up of the wire surface is shown and in (c) the grain boundaries are highlighted by blue lines. The grain boundaries of the polycrystalline silicon have been exposed via the Secco etching and can be identified by the deep dark channels. The grain size can be estimated to range between 500 nm and 1 μm.

8.2.2.2 Transmission Electron Microscopy

TEM imaging technique has been introduced in Section 3.3.1 together with the selected area diffraction pattern. For this analysis, the semiconductor modified fibre was sectioned using a focused ion beam, obtaining a sample less than 100 nm thick.

An annealed silicon sample has been investigated using TEM analysis to study its crystalline structure and understand the size and quality of the crystalline grains. Grain size has been confirmed to vary between 0.3 μm and 1 μm and an example of an observed grain is shown in Figure 8.8 (a). Closer investigation of the crystalline area reveals the high quality nature of the silicon, as shown by the ordered silicon atoms in Figure 8.8 (b). Further confirmation is provided by the electron diffraction pattern taken in the same area (Figure 8.8 (c)).

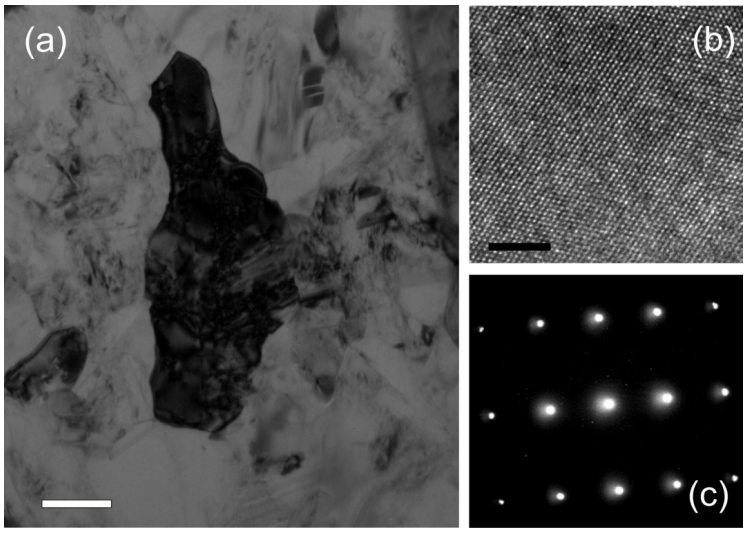

Figure 8.8 *TEM micrograph of polysilicon deposited in the fibre. (a) Example of a crystal grain (dark area), scale bar 300 nm. (b) Close up in the crystalline area: silicon atoms visibly ordered in the lattice. Scale bar 5 nm. (c) Electron diffraction pattern collected in the crystalline area.*

8.2.2.3 Raman Spectroscopy

Raman scattering theory has been introduced in Chapter 2 together with the corresponding spectroscopic technique. Raman spectroscopy has been used on a range of samples in order to provide information on the nature of the material (single crystal, polycrystalline and amorphous) and to reveal any evidence of strain in the lattice at the semiconductor/silica interface.

Raman spectra were taken using a conventional Renishaw Raman spectrometer in a backscattering geometry with a 633 nm HeNe laser source, operating at a typical power of 3 mW and using a 50× objective which corresponds to a spot size of ~2 μm. Raman spectra of germanium and silicon modified fibres have been taken by focusing the laser on the semiconductor wire through the transparent glass capillary and were compared with the corresponding bulk single crystal wafers.

Raman spectra taken for germanium deposited inside the fibre and a single crystal germanium wafer are shown in Figure 8.9 [*228*]. Deposited germanium shows a peak at 299.85 cm^{-1} with a 3.1 cm^{-1} FWHM, while the single crystalline germanium wafer shows a peak at 300 cm^{-1} with 2.4 cm^{-1} FWHM. Peak widths were obtained by using

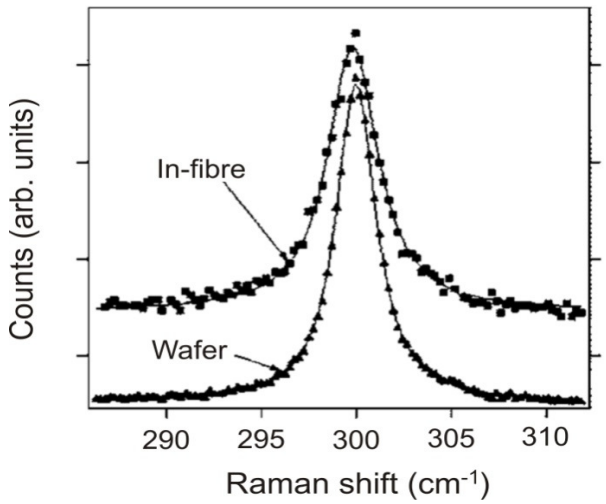

Figure 8.9 *Raman spectra of germanium deposited in fibre, compared to single crystal germanium wafer control sample [228].*

a Voigt fit, which consists in a combination of gaussian and lorentzian profiles. The very small shift in the position of the peak indicates little or no strain between the germanium wire and the silica due to germanium not bonding to silica, whilst the broadening observed in the deposited germanium peak compared to the single crystal germanium indicates a polycrystalline nature of the deposited semiconductor.

Silicon modified capillaries with ~6 μm core diameter fabricated under different conditions have also been investigated: two amorphous silicon deposited at ~500 ºC and ~400 ºC and three samples of polycrystalline silicon deposited at ~500 ºC annealed at three different temperatures (1125 ºC, 1200 ºC and 1325 ºC).

Raman spectra for both the amorphous silicon samples deposited at 400 °C (solid line) and 500 °C (dashed line) are plotted in Figure 8.10. These both exhibit a strong broad peak around 480 cm^{-1} and some weaker peaks at 300 cm^{-1} and 410 cm^{-1} associated with the amorphous silicon [*229*]. Measurements taken at larger shifts in the spectrum (see inset) reveal a peak around 2000 cm^{-1} associated with the stretching mode of Si-H bond [*230, 231*] in the first sample that is not observed in the second. This result confirms that amorphous silicon deposited at 400 °C is in fact hydrogenated amorphous silicon whilst silicon deposited at 500 °C is amorphous silicon with a low hydrogen content, if any.

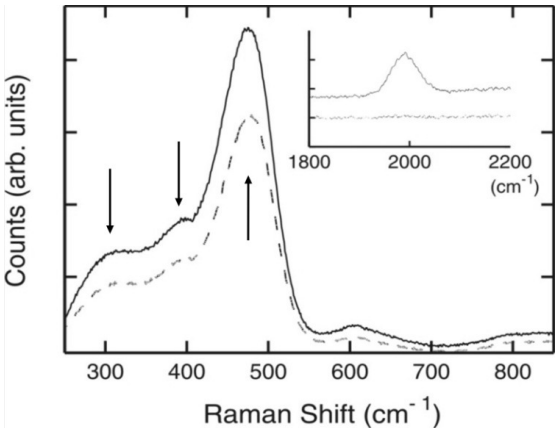

Figure 8.10 *Raman spectra of amorphous silicon deposited at 400 °C (solid line) and 500 °C (dashed line). Inset shows peak around 2000 cm^{-1} associated with the presence of hydrogen in silicon deposited at 400 °C (solid line) that is not detected in silicon deposited at 500 °C (dashed line).*

Raman spectra for the silicon modified capillaries annealed at 1120 °C, 1200 °C and 1325 °C are plotted in Figure 8.11, together with a single crystal silicon wafer spectrum as a control sample (bottom curve). From the fitted curves (dashed curves) values can be obtained for the peak position, peak width and asymmetries.

Firstly, deposited silicon annealed at 1125 °C, 1200 °C and 1325 °C show peak widths (from Voigt fits) respectively of 5.1 cm^{-1}, 4.5 cm^{-1} and 3.0 cm^{-1} and present small asymmetries.

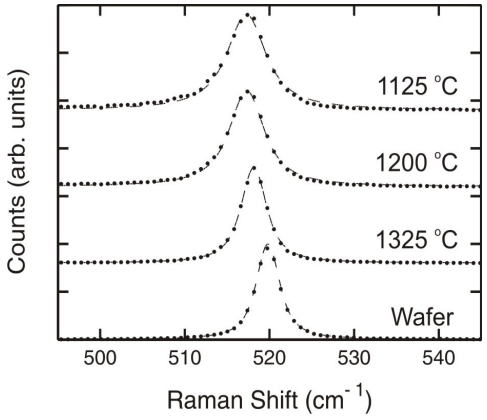

Figure 8.11 *Raman spectra of silicon modified capillary annealed at 1125 °C, 1200 °C and 1325 °C. Single crystal silicon wafer spectrum is also plotted as reference. Curves are offset for comparison.*

Comparing these values to the single crystal control sample peak width of 2.7 cm^{-1}, the larger width seen in the deposited silicon, particularly for the lower temperature annealed samples, are consistent with the polycrystalline nature of the material and are due to defects and crystal irregularities surrounding the crystalline grains. Moreover the reduced peak width for the higher annealing temperature is associated with a reduced content of defects in the material, thus an improved crystalline quality is achieved by raising the annealing temperature.

The position of the peaks for silicon deposited in the fibres occurs at 517 cm^{-1} for the samples annealed at 1125 °C and 1200 °C and at 518 cm^{-1} for the sample annealed at 1325 °C. All peaks are redshifted compared to the single crystal silicon control peak (520 cm^{-1}). The shift is associated with the strain at the silicon/silica interface, as silicon bonds more strongly with silica. The strain is originated upon cooling from annealing temperature by the difference in thermal expansion between the silicon wire and the silica fibre.

8.3 Electrical characterisation

Electrical characterisation of the semiconductor modified fibres is fundamental as it provides information about the deposition uniformity along the fibre length and other key parameters such as resistivity, carrier type, mobility and concentration. FET measurements were carried out to obtain values of these key parameters for the deposited material, hence deducing an indication of the quality of the deposited material by comparing the experimental values with the corresponding parameters reported for crystalline silicon. Three terminal measurements were preferred over two terminal measurements, as the latter would only provide resistivity information, and over the four terminal measurements as experimentally more practical to realise.

After an introductory section on field effect transistors, the realisation of FET devices using semiconductor modified capillaries will be described and results of two and three terminal measurements for both polycrystalline germanium and silicon will be reported. Being part of the preliminary investigations, reported measurements were conducted on germanium deposited at 500 °C and silicon deposited at 750 °C

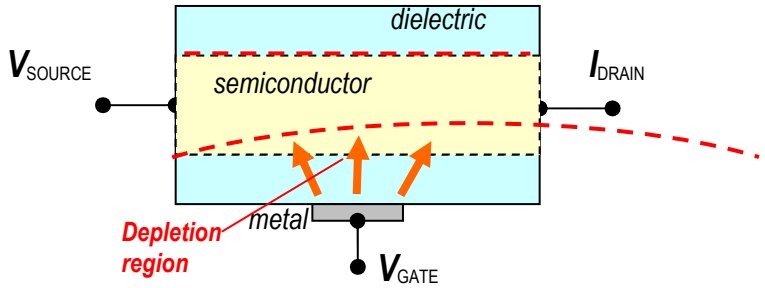

Figure 8.12 *Schematic of a Field Effect Transistor: applying a voltage at the gate induces a deformation in the channel between source and gate.*

(just above the respective crystal nucleation temperatures) without any further annealing process. Although results show an overall underperformance compared with values reported in the literature for polycrystalline germanium and silicon, these are the first electronic devices demonstrated in semiconductor optical fibres [*228*].

8.3.1 Field Effect Transistors

An FET device relies on an electric field (V_{gs} applied between gate and source terminals) to modulate the shape and hence the conductivity between the source and the drain terminals (see Figure 8.12).

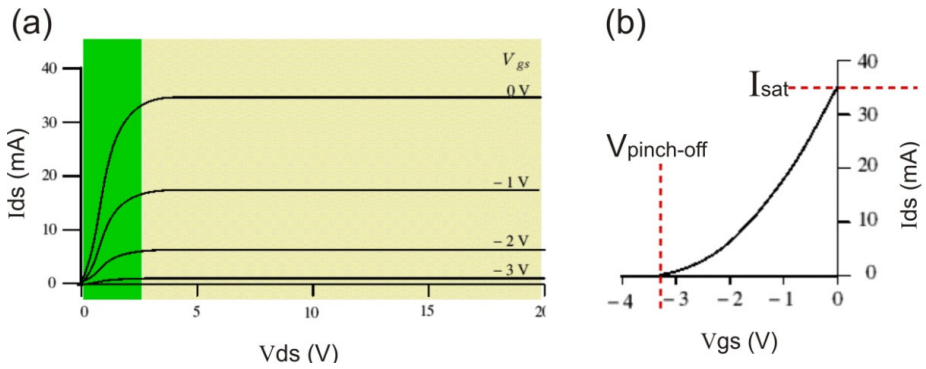

Figure 8.13 *Characteristics of a typical n-channel FET. a) Ohmic behaviour in the green area and saturation in the yellow area. b) After the pinch off, the current I_{ds} depends on the voltage applied to the gate, V_{gs}.*

The basic properties of an FET are described by two characteristic curves, determined by the drain current I_{ds} as a function of the source voltage V_{ds} and of the gate voltage V_{gs}. Figure 8.13 shows typical characteristic curves of an n-channel FET (electrons are the main carriers). The first graph (a) shows that the FET follows a linear (ohmic) behaviour for small values of drain-source voltage. When the potential difference between the source and drain terminals is large (above a few volts), this produces a significant increase of the current in the channel.

The resulting gradient of potential, from source to drain, causes the shape of the depletion region to become asymmetrical, because on the other side the gate-to-source potential is constant. This causes the end of the channel to narrow and the depletion region begins to close the channel. From this point, called the *pinch-off,* any increase of the drain-to-source voltage will increase the channel resistance proportionally so that the current flow is saturated. Once the V_{ds} is above the pinch off condition, the value of gate voltage V_{gs} determines the value of the constant current in the channel as shown in Figure 8.13 (b).

8.3.2 FET measurements

For the fabrication of FET devices two samples of polycrystalline germanium and silicon modified capillaries with 5μm diameter semiconductor wires were etched at both ends, as described in Section 8.2.1, to expose ~200 μm of the semiconductor core as shown in Figure 8.14.

~250 nm of aluminium was thermally evaporated onto the exposed semiconductor ends and sintered at 430 °C for 30 minutes to form ohmic contacts. Electrical connection to an external circuit, comprising a probe station and an Agilent 4155C semiconductor parameter analyser, was completed using indium gallium (Ga-In) eutectic electrodes applied to the Al-Ge alloyed contacts. An additional capacitatively coupled coaxial gate was also constructed by placing a drop of In-Ga eutectic onto a ~1 mm long section of the silica cladding.

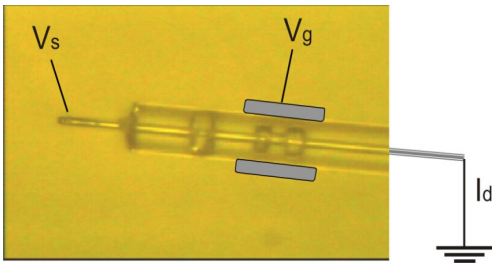

Figure 8.14 *Optical microscope picture and diagram of a germanium optical fibre as prepared for electrical characterization [228].*

By applying a bias to this contact it is possible to apply a radial electric field to the semiconductor core, using the silica cladding as a gate insulator. Details on the electrical parameter calculation method can be found in reference [*228*].

In the case of germanium the sample used had a 94 μm external silica cladding diameter and a total length of 11 mm. Firstly, two terminal measurements dV_S/dI_D for V_g=0 were performed obtaining the value of the resistance of the semiconductor core, with a correspondent resistivity calculated to be 5.6×10^{-2} Ωcm [*228*]. As the gate bias voltage is varied from -100 to +100 V (Figure 8.15) the conductance increases, indicating n-type carriers.

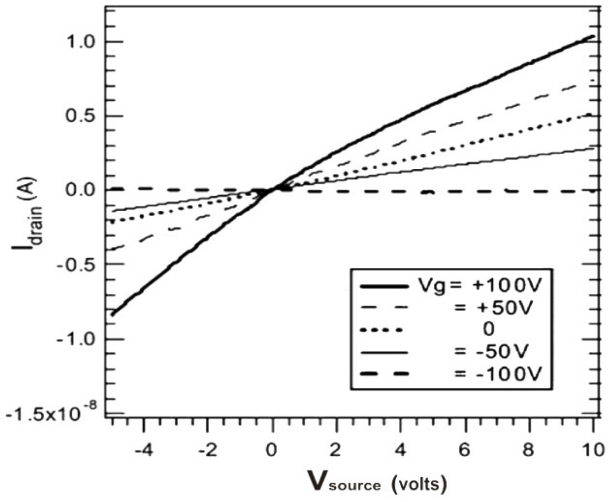

Figure 8.15 *Conductance measurements as a function of gate voltage (+100 to -100 V in 50 V steps) for germanium modified capillary. An increase in the resistance (curve slope) when the gate voltage increases indicates that the semiconductor is n-type [228].*

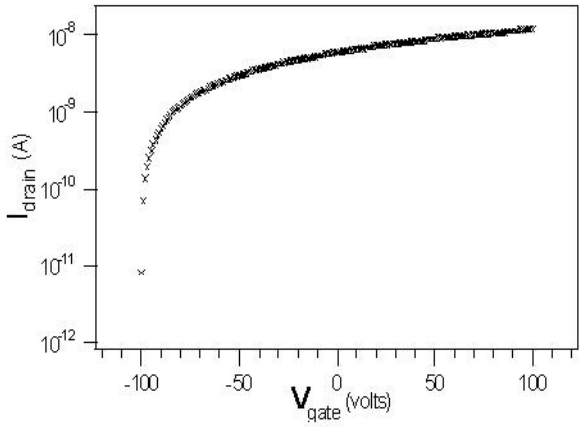

Figure 8.16 *Transconductance measurements for germanium modified capillary. The pinch off point is visible around $V_G \cong 100$ V.*

Electron mobility was calculated from the transconductance characteristic shown in Figure 8.16. For a 10 V source a transconductance value $dI_d/dVg \approx 5\times10^{-11}$ A/V was calculated, obtaining an estimated mobility of 1.05 cm^2/Vs at room temperature [*228*]. Comparing this result with the typical value for bulk polycrystalline germanium at room temperature which is ~100 cm^2/Vs [*232*], the low carrier mobility in the investigated samples can be attributed to high carrier scattering occurring during transport at defects sites, grain boundaries and lattice dislocation.

The concentration of free carriers was estimated by considering the gate voltage at which "pinch off" occurs for a drain current V_g (pinch off) ≅ -100 V as shown in Figure 8.16 which corresponds to a calculated free-carrier concentration of 2.1×10^{15} cm^{-3}.

The same set of measurements have been conducted on a polycrystalline silicon sample (750 °C deposition temperature) with a length of 18 mm and cladding diameter of 125 μm. Taking into account a 5 μm diameter core, two terminal measurement (Vg=0) results indicated a calculated resistivity of 0.21 Ωcm. In this case, the carrier mobility and concentration were calculated to be ~1.4×10^{-2} cm^2/Vs and 6.6×10^{15} cm^{-3}, respectively. As before, in this case the estimated carrier mobility is considerably lower than the value reported in the literature for polysilicon, which ranges from 10^2 to 10^4 cm^2/Vs.

In conclusion, both silicon and germanium samples deposited at 750 °C and 500 °C respectively, exhibit carrier mobilities which are at least two order of magnitude lower than the corresponding values reported in the literature for conventional planar samples. This has been attributed to charge scattering and charge recombination at the grain boundaries which may include nanocrystals and amorphous material. Furthermore, grain size, quality and consequently carrier mobility is expected to improve for higher deposition temperatures. This is consistent with germanium showing the best sample to reference mobility ratio which can be attributed to the deposition temperature being further from the crystal nucleation point ($\Delta T = T_{deposition}-T_{crystal} = 125$ °C) compared with the silicon deposition temperature ($\Delta T = 50$ °C).

The electrical characterisation, described above, provided information on the deposited material and, consequently, adjustments on the fabrication method were introduced in order to improve material quality. Annealing temperatures are now set at 1325 °C, limited only by the silica melting point at ~1625 °C. Samples annealed at high temperature are expected to give much better results also in terms of electrical behaviour, which is part of the future work.

Chapter 9

Optical transmission measurements of Si-modified MOFs

Silicon is well known as an electronic material and its technology has been developed for over half a century. As discussed in Section 7.3, with the on-chip technology now reaching its speed limit due to slow interconnection (bottleneck effect), silicon has attracted growing attention for possible applications as a photonic material owing to its high refractive index and infrared transparency. Another silicon optical property is its high Kerr coefficient, which makes it appealing also for non-linear photonics. In particular, the first silicon Raman laser has been realised by Boyraz and Jalali [*177*], opening the potential for an on chip silicon laser source. In order to target these applications for our semiconductor modified fibres, the obvious starting point is the full linear optical characterisation of silicon filled capillaries to determine linear loss parameters and mechanisms. In fact, before the nonlinear optical properties of these fibres can be exploited linear transmission losses need to be reduced under 3dB/cm.

As seen in Chapter 7, silicon has been successfully deposited in the pores of MOFs and it has been structurally characterised. Although fabrication parameters identified

during the structural characterisation were indicative of a good quality of the deposited materials by the PSU team, a further level of refinement of the fabrication parameter values was obtained at this stage, aimed at achieving a complete filling over some length of the capillary. As part of the deposition optimisation process, a range of samples were inspected for complete filling, providing a feedback to the collaborators at Penn State University. Successful samples were then prepared (see Section 9.1) and optically characterised. Firstly, single wavelength loss measurements at 1550 nm were performed in order to establish the order of magnitude of the optical losses for each sample. Then, wavelength dependent transmission losses measurements were performed on samples that showed losses under 30 dB/cm (at 1550 nm) in order to establish the linear loss mechanisms and ensure that the quality of the deposited material was high enough to reduce optical losses to a few dB/cm, which is the first step towards the realisation of a wide range of optical devices.

Specifically, wavelength-dependent loss measurements on a range of low loss silicon modified capillaries (amorphous, hydrogenated amorphous and polycrystalline obtained using different annealing conditions) have been performed to identify the scale and the nature of transmission losses for each core material. Details of the optical transmission set up used will be provided in Section 9.2, whilst loss measurements obtained using a cutback technique will be presented in Section 9.3. These results demonstrate measured polysilicon loss values that are some of the lowest reported (~8 dB/cm at 1550 nm), while the amorphous silicon sample yields the lowest loss value amongst all the tested samples at ~5 dB/cm (1550 nm). Both amorphous and polysilicon modified fibres can potentially be used for signal processing functions in all-fibre networks [*217*].

9.1 Sample preparation

Silicon modified capillaries were received as samples that are few centimetre long, without any coating and thus very fragile. The capillaries have an external diameter of ~175 μm, while the internal diameter corresponded to the diameter of choice for the silicon wire to be investigated. Samples fabricated at PSU were received in

batches of 3-6 silicon modified capillaries, typically ~20 cm long. These samples were analysed and tested as described below and feedback was reported to the fabrication team. Overall, about 100 silicon modified fibres were received for optical characterisation, 60 of which were 6 μm amorphous silicon core fibres (40 a-Si and 20 a-Si:H), 30 were 6 μm polysilicon core fibres and the remaining 10 were 1 μm polysilicon core fibres. Firstly, the transverse sections on both ends of the fibre were observed under the microscope (up to 100× magnification) to ensure that complete filling was achieved. If a hole was observed, a length of the sample would be cleaved off (3-4 mm in case of a large hole, ~1 mm in case of a small hole) and the newly exposed section observed again. This process was repeated until there were no holes at either end of the sample. Initially, starting with a-Si core fibres, most of the samples were not completely filled (only 2 samples out of the first 20 a-Si silicon core samples), but the deposition success rate grew relatively quickly thanks to the feedback provided, so that the fabrication team is soon expected to routinely produce completely filled samples. Then, Poly-Si and a-Si:H 6 μm core samples were fabricated as described in Section 8.1.1. Finally, 1 μm core samples were fabricated and analysed once satisfying results had been obtained with the 6 μm core samples, so they benefited from the advancement in the optimisation of the filling process. Overall about 2/3 of the received samples revealed an incomplete filling, obtaining a number of samples as shown in Table 9-1. Where observed, a completely filled section could be over 2 cm long, but typically was in the order of 1 cm.

	Number of samples	
	fabricated	100% filled
6 μm a-Si	40	6
6 μm a-Si:H	20	8
6 μm poly-Si	30	11
1 μm poly-Si	10	4

Table 9-1 *Total number of silicon modified samples which were fabricated and number of samples that were found completely filled at the cross-section microscope analysis.*

In order to facilitate handling, the selected sample placed in a hosting capillary of about 200 μm internal diameter and secured using wax or epoxy resins (brown substance in Figure 9.1), which infiltrate the interstice between sample and hosting capillary by capillary effect. The fluid would then harden by cooling down (wax) or heating up (epoxy resin) on a hot plate.

Both ends were then finished with a polishing process, necessary to ensure good coupling in the optical transmission measurements. Polishing paper from 9 μm down to 500 nm grade was used in consecutive steps until the surface appeared completely smooth under microscope, as shown in Figure 9.1.

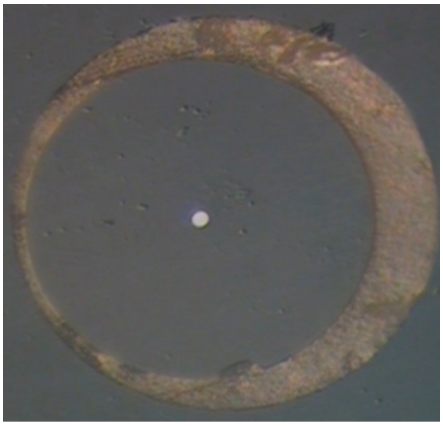

Figure 9.1 *Microscope imaging of a 6 μm core silicon modified capillary after polishing process. Epoxy resin (brown) and hosting capillary are also visible.*

Occasionally at this stage the smooth surface revealed holes in the silicon core which may have been too small to be noticed before. Air holes in the core are highly undesirable for optical transmission purposes as they create spots with a high refractive index contrast, thus generating strong scattering in the guided light. Therefore holes would be eliminated by further polishing. The final length of the treated sample was generally between 5 and 7 mm.

9.2 Optical transmission set up

Samples found to be completely filled were mounted and tested via transmission measurements. A first measurement of the optical transmission of each sample was taken at 1550 nm with the set-up designed for wavelength dependent loss measurements, which is represented in Figure 9.2.

Firstly, the source consists of a Fianium supercontinuum fibre laser combined with a tunable acousto-optic modulator to select the desired wavelength, which yielded an average power of ~0.5 mW per nanometre over the wavelength range 1200-1700 nm. This supercontinuum source has been chosen in order to obtain a wavelength dependent profile of the optical transmission losses over the entire telecoms wavelength range. This can provide additional information on the nature of the losses(see Section 9.3.2) in a region of the spectrum which is of interest for future applications.

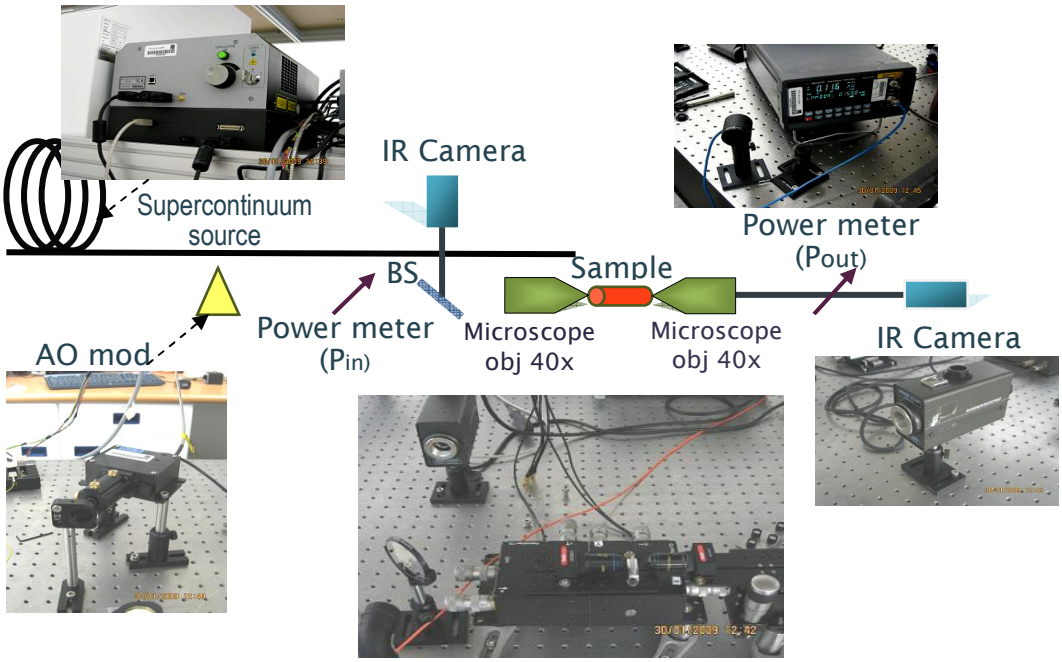

Figure 9.2 *Schematic with pictured elements of set-up used for wavelength dependent transmission loss measurements.*

The selected wavelength is launched into the silicon core using a 40× microscope objective, which corresponds to a spotsize of about 2 μm. For an optimum coupling, the spotsize needs to match or be less than the core size of the fibre, in this case of the silicon core. Although this choice is suitable for the 6 μm core samples, it is not the optimal condition for the 1 μm core, which would require a higher magnification (hence smaller spotsize) lens. As a result, some of the input power is lost for the experiments reported in Section 9.3.3.

A beam splitter is placed before the input microscope objective in order to direct the light reflected back from the input surface (due to Fresnel reflection, see Section 6.1.3) into an infrared camera allowing for the observation of the surface itself. The silicon core appears as a very bright spot due to the high reflection, thus facilitating launching. The output is collected through a 40× microscope objective with NA=0.65 and directed into an infrared camera (Hamamatsu). This was the highest NA available, which has been chosen in order to maximise the collection of the output power, as it will be discussed in the next section. Both objectives and the sample are placed on 3 independent translational stages, with the central one hosting the sample also being controlled by a piezoelectric controller to optimise the coupling, which was done at each wavelength. Once coupling is optimised, input and output powers at each wavelength are measured by a Newport 2832C power meter placed as in Figure 9.2.

Preliminary measurements on a short (4 mm) sample show that for the range of input powers used a linear response was measured for the power coupled out of the samples. This experiment was carried out in the same configuration described above, replacing the supercontinuum source with a diode laser emitting at 1550 nm, which yielded powers up to ~1 mW (see Figure 9.3). Such linear behaviour was expected as non-linear effects have been reported to appear for input average powers well above 1 mW in similar configurations (~3 μm^2 modal area, 1550 nm) [*186*], as discussed in Section 7.3. Also the overall losses of the set-up, including coupling, will be determined from the loss measurements to be about 60%, as described in the next section.

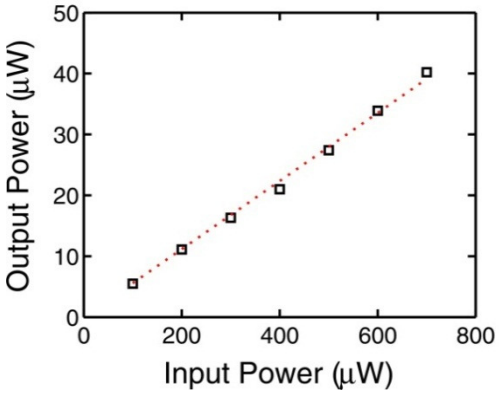

Figure 9.3 *Test for optical linear response of silicon samples for the power used in the transmission measurements at 1550.*

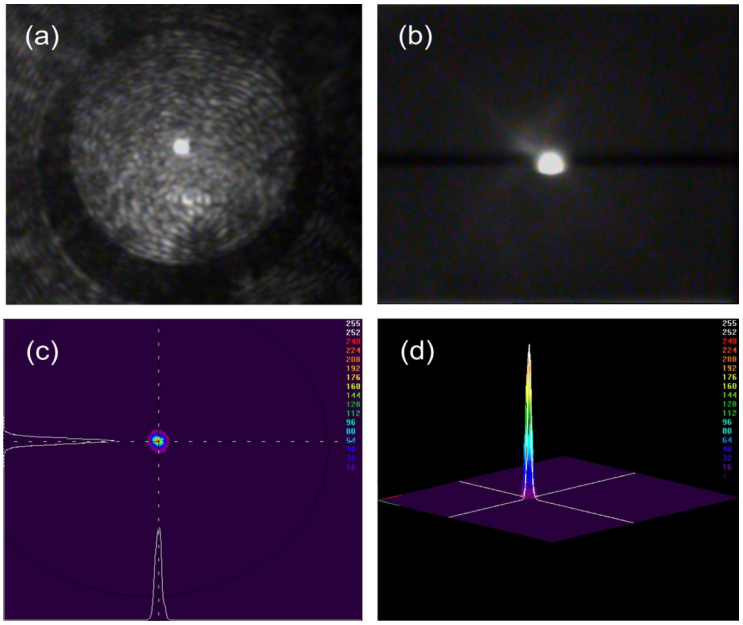

Figure 9.4 *Images of 5μm core silicon modified fibre transmission at 1550 nm using (a) infrared camera, input coupling not optimised (b) infrared camera, optimised coupling (c) 2-D intensity emission profile (arbitrary units) (d) 3-D intensity emission profile (arbitrary units).*

Each sample was tested selecting 1550 nm from the supercontinuum source for the alignment, yielding P_{in}≈0.7 mW, and the transmitted light was observed through the IR camera and projected on a screen. In case of a lossy [I don't know if this a word]samples (>60 dB/cm) no light was observed even when the sample was as short as 5 mm, whilst for this sample length or longer, a bright core would

corresponded to measurable losses. The loss measurements were performed according to the cut-back technique, which will be described in Section 9.3.1.

Examples of images of the output obtained via the infrared camera are shown in Figure 9.4. In (a) coupling is not optimised and the cladding light is visible revealing both the core and the inner edge of the hosting capillary, whereas in (b) coupling is optimised giving excellent contrast with the background. Intensity profile images of the output were taken using an Electrophysics 7290A infrared camera together with a Spiricon software and results are also shown in Figure 9.4 (c) and (d).

Owing to the low overall yield of samples selected through the preparation process, only 2-3 samples of each kind showed a considerable transmitted power (P_{out}≈30 μm with sample length ~7 mm), except for a-Si, which always maintained losses value above 40 dB/cm. The best samples obtained during this process were therefore tested for wavelength dependent loss measurements and results were compared, as will be described in the next section.

9.3 Wavelength dependent loss measurements

The linear attenuation coefficient α has been introduced in Sections 6.2 and can be calculated using Eq.(6.16), which is given again here:

$$\alpha[dB/m] = -\frac{10}{L}\log_{10}\left(\frac{P(L)}{P_0}\right). \tag{6.16}$$

This expression contains the input (coupled) power P_0, which can be estimated but it is experimentally difficult to determine.

For example, the silicon modified fibre numerical aperture (seen in section 6.1.2) can be calculated from Eq. (6.4)

$$NA = \left(n_{Si}^2 - n_{Silica}^2\right)^{1/2} \cong 3.18 \tag{9.1}$$

where n_{Si} is the silicon refractive index in the infrared (~3.5) and n_{silica} is the silica glass refractive index (1.45). This means that the light can emerge at the silicon/air

interface at angles of up to 90°, so not all the transmitted power P(L) will be collected by the microscope objective due to the mismatch in numerical aperture between output emission and collecting lens. Moreover, although experimentally the NA is not completely filled at the input, light will still emerge at the angle determined by the NA, mainly due to scattering mechanisms inside the core.

In the case of free space coupling in a silicon core, Fresnel reflection (see Section 6.1.3) also contributes significantly to coupling losses, having been calculated as:

$$R_{Fresnel} = \left(\frac{n_{Si} - n_{Air}}{n_{Si} + n_{Air}} \right)^2 \cong 30\% \tag{9.2}$$

therefore about 30% of the input light is reflected back at the input surface. Furthermore, surface scattering at both ends of the sample must be considered. Other sources of input power attenuation in the set-up are identified in both the microscope objectives, which are optimised for transmission at 1000 nm.

For these reasons, wavelength dependent transmission loss measurements have been performed in a range of selected samples using a cut back technique. This method is commonly used for reliable transmission loss measurements where it is not possible to quantify exactly all sources of coupling losses, in that it only depends on the attenuation coefficient α (see Sections 6.2) assuming that all the other sources of losses do not change.

9.3.1 Cutback technique

According to Eq.(6.15), the attenuation coefficient α for a fibre of length L_1 (expressed in cm) can be written as:

$$\alpha[dB/cm] = -\frac{10}{L_1} \log_{10}\left(\frac{P(L_1)}{P_0} \right) \tag{9.3}$$

where P_0 is the coupled input power. If the sample is cut-back and the sample length is now reduced to L_2, the new output power will be:

$$\alpha[dB/cm] = -\frac{10}{L_2}\log_{10}\left(\frac{P(L_2)}{P_0}\right) \tag{9.4}$$

Combining Eq.(9.3) and Eq.(9.4) the attenuation in dB/cm is readily obtained as:

$$\alpha(\lambda) = \frac{10}{L_1 - L_2}\log_{10}\left(\frac{P_1(\lambda)}{P_2(\lambda)}\right) \tag{9.5}$$

where $P_1=P(L_1)$, $P_2=P(L_2)$ and the wavelength dependence has been made explicit.

Transmission measurements were performed on the silicon modified fibre samples after preparation ($L_1 \approx$ 6-8 mm) and then a length of ~2-3 mm ($L_2 \approx$ 4 mm) was removed from the end (output) surface to perform the second set of measurements. Control measurements were performed at an intermediate length (≈ 5-6 mm) in order to check that the transmitted light would follow the expected behaviour with the wavelength, although these data were not used because of the high relative error. The input surface was preserved in order to keep input losses as reproducible as possible. The experimental data were analysed using Eq.(9.5) to obtain the optical loss in dB/cm as a function of wavelength.

9.3.2 Comparison of amorphous and polycrystalline silicon fibres

A ~6 μm core capillary has been chosen to deposit a range of materials: amorphous silicon (a-Si) deposited at 500 ºC, hydrogenated amorphous silicon (a-Si:H) deposited at 400 ºC and 3 samples of polycrystalline silicon (poly-Si) deposited at 500 ºC and annealed at 1125 ºC, 1200 ºC, 1325 ºC. These samples have been previously tested using Raman spectroscopy as shown in Section 8.2.2.3.

Transmission loss measurements showed that the amorphous sample was too high in loss to allow for a complete scan through the full wavelength range but an estimated loss of ~48 dB/cm at 1550 nm was obtained. For the other samples the wavelength dependent results are shown in Figure 9.5. In all cases the losses decrease with the increase of the wavelength, which suggests that scattering mechanisms contribute

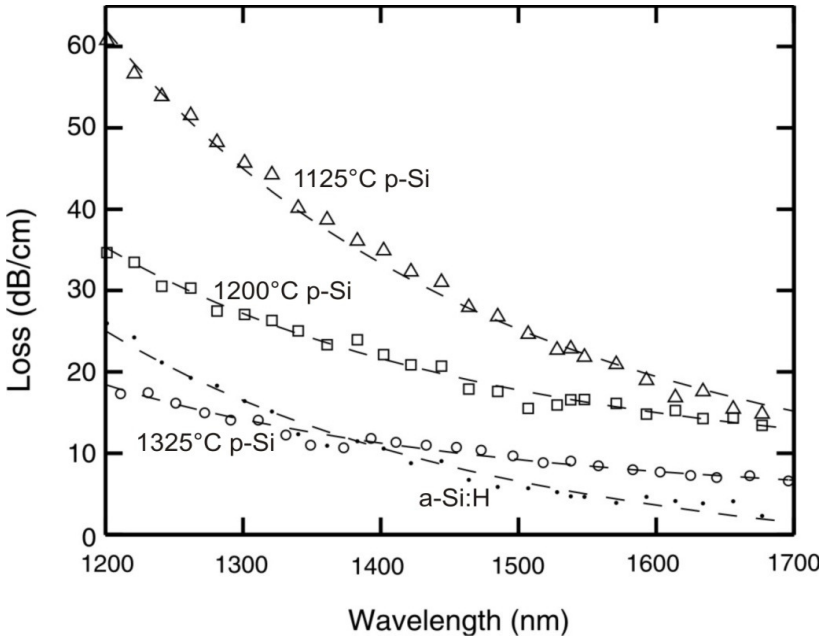

Figure 9.5 *Wavelength dependent loss measurements for 6 μm silicon core capillaries: polysilicon (p-Si) annealed at 1125ºC (triangles), 1200ºC (squares), 1325ºC (circles) and hydrogenated amorphous silicon (dots). Points represent experimental data while the dashed lines are the corresponding* λ^{-4} *fits.*

significantly and this is confirmed by fitting these curves with the λ^{-4} dependence associated with Rayleigh scattering (see Section 6.2.2.2).

Owing to the large core size, the light can be considered to travel entirely in the core, so in the polysilicon samples the Rayleigh scattering must arise at the grain boundaries as discussed in Section 7.3.2.

Comparing polysilicon samples it is clear that losses decrease with increasing annealing temperatures. This is consistent with the average larger grains that are expected at higher annealing temperatures. In fact larger grains mean that statistically in the same volume there will be larger ordered (crystalline) areas and fewer grain boundaries. Grain boundaries have been identified as the main reason for optical losses because of the related scattering and the absorption by defect material, therefore reducing grain boundaries by increasing grain size also decreases optical losses. Furthermore, polysilicon has a band edge at 1100 nm, so a small contribution to the loss due to a tail of the absorption peak should be considered, at the short wavelength.

On the other hand, the hydrogenated amorphous silicon sample shows loss values which are similar at each wavelength to the best polysilicon sample (1325 ºC annealing temperature), but decrease with the wavelength at a faster pace. The a-Si:H loss curve exhibits higher loss values compared with the 1325 ºC annealed polysilicon sample for wavelengths below ~1370 nm and lower loss values further in the spectrum, achieving the best loss value measured so far at 1550 nm (~5 dB/cm).

The different trend in the a-Si:H sample compared with the poly-Si ones suggests a different loss mechanism, although in both cases the loss is predominantly Rayleigh scattering. a-Si:H has a band edge at 730 nm and is expected to have negligible absorption losses in the infrared, although some absorption may result from the unpassivated dangling bonds. Rayleigh scattering is still present due to impurities and to the hydrogen, which is believed to cluster in the internal surface of microvoids in the material. These defects cause local density fluctuations, which translate in local variations of the refractive index and are known to also cause scattering in silica glasses [*233*].

Residuals of amorphous materials could also be at the origin of the steep slope in the 1125 ºC annealed polysilicon sample, which shows loss values consistent with the other polysilicon samples at the long wavelength, but retains a slope at the short wavelength which is more similar to the a-Si:H sample.

Overall the loss values at 1550 nm are summarised in Table 9-2:

6 µm core silicon modified fibre	Transmission Loss @1550 nm
a-Si	~50 dB/cm
a-Si:H	5 dB/cm
1125 °C p-Si	22 dB/cm
1200 °C p-Si	15 dB/cm
1325 °C p-Si	8 dB/cm

Table 9-2 *Transmission loss at 1550 nm for a range of ~6 µm core silicon modified fibre*

Low transmission losses make the a-Si:H samples suitable for applications in both linear optics and novel photonic devices, due to the high non-linear coefficient expected in hydrogenated amorphous silicon [*145*]. The results obtained for 1325 °C polysilicon are promising, showing loss values (8 dB/cm @1550 nm) which are among the best reported in the literature, but still too high for applications in non-linear optics.

9.3.3 Comparison of 6µm and 1µm core polysilicon fibres

The main requirements for non-linear processes are a high Kerr coefficient of the core material together with a high energy density (as shown in Section 6.2.3). The latter can be achieved by reducing the core size of the fibre whilst maintaining the light confined inside it. This is possible in the case of a fibre with large core-cladding index contrast, which allows for the mode and the majority of the energy to be still confined in a small, high index core. It is therefore highly desirable to reduce the core size of the polysilicon modified fibre, which has a large core-cladding index contrast, in order to induce non-linear effects.

On the other hand, despite the large index contrast, increasing the mode interaction with the core-cladding interface also increases scattering losses caused by interface roughness. For example, in rib waveguides the scattering surface roughness achievable during the fabrication process (few nanometres) has often limited the reduction of the rib size. For this purpose, optical losses in small core polysilicon modified fibres have been investigated and compared with the results obtained for the large core samples.

As discussed in Section 8.1.1, the deposition technique allows for strongly minimising core/cladding surface roughness as the deposition of amorphous silicon is conformal to the very smooth internal surface of a fibre (< 0.1 nm root mean square [*234*]) and the annealing process can keep this interface intact. Furthermore, reducing the core size can simply be achieved by choosing a smaller capillary for the deposition process; the deposition parameters would need to be adjusted accordingly but once the process is optimised the fabrication could be straightforward.

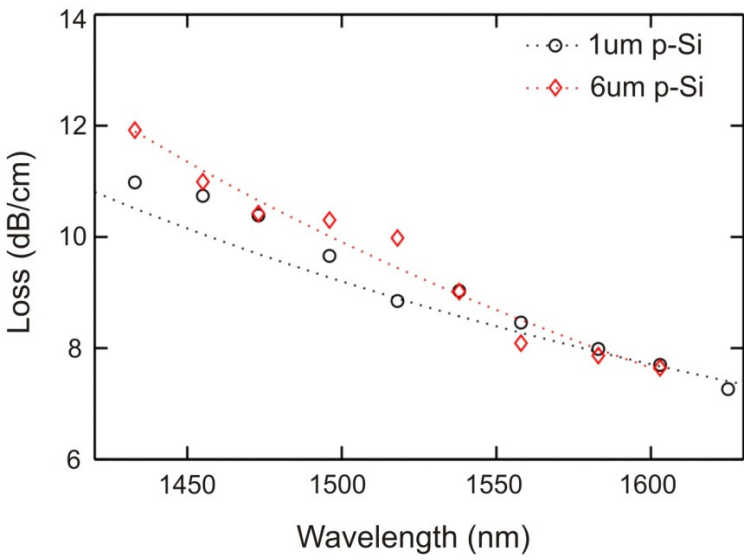

Figure 9.6 *Wavelength dependent loss measurements for 1 μm diameter core polysilicon capillary (circles) and 6 μm polysilicon core capillary (diamonds). Both samples were annealed at 1325 ºC. Points represent experimental data while the dashed lines are the corresponding* λ^{-4} *fits.*

In order to investigate the impact of the surface roughness at the core/cladding interface on the transmission loss, a small core polysilicon sample annealed at 1325 ºC has been fabricated inside a ~1 μm core capillary fibre. Loss measurements have been performed using a cut-back technique as described before and the results are plotted in Figure 9.6. Previous measurements obtained for the corresponding 6 μm core polysilicon sample are also plotted for comparison.

Measurements show that around the telecommunication wavelength range, transmission losses are comparable in both samples, suggesting that surface roughness plays a negligible role in terms of overall transmission losses as expected. This 1 μm core diameter polysilicon sample annealed at 1325 °C is the best candidate for non-linear application so far, allowing for high energy density and possibly acceptable transmission losses.

Further investigations for optical non-linear applications require a high power laser that was not available at the time that these measurements were performed. This experiment is part of the future work described in the next chapter.

Chapter 10

Summary and future directions for Part II

Semiconductor materials have dominated many modern technologies and group IV semiconductors in particular are being established as a photonic material in order to replace metallic interconnects [should that be interconnectors?] which will soon reach intrinsic speed limits. At the same time, optical fibres still dominate the field of data transmission for telecommunications and the introduction of MOFs has offered incredible versatility in design and control of guiding parameters.

Semiconductor modified microstructured optical fibres have been presented as a new platform technology that could potentially combine the rich optoelectronic properties of semiconductors in a fibre geometry. The fabrication process described in this thesis consists of a high pressure chemical vapour deposition technique which has been demonstrated to deposit high quality silicon and germanium in the high aspect ratio capillary pores. This technique is potentially adaptable to many more materials and it offers advantages in terms of design, which can be tailored by simply changing the MOFs used as template.

The first target was to achieve deposition of a good quality semiconductor material inside optical fibres and this has been demonstrated via structural characterisation.

SEM, TEM and Raman spectroscopy has shown a uniform, conformal deposition of good quality semiconductor materials inside the MOFs, up to the complete filling of the pores. Germanium and silicon deposited at relatively low temperatures have been found to both show a good electrical response, which is expected to improve for samples deposited, and annealed at higher temperatures.

Once the deposited material reached satisfying structural properties, the optical characterisation started. The investigation of the optical properties of semiconductor modified optical fibres has been focused on silicon modified fibres due to the silicon transparency at telecom wavelengths. Keeping in mind the non-linear applications targeted in this work, the first main step was identified in bringing linear optical transmission losses to a few dB/cm. Also in this case, a range of completely filled amorphous and polycrystalline silicon modified fibres have been tested by loss measurements at 1550 nm. These initial tests provided a feedback to the fabrication team to refine values for deposition parameters, bringing loss values down to 5 dB/cm at 1550. Then wavelength dependent loss measurements, performed on the best representative samples, provided an insight on the loss mechanisms in amorphous and polycrystalline samples, confirming hydrogenated amorphous silicon (5 dB/cm at 1550 nm) as the best candidate for both linear and non-linear silicon photonics applications. In polysilicon, transmission losses have been observed to decrease by increasing the temperature of the annealing step. The lowest loss in polycrystalline samples measured at 1550 nm were found to be 8 dB/cm in the samples annealed at 1325 °C both in 6 μm core and 1 μm core diameter. This result suggests that the conformal deposition of the semiconductor takes on the pristine internal surface of the fibre, leading to negligible core-cladding interface scattering loss.

Although these loss values are close to the target and are comparable with the best results reported in literature for amorphous and polycrystalline silicon waveguides, they are not yet low enough for observing significant non-linear effects (~3 dB/cm). But the feedback work provided to the fabrication team has been proven successful and in the future it will keep helping to refine parameters and improving results as the theoretical limit for material optical losses in silicon is as low as 0.1 dB/cm. Thanks to this feedback described in this thesis, the production of completely filled

samples went from about 10% about 80% of successful samples and very recently has reached nearly 100% combined with losses as low as 0.8 dB/cm at 1550 nm (unpublished work).

For future work, firstly, deposition parameters and annealing temperature can still be adjusted in order to further reduce losses. For example, the amorphous silicon deposition temperature can be optimised in order to maximise the hydrogen content which saturates dangling bonds. Also other techniques for the annealing step may be explored to achieve larger grains in polysilicon and, eventually, single crystalline silicon. For example, a laser at visible wavelengths focused into the core, transversally to the glass fibre, could heat up the silicon with virtually no effect on the silica glass.

Applications in a range of photonic devices may be investigated. Two main directions can be identified for silicon modified fibres: non-linear devices and mid-infrared photonics applications.

Silicon modified fibres with a core diameter <1 μm are the best candidate for non-linear applications, because of the high energy density, and ultimately single mode operation when < 400 nm [*169*]. Both amorphous and polycrystalline silicon could be used, as they have a high non-linear Kerr coefficient. For non-linear optics experiments, such as Raman devices, a pulsed high power laser would be required to achieve high peak power and overcome additional optical loss caused by TPA induced free carriers.

The first step towards non-linear application is the observation of phenomena such as self phase modulation or stimulated Raman scattering. The realisation of an all-fibre silicon Raman amplifier can be considered. To achieve this, an adaptation of the set up used by Jalali and co-workers to demonstrate a Raman amplifier in a rib waveguide [*235*] (~1×1 μm^2 cross section and 2 cm length) would be used (see Figure 10.1).

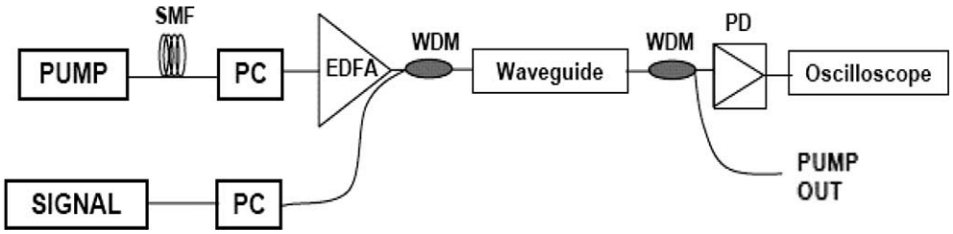

Figure 10.1 *Schematic of experimental set up used by Jalali and co-workers to demonstrate pulsed pump silicon Raman amplifier [235].*

Here the pump source was a mode locked fibre laser (λ_p=1427 nm) with 25 MHz repetition rate and ~1 ps output pulse width. This pulse was stretched to ~30 ps using a standard single mode fibre because the phonon response time in silicon is more than 3 ps, and then amplified again. The probe signal at 1542 nm (300 cm^{-1} away from λ_p, as dictated by the stoke shift in silicon) is provided by a diode laser, while two polarisation controllers are used to set TE polarisation to obtain maximum coupling in the waveguide and to adjust the relative polarisation of the signal with the pump. In the case of silicon modified fibre, the symmetrical cylindrical geometry of the waveguide affects the shape of the guided mode in that no preferential direction exists for maximum coupling, hence keeping a TE polarisation of the pump would no longer be required. Wavelength division multiplexer (WDM) is used to couple both waves into the waveguide and to demultiplex them after the waveguide. Finally the signal is detected by a photodiode (PD) and analysed.

A Raman laser was realised in a similar configuration [*177*], with the output signal looped back using a tap coupler with 5 to 95% splitting ratio and an optical fibre (~8 m, to match the cavity round trip with the pump pulse period). In this case they used a pump source at 1540 nm (obtaining the lasing at 1675 nm).

Alternatively mid-IR applications could be investigated, as suggested by the results obtained from wavelength dependent loss measurements, which showed that in all cases transmission loss decreases at longer wavelength. Moving towards wavelengths longer than 1550 nm can be considered to reduce guiding loss. In Figure 10.2 the absorption loss of single crystal silicon at room temperature is plotted as a function of wavelength from 1–100 μm together with its refractive index [*192*].

Moreover, as discussed in Section 7.3, also TPA is strongly reduced in silicon for $\lambda > 2.2$ μm. As a consequence, also non-linear absorption losses caused by TPA-induced free carriers can become negligible.

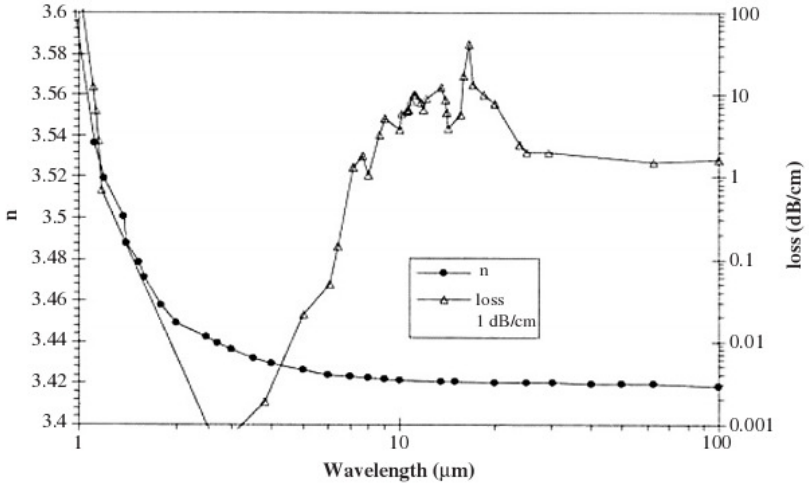

Figure 10.2 *Refractive index and absorption loss of crystal silicon at room temperature as a function of wavelength from 1–100μm [192].*

Ge-Si heterostructures have also been proposed for longwave infrared applications. Firstly, for wavelengths beyond 1.9 μm germanium also becomes transparent thus Ge-on-Si waveguides have been proposed [*192*] between 1.9 and 16.7 μm transmission wavelength. In these applications germanium can replace silica as cladding material, because silica is not transparent in the mid-IR. Moreover Si-Ge structures have also been demonstrated to provide midwave (3-5 μm), longwave (8-14 μm) and very longwave (30-100 μm or THz) electrically pumped infrared sources (quantum cascade emitters) and photodetectors [*236, 237*].

Our group has already reported sequential deposition of Ge-Si structures inside optical fibre [*219*], so Ge-Si clad-core structures could be engineered to move to a wider range of wavelength beyond 2μm. Deposition of other materials is also under current investigation.

In conclusion, a range of optical devices based on semiconductor modified microstructured optical fibres can be envisioned starting from telecoms applications at the near IR with the potential to extend to mid-IR applications.

Chapter 11

Conclusion

In this thesis I have presented two examples of how materials such as metals and semiconductors, traditionally used for their electronic properties, can be engineered for photonics applications. The fundamental component of this engineering process is the ability of utilise micro and nano structures to control their optical properties.

Metal nanoparticles have plasmonic properties that can enhance optical responses of nearby molecules, so they have been impregnated into polycarbonate strips for the fabrication of a new class of inexpensive, robust, long lasting plasmonic substrates.

Together with its electronic properties, silicon also has a high refractive index and is transparent in the infrared, so it lends itself for photonics applications such as waveguiding. For these reasons silicon has been proposed to replace traditional metallic interconnects for monolithic on-chip devices. Further engineering has also led to the development of active silicon photonic devices. Part II demonstrated how silicon has been successfully deposited inside optical fibres, with good results in terms of optical transmission. This technique lays down the fundamentals for a new generation of all-fibre photonic devices.

In both cases materials and structures were quite different: metals and semiconductors, nanoparticles and microwires, planar substrate and optical

waveguides. These examples of electronic materials applied to photonics could not be more diverse, yet they are not unconnected. For example, hybrid devices where metallic nanoparticles are used to enhance light emission in silicon nanocrystals [*238, 239*] or light absorption in silicon thin films for solar cells [*240*], have already being proposed in literature.

Many other materials and structures are also being considered by the scientific community to deliver solutions to new technological challenges in these areas. Their common ground is the engineering of materials and their substrates, with the ultimate aim of manipulating and controlling light on a “small” scale.

Appendix A

Mie theory simulation

The extinction cross section for a spherical particle of radius a and refractive index n_s, immersed in a dielectric medium of refractive index n_m, can be calculated by Mie theory as described in reference [*27*] as:

$$C_{ext} = \frac{2\pi}{k^2}\sum_n (2n+1)\mathrm{Re}[a_n + b_n]$$

with $k = \frac{2\pi \cdot n_m}{\lambda}$ and a_n , b_n being the scattering coefficients written as:

$$a_n = \frac{m\,\phi_n(mx)\cdot\phi_n'(x) - \phi_n(x)\cdot\phi_n'(mx)}{m\,\phi_n(mx)\cdot\xi_n'(x) - \xi_n(x)\cdot\phi_n'(mx)}$$

$$b_n = \frac{\phi_n(mx)\cdot\phi_n'(x) - m\,\phi_n(x)\cdot\phi_n'(mx)}{\phi_n(mx)\cdot\xi_n'(x) - m\,\xi_n(x)\cdot\phi_n'(mx)}$$

where $m = \frac{n_s}{n_m}$, $x = ka$ and ϕ_n and ξ_n can be expressed in terms of the Bessel functions J and Y as:

$$\phi_n(x) = \sqrt{\frac{\pi x}{2}} J_{n+1/2}(x)$$

$$\xi_n = \sqrt{\frac{\pi x}{2}}\left[J_{n+1/2}(x) + iY_{n+1/2}(x)\right].$$

For computational purpose the scattering coefficients a_n , b_n can be rewritten using the logarithmic derivative

$$D_n(\rho) = \frac{d}{d\rho}\ln\phi_n(\rho)$$

with $\rho = mx$, as:

$$a_n = \frac{\left[D_n(mx)/m + n/x\right]\cdot\phi_n(x) - \phi_{n-1}(x)}{\left[D_n(mx)/m + n/x\right]\cdot\xi_n(x) - \xi_{n-1}(x)}$$

$$b_n = \frac{\left[mD_n(mx) + n/x\right]\cdot \phi_n(x) - \phi_{n-1}(x)}{\left[mD_n(mx) + n/x\right]\cdot \xi_n(x) - \xi_{n-1}(x)}.$$

All the above relations are included in the Matlab code which calculates the extinction cross section for silver nanoparticles used to plot Figure 3.10. Data for the silver refractive index as function of wavelength were taken from reference [*29*].

Appendix B

Publications

Journal papers:

1.L. Lagonigro, N. Healy, J. R. Sparks, N. F. Baril, P. J. A. Sazio, J. V. Badding, and A. C. Peacock *"Low loss silicon fibres for photonics applications"* **Applied Physics Letters, 96, 041105 (2010)**

2.L. Lagonigro, A. C. Peacock, S. Rohrmoser, T. Hasell, S. M. Howdle, P. J. A. Sazio, P. Lagoudakis "*Time and spectrally resolved enhanced fluorescence using silver nanoparticle impregnated polycarbonate substrates*", **Applied Physics Letters, 93, 261114 (2008)**

3.T. Hasell*, L. Lagonigro*, A. C. Peacock, S. Yoda, P. D. Brown, P. J. A. Sazio, S. M. Howdle **"***Silver Nanoparticle Impregnated Polycarbonate Substrates for Surface Enhanced Raman Spectroscopy*", **Advanced Functional Materials, 18, 1265-1271 (2008)**

Conference papers:

1.L. Lagonigro, N. V. Healy, J. R. Sparks, N. F. Baril, P. J. A. Sazio, J. V. Badding, A. C. Peacock "Wavelength-dependent loss measurements in polysilicon modified optical fibres" **CLEO/Europe-IQEC 2009**, Munich (Germany) – 15/06/2009

2.L. Lagonigro, A. C. Peacock, S. Rohrmoser, T. Hasell, S. M. Howdle, P. J. A. Sazio, P. Lagoudakis "Silver nanoparticle impregnated polycarbonate substrates for plasmonic applications" **IEEE/LEOS Winter Topicals 2009,** Innsbruck (Austria) - 12-14/01/2009

3.L. Lagonigro, A. C. Peacock, P. J. A. Sazio, T. Hasell, P.D. Brown and S. M. Howdle "Surface-Enhanced Raman Spectroscopy using silver impregnated polycarbonate substrates" **CLEO/Europe-IQEC 2007**, Munich (Germany) – 18/06/2007

APPLIED PHYSICS LETTERS 96, 041105 (2010)

Low loss silicon fibers for photonics applications

Laura Lagonigro,[1] Noel Healy,[1] Justin R. Sparks,[2] Neil F. Baril,[2] Pier J. A. Sazio,[1] John V. Badding,[2] and Anna C. Peacock[1,a)]
[1]*Optoelectronics Research Centre, University of Southampton, Southampton SO17 1BJ, United Kingdom*
[2]*Department of Chemistry and Materials Research Institute, Pennsylvania State University, 16802 Pennsylvania, USA*

(Received 4 December 2009; accepted 21 December 2009; published online 27 January 2010)

Silicon fibers are fabricated using a high pressure chemical deposition technique to deposit the semiconductor material inside a silica capillary. The silicon is deposited in an amorphous state into pure silica capillaries and can be crystallized to polysilicon after the deposition via a high temperature anneal. Optical transmission measurements of various amorphous and polycrystalline core materials were performed in order to determine their linear losses. Incorporating silicon functionality inside the fiber geometry opens up new possibilities for the next generation of integrated silicon photonics devices. © *2010 American Institute of Physics*.
[doi:10.1063/1.3294630]

Continuous advancements in silicon photonics have led to the demonstration of a number of compact optoelectronic devices. To date much of the progress in this area has been based on photolithographically defined single crystal silicon-on-insulator (SOI) devices. However, in an attempt to break the bottleneck of limited real estate, recently attention has turned to complementary metal-oxide-semiconductor (CMOS) compatible structures based on amorphous and polycrystalline silicon. Devices made of these materials are not only easier, but also much cheaper to fabricate making them ideal candidates for use in silicon interconnect technology. For example, using standard CMOS techniques researchers have demonstrated the fabrication of a vertically integrated polysilicon waveguide on a single chip.[1] As materials for photonics applications, most of the research on amorphous and polysilicon has focused on reducing the optical transmission losses.[2,3] Nevertheless, some important active on-chip devices have been reported of late, including optical switches and modulators.[4,5]

An alternative approach to the all optical planar integrated circuit is to incorporate the active semiconductor component into the fiber geometry so that signal processing functions can be carried out inside the data transport medium. Using a high pressure chemical processing technique bulk silicon has been deposited into the internal holes of pure silica capillaries to fabricate some of the earliest silicon optical fibers.[6] Typically the silicon is deposited at low temperatures so that it forms in an amorphous state which can be crystallized to polysilicon after the deposition via a high temperature anneal. This simple and low cost fabrication procedure can be easily modified to fill a range of capillary sizes so that the waveguide dimensions can be optimized for the specific application.

In this letter we investigate the optical transmission losses of these silicon fibers with both amorphous and polysilicon core materials. Conditions are optimized to control the deposition of the semiconductor material which is important for obtaining both low loss amorphous and high quality polysilicon materials. For example, in conventional plasma enhanced chemical vapor deposition (PECVD), the incorporation of hydrogen into the amorphous material is known to saturate the dangling bonds, thus reducing the absorption losses.[7] Unfortunately, however, hydrogen is detrimental to the crystallization of polysilicon as it reduces the density of the silicon material so that it shrinks and detaches from the silica cladding as hydrogen is driven out during the high temperature anneal.[8] Here we have compared a range of deposited materials and annealing conditions to establish key parameters to obtaining low loss silicon fibers. The results demonstrate the potential for both amorphous and polysilicon materials to be used in all-fiber networks.

The silicon fiber structures are fabricated by depositing the semiconductor material inside pure silica capillaries using a high pressure microfluidic chemical deposition technique.[6] Glass capillaries make excellent templates for materials deposition as their mechanical strength allows them to withstand the extreme deposition conditions,[9] they have especially smooth internal surfaces [0.1 nm root mean square roughness (Ref. 10)], and the hole dimensions can be easily scaled to the desired core size. The deposition process is conducted by forcing a mixture of silane and helium (SiH_4/He) to flow through the central hole under high pressures ~35 MPa and temperatures that range between 400–500 °C. At these temperatures the material deposits in an amorphous state which ensures that it bonds smoothly to the silica walls, thus minimizing the roughness at the silicon-silica interfaces.[11] If required, crystallization to polysilicon is then performed after the deposition process via annealing at temperatures up to 1325 °C.

The fibers used in our investigations are fabricated by depositing silicon inside capillaries with a ~6 μm inner diameter. Owing to the large index difference between the silicon core and silica cladding, the guided light is well confined to the micron sized core. Figure 1(a) shows a SEM micrograph of a silicon fiber where the core has been slightly etched out of the silica cladding to facilitate imaging. To obtain optimal coupling into and out of these fibers we first mount them inside thicker silica capillary tubes and then use a standard polishing technique to finish the end faces. Figure 1(b) shows an example of a polished fiber imaged using an

a)Electronic mail: acp@orc.soton.ac.uk.

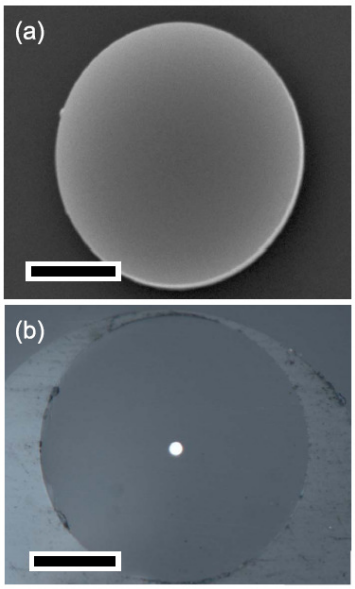

FIG. 1. (Color online) (a) SEM micrograph of a silicon fiber with the core slightly etched from the cladding; scale bar 2 μm. (b) Polished fiber for optical coupling, mounted inside a thicker capillary; scale bar 40 μm.

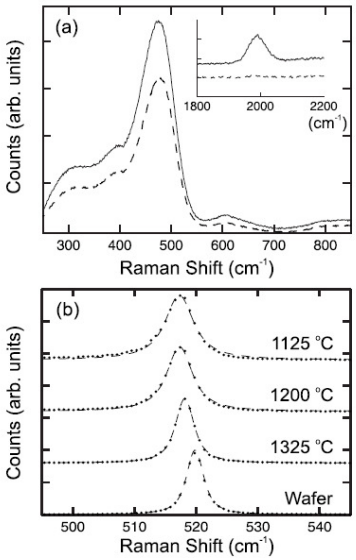

FIG. 2. (a) Raman spectra for the amorphous silicon fibers; sample A (solid curve) and sample B (dashed curve). Inset indicates the presence of hydrogen in sample A. (b) Raman spectra of the polysilicon fibers (top 3 curves) and a single crystal silicon wafer (bottom curve). Dashed lines are Voigt fits.

optical microscope. We consider five silicon fibers fabricated under different conditions: (A) amorphous silicon deposited at ~400 °C, (B) amorphous silicon deposited at ~500 °C, (C) polysilicon deposited at ~500 °C and annealed up to 1125 °C, (D) polysilicon deposited at ~500 °C and annealed up to 1200 °C, and (E) polysilicon deposited at ~500 °C and annealed up to 1325 °C.

To determine the quality of the deposited material of the various fibers we conducted micro-Raman measurements on the silicon rods. In all cases a 633 nm HeNe laser was focused onto the silicon through the side of the transparent silica cladding, with a spot size of ~2 μm and ~3 mW of power at the outer surface, and the backscattered radiation recorded on a thermoelectrically cooled Horiba Jobin Yvon Synapse CCD detector. Figure 2(a) shows the Raman spectra of the two amorphous silicon fibers. Both fibers exhibit a strong broad peak around 480 cm^{-1} corresponding to the transverse optical mode, with some weaker subsidiary peaks associated with the other known vibrational modes of amorphous silicon.[12] Interestingly, looking to the higher frequency regime, as shown in the inset, sample A (solid line) also has a peak at ~2000 cm^{-1} which is typically associated with the presence of hydrogen.[13] This peak is absent in sample B (dashed line) indicating that, as in the case of PECVD, hydrogen may be incorporated into the amorphous material at low deposition temperatures.[14] The effects of hydrogen incorporation via this method are currently under investigation and will be the subject of a future publication. However, based on this observation, we chose to only investigate polysilicon fibers that were annealed from amorphous samples deposited at ~500 °C to avoid the possibility of hydrogen out diffusion. The Raman spectra for the polysilicon samples are then shown in Fig. 2(b), together with a reference spectrum taken of a single crystal silicon wafer (bottom curve). To estimate the Raman peak widths, the spectra are fitted with Voigt profiles (dashed curves) to account for the 1.5 cm^{-1} Gaussian instrument contribution. The silicon wafer has a Lorentzian FWHM of 2.7 cm^{-1}, centered at 520 cm^{-1}, with the polysilicon widths measured to be 5.1 cm^{-1}, 4.5 cm^{-1}, and 3.0 cm^{-1} for samples C (1125 °C anneal), D (1200 °C anneal), and E (1325 °C anneal), respectively. The larger widths and the asymmetries seen in the polysilicon peaks, particularly for the lower temperature annealed samples, are due to contributions from the defect and amorphous materials, that surround the single crystal grains, which are associated with vibrations at frequencies in the range 500–517 cm^{-1}.[15] We attribute the smaller width of the Raman peak of sample E to a reduction in the defect and amorphous content, and hence an improvement in the overall crystallinity.[2] From previous depositions with similar linewidths we anticipate the crystal grain sizes to be of the order 0.5–1 μm.[6,16] While the slight red shift of the polysilicon peaks (517 cm^{-1} for samples C and D, and 518 cm^{-1} for sample E) is, in part, due to the material surrounding the crystal grains, we also expect there to be a small contribution from the residual stress induced across the silicon-silica boundaries which are introduced during annealing, and are a result of the differences in the thermal expansion of the strongly bonded materials.[16]

Optical transmission losses of the fibers as a function of the guided wavelength were determined using a cut-back method, where the typical starting length was ~8 mm and we polished 1 mm off the samples between each measurement. A supercontinuum source was filtered using a tunable acousto-optic device to yield an average power of ~0.5 mW over the wavelength range 1.2–1.7 μm, and launched into the silicon cores via free space coupling using a 25× micro-

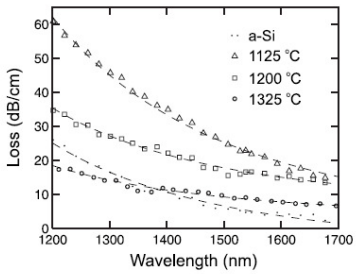

FIG. 3. Transmission losses as a function of wavelength for amorphous sample (A) and polysilicon samples (C) 1125 °C, (D) 1200 °C, and (E) 1325 °C. Dashed lines are λ^{-4} fits.

scope objective lens. A second 40× objective is used to capture the transmitted light and focus it onto a Newport 2832C power meter. The results of the loss measurements are plotted in Fig. 3 for all but the amorphous sample B. Without hydrogen to saturate the dangling bonds, amorphous silicon is highly lossy over the infrared wavelength range and the large loss of 50 dB/cm at 1550 nm measured in sample B is not unexpected. At wavelengths less than 1550 nm the losses in this fiber increase dramatically so that most or all of the transmitted light is absorbed, while at the longer wavelengths the measurements were limited by the detector sensitivity.

From the curves measured for the remaining samples, it is clear that in all cases the losses decrease for increasing wavelength, which suggests that scattering mechanisms contribute significantly. Further evidence to this is provided by the good agreement with the fitted curves which display the λ^{-4} dependence associated with Rayleigh scattering, which is in accordance with previous measurements.[2,17] Comparison of the polysilicon loss curves shows that there is a clear reduction in the losses as the annealing temperature is increased, which follows from our earlier Raman observations that the higher temperature anneal leads to an improvement in the polycrystalline quality. From sample E, we determine the loss at 1550 nm to be ~8 dB/cm, which is close to the lowest loss measured in a polysilicon fiber.[6] Although the amorphous sample A shows a similar wavelength dependence, the slope of this data set is much steeper than the two higher temperature annealed samples which we expect to be predominantly crystalline in nature. Thus we attribute the sharp increase in the losses at short wavelengths in the low temperature anneal sample C to a contribution from the amorphous silicon material which surrounds the crystal grains. Significantly, sample A yields the lowest loss of ~5 dB/cm at 1550 nm, which suggests that the incorporation of hydrogen, which was evident from the Raman curve, has resulted in an appreciable saturation of dangling bonds in the material.

The results of the transmission measurements indicate that by further optimizing the deposition and annealing processes to obtain either high quality low loss amorphous silicon or polysilicon core materials, it should be possible to obtain silicon fibers with losses that approach those of the lowest recorded values in on-chip waveguides of around a few decibels per centimeter.[7,18] The observed reduction in optical losses as the transmission wavelength increases suggests that silicon device performance and efficiency can be improved by operating at longer wavelengths. The versatile nature of the deposition technique to deposit a range of silicon materials inside the capillary template opens up new possibilities for the next generation of integrated silicon photonics devices for all-fiber networking.

The authors acknowledge EPSRC (Grant No. EP/G028273/1), NSF (Grant No. DMR-0806860), and the Penn State Materials Research Science and Engineering Center (NSF Grant No. DMR-0820404) for financial support. A.C.P. is a holder of a Royal Academy of Engineering fellowship.

[1]K. Preston, B. Schmidt, and M. Lipson, Opt. Express **15**, 17283 (2007).
[2]L. Liao, D. R. Lim, A. M. Agarwal, X. M. Duan, K. K. Lee, and L. C. Kimerling, J. Electron. Mater. **29**, 1380 (2000).
[3]A. Harke, M. Krause, and J. Mueller, Electron. Lett. **41**, 1377 (2005).
[4]K. Preston, P. Dong, B. Schmidt, and M. Lipson, Appl. Phys. Lett. **92**, 151104 (2008).
[5]F. G. Della Corte, S. Rao, M. A. Nigro, F. Suriano, and C. Summonte, Opt. Express **16**, 7540 (2008).
[6]P. J. A. Sazio, A. Amezcua-Correa, C. E. Finlayson, J. R. Hayes, T. J. Scheidemantel, N. F. Baril, B. R. Jackson, D.-J. Won, F. Zhang, E. R. Margine, V. Gopalan, V. H. Crespi, and J. V. Badding, Science **311**, 1583 (2006).
[7]G. Cocorullo, F. G. Della Corte, R. De Rosa, I. Rendina, A. Rubino, and E. Terzini, IEEE J. Sel. Top. Quantum Electron **4**, 997 (1998).
[8]Z. Remeš, M. Vaněček, A. H. Mahan, and R. S. Crandall, Phys. Rev. B **56**, R12710 (1997).
[9]C. R. Kurkjian, J. T. Krause, and M. J. Matthewson, J. Lightwave Technol. **7**, 1360 (1989).
[10]P. J. Roberts, F. Couny, H. Sabert, B. J. Mangan, D. P. Williams, L. Farr, M. W. Mason, A. Tomlinson, T. A. Birks, J. C. Knight, and P. St. J. Russell, Opt. Express **13**, 236 (2005).
[11]L. Lagonigro, N. V. Healy, J. R. Sparks, N. F. Baril, P. J. A. Sazio, J. V. Badding, and A. C. Peacock, CLEO/Europe-EQEC **CE3** (2009).
[12]D.-J. Won, M. O. Ramirez, H. Kang, V. Gopalan, N. F. Baril, J. Calkins, J. V. Badding, and P. J. A. Sazio, Appl. Phys. Lett. **91**, 161112 (2007).
[13]M. H. Brodsky, M. Cardon, and J. J. Cuomo, Phys. Rev. B **16**, 3556 (1977).
[14]R. Sun, K. McComber, J. Cheng, D. K. Sparacin, M. Beals, J. Michel, and L. C. Kimerling, Appl. Phys. Lett. **94**, 141108 (2009).
[15]A. A. Parr, D. J. Gardiner, R. T. Carline, D. O. King, and G. M. Williams, J. Mater. Sci. **36**, 207 (2001).
[16]C. E. Finlayson, A. Amezcua-Correa, P. J. A. Sazio, N. F. Baril, and J. V. Badding, Appl. Phys. Lett. **90**, 132110 (2007).
[17]N. Healy, J. R. Sparks, M. N. Petrovich, P. J. A. Sazio, J. V. Badding, and A. C. Peacock, Opt. Express **17**, 18076 (2009).
[18]Q. Fang, J. F. Song, S. H. Tao, M. B. Yu, G. Q. Lo, and D. L. Kwong, Opt. Express **16**, 6425 (2008).

APPLIED PHYSICS LETTERS 93, 261114 (2008)

Time and spectrally resolved enhanced fluorescence using silver nanoparticle impregnated polycarbonate substrates

Laura Lagonigro,[1] Anna C. Peacock,[1,a)] Stefan Rohrmoser,[2] Tom Hasell,[3] Steven M. Howdle,[3] Pier J. A. Sazio,[1] and Pavlos G. Lagoudakis[2]
[1]*Optoelectronics Research Centre, University of Southampton, Southampton SO17 1BJ, United Kingdom*
[2]*School of Physics and Astronomy, University of Southampton, Southampton SO17 1BJ, United Kingdom*
[3]*School of Chemistry, University of Nottingham, Nottingham NG7 2RD, United Kingdom*

(Received 1 August 2008; accepted 3 December 2008; published online 31 December 2008)

Silver nanoparticle impregnated polycarbonate strips have been investigated as substrates for metal-enhanced photoluminescence of a blue emitting dye molecule (coumarin 102). By considering simultaneous time and spectrally resolved photoluminescence we observed fluorescence enhancement resulting from plasmon coupling with an increase in the emission by a factor of ~8.5 with an associated reduction in the photon lifetime. We relate the fast and slow components of the observed emission decay to the presence of both monomers and aggregates in the films and we discuss their different responses to the plasmon coupling. © *2008 American Institute of Physics*. [DOI: 10.1063/1.3059567]

Photoluminescence (PL) plays a central role in many aspects of biological and medical research with applications including DNA sequencing,[1] cell imaging,[2] and sensing.[3] Recently there has been much interest in modifying the photonic mode density of states around the fluorescent molecule using surface plasmon excitation on metal nanoparticles.[4] The large electric fields associated with plasmon modes can enhance photon-matter interaction to modify the excitation cross section[5] and the radiative decay rate, resulting in increased fluorescence intensities of molecules in close proximity to the metal.[6] Metal-enhanced fluorescence (MEF) has led to the demonstration of optical probes with enhanced brightness so that we expect it to play an important role in the next generation of photonic devices.[4]

If MEF is to be used readily in routine procedures, then ideally the substrates need to be robust, stable, and most importantly, biocompatible. To date, typical substrates employed for MEF were similar to those used for other optical-plasmonic applications such as surface enhanced Raman scattering (SERS) spectroscopy.[7] Conventional processing techniques for the fabrication of planar SERS substrates are often expensive and in general have the active metal surface exposed to air so that they not only suffer from poor temporal stability, resulting from oxidation, but are also fragile. We have recently reported substrates fabricated via a supercritical technique where metal nanoparticles are embedded into polymer substrates that were shown to exhibit an efficient SERS response.[8] The nanoparticle composites are fabricated using polycarbonate as the host polymer, which has excellent biocompatibility, as well as superior optical and mechanical properties.[9] These composite structures offer a number of advantages over previously reported metal-polymer substrates fabricated via surface functionalization[10] in that by embedding the nanoparticles in the polymer they are protected from the surrounding environment, thus yielding a high degree of temporal stability. In this paper we investigate the MEF properties of these substrates and show them to be excellent candidates for light emitting applications.

The silver nanoparticles are synthesized *in situ* within the polycarbonate strips using a high-pressure processing technique that diffuses an organometallic precursor into the hosting material[11] via a supercritical carbon dioxide ($scCO_2$) solvent, as reported in detail in Ref. 8. Transmission electron microscopy (TEM) and energy dispersive characterization of the silver impregnated polymer substrates confirmed the presence of a homogeneous band of metallic silver nanoparticles located along the edge of the polycarbonate strips with a size distribution of ~2–10 nm in diameter (see supplementary information in Ref. 8). To illustrate the uniformity of the nanoparticle films, Fig. 1(a) shows a TEM micrograph of the cross section of a silver-polycarbonate substrate (~100 nm thick) where we can see a precisely defined film thickness of ~6.5 μm. The inset shows a closeup of the silver particles on the outside edge of the polycarbonate. As MEF is a highly localized effect, acting over nanometer length scales, only the particles situated in close proximity to the surface will contribute to the fluorescence enhancement of molecules deposited on the substrates. The measured UV-visible extinction spectrum of the silver-polycarbonate substrate (solid line) is shown in Fig. 1(b), together with a digital photograph

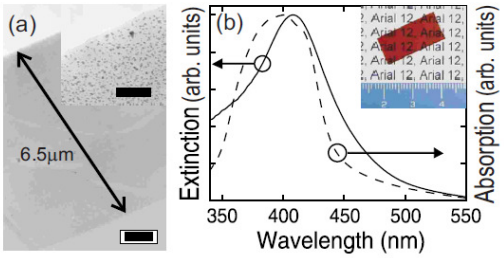

FIG. 1. (Color online) (a) TEM image of AgPC substrate (scale bar: 1 μm). Inset: closeup of surface nanoparticles (scale bar: 200 nm). (b) Normalized extinction of AgPC (solid) and absorption of coumarin on PC (dashed). Inset: photograph of AgPC substrate.

a)Electronic mail: acp@orc.soton.ac.uk.

of the substrate to highlight the transparency and the homogeneity of the silver films. The plasmonic peak is centered around 408 nm and is relatively broad due to the nanoparticle size dispersion. The position of the peak is in excellent agreement with the predictions of Mie scattering theory[12] for particles with diameters <10 nm embedded in a dielectric host with a refractive index of the pure polycarbonate $n=1.585$ (mean peak position ~411 nm), providing further confirmation of the TEM size estimates.

To test the metal-polymer composites for MEF we prepared the silver-modified (AgPC) and pure polycarbonate (PC) substrates by spin coating a weak 0.5 mM solution of coumarin 102 (2,3,5,6−1*H*,4*H*-tetrahydro-8-methylquinolazin-[9,9a,1-gh]), purchased from Radiant Dyes Laser & Accessories GmbH, in ethanol at 3000 rpm for 1 min. The deposition conditions were monitored in order to reproduce the same solution film thickness for both samples. For comparison, the normalized absorption spectrum of coumarin on the PC substrate is plotted with the AgPC extinction spectrum in Fig. 1(b) (dashed line), showing a strong spectral overlap so that we expect an efficient coupling between the plasmon modes excited on the metal nanoparticles and fluorescing dye molecules.

Confirmation of MEF can be provided through an observed reduction in the photon lifetime using simultaneous time and spectral resolved measurements. To investigate this, the samples were excited with a frequency-doubled mode-locked Ti:sapphire laser (400 nm excitation wavelength, ~120 fs pulse width, 80 MHz repetition rate with an average power of 1.5 mW, and a spot size of 30 μm), resonant with the plasmonic peak of the AgPC substrate. The emitted fluorescence from the dye molecules was collected in reflection, coupled into a multimode fiber, and analyzed by a synchroscan streak camera (Hamamatsu C5680) with a time resolution of 25 ps coupled to the exit of a 25 cm monochromator with a 300 gr/mm grating.

Preliminary photon lifetime measurements were performed on both high (~0.04M saturated solution) and low (1000 times diluted) concentration solutions of coumarin in ethanol. In both cases the photon lifetime decay curves could be fitted with a single exponential decay, with photon lifetimes equal to $\tau_H=364\pm3$ and $\tau_L=452\pm3$ ps, respectively. The faster decay of the high concentration solution is expected as in saturated solutions the intermolecular interactions introduce deactivation channels. In addition, when the dye molecules aggregate then a further reduction in lifetime will occur due to the formation of *J*-band excitons, as observed in thin (even down to monolayer coverage) film depositions,[13] so that we anticipate the dye molecules to exhibit an even shorter lifetime once deposited on the substrates.

Time-spectral resolved PL measurements were then performed on both the (a) PC and (b) AgPC substrates with the resulting profiles shown in Fig. 2. From these we can obtain both the time integrated PL spectra (c) and the averaged PL decay curves (d) for the wavelength range of 438–468 nm where the emission was greatest. Comparing the PL spectra we observe that while both profiles have the same shape, the emission intensity is ~8.5 times higher for coumarin when deposited on the AgPC substrate, an enhancement of similar magnitude to those reported elsewhere in literature.[10] Furthermore, from the decay curves it is clear that this enhanced

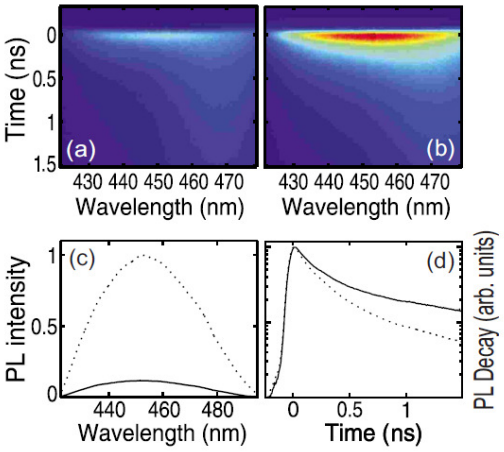

FIG. 2. (Color online) Time and spectrally resolved PL for coumarin on (a) PC and (b) AgPC substrates. (c) Integrated PL spectra and (d) average PL decays on PC (solid) and AgPC (dotted).

fluorescence is accompanied by a reduction in the photon lifetime.

With the PL decay profiles plotted on a logarithmic scale, it is clear that the coumarin films on both the AgPC and PC substrates are now characterized by a biexponential behavior. From our previous observations, we attribute this behavior to the coexistence of aggregates, as the fast species, and monomers, as the slow species, in the films. Fitting these curves with double exponentials to obtain both the fast (τ_1) and slow (τ_2) components we obtained $\tau_1=172\pm2$ and $\tau_2=1627\pm37$ ps for the PC substrate and the modified lifetimes of $\tau_1^*=154\pm3$ and $\tau_2^*=889\pm26$ ps for the AgPC substrate. While in both cases there is an observed reduction in lifetime, it is clear that the lifetime of the monomers is more greatly affected by the presence of the Ag. Calculating the Purcell enhancement factors[14] F for the two species yields $F_1=\tau_1/\tau_1^*=1.12\pm0.03$ and $F_2=\tau_2/\tau_2^*=1.83\pm0.10$. This difference in the enhancement factors can be attributed to a delocalization of the excitonic dipole in the aggregates,[15] so that the overlap with the plasmon enhanced field is reduced for the aggregates compared with the monomers. The small Purcell factors compared to the large (~8.5 times) PL enhancement suggest that the increased fluorescence is not only due to a modification of the radiative channels, but that additional factors, such as an increase in the absorption cross section,[16] also need to be considered.

Further to this, we have also investigated the emission rates, where $k=1/\tau$, and Purcell factors as functions of wavelength. Figure 3 shows both the (a) fast and (b) slow components of the photon emission rate for the two substrates, as calculated from the time-spectral profiles in Figs. 2(a) and 2(b) for selected wavelengths over the emission peak. The corresponding Purcell factor $F(\lambda)=k^*(\lambda)/k(\lambda)$ is then plotted in Fig. 3(c), where we see that the fast and slow components show a different response to the surface plasmon excitation as a function of wavelength. In particular, the rate enhancement $F_2(\lambda)$ of the slow component, associated with the dye monomers, exhibits an oscillatory behavior, which is similar to the results previously reported by Okamoto *et al.*[17] How-

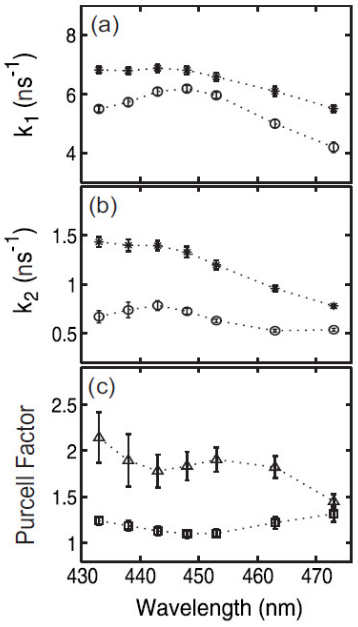

FIG. 3. (a) Fast and (b) slow components of the photon emission rate for coumarin on PC (circle) and AgPC (star) as functions of wavelength; data points averaged over ±5 nm. (c) Purcell factor for the fast (square) and slow (triangle) components.

ever, the fast component $F_1(\lambda)$ appears to only exhibit a minimum around the emission peak at 450 nm, though this could also be due to an oscillatory behavior on a different wavelength scale.

In summary, we report the use of silver impregnated polymer substrates as enhanced fluorescence probes. These composite films combine the excellent plasmonic properties of silver nanoparticles to yield large electric fields in the vicinity of the fluorophore, with the convenience of a robust, biocompatible polymer host matrix. MEF of coumarin 102 on the silver-polycarbonate substrates was demonstrated using simultaneous time and spectrally resolved PL. Owing to the versatility of this supercritical technique and its potential to be employed with a range of host polymer matrices and metal precursors, these substrates can be readily tailored for a wide range of applications in medicine and biology.

This work was supported by EPSRC-GB (Grant No. EP/F013876/1), the University of Southampton Annual Adventure in Research Grant No. A2005/18, and A.C.P. holds a Royal Academy of Engineering fellowship.

[1]L. M. Smith, J. Z. Sanders, R. J. Kaiser, P. Hughes, C. Dodd, C. R. Connell, C. Heiner, S. B. H. Kent, and L. E. Hood, Nature (London) **321**, 674 (1986).
[2]D. J. Stephens and V. J. Allan, Science **300**, 82 (2003).
[3]P. K. Jain, X. Huang, I. H. El-Sayed, and M. A. El-Sayad, Plasmonics **2**, 107 (2007).
[4]J. R. Lakowicz, J. Malicka, I. Gryczynski, Z. Gryczynski, and C. D. Geddes, J. Phys. D **36**, R240 (2003).
[5]J. S. Biteen, D. Pacifici, N. S. Lewis, and H. A. Atwater, Nano Lett. **5**, 1768 (2005).
[6]J. R. Lakowicz, Anal. Biochem. **337**, 171 (2005).
[7]D. S. dos Santos Jr. and R. F. Aroca, Analyst (Cambridge, U.K.) **132**, 450 (2007).
[8]T. Hasell, L. Lagonigro, A. C. Peacock, S. Yoda, P. D. Brown, P. J. A. Sazio, and S. M. Howdle, Adv. Funct. Mater. **18**, 1265 (2008).
[9]K. Aslan, P. Holley, and C. D. Geddes, J. Mater. Chem. **16**, 2846 (2006).
[10]K. Aslan, Z. Leonenko, J. R. Lakowicz, and C. D. Geddes, J. Fluoresc. **15**, 643 (2005).
[11]T. Hasell, K. J. Thurecht, R. D. W. Jones, P. D. Brown, and S. M. Howdle, Chem. Commun. (Cambridge) **2007**, 3933.
[12]C. F. Bohren, *Absorption and Scattering of Light by Small Particles* (Wiley, Weinheim, Germany, 1940).
[13]K. Ray, A. K. Dutta, and T. N. Misra, J. Lumin. **71**, 123 (1997).
[14]M. Boroditsky, R. Vrijen, T. F. Krauss, R. Coccioli, R. Bhat, and E. Yablonovitch, J. Lightwave Technol. **17**, 2096 (1999).
[15]P. G. Lagoudakis, M. M. de Souza, F. Schindler, J. M. Lupton, J. Feldmann, J. Wenus, and D. G. Lidzey, Phys. Rev. Lett. **93**, 257401 (2004).
[16]J. S. Biteen, D. Pacifici, N. S. Lewis, and H. A. Atwater, Nano Lett. **5**, 2116 (2005); F. Tam, G. P. Goodrich, B. R. Johnson, and N. J. Halas, *ibid.* **7**, 496 (2007).
[17]K. Okamoto, I. Niki, A. Scherer, Y. Narukawa, T. Mukai, and Y. Kawakami, Appl. Phys. Lett. **87**, 071102 (2005).

ADVANCED FUNCTIONAL MATERIALS

FULL PAPER

DOI: 10.1002/adfm.200701429

Silver Nanoparticle Impregnated Polycarbonate Substrates for Surface Enhanced Raman Spectroscopy**

By *T. Hasell, L. Lagonigro, A. C. Peacock,* S. Yoda, P. D. Brown, P. J. A. Sazio,* and *S. M. Howdle**

The embedding of nanoscopic metal structures into polymeric matrices represents a convenient way to stabilise a controlled dispersion of protected nanoparticles whilst taking advantage of their physical characteristics. Supercritical carbon dioxide ($scCO_2$) has been used to produce silver nanoparticles in optically transparent polycarbonate (PC) matrices allowing fine scale dispersions of particles to be produced within a prefabricated polymer component. Characterization of these nanocomposites has been performed using transmission electron microscopy (TEM) and UV-vis spectroscopy. The substrates give excellent responses in surface-enhanced Raman spectroscopy (SERS) for both 4-aminothiophenol and rhodamine 6G target molecules. They offer significant benefits over more conventional SERS substrates in that they are cheap, flexible, mechanically robust and temporally stable. Post-processing the films via simple etching techniques, provides an additional degree of design control and the potential to fabricate devices with unique excitation and detection geometries for a wide range of applications.

1. Introduction

Novel substrates based on noble metal nanoparticles are currently the subject of extensive research in areas such as biological sensing,[1] medicine,[2] optical microscopy[3] and nano-photonics[4] due to the large electromagnetic fields generated in the vicinity of the metal surface when excited near the plasmon frequency. Under these conditions, the conduction electrons of the nanoparticles oscillate in phase leading to a build up of polarization charges on the metal surface to generate a localized surface plasmon mode. The high localization of the electromagnetic energy in the vicinity of the surface renders plasmons as excellent probes of the surrounding environment and allows for the enhancement of weak nonlinear interactions of light. In particular, metallic nanostructures are often used to mediate surface enhanced Raman scattering (SERS) effects where the electromagnetic fields associated with the plasmon modes are used to increase the extremely small Raman cross-sections resulting in strongly enhanced vibrational signals from the target molecules.[5] With enhancement factors of the order of 10^{14} possible, this makes SERS an extremely sensitive spectroscopic technique for applications down to single molecule detection.[6]

SERS spectroscopy is a valuable tool for chemical structure analysis as it provides a molecular finger print of the molecules under investigation via the vibrational modes. However, if SERS is to be used readily in routine procedures, the substrates need to be cheap, robust, reproducible and stable so that they can be stored for long lengths of time between measurements. Recently there have been tremendous developments in the surface sciences and nano-processing techniques that have permitted the fabrication of substrates that can provide high SERS signals reproducibly over the active region. For example, using conventional semiconductor processing technologies, SERS templates have been produced via electron beam lithography,[7] focused ion beam patterning,[8] thermal evaporation[9] and chemical colloid reactions.[10] Unfortunately, the processing techniques used are often costly and time consuming, or on a prohibitively small scale, and the substrates are often fragile and suffer from poor temporal stability.

In this paper we present a new class of SERS substrates fabricated via a supercritical technique where metal nanoparticles are embedded into polymer substrates. These metal-polymer composites allow for the construction of optical-plasmonic devices that could exploit the mechanical robustness and flexibility of the polymers whilst providing protection of the particles from the surrounding environment to yield a high degree of temporal stability. Silver nanoparticles

[*] Dr. A. C. Peacock, Dr. P. J. A. Sazio, L. Lagonigro
Optoelectronics Research Centre
University of Southampton
Southampton, SO17 1BJ (UK)
E-mail: apc@orc.soton.ac.uk

Prof. S. M. Howdle, T. Hasell
School of Chemistry
University of Nottingham
Nottingham, NG7 2RD (UK)
E-mail: steve.howdle@nottingham.ac.uk

Prof. P. D. Brown
School of Mechanical, Materials and Manufacturing Engineering
University of Nottingham
Nottingham, NG7 2RD (UK)

Dr. S. Yoda
Nanotechnology Research Institute,
National Institute of Advanced Industrial Science and Technology,
1-1-1 Higashi, Tsukuba, Ibaraki, 305-8565 (Japan)

[**] T. Hasell and L. Lagonigro contributed equally to this work. A. C. Peacock holds a Royal Society of Engineering fellowship and S. M. Howdle holds a Royal Society Wolfson Research Merit Award. We acknowledge the technical help of P. Fields and R. Wilson. Supporting Information is available online from Wiley InterScience or from the author.

ADVANCED FUNCTIONAL MATERIALS

are known to have superior plasmonic properties[11] but are predisposed to oxidation leading to problems with long term storage. Although there has been some progress in developing methods to coat silver SERS substrates to improve their temporal stability, this often requires complicated multiple processing with the resulting SERS response being highly sensitive to the affinity of the target molecule to the coating material and the layer thickness.[12]

Polymer matrices offer a number of advantages as host materials as they are cheap, stable, bio-compatible and can easily be processed. The polymer matrix not only forms the structure of the device, but also protects the nanoparticles and prevents agglomeration. Furthermore, as the plasmon resonance wavelength depends on the particle size, local dielectric environment and interparticle spacing,[13] these substrates can be engineered to target specific requirements, simply by changing the impregnation conditions and/or using different polymers. The nanocomposite material described herein has applications not only for SERS, but also for non-linear optical limitation,[14] plasmon waveguides,[15] and metal enhanced fluorescence.[16] Silver is an advantageous choice of metal for the nanoparticles as it has a plasmon resonance in the visible wavelength range which has been found to be the most efficient mechanism by which light interacts with matter.[17]

Supercritical carbon dioxide ($scCO_2$) processing provides a simple route to produce the metal nanoparticles *in situ* within prefabricated polymeric materials.[18] This is preferable to mixing pre-formed nanoparticles into a polymer as it does not require surface modification of the nanoparticles and avoids the possibility of aggregation during processing. Importantly, the polymeric materials can be impregnated with nanoparticles after they have been processed into their final form. Our process utilises $scCO_2$ as a solvent for an organometallic precursor molecule which provides rapid diffusion into the polymer. The precursor can then be reduced to form elemental silver nanoparticles. The precursor chosen for this work, (1,5-cyclooctadiene)(1,1,1,5,5,5-hexafluoroacetylacetonate)silver(I) – Ag(hfac)COD, has been previously shown to be effective in the production of silver nanoparticles in polyimide by $scCO_2$ impregnation.[19] Briefly, polycarbonate strips are placed inside an autoclave, which is then filled with CO_2 at pressure and temperature above the critical point of CO_2. Under these conditions, the precursor silver complex dissolves and as the $scCO_2$ penetrates and swells the polycarbonate, it is infused into the structure. The CO_2 is then removed by carefully releasing the pressure, leaving the silver complex trapped in the polycarbonate. In a second step, the autoclave is filled with hydrogen and heated to facilitate the reduction of the silver complex to elemental silver in the form of metallic nanoparticles trapped inside the polymer substrate. The silver nanoparticles are stabilized against aggregation by the physical constraint of the polymer substrate. Polycarbonate was chosen as an ideal model polymer for this process because of its excellent optical and mechanical properties and bio-compatibility.[16]

2. Results and Discussion

2.1. Nanocomposite Formation and Structural Characterization

A series of impregnations were performed between 1 and 24 hours under a $scCO_2$ pressure of 10.3 MPa, and at a temperature of 40 °C. The polycarbonate strip products appear brown in color, but are transparent and homogeneous. TEM imaging was performed on cross sections of each of the products to allow the size and distribution of nanoparticles to be observed. Characterization of a sample produced with an impregnation time of 24 hours at a pressure of 10.3 MPa (Fig. 1(a)) reveals a uniform band of nanoparticles located along the outermost edge of the cross section with a thickness of ~6.5 μm. The silver particles are ~2–10 nm in diameter, roughly spherical, and of relatively uniform size and distribution on a local scale. TEM images of the near surface region

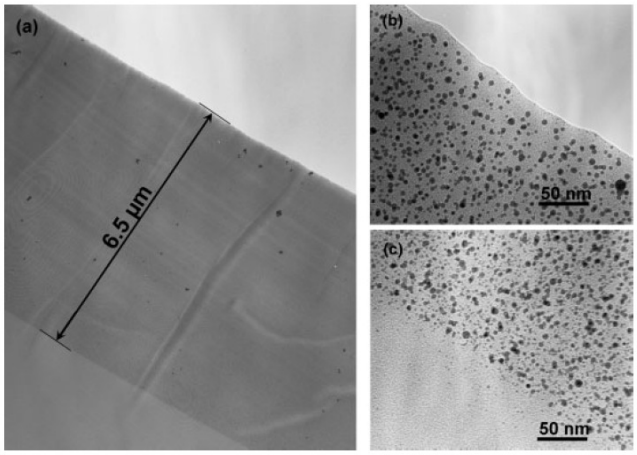

Figure 1. Bright field TEM micrographs of sample A (produced at 10.3 Mpa impregnation pressure). (a) The surface located band of silver nanoparticles in a cross section of the polycarbonate substrate. (b) A magnified section showing nanoparticles at the outside edge of the polymer. (c) A magnified section showing nanoparticles at the limit of furtheset impregnation of the nanoparticles.

ADVANCED FUNCTIONAL MATERIALS

were analysed to determine the nanoparticle size distribution (see supporting information for histogram). This showed a unimodal distribution with an average size of 4.1 nm. The nanoparticles are present up to the outer surface of the polymer, (Fig. 1(b)) but at the limit of furthest infusion a very definite boundary is evident, after which the nanoparticles cease abruptly (Fig. 1(c)). This depth limited incorporation of nanoparticles suggests a time dependent infusion of the organometallic precursor into the polymer during the impregnation step. In fact, the rate of diffusion of the organometallic complex into the polycarbonate is relatively slow, allowing a degree of control to be obtained in terms of the thickness of the nanoparticle band produced. The depth dependent impregnation process is reproducible (±10% depth) over a number of reactions and is also time dependent, providing another element of control (Fig. 2(a)). Selected area electron diffraction patterns taken from regions containing the nanoparticles show them to be metallic silver (Fig. 2(b)). Energy dispersive x-ray analysis (EDX) spectra taken within the nanoparticle band, and beyond, confirm the presence and absence of silver, respectively (Fig. 2(c) and 2(d)). The peak observed for silicon is likely to be caused by silicon containing oils removed from the sealing O-ring of the autoclave and impregnated into the polycarbonate by the action of the $scCO_2$.

The effect of impregnation pressure can be seen by comparing sample A (10.3 MPa) with a second sample B produced at a lower pressure (9.0 MPa). TEM micrographs of the cross-sections of the two samples (Fig. 1 and Fig. 3) show that in both cases there is a locally uniform distribution of embedded nanoparticles but, substrate A has a defined film thickness of ~6.5 μm whilst the particles in substrate B penetrate much deeper, with no definite boundary of furthest infusion being observed. At the lower pressure it is well known that $scCO_2$ is less dense and has a lower solvating power for the silver complex. At the higher pressure the solubility of the precursor is 5×10^{-3} mol mol^{-1} and at the lower pressure it is 4×10^{-4} mol mol^{-1}, in terms of moles of complex per mole of CO_2 (see supporting information for solubility measurements). The relative proportion of silver complex that infuses into the polymer during the impregnation step depends on the ratio of the solubility in the $scCO_2$ compared to the solubility in the polymer. Therefore the partitioning of the silver complex into the polycarbonate at the lower pressure is likely to be favoured leading to deeper impregnation of nanoparticles compared to the high pressure impregnation. However, at lower pressure and $scCO_2$ density the system may be less homogeneous and this could also contribute to the loss of the definite nanoparticle limit.

The reflection spectra of the two samples taken using a UV-VIS spectrometer are plotted (Fig. 4(a)) together with a digital photograph of Sample A to highlight the transparency and the homogeneity of the silver films. The positions of the main absorption dips are close to the predicted extinction peak of ~410 nm for a distribution of particles with diameters <10 nm in a dielectric host with a refractive index of the pure polycarbonate (n = 1.585), as calculated using Mie scattering theory.[20] We attribute the observed blue shift in the dip minima (from the ideal 410 nm) to a contribution from the metal particles at the surface, which are partially exposed to air, and the slight difference between the two substrates to a small increase in the observed particle sizes in substrate B. The appearance of a second absorption dip in substrate A at ~510 nm is likely to arise due to contributions from interactions between neighbouring particles, which is known to shift the plasmon resonance out to longer wavelengths,[21] indicating an increased silver density in substrate A. To investigate this, the refractive index of the nanoparticle composites were measured using a prism coupling technique.[22] In this technique a 633nm He-Ne source is

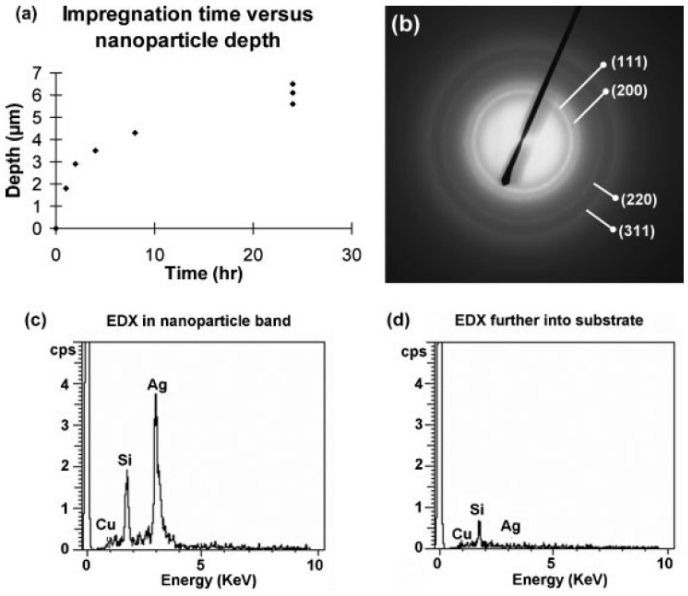

Figure 2. (a) Graph of the nanoparticle infusion depths found for a series of reactions at different impregnation times. (b) Selected area electron diffraction from the nanoparticle region. The spacing between the bands identifies the nanoparticles as metallic silver. (c) EDX spectrum taken inside the nanoparticle region. (d) EDX spectrum further into the polymer, past the limit of impregnation.

ADVANCED FUNCTIONAL MATERIALS

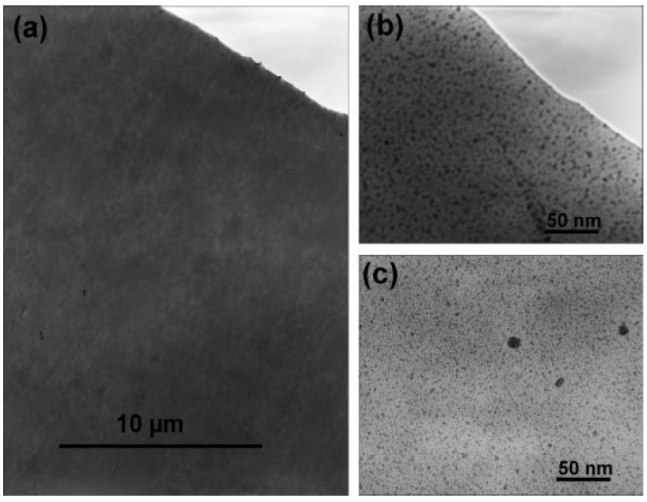

Figure 3. Bright field TEM micrographs of sample B (produced at 9.0 MPa impregnation pressure). (a) A cross section of the near surface region of the polycarbonate. Note the absence of a clearly defined limit of impregnation. (b) A magnified section showing nanoparticles at the outside edge of the polymer. (c) A magnified section showing nanoparticles deeper into the polymer substrate.

launched onto the surface of our substrate, through a GGG prism ($n = 1.965$), at varying angles of incidence and the reflected light is collected with a photodetector. Fig. 4(b) plots the collected transverse electric (TE) polarised spectra for both substrates A and B (solid curves) as functions of the effective refractive index, related to the incident angle θ_0 via: $n_{eff} = n_{prism}\sin\theta_0$. The refractive index of the composite film is found from the angle at which the reflection intensity starts to drop off and corresponds to the point where the light starts to couple into the thin film, with the decreasing intensity being due to the absorption of the silver nanoparticles. The oscillations in substrate A are due to interference effects in the multilayer film, thus providing information about the film thickness, and their absence in substrate B is due to the lack of definite silver film thickness, where we attribute the single absorption dip to scattering losses. To obtain the most accurate values for the film parameters the curves were fitted using a multilayer reflection calculation for both the TE and TM (transverse magnetic curves not shown) polarisation spectra (dashed curves). From this we obtained the refractive indices of: $n = 1.611 \pm 0.003$ for substrate A and $n = 1.602 \pm 0.005$ for substrate B, and a film thickness of ~7 μm for substrate A, in good agreement with the TEM measurement. The higher average index obtained for substrate A over that of substrate B confirms the higher particle density in A compared with B and further evidence to this is provided via close examination of the TEM images in Fig. 1 and Fig. 3.

2.2. Surface Enhanced Raman Characterization

To test the metal-polymer substrates for SERS activity we first considered 4–aminothiophenol (4–ATP) as a target molecule because it has very distinct Raman features and it is known to form an ordered self-assembled monolayer on coinage-metal surfaces. All measurements were conducted using a conventional Renishaw Raman spectrometer with a 633 nm He-Ne excitation source launched via a 50× microscope objective to produce a spot size of ~2 μm in diameter with ~3 mW of optical power. The samples were treated by drop casting a 0.5 mM solution of 4–ATP in ethanol and allowing the solvent to evaporate. Significantly, polycarbonate is only moderately resistant to ethanol so that we expect the solution to slightly permeate the substrates and thus access more of the silver nanoparticles. The measured SERS spectra for the two substrates are shown in Fig. 5(a) together with a control spectrum taken on an undoped (silver-free) polycarbonate sample treated with 4–ATP in the same manner. The peaks in the control sample simply correspond to the Raman spectrum of the polycarbonate whilst those of the silver nanoparticle loaded sample clearly show strong features of the main vibrational modes of the target molecule, as assigned in the reported literature.[23] Near-monolayer detection of 4-ATP on the silver nanoparticles is suggested by a shift in the vibrational spectra compared to the bulk response of ATP. Furthermore, the absence of vibrational peaks that are typically only seen in the bulk also suggests that only a very thin layer of analyte is present. Comparing the SERS signals from the two metal composites, the stronger SERS signal obtained from substrate A is as we would expect from the higher nanoparticle density and also in part to the presence of the second plasmon resonance at ~510 nm, which is closer to the laser excitation wavelength. Since the SERS active metal nanoparticles are partially embedded in the substrate, calculation of a precise enhancement factor is difficult. However, from the TEM micrograph of substrate A we have estimated an upper bound on the exposed silver to be 30% of the surface area. Thus, comparing the SERS response to that of a bulk 4–ATP Raman signal, and assuming a monolayer coverage with a packing density of 8×10^{14} molecules/cm^2,[24] the resulting enhancement factor is estimated to be of order greater than 10^7,[25] which compares favourably to enhancements reported elsewhere in the literature.

Motivated by the potential biocompatibility offered by our plasmonically active polycarbonate substrates, with inherent

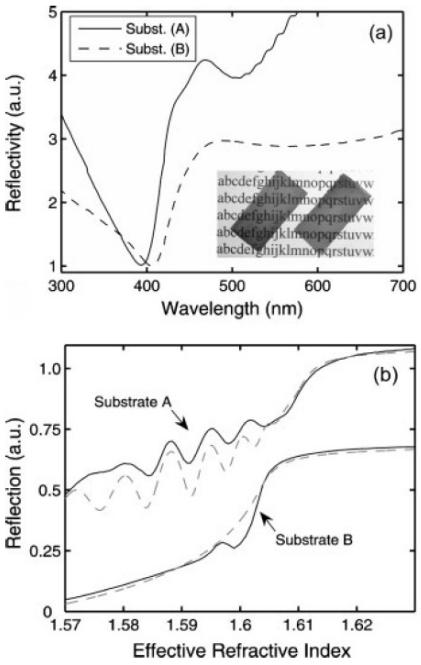

Figure 4. (a) Reflectivity spectra of the two polycarbonate substrates. Inset shows a photograph of substrate A on 12 point font. (b) TE reflection spectra for varying incident angles, plotted as a function of the effective refractive index, obtained from the prism coupling measurements (solid curves) together with the calculations for a multilayer film (dashed curves).

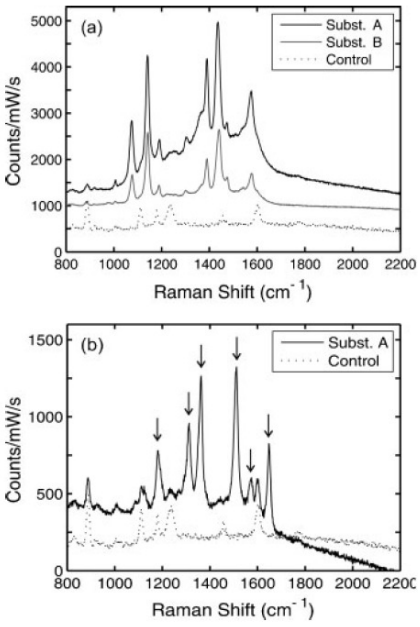

Figure 5. (a) SERS spectra of 4–ATP on the two metal-polycarbonate substrates (A and B) and (b) SERS spectrum of R6G taken on substrate A, where the arrows indicate the vibrational peaks of the dye. Both figures are plotted together with a control spectrum taken on undoped polycarbonate and the spectra are offset for clarity.

advantages for the detection of biological pathogens in their native aqueous environment by exploiting SERS as a whole-organism fingerprinting technique,[26,27] the SERS activity of substrate A has also been investigated using a water soluble target molecule, Rhodamine 6G (R6G). This is a useful biological analogue as the dye is dissolved in an aqueous solution that does not permeate the polycarbonate. The SERS spectrum of a 2 mM R6G solution drop cast on substrate A is shown in Fig. 5(b). In this figure six vibrational bands of R6G can be clearly identified, as indicated by the arrows,[28] with the remaining peaks being the underlying polycarbonate modes. The much weaker SERS signal obtained using this dye can be attributed to weaker bonding of the R6G molecules to the Ag metal, the more passive nature of the water solvent so that only the pre-exposed particles contribute to the response, as well as the larger size of the R6G molecules and their tendency to attach to surfaces in a random orientation.[29]

As previously mentioned, if these samples are to find wide use in routine SERS analysis then temporal stability of the substrates is of vital importance. The fact that the metal nanoparticles are embedded in the polycarbonate means that the substrates have an extremely long shelf life and to date we have successfully measured SERS responses from substrates stored in air which are over a year old. However, what is more surprising is the temporal stability of the substrates after use. Indeed, we have demonstrated that our samples still yield comparable SERS measurements up to one month after treatment with a 4–ATP solution. Such long lifetimes are likely to be a result of the small percentage of silver that is exposed to the atmosphere and thus we expect that in this instance the bulk of the response is coming from Raman probe molecules which have penetrated down to attach to the more deeply embedded particles. This ability to check measurements over time scales of weeks is a significant advantage.

2.3. Plasma Etching of Nanoparticle Films

The ability to post-process the metal-polymer films is of considerable interest not only as it allows access to deeper areas of the deposition, where the particle distribution may

ADVANCED FUNCTIONAL MATERIALS

differ, but also as a means to introduce an additional level of structural design to the substrates and, for example, to fabricate optical waveguides. SERS substrates that incorporate waveguiding geometries into the devices are advantageous as the enhanced propagation lengths average over many plasmon-analyte interactions thus offering increased sensitivity and reproducibility of the measured response. To etch the metal impregnated films we use an oxygen plasma etching technique as typically employed for the processing of pure polycarbonate substrates.[30] As a simple mask, we placed a coverslip over half of the substrate before loading it in an Oxford Instruments Plasma Technology RIE80plus Reactive ion etcher. The chamber was then evacuated to 5×10^{-6} torr before 5 sccm of oxygen and 5 sccm of argon were flowed into the chamber under a controlled pressure of 50 mtorr. After 20 mins of etching the sample was removed and it was noted that the exposed half of the substrate was now darker and cloudier than the untreated side. Transparency of the etched side was improved on washing with ethanol to remove some of the roughness in the surface layer. The resulting substrate was then analyzed using a stylus profiler (KLA Tencor P16) which revealed an etched step of ~2 μm with a surface roughness of <50 nm (Fig. 6(a)).

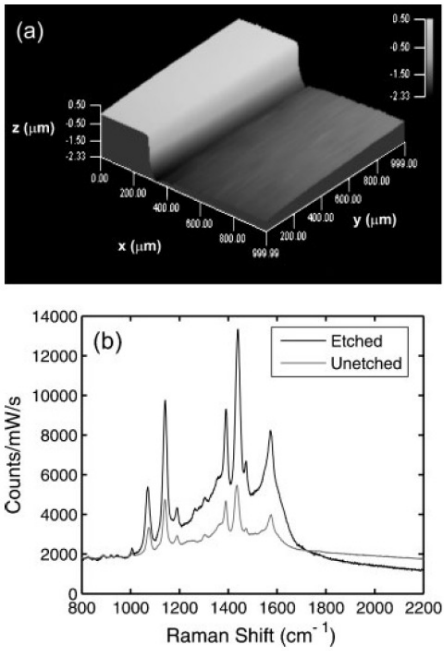

Figure 6. (a) 3D profile image of the etched metal-polycarbonate substrate. (b) SERS spectra of 4–ATP on both the etched and unetched regions of the substrate in (a).

To test the SERS activity of the etched region we repeated the earlier Raman measurements using 4–ATP as the target molecule. The sample used in the etching process was fabricated using the same parameters as substrate A above and showed a similar SERS response to that in Fig. 5(a). Fig. 6(b) shows the measured SERS spectra on both the etched and the unetched regions of the sample. Despite fears that the etch process may oxidize the metal nanoparticles, clearly this is not the case and in fact we obtain a signal which is >2× stronger than the unetched region. This additional enhancement can be attributed to an increase in the density of the nanoparticles going deeper into the film (as confirmed from the TEM micrographs) and importantly this also results in an improvement in the reproducibility of the SERS measurements across the etched region.

3. Conclusion

It has been shown that $scCO_2$ is a viable technique to produce uniform and transparent plasmonic nanocomposites. The impregnation process shows good potential for control of both depth and size/concentration of the nanoparticles by modification of time and pressure variables. The method presented here is ideally suited for the production of optical and photonic materials as it does not require surface modification of the nanoparticles and avoids aggregation of the nanoparticles in the polymer.

The silver impregnated polycarbonate films have been demonstrated as unique substrates for routine SERS analysis. These substrates offer a number of significant benefits over more conventional SERS substrates in that they are cheap, flexible, mechanically robust and temporally stable so that they can be stored for long lengths of time, easily handled and discarded after use to avoid cross contamination. Post-processing of the films via simple etching techniques has been demonstrated without compromising the SERS capabilities thus providing the opportunity to introduce additional structural features into the substrates such as optical waveguides. The robustness of the substrates and the bio-compatibility of the polycarbonate host opens up significant new possibilities for the next generation of plasmonic devices and sensors and in particular biological or *in vivo* monitoring.[31]

4. Experimental

Materials: The CO_2 (BOC, food grade) and H_2 (BOC, 99.995% minimum) gases were obtained in gas cylinders and used as received. The organometallic precursor Ag(hfac)COD (Aldrich, 99%) was used as received. Polycarbonate (Nigel Smith Alloys Ltd) was obtained as 0.5 mm thick sheets and processed in house to form 22×10 mm rectangles. Reactions were conducted in a custom built high pressure, clamp sealed autoclave of 60 ml volume which contains a directly coupled magnetically driven agitator [32]. The CO_2 was compressed using a PM-101 pump (New Ways of Analytics, Lörrach, Germany) and the temperature within the autoclave was regulated by means of an external heating jacket controlled to ±1 °C using a Cal 3200 digital

heating controller (RS, England). The reactor was modified to enable the polycarbonate strips to be attached vertically to the sides of the agitator bar to provide a symmetric and dynamic environment during the reaction.

Process: The reaction process used to prepare the nanocomposites consists of two steps: impregnation and decomposition. The temperature of the fluid was at all times monitored directly via an in situ thermocouple. During impregnation, the polymer host (~500 mg) and the precursor complex (200 mg) were placed in an autoclave which was then filled with ~5.5 MPa of CO_2. The autoclave was then heated to 40 °C and topped up to 9.0 MPa or 10.3 MPa. The $scCO_2$ was maintained under these conditions for a duration (normally 24 hours) in order to dissolve the precursor complex and infuse into the polymer. The $scCO_2$ was then vented evenly over 5 minutes, leaving the precursor dispersed within the polymer. During decomposition, the autoclave was pressurised to 7.0 MPa of hydrogen and heated to 80 °C in order to reduce the precursor complex to form silver nanoparticles and dissociated ligands. These conditions were maintained for 3 hours before venting the autoclave to atmospheric pressure over 5 minutes.

Characterization: Characterization of the composites was performed by reflectance UV-visible spectroscopy and transmission electron microscopy (TEM). UV-VIS was performed on the polycarbonate strips with no modification using a Jasco V570 UV/VIS/NIR spectrometer. For the TEM measurements, the samples were sectioned with a diamond knife to a thickness of ~100 nm (Reichet Ultra-microtome) and supported on 300 mesh copper grids. Conventional bright field images were acquired using a JEOL JEM-2000 FXII TEM operating at 200 kV under low dose conditions to minimize sample degradation under the imaging electron beam.

Received: December 06, 2007
Revised: February 04, 2008

[1] a) Y. Lu, G. L. Liu, L. P. Lee, *Nano Lett.* **2005**, *5*, 5–9. b) J. Homola, S. S. Yee, G. Gauglitz, *Sens. Actuators B* **1999**, *54*, 3.
[2] F. Furno, K. S. Morley, B. Wong, B. L. Sharp, P. L. Arnold, S. M. Howdle, R. Bayston, P. D. Brown, P. D. Winship, H. J. Reid, *J. Antimicrob. Chemother.* **2004**, *54*, 1019.
[3] J. M. Brockman, B. P. Nelson, R. M. Corn, *Annu. Rev. Phys. Chem.* **2000**, *51*, 41.
[4] E. Hutter, J. H. Fendler, *Adv. Mater.* **2004**, *16*, 1685.
[5] a) G. A. Baker, D. S. Moore, *Anal. Bioanal. Chem.* **2005**, *382*, 1751. b) R. Aroca, *Surface-Enhanced Vibrational Spectroscopy*, John Wiley & Sons, Chichester, UK **2006**.
[6] K. Kneipp, Y. Wang, H. Kneipp, L. T. Perelman, I. Itzkan, R. Dasari, M. S. Feld, *Phys. Rev. Lett.* **1997**, *78*, 1667.
[7] L. Gunnarsson, E. J. Bjerneld, H. Xu, S. Petronis, B. Kasemo, M. Kall, *Appl. Phys. Lett.* **2001**, *78*, 802.
[8] A. G. Brolo, E. Arctander, R. Gordon, B. Leathem, K. L. Kavanagh, *Nano Lett.* **2004**, *4*, 2015.
[9] T. Vo-Dinh, *Sensors Actuators B* **1995**, *29*, 183.
[10] E. J. Bjerneld, F. Svedberg, M. Kall, *Nano Lett.* **2003**, *3*, 593.
[11] P. B. Johnson, R. W. Christy, *Phys. Rev. B* **1972**, *6*, 4370.
[12] X. Zhang, J. Zhao, A. V. Whitney, J. W. Elam, R. P. Van Duyne, *J. Am. Chem. Soc.* **2006**, *128*, 10304.
[13] K. L. Kelly, E. Coronado, L. L. Zhao, G. C. Schatz, *J. Phys. Chem. B* **2003**, *107*, 668.
[14] a) Y. P. Sun, J. E. Riggs, H. W. Rollins, R. Guduru, *J. Phys. Chem. B* **1999**, *103*, 77. b) R. B. Martin, M. J. Meziani, P. Pathak, J. E. Riggs, D. E. Cook, S. Perera, Y. P. Sun, *Opt. Mater.* **2007**, *29*, 788. c) S. Porel, S. Singh, S. S. Harsha, D. N. Rao, T. P. Radhakrishnan, *Chem. Mater* **2005**, *17*, 9. d) S. Porel, N. Venkatrarn, D. N. Rao, T. P. Radhakrishnan, *J. Appl. Phys.* **2007**, *102*, 033107.
[15] N. K. Grady, N. J. Halas, P. Nordlander, *Chem. Phys. Lett.* **2004**, *399*(1–3), 167.
[16] K. Aslan, P. Holley, C. D. Geddes, *J. Mater. Chem.* **2006**, *16*(27), 2846.
[17] D. D. Evanoff, G. Chumanov, *Chemphyschem* **2005**, *6*(7), 1221.
[18] a) J. J. Watkins, T. J. McCarthy, *Chem. Mater.* **1995**, *7*, 1991. b) I. Kikic, F. Vecchione, *Curr. Opin. Solid State Mater. Sci.* **2003**, *7*, 399. c) K. S. Morley, P. Licence, P. C. Marr, J. R. Hyde, P. D. Brown, R. Mokaya, Y. D. Xia, S. M. Howdle, *J. Mater. Chem.* **2004**, *14*, 1212. d) K. S. Morley, P. C. Marr, P. B. Webb, A. R. Berry, F. J. Allison, G. Moldovan, P. D. Brown, S. M. Howdle, *J. Mater. Chem.* **2002**, *12*, 1898. e) S. Yoda, A. Hasegawa, H. Suda, Y. Uchimaru, K. Haraya, T. Tsuji, K. Otake, *Chem. Mater.* **2004**, *16*, 2363. f) S. Yoda, Y. Takebayashi, T. Sugeta, K. Otake, *J. Non-Cryst. Solids* **2004**, *350*, 320. g) Y. Zhang, C. Erkey, *J. Supercrit. Fluids* **2006**, *38*, 252.
[19] a) R. K. Boggess, L. T. Taylor, D. M. Stoakley, A. K. St. Clair, *J. Appl. Polym. Sci.* **1997**, *64*, 1309. b) J. Rosolovsky, R. K. Boggess, A. F. Rubira, L. T. Taylor, D. M. Stoakley, A. K. St. Clair, *J. Mater. Res* **1997**, *12*, 3127.
[20] C. F. Bohren, *Absorption and Scattering of Light by Small Particles*, VCH, Weinheim, Germany **1940**.
[21] E. Hao, G. C. Schatz, *J. Phys. Chem.* **2004**, *120*, 357.
[22] T. Sharda, T. Soga, T. Jimbo, *J. Appl. Phys.* **2003**, *93*, 101.
[23] M. Osawa, N. Matsuda, K. Yoshii, I. Uchida, *J. Phys. Chem.* **1994**, *98*, 12702.
[24] L. Sun, R. C. Thomas, R. M. Crooks, *J. Am. Chem. Soc.* **1991**, *113*, 8550.
[25] Z. Zhu, T. Zhu, Z. Liu, *Nanotechnology* **2004**, *15*, 357.
[26] R. M. Jarvis, R. Goodacre, *Anal. Chem.* **2004**, *76*, 40.
[27] F. Yan, M. B. Wabuyele, G. D. Griffin, A. A. Vass, T. Vo-Dinh, *IEEE Sensors Journal* **2005**, *5*, 665.
[28] H. Chen, Y. Wang, S. Dong, E. Wang, *Spectrochim. Acta A* **2006**, *64*, 343.
[29] H. Watanabe, N. Hayazawa, Y. Inouye, S. Kawata, *J. Chem. Phys. B* **2005**, *109*, 5012.
[30] J. W. Kang, J. S. Kim, J. J. Kim, *J. Appl. Phys.* **2001**, *41*, 3215.
[31] S. M. Moghimi, K. D. Pavey, A. C. Hunter, *FEBS Lett.* **2003**, *547*, 177.
[32] W. X. Wang, R. M. T. Griffiths, A. Naylor, M. R. Giles, D. J. Irvine, S. M. Howdle, *Polymer* **2002**, *43*, 6653.

Wavelength-dependent loss measurements in polysilicon modified optical fibres

L. Lagonigro[1], N.V. Healy[1], J.R. Sparks[2], N.F. Baril[2], P.J.A. Sazio[1], J.V. Badding[2], A.C. Peacock[1]
[1] *Optoelectronics Research Centre, University of Southampton, SO17 1BJ, UK*
[2] *Department of Material Science, Pennsylvania State University, 16802 PA, USA*

The recent advancements in on-chip silicon photonics has lead to the demonstration of a number of compact optoelectronic devices owing to the unique material properties of the semiconductor. Although to date most of the major advancements have been based on single-crystal silicon waveguides, lately there has been an increased interest in polycrystalline structures for integrated devices as the deposition process is easier, allowing for more design flexibility. As a photonics material, polysilicon offers good optical and electronic properties but it is typically associated with large losses due to scattering off grain boundaries and surface imperfections at the core-cladding interface.

Our silicon core optical fibres are fabricated by depositing silicon inside a silica capillary template using a high-pressure processing technique [1]. This process has several advantages: firstly, the potential to integrate the semiconductor chip and optical fibre technologies will greatly simplify device coupling and design. Secondly, using silica capillaries as templates (which have an internal surface roughness of <1nm) ensures an extremely smooth core-cladding interface, so that the waveguide losses are primarily due to the bulk material losses. Furthermore, this technique allows for easy control of the waveguide dimensions by simply choosing the appropriate silica capillary template, giving a further degree of design flexibility so that the mode confinement and dispersion properties can be tailored.

In this paper we present measurements of the optical losses of our silicon core fibres as a function of wavelength. Fig. 1(a) shows a silicon core fibre under brightfield microscope illumination. The lack of scatter and the smooth core-cladding boundaries indicate an absence of microscopic imperfections. The polycrystalline grain size has been estimated by TEM measurements, shown in Fig. 1(b), to be 0.5-1μm. To quantify the wavelength dependent losses of the silicon fibres we have preformed cut-back measurements by filtering the output of a supercontinuum source to yield an average launch power of ~0.5mW. Fig. 1(c) shows loss measurements for a 5.6μm silicon core fibre. From these we obtain a loss of ~8dB/cm at 1.55μm, comparable with the lowest losses reported in the literature, and the good agreement with a λ^{-4} fit indicates that the losses are primarily due to Rayleigh scattering. Comparing these measurements over the telecoms wavelength band with a silicon fibre with a reduced core size of 1.3μm, so that the waveguided modes have a larger interaction with the core-cladding interface, we have found that the losses are comparable as shown Fig. 1(d), confirming the negligible role of surface scatter. Using this technique, we have the potential to fabricate silicon core waveguides with dimensions down to hundreds of nm, where the losses are primarily limited by the materials quality.

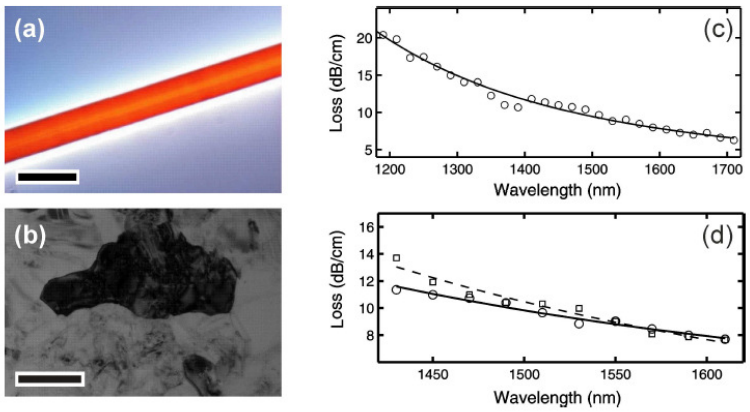

Fig. 1 a) Brightfield illumination of a silicon core fibre, scale bar 10μm. b) TEM showing polycrystalline grains, scale bar 0.4μm. (c) Optical losses for a 5.6 μm diameter silicon core together with a λ^{-4} fit. (d) Losses of 5.6μm (circles) and 1.3μm (squares) core silicon fibres over the telecoms wavelength band, together with λ^{-4} fits.

Reference

[1] P.J.A. Sazio, A. Amezcua-Correa, C.E. Finlayson, J.R. Hayes, T.J. Scheidemantel, N.F. Baril, B.R. Jackson, D.J. Won, F. Zhang, E.R. Margine, V. Gopalan, V.H. Crespi, J.V. Badding "Microstructured Optical Fibres as High-Pressure Microfluidic Reactors", Science **311**, 1583 (2006)

Silver nanoparticle impregnated polycarbonate substrates for plasmonic applications

L. Lagonigro,[1] T. Hasell,[2] S. Rohrmoser,[3] S. M. Howdle,[2] P.J.A. Sazio,[1] P.G. Lagoudakis,[3] A.C. Peacock[1]

[1] Optoelectronics Research Centre, University of Southampton, Southampton SO17 1BJ, UK
[2] School of Chemistry, University of Nottingham, NG7 2RD, UK
[3] School of Physics and Astronomy, University of Southampton, SO17 1BJ, UK
e-mail: acp@orc.soton.ac.uk

Abstract— **We present a new class of plasmonic substrates where silver nanoparticles are impregnated into a polycarbonate host. The substrates are shown to be exceptional candidates for SERS and metal enhanced fluorescence applications.**

I. Introduction

Novel substrates based on noble metal nanoparticles are currently the subject of extensive research in fields such as biological sensing, medicine, spectroscopy and nano-photonics due to the large electromagnetic fields generated in the vicinity of the metal surface via a surface plasmon resonance [1]. Here we report on a new class of plasmonic substrate where silver nanoparticles are impregnated into a polycarbonate host using a high-pressure processing technique. The substrates are shown to be exceptional candidates for SERS and metal enhanced fluorescence (MEF) applications offering a number of advantages over existing substrates in that they are cheap, can be easily processed, and are bio-compatible. Furthermore, the embedding of silver nanoparticles into polymer substrates offers substantial environmental protection, allowing for the construction of temporally stable devices that can exploit the mechanical flexibility of the polymers.

II. Substrate Characterization

Fabrication of the substrates is based on supercritical carbon dioxide processing to produce silver nanoparticles in situ within prefabricated optically transparent polycarbonate strips [2]. The substrates have been characterized by energy dispersive x-ray (EDX) analysis, transmission electron microscopy (TEM) and UV-vis absorption measurements. Fig. 1(a) shows the EDX spectrum which confirms the presence of metallic silver in the films. A TEM micrograph of a cross section of the silver-polycarbonate strip is shown in the inset revealing a nanoparticle band of uniform thickness ($\sim 6.5\,\mu$m) and composition along the length of the sample. A close up of the nanoparticles near the surface of the film is also provided as, owing to the highly localized electric field enhancements, it is these that are largely responsible for the plasmonic effects. From these images we estimate the size distribution of the nanoparticles to be $\sim 2-10$ nm. UV-vis absorption measurements of these substrates, plotted in Fig. 1(b), show a surface plasmon resonance around 410 nm, in agreement with calculations based on Mie scattering theory for particles

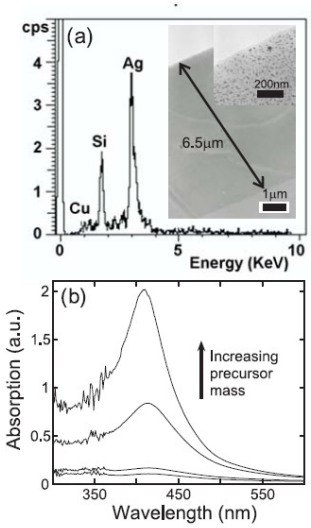

Fig. 1. (a) EDX spectrum of the nanoparticle band shown in the TEM micrograph of the AgPC substrate, plotted in the inset. Close up shows the surface particles. (b) UV-vis absorption spectra for various precursor concentrations.

with diameters < 10 nm embedded in a dielectric host with a refractive index of the pure polycarbonate. The intensity of the peak increases with the amount of precursor used, indicating an increase in the concentration of nanoparticles produced.

III. SERS Response

To investigate the SERS response of the metal-polymer composites, we drop cast 0.5 mM of 4-aminothiophenol (4-ATP) in ethanol onto the surfaces of both a silver impregnated (AgPC) and a pure (PC) polycarbonate substrate. The measured Raman spectra are plotted in Fig. 2(a) with the AgPC substrate (black line) clearly showing the main vibrational modes of 4-ATP, as assigned to those reported in the literature, whilst no Raman peaks were observed on the PC sample (grey line). SERS spectra collected a month after the 4-ATP deposition produced results of comparable intensity,

confirming the temporal stability of the substrates. Further to this, we have also demonstrated the ability to post-process the films via simple oxygen plasma etching techniques, thus providing an additional degree of substrate design control. The measured SERS spectra on both the etched and the unetched regions of the sample are plotted in Fig. 2(b) with the etched profile shown in the inset (step of $\sim 2\,\mu$m). We attribute the enhanced SERS response on the etched region to an increase in the density of the nanoparticles going deeper into the film.

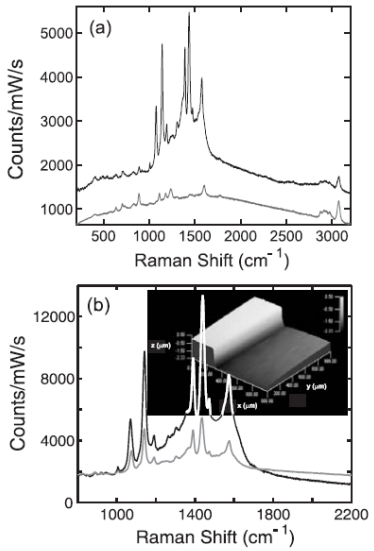

Fig. 2. (a) SERS spectra of 4-ATP deposited on AgPC (black line) and PC (grey line) substrates. (b) SERS spectra on the etched (black) and unetched (grey) regions of the substrate with a 3D profile image of the etched step shown in the inset.

IV. Observation of MEF

The metal-polymer composites were also tested for MEF using simultaneous time and spectral resolved measurements. We spin-coated a weak 0.5 mM solution of Coumarin 102 in ethanol again onto both an AgPC and a PC substrate. The time-spectral PL profiles obtained from the (a) PC and (b) AgPC substrates are plotted in Fig. 3, clearly showing an enhanced emission from the metal-polymer composite. From these we can obtain both the time integrated PL spectra (c) and the averaged PL decay curves (d), taken over the peak emission wavelength range $438 - 468$ nm. The enhanced fluorescence (~ 8.5x), accompanied by a reduction in the photon lifetime, confirms the observation of MEF which is known to be associated with a change in the radiative decay rate [3].

V. Conclusion

Silver nanoparticle impregnated polycarbonate films have been demonstrated as unique substrates for plasmonic applications including routine SERS analysis and enhanced

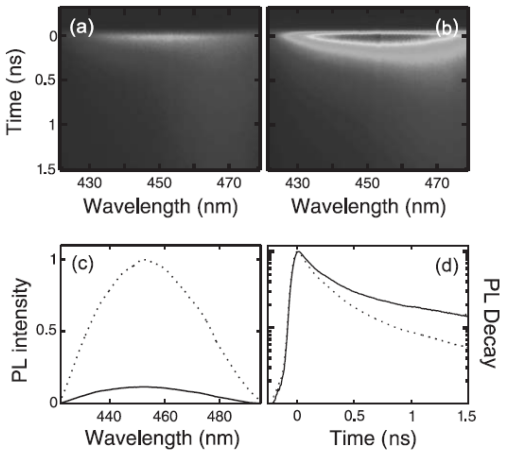

Fig. 3. (a) Time-spectral PL profiles for Coumarin on the (a) PC and (b) AgPC substrates. (c) Integrated PL spectra and (d) average PL decays for Coumarin on PC (solid line) and AgPC (dotted line) substrates.

fluorescence probes. Owing to the versatility of this high-pressure particle impregnation technique, and its potential to be employed with a range of host polymer matrices and metal precursors, these substrates can be readily tailored for a wide range of applications in medicine and biology.

VI. Acknowledgment

ACP acknowledges support from the Royal Academy of Engineering via a post-doctoral research fellowship.

References

[1] E. Hutter and J. H. Fendler, "Exploitation of Localized Surface Plasmon Resonance," Adv. Mater. **16,** 1685 (2004).
[2] T. Hasell, L. Lagonigro, A. C. Peacock, S. Yoda, P. D. Brown, P. J. A. Sazio, and S. M. Howdle, "Silver Nanoparticle Impregnated Polycarbonate Substrates for Surface Enhanced Raman Spectroscopy," Adv. Func. Mater. **18,** 1265 (2008).
[3] J. R. Lakowicz, Y. Shen, S. D'Auria, J. Malicka, J. Fang, Z. Gryczynski, and I. Gryczynski, "Radiative Decay Engineering: 2. Effects of Silver Island Films on Fluorescence Intensity, Lifetimes, and Resonance Energy Transfer," Anal. Biochem. **301,** 261 (2002).

Surface-Enhanced Raman Spectroscopy using silver impregnated polycarbonate substrates

L. Lagonigro, A. C. Peacock, P. J. A. Sazio
Optoelectronics Research Centre, University of Southampton, SO17 1BJ, UK

T. Hasell, P. D. Brown and S. M. Howdle
School of Chemistry, University of Nottingham, NG7 2RD, UK

Novel substrates based on noble metal nanoparticles are currently the subject of extensive research in fields such as biological sensing, medicine, spectroscopy and nano-photonics due to the large electromagnetic fields generated in the vicinity of the metal surface via a surface plasmon resonance. The dependence of the resonance wavelength on the size, shape, local dielectric environment and interparticle spacing, enables engineering of the metal nanoparticle substrates to target specific requirements [1]. Here we report the fabrication of silver impregnated polycarbonate composites as substrates for surface enhanced Raman spectroscopy (SERS) where the plasmonic properties can be controlled via the reaction parameters. Although silver has superior plasmonic properties to other metals, it is often over looked for SERS substrates as it is highly prone to oxidation. The embedding of silver nanoparticles into polymer substrates offers substantial environmental protection, allowing for the construction of temporally stable plasmonic devices that can exploit the mechanical flexibility of the polymers and prevent particle agglomeration. These nanoparticle composites offer a number of advantages as SERS substrates as they are cheap, easily processed, and are bio-compatible.

Fabrication of the substrate is based on supercritical carbon dioxide processing to produce silver nanoparticles *in situ* within prefabricated optically transparent polycarbonate strips. The substrates have been characterised by TEM, UV-Vis absorption and Raman scattering measurements. Fig. 1(a) shows a TEM micrograph of a cross section of the silver-polycarbonate strip revealing a nanoparticle band of uniform thickness (~5.5μm) and composition along the length of the sample. The inset shows a close up of the SERS active nanoparticles near the surface of the film, where we can estimate the size of the nanoparticles to be ~15nm. UV-Vis absorption measurements plotted in Fig. 1(b) show a surface plasmon resonance around 410 nm, in agreement with calculations based on Mie scattering. The intensity of the peak increases with the amount of precursor used, indicating an increase in the concentration of nanoparticles produced.

To test the silver-polycarbonate substrates for SERS activity, we drop cast 0.5 mM of aminothiophenol in ethanol onto the silver surface. The Raman spectrum for a sample with a high concentration of nanoparticles at the surface is plotted in Fig. 1(c) (black line) clearly showing the main vibrational modes of aminothiophenol as assigned to those reported in the literature [2]. Additionally no Raman peaks of the target molecule were observed on a control undoped polycarbonate sample treated in the same manner (grey line). SERS spectra collected a month after the aminothiophenol deposition produced results of comparable intensity, confirming the temporal stability of the substrates. We will discuss alternative excitation geometries via waveguiding in the high index metal nanoparticle strip using simple lithographic processing techniques.

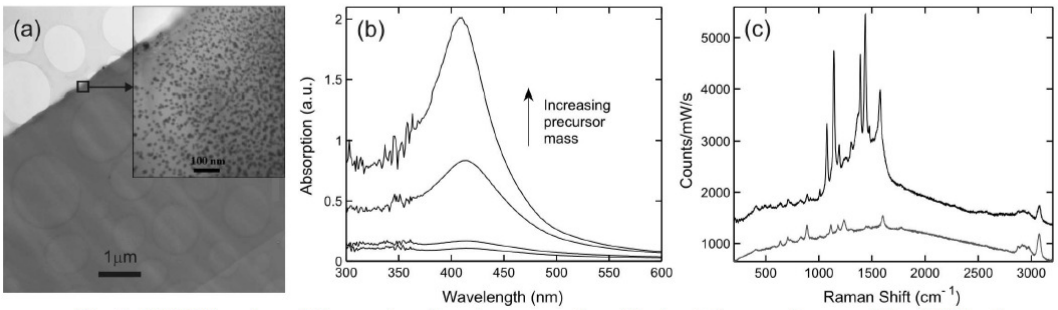

Fig. 1 a) TEM imaging of silver-polycarbonate cross-section. The inset shows a close up of the SERS active nanoparticles near the surface. b) UV-Vis spectra for various precursor concentrations. c) Raman spectra of aminothiophenol deposited on silver-polycarbonate strip (black line) and on undoped polycarbonate sample (grey line).

References

[1] E. Hutter and J. H. Fendler "Exploitation of Localized Surface Plasmon Resonance," Adv. Mater. **16**, 1685 (2004)
[2] M. Osawa *et al.* "Charge Transfer Resonance Process in Surface-Enhanced Raman Scattering from *p*-Aminothiophenol Adsorbed on Silver: Herzberg-Teller Contribution," J. Phys. Chem. **98**, 12702 (1994)

Bibliography

1. Z. Gaburro, Optical interconnect. *Silicon Photonics* **94**, 121 (2004).

2. J. I. Dadap, N. C. Panoiu, X. Chen, I. W. Hsieh, X. Liu, C.-Y. Chou, E. Dulkeith, S. J. McNab, F. Xia, W. M. J. Green, L. Sekaric, Y. A. Vlasov, J. R. M. Osgood, Nonlinear-optical phase modification in dispersion-engineered Si photonic wires. *Optics Express* **16**, 1280 (2008).

3. J. Homola, S. S. Yee, G. Gauglitz, Surface plasmon resonance sensors: review. *Sens. Actuator B-Chem.* **54**, 3 (Jan, 1999).

4. J. M. Brockman, B. P. Nelson, R. M. Corn, Surface plasmon resonance imaging measurements of ultrathin organic films. *Annual Review of Physical Chemistry* **51**, 41 (2000).

5. F. Furno, K. S. Morley, B. Wong, B. L. Sharp, P. L. Arnold, S. M. Howdle, R. Bayston, P. D. Brown, P. D. Winship, H. J. Reid, Silver nanoparticles and polymeric medical devices: a new approach to prevention of infection? *Journal of Antimicrobial Chemotherapy* **54**, 1019 (2004).

6. E. Hutter, J. H. Fendler, Exploitation of localized surface plasmon resonance. *Advanced Materials* **16**, 1685 (2004).

7. M. Moskovits, Surface-enhanced Raman spectroscopy: a brief retrospective. *Journal of Raman Spectroscopy* **36**, 485 (2005).

8. A. Ramazani S.A, S. A. Mousavi, E. Seyedjafari, R. Poursalehi, S. Sareh, K. Silakhori, A. A. Poorfatollah, A. N. Shamkhali, Polycarbonate surface cell's adhesion examination after Nd:YAG laser irradiation. *Materials Science and Engineering: C* **29**, 1491 (2009).

9. A. J. Haes, D. A. Stuart, S. M. Nie, R. P. Van Duyne, Using solution-phase nanoparticles, surface-confined nanoparticle arrays and single nanoparticles as biological sensing platforms. *J. Fluoresc.* **14**, 355 (Jul, 2004).

10. Y. Dirix, C. Bastiaansen, W. Caseri, P. Smith, Oriented pearl-necklace arrays of metallic nanoparticles in polymers: A new route toward polarization-dependent color filters. *Advanced Materials* **11**, 223 (1999).

11. C. L. Haynes, R. P. Van Duyne, Dichroic optical properties of extended nanostructures fabricated using angle-resolved nanosphere lithography. *Nano Letters* **3**, 939 (2003).

12. S. R. Nicewarner-Pena, R. G. Freeman, B. D. Reiss, L. He, D. J. Pena, I. D. Walton, R. Cromer, C. D. Keating, M. J. Natan, Submicrometer metallic barcodes. *Science* **294**, 137 (2001).

13. H. Raether, *Surface Plasmons on smooth and rough surfaces and on grating*. Springer-Verlag, Ed., (Springer-Verlag, New York, 1988).

14. W. L. Barnes, A. Dereux, T. W. Ebbesen, Surface plasmon subwavelength optics. *Nature* **424**, 824 (2003).

15. H. Ditlbacher, J. R. Krenn, G. Schider, A. Leitner, F. R. Aussenegg, Two-dimensional optics with surface plasmon polaritons. *Applied Physics Letters* **81**, 1762 (Sep, 2002).

16. D. M. Koller, A. Hohenau, H. Ditlbacher, N. Galler, F. Reil, F. R. Aussenegg, A. Leitner, E. J. W. List, J. R. Krenn, Organic plasmon-emitting diode. *Nat. Photonics* **2**, 684 (Nov, 2008).

17. B. Steinberger, A. Hohenau, H. Ditlbacher, A. L. Stepanov, A. Drezet, F. R. Aussenegg, A. Leitner, J. R. Krenn, Dielectric stripes on gold as surface plasmon waveguides. *Applied Physics Letters* **88**, 081111 (Feb, 2006).

18. L. Chen, J. Shakya, M. Lipson, Subwavelength confinement in an integrated metal slot waveguide on silicon. *Opt. Lett.* **31**, 2133 (2006).

19. B. Lamprecht, J. R. Krenn, G. Schider, H. Ditlbacher, M. Salerno, N. Felidj, A. Leitner, F. R. Aussenegg, J. C. Weeber, Surface plasmon propagation in microscale metal stripes. *Applied Physics Letters* **79**, 51 (2001).

20. S. I. Bozhevolnyi, J. Erland, K. Leosson, P. M. W. Skovgaard, J. M. Hvam, Waveguiding in surface plasmon polariton band gap structures. *Physical Review Letters* **86**, 3008 (2001).

21. S. I. Bozhevolnyi, V. S. Volkov, K. Leosson, J. Erland, Observation of propagation of surface plasmon polaritons along line defects in a periodically corrugated metal surface. *Opt. Lett.* **26**, 734 (2001).

22. E. Cubukcu, E. A. Kort, K. B. Crozier, F. Capasso, Plasmonic laser antenna. *Applied Physics Letters* **89**, 093120 (Aug, 2006).

23. M. I. Stockman, Nanofocusing of optical energy in tapered plasmonic waveguides. *Physical Review Letters* **93**, 137404 (2004).

24. E. Verhagen, L. Kuipers, A. Polman, Enhanced nonlinear optical effects with a tapered plasmonic waveguide. *Nano Letters* **7**, 334 (Feb, 2007).

25. J. C. Weeber, J. R. Krenn, A. Dereux, B. Lamprecht, Y. Lacroute, J. P. Goudonnet, Near-field observation of surface plasmon polariton propagation on thin metal stripes. *Phys. Rev. B* **64**, 045411 (2001).

26. K. L. Kelly, E. Coronado, L. L. Zhao, G. C. Schatz, The optical properties of metal nanoparticles: The influence of size, shape, and dielectric environment. *J. Phys. Chem. B* **107**, 668 (2003).

27. C. F. Bohren, *Absorption and scattering of light by small particles*. VCH (Weinheim, Germany, 1940).

28. S. A. Maier, *Plasmonics: Fundamentals and Applications*. Springer, Ed., (Springer Science+ Business Media LLC, New York, 2007).

29. P. B. Johnson, R. W. Christy, OPTICAL-CONSTANTS OF NOBLE-METALS. *Phys. Rev. B* **6**, 4370 (1972).

30. C. Kittel, *Introduction to solid state physics*. (John Wiley & Sons Inc., New York, 1963), pp. 617.

31. M. M. Alvarez, J. T. Khoury, T. G. Schaaff, M. N. Shafigullin, I. Vezmar, R. L. Whetten, Optical absorption spectra of nanocrystal gold molecules. *J. Phys. Chem. B* **101**, 3706 (May, 1997).

32. S. Link, M. A. El-Sayed, Spectral properties and relaxation dynamics of surface plasmon electronic oscillations in gold and silver nanodots and nanorods. *J. Phys. Chem. B* **103**, 8410 (Oct, 1999).

33. S. Link, M. A. El-Sayed, Size and temperature dependence of the plasmon absorption of colloidal gold nanoparticles. *J. Phys. Chem. B* **103**, 4212 (May, 1999).

34. M. Barbic, J. J. Mock, D. R. Smith, S. Schultz, Single crystal silver nanowires prepared by the metal amplification method. *Journal of Applied Physics* **91**, 9341 (2002).

35. Z. L. Wang, J. M. Petroski, T. C. Green, M. A. El-Sayed, Shape transformation and surface melting of cubic and tetrahedral platinum nanocrystals. *J. Phys. Chem. B* **102**, 6145 (1998).

36. R. C. Jin, Y. W. Cao, C. A. Mirkin, K. L. Kelly, G. C. Schatz, J. G. Zheng, Photoinduced conversion of silver nanospheres to nanoprisms. *Science* **294**, 1901 (Nov, 2001).

37. C. L. Nehl, H. W. Liao, J. H. Hafner, Optical properties of star-shaped gold nanoparticles. *Nano Letters* **6**, 683 (2006).

38. C. E. Talley, J. B. Jackson, C. Oubre, N. K. Grady, C. W. Hollars, S. M. Lane, T. R. Huser, P. Nordlander, N. J. Halas, Surface-enhanced Raman scattering from individual Au nanoparticles and nanoparticle dimer substrates. *Nano Letters* **5**, 1569 (2005).

39. K. A. Willets, R. P. Van Duyne, Localized surface plasmon resonance spectroscopy and sensing. *Annual Review of Physical Chemistry* **58**, 267 (2007).

40. K. Kneipp, M. Moskovits, H. Kneipp, *Surface Enhanced Raman Scattering: Physics and Applications*. Springer-Verlag, Ed., (Berlin Heidelberg, 2006).

41. A. Campion, P. Kambhampati, Surface-enhanced Raman scattering. *Chemical Society Reviews* **27**, 241 (1998).

42. P. Kambhampati, C. M. Child, M. C. Foster, A. Campion, On the chemical mechanism of surface enhanced Raman scattering: Experiment and theory. *Journal of Chemical Physics* **108**, 5013 (1998).

43. H. Xu, J. Aizpurua, M. Käll, P. Apell, Electromagnetic contributions to single-molecule sensitivity in surface-enhanced Raman scattering. *Physical Review E* **62**, 4318 (2000).

44. M. Kerker, D. S. Wang, H. Chew, Surface Enhanced Raman Scattering (SERS) by Molecules Adsorbed at Spherical Particles. *Appl. Optics* **19**, 3373 (1980).

45. H. Xu, X.-H. Wang, M. P. Persson, H. Q. Xu, M. Käll, P. Johansson, Unified Treatment of Fluorescence and Raman Scattering Processes near Metal Surfaces. *Physical Review Letters* **93**, 243002 (2004).

46. M. I. Stockman, Inhomogeneous eigenmode localization, chaos, and correlations in large disordered clusters. *Physical Review E* **56**, 6494 (1997).

47. S. M. Nie, S. R. Emery, Probing single molecules and single nanoparticles by surface-enhanced Raman scattering. *Science* **275**, 1102 (1997).

48. K. Kneipp, Y. Wang, H. Kneipp, L. T. Perelman, I. Itzkan, R. Dasari, M. S. Feld, Single molecule detection using surface-enhanced Raman scattering (SERS). *Physical Review Letters* **78**, 1667 (1997).

49. A. M. Polubotko, The phenomenon of single-molecule detection by the SERS method and the SERS quadrupole theory. *Journal of Optics a-Pure and Applied Optics* **1**, L18 (1999).

50. M. Moskovits, Tay L., Yang J., Haslett T., in *Optical Properties of Nanostructured Random Media,* Springer, Ed. (Springer, Berlin/Heidelberg, 2002).

51. L. M. Smith, J. Z. Sanders, R. J. Kaiser, P. Hughes, C. Dodd, C. R. Connell, C. Heiner, S. B. H. Kent, L. E. Hood, Fluorescence Detection In Automated Dna-Sequence Analysis. *Nature* **321**, 674 (Jun 12, 1986).

52. D. J. Stephens, V. J. Allan, Light microscopy techniques for live cell Imaging. *Science* **300**, 82 (Apr 4, 2003).

53. P. K. Jain, X. Huang, I. H. El-Sayed, M. A. El-Sayad, Review of some interesting surface plasmon resonance-enhanced properties of noble metal nanoparticles and their applications to biosystems. *Plasmonics* **2**, 107 (Sep, 2007).

54. C. D. Geddes, H. Cao, I. Gryczynski, Z. Gryczynski, J. Y. Fang, J. R. Lakowicz, Metal-enhanced fluorescence (MEF) due to silver colloids on a planar surface: Potential applications of indocyanine green to in vivo imaging. *Journal of Physical Chemistry A* **107**, 3443 (May 8, 2003).

55. J. R. Lakowicz, Radiative decay engineering 5: metal-enhanced fluorescence and plasmon emission. *Analytical Biochemistry* **337**, 171 (Feb 15, 2005).

56. J. Kümmerlen, A. Leitner, H. Brunner, F. R. Aussenegg, A. Wokaun, Enhanced dye fluorescence over silver island films: analysis of the distance dependence. *Molecular Physics* **80**, 1031 (1993/12/10, 1993).

57. K. Sokolov, G. Chumanov, T. M. Cotton, Enhancement of Molecular Fluorescence near the Surface of Colloidal Metal Films. *Analytical Chemistry* **70**, 3898 (1998).

58. J. R. Lakowicz, J. Malicka, I. Gryczynski, Z. Gryczynski, C. D. Geddes, Radiative decay engineering: the role of photonic mode density in biotechnology. *Journal of Physics D-Applied Physics* **36**, R240 (2003).

59. K. Okamoto, S. Vyawahare, A. Scherer, Surface-plasmon enhanced bright emission from CdSe quantum-dot nanocrystals. *Journal of the Optical Society of America B-Optical Physics* **23**, 1674 (2006).

60. E. Dulkeith, A. C. Morteani, T. Niedereichholz, T. A. Klar, J. Feldmann, S. A. Levi, F. van Veggel, D. N. Reinhoudt, M. Moller, D. I. Gittins, Fluorescence quenching of dye molecules near gold nanoparticles: Radiative and nonradiative effects. *Physical Review Letters* **89**, 203002 (2002).

61. E. Dulkeith, M. Ringler, T. A. Klar, J. Feldmann, A. M. Javier, W. J. Parak, Gold nanoparticles quench fluorescence by phase induced radiative rate suppression. *Nano Letters* **5**, 585 (2005).

62. S. Haroche, D. Kleppner, Cavity quantum electrodynamics. *Physics Today* **42**, 24 (1989).

63. K. J. Vahala, Optical microcavities. *Nature* **424**, 839 (2003).

64. E. M. Purcell, Spontaneous emission probabilities at radio frequencies. *Physical Review* **69**, 681 (1946).

65. E. M. Purcell, H. C. Torrey, R. V. Pound, Resonance Absorption by Nuclear Magnetic Moments in a Solid. *Physical Review* **69**, 37 (1946).

66. J. M. Gerard, B. Gayral, Strong Purcell effect for InAs quantum boxes in three-dimensional solid-state microcavities. *Journal of Lightwave Technology* **17**, 2089 (1999).

67. A. Kress, F. Hofbauer, N. Reinelt, H. J. Krenner, M. Bichler, D. Schuh, R. Meyer, G. Abstreiter, J. J. Finley, Investigation of cavity modes and direct observation of Purcell enhancement in 2D photonic crystal defect microcavities. *Physica E: Low-dimensional Systems and Nanostructures* **26**, 351 (2005).

68. C. Hermann, O. Hess, Modified spontaneous-emission rate in an inverted-opal structure with complete photonic bandgap. *Journal of Optics Society of America B* **19**, 3013 (2002).

69. P. Bharadwaj, L. Novotny, Spectral dependence of single molecule fluorescence enhancement. *Optics Express* **15**, 14266 (Oct 17, 2007).

70. J. Zhang, J. R. Lakowicz, Metal-enhanced fluorescence of an organic fluorophore using gold particles. *Optics Express* **15**, 2598 (2007).

71. K. Okamoto, I. Niki, A. Scherer, Y. Narukawa, T. Mukai, Y. Kawakami, Surface plasmon enhanced spontaneous emission rate of InGaN/GaN quantum wells probed by time-resolved photoluminescence spectroscopy. *Applied Physics Letters* **87**, 071102 (2005).

72. K. Okamoto, I. Niki, A. Scherer, Y. Narukawa, T. Mukai, Y. Kawakami, Surface plasmon enhanced spontaneous emission rate of InGaN/GaN quantum wells probed by time-resolved photoluminescence spectroscopy. *Appl. Phys. Lett.* **87**, (Aug, 2005).

73. K. Aslan, P. Holley, C. D. Geddes, Metal-enhanced fluorescence from silver nanoparticle-deposited polycarbonate substrates. *Journal of Materials Chemistry* **16**, 2846 (2006).

74. S. Baluschev, F. Yu, T. Miteva, S. Ahl, A. Yasuda, G. Nelles, W. Knoll, G. Wegner, Metal-enhanced up-conversion fluorescence: Effective triplet-triplet annihilation near silver surface. *Nano Letters* **5**, 2482 (Dec, 2005).

75. F. Tam, G. P. Goodrich, B. R. Johnson, N. J. Halas, Plasmonic enhancement of molecular fluorescence. *Nano Letters* **7**, 496 (Feb, 2007).

76. K. Okamoto, I. Niki, A. Shvartser, Y. Narukawa, T. Mukai, A. Scherer, Surface plasmon enhanced light emitters based on InGaN quantum wells. *Nature material* **3**, 601 (2004).

77. Y. Han, R. Lupitskyy, T. Chou, C. M. Stafford, H. Du, S. A. Sukhishvili, Effect of oxidation on SERS activity of silver nanoparticles: a quantitative correlation. *Analytical Chemistry*, null (2011).

78. L. Gunnarsson, E. J. Bjerneld, H. Xu, S. Petronis, B. Kasemo, M. Kall, Interparticle coupling effects in nanofabricated substrates for surface-enhanced Raman scattering. *Applied Physics Letters* **78**, 802 (Feb 5, 2001).

79. A. G. Brolo, E. Arctander, R. Gordon, B. Leathem, K. L. Kavanagh, Nanohole-enhanced Raman scattering. *Nano Letters* **4**, 2015 (Oct, 2004).

80. T. Vo-Dinh, SERS chemical sensors and biosensors: new tools for environmental and biological analysis. *Sens. Actuator B-Chem.* **29**, 183 (1995).

81. E. J. Bjerneld, F. Svedberg, M. Kall, Laser-induced growth and deposition of noble-metal nanoparticles for surface-enhanced Raman scattering. *Nano Letters* **3**, 593 (2003).

82. T. Hasell, S. Yoda, S. M. Howdle, P. D. Brown, Microstructural characterisation of silver/polymer nanocomposites prepared using supercritical carbon dioxide. *Journal of Physics: Conference Series* **26**, 276 (2006).

83. W. X. Wang, R. M. T. Griffiths, A. Naylo, M. R. Giles, D. J. Irvine, S. M. Howdle, Preparation of cross-linked microparticles of poly(glycidyl methacrylate) by dispersion polymerization of glycidyl methacrylate using a PDMS macromonomer as stabilizer in supercritical carbon dioxide. *Polymer* **43**, 6653 (2002).

84. M. Piliakoff, S. M. Howdle, Supercritical chemistry: Synthesis with a spanner. *Chemistry in Britain*, 118 (1995).

85. J. M. H. Levelt Sengers, Ed., *Supercritical fluids*, (Kluwer Academic Publishers, 2000).

86. A. I. Cooper, Polymer synthesis and processing using carbon dioxide. *Journal of Materials Chemistry* **10**, 207 (2000).

87. K. S. Morley, P. C. Marr, P. B. Webb, A. R. Berry, F. J. Allison, G. Moldovan, P. D. Brown, S. M. Howdle, Clean preparation of nanoparticulate metals in porous supports: a supercritical route. *Journal of Materials Chemistry* **12**, 1898 (2002).

88. J. J. Watkins, T. J. McCarthy, Polymer/metal nanocomposite synthesis in supercritical CO2. *Chemistry of Materials* **7**, 1991 (1995).

89. D. Reinhard, B. D. Hall, D. Ugarte, R. Monot, Size-independent fcc-to-icosahedral structural transition in unsupported silver clusters: An electron diffraction study of clusters produced by inert-gas aggregation. *Phys. Rev. B* **55**, 7868 (1997).

90. T. Sharda, T. Soga, T. Jimbo, Optical properties of nanocrystalline diamond films by prism coupling technique. *Journal of Applied Physics* **93**, 101 (2003).

91. M. Born, E. Wolf, *Principle of optics:electromagnetic theory of propagation, interference and diffraction of light.* P. Press, Ed., (Pergamon Press, Oxford, 1964).

92. G. A. Baker, D. S. Moore, Progress in plasmonic engineering of surface-enhanced Raman-scattering substrates toward ultra-trace analysis. *Analytical and Bioanalytical Chemistry* **382**, 1751 (2005).

93. R. Petry, M. Schmitt, J. Popp, Raman Spectroscopy - A prospective tool in the life sciences. *Chemphyschem* **4**, 14 (2003).

94. T. M. Cotton, J. H. Kim, G. D. Chumanov, Application of surface-enhanced Raman spectroscopy to biological systems. *Journal of Raman Spectroscopy* **22**, 729 (1991).

95. W. Li, Y. Guo, P. Zhang, SERS-Active Silver Nanoparticles Prepared by a Simple and Green Method. *The Journal of Physical Chemistry C* **114**, 6413 (2010).

96. J. Theiss, P. Pavaskar, P. M. Echternach, R. E. Muller, S. B. Cronin, Plasmonic Nanoparticle Arrays with Nanometer Separation for High-Performance SERS Substrates. *Nano Letters* **10**, 2749 (2010).

97. W. Shi, S. Sun, X. Li, H. Ma, Imaging Different Interactions of Mercury and Silver with Live Cells by a Designed Fluorescence Probe Rhodamine B Selenolactone. *Inorganic Chemistry* **49**, 1206 (2009).

98. M. Osawa, N. Matsuda, K. Yoshii, I. Uchida, Charge-transfer resonance Raman process in surface-enhanced Raman scattering from p-aminothiophenol adsorbed on silver-Herzberg-Teller contribution. *Journal of Physical Chemistry* **98**, 12702 (1994).

99. Z. H. Zhu, T. Zhu, Z. F. Liu, Raman scattering enhancement contributed from individual gold nanoparticles and interparticle coupling. *Nanotechnology* **15**, 357 (2004).

100. W. B. Cai, B. Ren, X. Q. Li, C. X. She, F. M. Liu, X. W. Cai, Z. Q. Tian, Investigation of surface-enhanced Raman scattering from platinum electrodes using a confocal Raman microscope: dependence of surface roughening pretreatment. *Surf. Sci.* **406**, 9 (1998).

101. L. Sun, R. C. Thomas, R. M. Crooks, A. J. Ricco, Real-Time Analysis of Chemical Reactions Occurring at a Surface-Confined Organic Monolayer. *Journal of the American Chemical Society* **113**, 8550 (1991).

102. C. X. Wang, W. D. Ruan, N. Ji, W. Ji, S. Lv, C. Zhao, B. Zhao, Preparation of Nanoscale Ag Semishell Array with Tunable Interparticle Distance and Its Application in Surface-Enhanced Raman Scattering. *J. Phys. Chem. C* **114**, 2886 (Feb, 2010).

103. M. Green, F. M. Liu, SERS substrates fabricated by island lithography: The silver/pyridine system. *J. Phys. Chem. B* **107**, 13015 (Nov, 2003).

104. L. Baia, M. Baia, J. Popp, S. Astilean, Gold films deposited over regular arrays of polystyrene nanospheres as highly effective SERS substrates from visible to NIR. *J. Phys. Chem. B* **110**, 23982 (Nov, 2006).

105. F. Yan, M. B. Wabuyele, G. D. Griffin, A. A. Vass, T. Vo-Dinh, Surface-enhanced Raman scattering, detection of chemical and biological agent simulants. *Ieee Sensors Journal* **5**, 665 (2005).

106. R. M. Jarvis, R. Goodacre, Discrimination of bacteria using surface-enhanced Raman spectroscopy. *Analytical Chemistry* **76**, 40 (2004).

107. L. Jensen, G. C. Schatz, Resonance Raman Scattering of Rhodamine 6G as Calculated Using Time-Dependent Density Functional Theory. *The Journal of Physical Chemistry A* **110**, 5973 (2006).

108. H. Watanabe, N. Hayazawa, Y. Inouye, S. Kawata, DFT vibrational calculations of Rhodamine 6G adsorbed on silver: Analysis of tip-enhanced Raman spectroscopy. *J. Phys. Chem. B* **109**, 5012 (2005).

109. J. W. Kang, J. S. Kim, J. J. Kim, Optimized Oxygen Plasma Etching of Polycarbonate for Low-Loss Optical Waveguide Fabrication. *Japanese Journal of Applied Physics* **40**, 3215 (2001).

110. X. Wang, G. Grundmeier, Surface analytical studies of Ar-plasma etching of thin heptadecafluoro-1-decene plasma polymer films. *Applied Surface Science* **252**, 8331 (2006).

111. Y. Zhang, K. Aslan, S. N. Malyn, C. D. Geddes, Metal-enhanced phosphorescence (MEP). *Chemical Physics Letters* **427**, 432 (2006).

112. Y. Chen, K. Munechika, D. S. Ginger, Dependence of fluorescence intensity on the spectral overlap between fluorophores and plasmon resonant single silver nanoparticles. *Nano Letters* **7**, 690 (2007).

113. K. Ray, A. K. Dutta, T. N. Misra, Spectroscopic properties of 3-(2-benzothiazolyl)-7-octadecyloxy coumarin in Langmuir-Blodgett films. *J. Lumines.* **71**, 123 (Mar, 1997).

114. K. Aslan, Z. Leonenko, J. R. Lakowicz, C. D. Geddes, Annealed silver-island films for applications in metal-enhanced fluorescence: Interpretation in terms of radiating plasmons. *J. Fluoresc.* **15**, 643 (Sep, 2005).

115. A. S. Alekseev, T. V. Konforkina, V. V. Savransky, M. F. Kovalenko, A. Jutila, H. Lemmetyinen, Langmuir-Blodgett films of a rigidified 7-aminocoumarin derivative and their absorption and emission properties. *Langmuir* **9**, 376 (1993).

116. M. Boroditsky, R. Vrijen, T. F. Krauss, R. Coccioli, R. Bhat, E. Yablonovitch, Spontaneous emission extraction and Purcell enhancement from thin-film 2-D photonic crystals. *Journal of Lightwave Technology* **17**, 2096 (1999).

117. P. G. Lagoudakis, M. M. de Souza, F. Schindler, J. M. Lupton, J. Feldmann, J. Wenus, D. G. Lidzey, Experimental evidence for exciton scaling effects in self-assembled molecular wires. *Phys. Rev. Lett.* **93**, (Dec, 2004).

118. J. S. Biteen, D. Pacifici, N. S. Lewis, H. A. Atwater, Enhanced radiative emission rate and quantum efficiency in coupled silicon nanocrystal-nanostructured gold emitters (vol 5, 1773, 2005). *Nano Letters* **5**, 2116 (Oct, 2005).

119. J. S. Biteen, D. Pacifici, N. S. Lewis, H. A. Atwater, Enhanced radiative emission rate and quantum efficiency in coupled silicon nanocrystal-nanostructured gold emitters. *Nano Letters* **5**, 1768 (2005).

120. H. Szmacinski, K. Ray, J. R. Lakowicz, Effect of plasmonic nanostructures and nanofilms on fluorescence resonance energy transfer. *Journal of Biophotonics* **2**, 243 (2009).

121. J. V. Badding, V. Copalan, P. J. A. Sazio, Building semiconductor structures in optical fiber. *Photonics Spectra* **40**, 80 (2006).

122. G. P. Agrawal, *Fibre-Optic Communication Systems*. (John Wiley and Sons, Inc., 2002).

123. F. P. Kapron, D. B. Keck, R. D. Maurer, Radiation Losses in Glass Optical Waveguides. *Applied Physics Letters* **17**, 423 (1970).

124. G. J. Holzmann, B. Pehrson, *The Early History of Data Networks*. (IEEE ComputerSociety Press, Los Alamitos, CA, 1995).

125. J. Tyndall, On some phenomena connected with the motion of liquids. *Proceedings of the Royal Institution of Great Britain* **1**, 446 (1854).

126. J. L. Baird, BritishPatent, Ed. (1927), vol. 285.738.

127. A. C. S. Van Heel, A New Method of transporting Optical Images without Aberrations. *Nature* **173**, 39 (1954).

128. B. I. Hirschowitz, L. E. Curtiss, C. W. Peters, H. M. Pollard, Demonstration of a new gastroscope, the fiberscope. *Gastroenterology* **35**, 50; discussion 51 (1958).

129. P. Kaiser, E. A. J. Marcatili, S. E. Miller, A new optical fiber. *Bell System Technical Journal* **52**, 265 (1973).

130. T. A. Birks, P. J. Roberts, P. S. J. Russel, D. M. Atkin, T. J. Shepherd, Full 2-D photonic bandgaps in silica/air structures. *Electron. Lett.* **31**, 1941 (1995).

131. V. M. Aroutiounian, K. Martirosyan, P. Soukiassian, Almost zero reflectance of a silicon oxynitride/porous silicon double layer antireflection coating for

silicon photovoltaic cells. *Journal of Physics D-Applied Physics* **39**, 1623 (2006).

132. G. P. Agrawal, *Nonlinear Fibre Optics*. I. P. K. P.L. Kelley, G.P. Agrawal, Ed., (Academic Press, San Diego, 2001).

133. P. Mehta, N. Healy, N. F. Baril, P. J. A. Sazio, J. V. Badding, A. C. Peacock, Nonlinear transmission properties of hydrogenated amorphous silicon core optical fibers. *Optics Express* **18**, 16826 (2010).

134. C.-A. Bunge, R. Kruglov, H. Poisel, Rayleigh and Mie Scattering in Polymer Optical Fibers. *Journal of Lightwave Technology* **24**, 3137 (2006).

135. H. K. Tsang, Y. Liu, Nonlinear optical properties of silicon waveguides. *Semiconductor Science and Technology* **23**, 064007 (2008).

136. R. H. Stolen, C. Lin, Self-phase-modulation in silica optical fibers. *Physical Review A* **17**, 1448 (1978).

137. M. Fiorentino, J. E. Sharping, P. Kumar, A. Porzio, R. S. Windeler, Soliton squeezing in microstructure fiber. *Opt. Lett.* **27**, 649 (2002).

138. X. Liu, C. Xu, W. H. Knox, J. K. Chandalia, B. J. Eggleton, S. G. Kosinski, R. S. Windeler, Soliton self-frequency shift in a short tapered air-silica microstructure fiber. *Opt. Lett.* **26**, 358 (2001).

139. J. M. Dudley, G. Genty, S. Coen, Supercontinuum generation in photonic crystal fiber. *Reviews of Modern Physics* **78**, 1135 (2006).

140. E. H. Lee, K. H. Kim, H. K. Lee, Nonlinear effects in optical fiber: Advantages and disadvantages for high capacity all-optical communication application. *Optical and Quantum Electronics* **34**, 1167 (2002).

141. A. R. Chraplyvy, R. W. Tkach, in *Nonlinear Optics: Materials, Fundamentals, and Applications, 1994. NLO '94 IEEE*. (1994), pp. 302.

142. L. Yin, Q. Lin, G. P. Agrawal, Soliton fission and supercontinuum generation in silicon waveguides. *Opt. Lett.* **32**, 391 (2007).

143. L. Yin, G. P. Agrawal, Impact of two-photon absorption on self-phase modulation in silicon waveguides. *Opt. Lett.* **32**, 2031 (2007).

144. R. Dekker, N. Usechak, M. Forst, A. Driessen, Ultrafast nonlinear all-optical processes in silicon-on-insulator waveguides. *Journal of Physics D-Applied Physics* **40**, R249 (2007).

145. K. Narayanan, S. F. Preble, Optical nonlinearities in hydrogenated-amorphous silicon waveguides. *Optics Express* **18**, 8998 (2010).

146. L. G. Cohen, P. Kaiser, J. B. Macchesney, P. B. Oconnor, H. M. Presby, Transmission properties of a low-loss near-parabolic-index fiber. *Applied Physics Letters* **26**, 472 (1975).

147. P. Kaiser, A. C. Hart, L. L. Blyler, Low-loss fep-clad silica fibers. *Appl. Optics* **14**, 156 (1975).

148. P. Yeh, A. Yariv, E. Marom, Theory of Bragg fibre. *Journal of the Optical Society of America* **68**, 1196 (1978).

149. S. R. Nagel, J. B. Macchesney, K. L. Walker, An Overview of the Modified Chemical Vapor Deposition (MCVD) Process and Performance. *Ieee Journal of Quantum Electronics* **18**, 459 (1982).

150. J. C. Knight, T. A. Birks, P. S. Russell, D. M. Atkin, All-silica single-mode optical fiber with photonic crystal cladding. *Opt. Lett.* **21**, 1547 (1996).

151. J. Limpert, T. Schreiber, S. Nolte, H. Zellmer, A. Tunnermann, R. Iliew, F. Lederer, J. Broeng, G. Vienne, A. Petersson, C. Jakobsen, High-power air-clad large-mode-area photonic crystal fiber laser. *Optics Express* **11**, 818 (2003).

152. W. N. MacPherson, M. J. Gander, R. McBride, J. D. C. Jones, P. M. Blanchard, J. G. Burnett, A. H. Greenaway, B. Mangan, T. A. Birks, J. C. Knight, P. S. Russell, Remotely addressed optical fibre curvature sensor using multicore photonic crystal fibre. *Optics Communications* **193**, 97 (2001).

153. J. K. Ranka, R. S. Windeler, A. J. Stentz, Visible continuum generation in air-silica microstructure optical fibers with anomalous dispersion at 800 nm. *Opt. Lett.* **25**, 25 (Jan, 2000).

154. A. Ortigosa-Blanch, J. C. Knight, W. J. Wadsworth, J. Arriaga, B. J. Mangan, T. A. Birks, P. S. J. Russell, Highly birefringent photonic crystal fibers. *Opt. Lett.* **25**, 1325 (2000).

155. W. H. Reeves, D. V. Skryabin, F. Biancalana, J. C. Knight, P. S. Russell, F. G. Omenetto, A. Efimov, A. J. Taylor, Transformation and control of ultra-short pulses in dispersion-engineered photonic crystal fibres. *Nature* **424**, 511 (2003).

156. J. M. Fini, Microstructure fibres for optical sensing in gases and liquids. *Measurement Science & Technology* **15**, 1120 (2004).

157. R. T. Bise, R. S. Windeler, K. S. Kranz, C. Kerbage, B. J. Eggleton, D. J. Trevor, Tunable photonic band gap fiber. *Optical Fiber Communications Conference. (OFC). Postconference Technical Digest (IEEE Cat. No.02CH37339)*, 466 (2002).

158. C. Kittel, *Introduction to Solid State Physics*. (John Wiley and Sons ltd, New York, 2005).

159. R. Hull, *Properties of crystalline silicon*. R. Hull, Ed., (IET, 1999), vol. 20.

160. H. R. B. O'Mara W.C., Hunt L.P., *Handbook of semiconductor silicon technology*. (Crest Publishing House, 1990).

161. R. Soref, Mid-infrared photonics in silicon and germanium. *Nat. Photonics* **4**, 495 (2010).

162. M. Dinu, F. Quochi, H. Garcia, Third-order nonlinearities in silicon at telecom wavelengths. *Applied Physics Letters* **82**, 2954 (2003).

163. S. E. Plunkett, S. Propst, M. S. Braiman, Supported planar germanium waveguides for infrared evanescent-wave sensing. *Appl. Optics* **36**, 4055 (1997).

164. J. Vongsvivut, J. Fernandez, S. Ekgasit, M. S. Braiman, Characterization of supported cylinder-planar germanium waveguide sensors with synchrotron infrared radiation. *Applied Spectroscopy* **58**, 143 (2004).

165. O. Vendier, S. W. Bond, Y. Lee, S. Jung, M. Brooke, N. M. Jokerst, R. P. Leavitt, Stacked silicon CMOS circuits with a 40-Mb/s through-silicon optical interconnect. *IEEE Photonics Technol. Lett.* **10**, 606 (Apr, 1998).

166. U. Fischer, T. Zinke, J. R. Kropp, F. Arndt, K. Petermann, 0.1 dB/cm waveguide losses in single-mode SOI rib waveguides. *IEEE Photonics Technol. Lett.* **8**, 647 (May, 1996).

167. K. K. Lee, D. R. Lim, L. C. Kimerling, J. Shin, F. Cerrina, Fabrication of ultralow-loss Si/SiO2 waveguides by roughness reduction. *Opt. Lett.* **26**, 1888 (2001).

168. J. Cardenas, C. B. Poitras, J. T. Robinson, K. Preston, L. Chen, M. Lipson, Low loss etchless silicon photonic waveguides. *Optics Express* **17**, 4752 (2009).

169. Y. A. Vlasov, S. J. McNab, Losses in single-mode silicon-on-insulator strip waveguides and bends. *Optics Express* **12**, 1622 (19 April, 2004).

170. K. K. Lee, D. R. Lim, H. C. Luan, A. Agarwal, J. Foresi, L. C. Kimerling, Effect of size and roughness on light transmission in a Si/SiO2 waveguide: Experiments and model. *Applied Physics Letters* **77**, 1617 (Sep, 2000).

171. F. P. Payne, J. P. R. Lacey, A theoretical analysis of scattering loss from planar optical waveguides. *Optical and Quantum Electronics* **26**, 977 (1994).

172. D. K. Sparacin, S. J. Spector, L. C. Kimerling, Silicon waveguide sidewall smoothing by wet chemical oxidation. *Journal of Lightwave Technology* **23**, 2455 (2005).

173. D. Liang, J. E. Bowers, Recent progress in lasers on silicon. *Nat. Photonics* **4**, 511 (2010).

174. H. S. Rong, Y. H. Kuo, S. B. Xu, A. S. Liu, R. Jones, M. Paniccia, Monolithic integrated Raman silicon laser. *Optics Express* **14**, 6705 (Jul, 2006).

175. B. Jalali, S. Fathpour, Silicon photonics. *Journal of Lightwave Technology* **24**, 4600 (Dec, 2006).

176. R. Claps, D. Dimitropoulos, V. Raghunathan, Y. Han, B. Jalali, Observation of stimulated Raman amplification in silicon waveguides. *Optics Express* **11**, 1731 (2003).

177. O. Boyraz, B. Jalali, Demonstration of a silicon Raman laser. *Optics Express* **12**, 5269 (2004).

178. T. K. Liang, H. K. Tsang, Role of free carriers from two-photon absorption in Raman amplification in silicon-on-insulator waveguides. *Applied Physics Letters* **84**, 2745 (2004).

179. R. Claps, V. Raghunathan, D. Dimitropoulos, B. Jalali, Influence of nonlinear absorption on Raman amplification in Silicon waveguides. *Optics Express* **12**, 2774 (2004).

180. H. S. Rong, A. S. Liu, R. Nicolaescu, M. Paniccia, O. Cohen, D. Hak, Raman gain and nonlinear optical absorption measurements in a low-loss silicon waveguide. *Applied Physics Letters* **85**, 2196 (2004).

181. Q. Lin, O. J. Painter, G. P. Agrawal, Nonlinear optical phenomena in silicon waveguides: Modeling and applications. *Optics Express* **15**, 16604 (2007).

182. H. S. Rong, R. Jones, A. S. Liu, O. Cohen, D. Hak, A. Fang, M. Paniccia, A continuous-wave Raman silicon laser. *Nature* **433**, 725 (2005).

183. M. Lipson, Guiding, modulating, and emitting light on silicon - Challenges and opportunities. *Journal of Lightwave Technology* **23**, 4222 (Dec, 2005).

184. T. Barwicz, M. A. Popovic, M. R. Watts, P. T. Rakich, E. P. Ippen, H. I. Smith, Fabrication of add-drop filters based on frequency-matched microring resonators. *Journal of Lightwave Technology* **24**, 2207 (2006).

185. J. Leuthold, C. Koos, W. Freude, Nonlinear silicon photonics. *Nat. Photonics* **4**, 535 (2010).

186. P. Koonath, D. R. Solli, B. Jalali, Continuum generation and carving on a silicon chip. *Applied Physics Letters* **91**, 061111 (2007).

187. N. M. Jokerst, L. Luan, S. Palit, M. Royal, S. Dhar, M. A. Brooke, T. Tyler, Progress in Chip-Scale Photonic Sensing. *IEEE Trans. Biomed. Circuits Syst.* **3**, 202 (Aug, 2009).

188. M. S. Luchansky, R. C. Bailey, Silicon Photonic Microring Resonators for Quantitative Cytokine Detection and T-Cell Secretion Analysis. *Analytical Chemistry* **82**, 1975 (Mar, 2010).

189. R. Soref, The past, present, and future of silicon photonics. *Ieee Journal of Selected Topics in Quantum Electronics* **12**, 1678 (2006).

190. B. Jalali, V. Raghtmathan, R. Shori, S. Fathpour, D. Dimitropoulos, O. Stafsudd, Prospects for silicon mid-IR Raman lasers. *Ieee Journal of Selected Topics in Quantum Electronics* **12**, 1618 (2006).

191. V. Raghunathan, D. Borlaug, R. R. Rice, B. Jalali, Demonstration of a mid-infrared silicon Raman amplifier. *Optics Express* **15**, 14355 (2007).

192. R. A. Soref, S. J. Emelett, A. R. Buchwald, Silicon waveguided components for the long-wave infrared region. *Journal of Optics a-Pure and Applied Optics* **8**, 840 (2006).

193. R. Hanna, Infrared Absorption Spectrum of Silicon Dioxide. *Journal of the American Ceramic Society* **48**, 595 (1965).

194. P. Y. Yang, S. Stankovic, J. Crnjanski, T. Ee, D. Thomson, A. Bettiol, M. Breese, W. Headley, C. Giusca, G. Reed, G. Mashanovich, Silicon photonic waveguides for mid- and long-wave infrared region. *Journal of Materials Science: Materials in Electronics*, 159 (2009).

195. L. Colace, G. Masini, A. Altieri, G. Assanto, Waveguide photodetectors for the near-infrared in polycrystalline germanium on silicon. *IEEE Photonics Technol. Lett.* **18**, 1094 (2006).

196. S. Assefa, F. N. Xia, S. W. Bedell, Y. Zhang, T. Topuria, P. M. Rice, Y. A. Vlasov, CMOS-integrated high-speed MSM germanium waveguide photodetector. *Optics Express* **18**, 4986 (2010).

197. T. Yin, R. Cohen, M. M. Morse, G. Sarid, Y. Chetrit, D. Rubin, M. J. Paniccia, 31GHz Ge n-i-p waveguide photodetectors on Silicon-on-Insulator substrate. *Optics Express* **15**, 13965 (2007).

198. G. Masini, S. Sahni, G. Capellini, J. Witzens, C. Gunn, High speed near infrared optical receivers based on Ge waveguide photodetectors integrated in a CMOS process. *Advances in Optical Technologies*, 196572 (2008).

199. J. Michel, J. F. Liu, L. C. Kimerling, High-performance Ge-on-Si photodetectors. *Nat. Photonics* **4**, 527 (2010).

200. L. Chen, M. Lipson, Ultra-low capacitance and high speed germaniumphotodetectors on silicon. *Optics Express* **17**, 7901 (2009).

201. D. Ahn, C.-y. Hong, J. Liu, W. Giziewicz, M. Beals, L. C. Kimerling, J. Michel, J. Chen, F. X. Kärtner, High performance, waveguide integrated Ge photodetectors. *Optics Express* **15**, 3916 (2007).

202. H. R. Philipp, E. A. Taft, Optical Constants of Germanium in the Region 1 to 10 ev. *Physical Review* **113**, 1002 (1959).

203. M. J. A. de Dood, A. Polman, T. Zijlstra, E. van der Drift, Amorphous silicon waveguides for microphotonics. *Journal of Applied Physics* **92**, 649 (2002).

204. M. Mulato, I. Chambouleyron, E. G. Birgin, J. M. Martinez, Determination of thickness and optical constants of amorphous silicon films from transmittance data. *Applied Physics Letters* **77**, 2133 (2000).

205. G. D. Cody, T. Tiedje, B. Abeles, B. Brooks, Y. Goldstein, Disorder and the optical absorption edge of hydrogenated amorphous silicon. *Physical Review Letters* **47**, 1480 (1981).

206. R. A. Street, *Hydrogenated amorphous silicon*. (Cambridge University Press, 1991).

207. W. S. Wong, S. E. Ready, J. P. Lu, R. A. Street, Hydrogenated amorphous silicon thin-film transistor arrays fabricated by digital lithography. *Ieee Electron Device Letters* **24**, 577 (2003).

208. A. Harke, M. Krause, J. Mueller, Low-loss singlemode amorphous silicon waveguides. *Electron. Lett.* **41**, 1377 (Dec, 2005).

209. S. Rong, C. Jing, J. Michel, L. Kimerling, Transparent amorphous silicon channel waveguides and high-Q resonators using a damascene process. *Opt. Lett.* **34**, 2378 (1 August, 2009).

210. G. Cocorullo, F. G. DellaCorte, I. Rendina, C. Minarini, A. Rubino, E. Terzini, Amorphous silicon waveguides and light modulators for integrated photonics realized by low-temperature plasma-enhanced chemical-vapor deposition. *Opt. Lett.* **21**, 2002 (Dec, 1996).

211. S. K. Selvaraja, E. Sleeckx, M. Schaekers, W. Bogaerts, D. V. Thourhout, P. Dumon, R. Baets, Low-loss amorphous silicon-on-insulator technology for photonic integrated circuitry. *Optics Communications* **282**, 1767 (2009).

212. J. S. Foresi, M. R. Black, A. M. Agarwal, L. C. Kimerling, Losses in polycrystalline silicon waveguides. *Applied Physics Letters* **68**, 2052 (Apr, 1996).

213. A. Shah, P. Torres, R. Tscharner, N. Wyrsch, H. Keppner, Photovoltaic Technology: The Case for Thin-Film Solar Cells. *Science* **285**, 692 (July 30, 1999, 1999).

214. L. Liao, D. R. Lim, A. M. Agarwal, X. M. Duan, K. K. Lee, L. C. Kimerling, Optical transmission losses in polycrystalline silicon strip waveguides: Effects of waveguide dimensions, thermal treatment, hydrogen passivation, and wavelength. *Journal of Electronic Materials* **29**, 1380 (2000).

215. A. M. Agarwal, L. Liao, J. S. Foresi, M. R. Black, X. M. Duan, L. C. Kimerling, Low-loss polycrystalline silicon waveguides for silicon photonics. *Journal of Applied Physics* **80**, 6120 (Dec, 1996).

216. K. Preston, S. Manipatruni, A. Gondarenko, C. B. Poitras, M. Lipson, Deposited silicon high-speed integrated electro-optic modulator. *Optics Express* **17**, 5118 (2009).

217. K. Preston, B. Schmidt, M. Lipson, Polysilicon photonic resonators for large-scale 3D integration of optical networks. *Optics Express* **15**, 17283 (2007).

218. K. Preston, P. Dong, B. Schmidt, M. Lipson, High-speed all-optical modulation using polycrystalline silicon microring resonators. *Applied Physics Letters* **92**, 151104 (Apr, 2008).

219. P. J. A. Sazio, A. Amezcua-Correa, C. E. Finlayson, J. R. Hayes, T. J. Scheidemantel, N. F. Baril, B. R. Jackson, D. J. Won, F. Zhang, E. R. Margine, V. Gopalan, V. H. Crespi, J. V. Badding, Microstructured optical fibers as high-pressure microfluidic reactors. *Science* **311**, 1583 (2006).

220. B. J. Eggleton, B. Luther-Davies, K. Richardson, Chalcogenide photonics. *Nat Photon* **5**, 141 (2011).

221. P. A. Thielen, L. B. Shaw, P. C. Pureza, V. Q. Nguyen, J. S. Sanghera, I. D. Aggarwal, Small-core As-Se fiber for Raman amplification. *Opt. Lett.* **28**, 1406 (2003).

222. F. S. d. Aragona, Dislocation Etch for (100) Planes in Silicon. *Journal of The Electrochemical Society* **119**, 948 (1972).

223. A. C. Jones, P. O'Brien, *CVD of compound semiconductors. Precursor synthesis, development and applications*. A. C. Jones, P. O'Brien, Eds., CVD of compound semiconductors. Precursor synthesis, development and applications (Wiley-VCH Verlag GmbH, 1997), pp. 352.

224. N. R. B. Coleman, M. A. Morris, T. R. Spalding, J. D. Holmes, The formation of dimensionally ordered silicon nanowires within mesoporous silica. *Journal of the American Chemical Society* **123**, 187 (2001).

225. N. R. B. Coleman, K. M. Ryan, T. R. Spalding, J. D. Holmes, M. A. Morris, The formation of dimensionally ordered germanium nanowires within mesoporous silica. *Chemical Physics Letters* **343**, 1 (2001).

226. A. Amezcua-Correa, A. C. Peacock, J. Yang, P. J. A. Sazio, S. M. Howdle, Loss measurements of microstructured optical fibres with metal-nanoparticle inclusions. *Electron. Lett.* **44**, 795 (2008).

227. A. C. Peacock, A. Amezcua-Correa, Y. Jixin, P. J. A. Sazio, S. M. Howdle, Highly efficient surface enhanced Raman scattering using microstructured optical fibers with enhanced plasmonic interactions. *Applied Physics Letters*, 141113 (2008).

228. C. E. Finlayson, A. Amezcua-Correa, P. J. A. Sazio, N. F. Baril, J. V. Badding, Electrical and Raman characterization of silicon and germanium-filled microstructured optical fibers. *Applied Physics Letters* **90**, (Mar, 2007).

229. D. J. Won, M. O. Ramirez, H. Kang, V. Gopalan, N. F. Baril, J. Calkins, J. V. Badding, P. J. A. Sazio, All-optical modulation of laser light in amorphous silicon-filled microstructured optical fibers. *Applied Physics Letters* **91**, 161112 (2007).

230. M. H. Brodsky, M. Cardona, J. J. Cuomo, Infrared and Raman spectra of silicon-hydrogen bonds in amorphous silicon prepared by glow-discharge and sputtering. *Phys. Rev. B* **16**, 3556 (1977).

231. V. N. Denisov, B. N. Mavrin, M. Koosh, I. Pochik, Raman scattering in hydrogenated amorphous silicon films. *Journal of Applied Spectroscopy* **55**, 1037 (1991).

232. Z. G. Meng, Z. H. Jin, G. A. Bhat, P. Chu, H. S. Kwok, M. Wong, On the formation of solid state crystallized intrinsic polycrystalline germanium thin films. *Journal of Materials Research* **12**, 2548 (1997).

233. S. Sakaguchi, S. i. Todoroki, S. Shibata, Rayleigh Scattering in Silica Glasses. *Journal of the American Ceramic Society* **79**, 2821 (1996).

234. P. Roberts, F. Couny, H. Sabert, B. Mangan, D. Williams, L. Farr, M. Mason, A. Tomlinson, T. Birks, J. Knight, P. St. J. Russell, Ultimate low loss of hollow-core photonic crystal fibres. *Optics Express* **13**, 236 (2005).

235. B. Jalali, V. Raghunathan, D. Dimitropoulos, O. Boyraz, Raman-based silicon photonics. *Ieee Journal of Selected Topics in Quantum Electronics* **12**, 412 (2006).

236. K. M. Hung, J. Y. Kuo, C. C. Hong, H. H. Cheng, G. Sun, R. A. Soref, Carrier dynamics of terahertz emission based on strained SiGe/Si single quantum well. *Applied Physics Letters* **96**, 213502 (2010).

237. R. Soref, in *Proceedings of the SPIE - The International Society for Optical Engineering*. (2005), vol. 5730.

238. H. Mertens, J. S. Biteen, H. A. Atwater, A. Polman, Polarization-Selective Plasmon-Enhanced Silicon Quantum-Dot Luminescence. *Nano Letters* **6**, 2622 (2006).

239. J. S. Biteen, N. S. Lewis, H. A. Atwater, H. Mertens, A. Polman, Spectral tuning of plasmon-enhanced silicon quantum dot luminescence. *Applied Physics Letters* **88**, 131109 (2006).

240. S. Pillai, K. R. Catchpole, T. Trupke, M. A. Green, Surface plasmon enhanced silicon solar cells. *Journal of Applied Physics* **101**, 093105 (2007).